# Numerical Investigation on the Aerodynamic Impact of Parametric Tire Deformations

## A statistical and vortex identification-based analysis approach

Alejandro Martinez Navarro

Delft University of Technology

TU Delft

# Numerical Investigation on the Aerodynamic Impact of Parametric Tire Deformations

## A statistical and vortex identification-based analysis approach

by

Alejandro Martinez Navarro

to obtain the degree of Master of Science

at the Delft University of Technology,

to be defended publicly on Tuesday November 19th, 2024 at 12:45h.


| | | |
|---|---|---|
| Student number: | 5605881 | |
| Thesis supervisors: | Prof. dr. ir. M.I. Gerritsma, | TU Delft, supervisor |
| | Prof. dr. D. Casalino, | TU Delft |
| | Ir. G. Parenti, | Dassault Systèmes® |
| Institution: | Delft University of Technology | |
| Place: | Faculty of Aerospace Engineering, Delft | |
| | Dassault Systèmes®, Lund | |


An electronic version of this thesis is available at http://repository.tudelft.nl/.

TU Delft

# Abstract

As the automotive industry increasingly shifts toward electrification, reducing vehicle drag becomes crucial for enhancing battery range and meeting consumer expectations. Additionally, recent European regulations require tire and car manufacturers to provide reliable drag data. A significant factor influencing vehicle drag is the highly turbulent wake generated by rotating tires. Accurate correlation between wind tunnel experiments and numerical simulations is essential, yet discrepancies often arise due to the dynamic behaviour and technical challenges in measuring tire deformation, leading to inconsistencies between tire deformations observed in wind tunnels and those modelled in simulations.

This Master's Thesis investigates the aerodynamic impact of realistic tire deformation parameters—specifically, bulge and contact patch deformations—using Computational Fluid Dynamics (CFD) simulations conducted with PowerFLOW®. The deformation parameter tests are carried out in a standalone tire setup, which is validated from previous work by Dassault Systèmes® and experimental results obtained by Schenpf et al. [55]. To further assess the impact of these deformations on vehicle drag, the tests were repeated using the *DrivAer* model, an IP free model provided by the Technical University of Munich. Given the complexity of the flow features in a tire wake, the analysis of the results consisted of two different approaches: a statistical approach based on Principal Component Analysis (PCA), and a vortex behaviour and wake development analysis, including a vortex tracking algorithm based on the $\Gamma_2$-Criterion and single-link hierarchical clustering.

The results identify the most influential deformation parameters based on their impact on the drag coefficient and the wake behaviour changes. Two primary wake development behaviours were identified: wake contraction and wake expansion. An analysis of the transient flow showed how these two trends resulted from changes in the unsteady behaviour introduced by certain deformation parameters. The relevance of these wake development changes was portrayed by the impact of certain deformations on the full vehicle drag as a result of complex wake interactions.

# Preface

This report marks the culmination of my Master's degree, as its completion fulfils the requirements for the Master of Science in Aerospace Engineering at Delft University of Technology.

Firstly, I would like to express my sincere gratitude to my supervisors, Prof. dr. ir. M.I. Gerritsma, Prof. dr. D. Casalino, and G. Parenti, for their unwavering support and guidance, which have been crucial to the successful completion of this work. I would also like to extend my appreciation to Dassault Systèmes®, for giving me the opportunity to complete my internship and Master's thesis in collaboration with them.

I am grateful for the friendships formed throughout this incredible journey in the Master's program at TU Delft. We have shared late, stressful evenings preparing for exams and meeting deadlines, as well as memorable moments in Delft, Stuttgart and Lund.

At the time of writing, two weeks have passed since the devastating floods in my home town of Valencia, where hundreds have lost their lives, and many are still missing. My thoughts are with the victims of this catastrophe, which will require months of recovery efforts. I would like to express my heartfelt sympathy to my friends and neighbours who have lost their homes, and in the worst cases, their loved ones. Please know that I will soon be with you, helping clear the mud and debris from the streets and parks where we once played together in our childhood.

*"Allò que val és la consciència*
*de no ser res si no s'és poble."*

Vicent Andrés Estellés, *Assumiràs la veu d'un poble*

Finalmente, quiero agradecer a mi familia todo el apoyo y cariño que me han brindado durante estos años que he pasado lejos de casa. Gracias por creer en mí y permitirme seguir el camino que consideré correcto. Lamento haberme perdido momentos importantes de vuestras vidas y no haber estado con vosotros en los últimos momentos de Noah, quien se fue demasiado pronto.

*Alejandro Martinez Navarro*
*Lund, November 2024*

# Contents

# List of Figures

# List of Tables

# Nomenclature

## Abbreviations

| Abbreviation | Definition |
|---|---|
| *BC* | Boundary Condition |
| *BCs* | Boundary Conditions |
| *CAD* | Computer-Aided Design |
| *CFD* | Computational Fluid Dynamics |
| *DRTT* | Deformable Rotating Treaded Tire |
| *IBM* | Immersed Boundary Method |
| *IP* | Intellectual Property |
| *LDA* | Laser Doppler Anemometry |
| *LBM* | Lattice-Boltzmann Method |
| *MRF* | Moving Reference Frame |
| *MRFg* | Moving Reference Frame - grooved |
| *OEMs* | Original Equipment Manufacturers |
| *PCA* | Principal Components Analysis |
| *PCs* | Principal Components |
| *PDF* | Particle Distribution Function |
| *PIV* | Particle Image Velocimetry |
| *RANS* | Reynolds-Averaged Navier Stokes |
| *RTT* | Rotating Treaded Tire |
| *RW* | Rotating Wall |
| *SVD* | Singular Value Decomposition |
| *SM* | Sliding Mesh |
| *URANS* | Unsteady Reynolds-Averaged Navier Stokes |
| *VR* | Variable Resolution |
| *WLTP* | Harmonised Light Vehicle Test Procedure [1] |

## Greek Symbols

| Symbol | Definition | Unit |
|---|---|---|
| $\Delta$ | Vortex identification function, $\Delta$-Criterion | [$s^{-2}$] |
| $\Delta_t$ | Time step | [s] |
| $\Delta_{x_c}$, $\Delta_{y_c}$ | Cartesian components of the centre distance to the theoretical centre | [m] |
| $\epsilon$ | Turbulent dissipation | [$m^2/s^3$] |
| $\gamma$ | Maximum circulation criterion | [$m^2/s$] |
| $\Gamma$ | Circulation | [$m^2/s$] |
| $\Gamma_1$ | Vortex identification function by Michard et al. [26] | [-] |
| $\Gamma_2$ | Vortex identification function, Galilean invariant, by Michard et al. [26] | [-] |
| $\lambda$ | Mean free path | [m] |
| $\mu$ | Dynamic Viscosity | [kg/m· s] |
| $\nu$ | Kinematic viscosity | [$m^2/s$] |
| $\rho$ | Air density | [$kg/m^3$] |

# Latin Symbols

| Symbol | Definition | Unit |
|---|---|---|
| $A_x$ | Vehicle reference area in the $x$-direction | [m$^2$] |
| $a$ | Speed of sound | [m/s] |
| $C_{D_l}$ | Microdrag | [-] |
| $C_D$ | Drag Coefficient | [-] |
| $C_L$ | Lift Coefficient | [-] |
| $C_{tot}$ | Total pressure coefficient | [-] |
| $C_x$, $C_y$, $C_z$ | Force coefficient in $x/y/z$-direction | [-] |
| $C_{M_x}$, $C_{M_y}$, $C_{M_z}$ | Moment coefficient in $x/y/z$-direction | [-] |
| $D$ | Wheel diameter | [m] |
| $d_c$ | Theoretical centre of the vortex | [m] |
| $F_x$, $F_y$, $F_z$ | Force in $x/y/z$-direction | [N] |
| $k$ | Turbulent kinetic energy | [m$^2$/s$^2$] |
| $Kn$ | Knudsen number | [-] |
| $L$ | Reference length | [m] |
| $L_c$ | Characteristic length | [m] |
| $M_x$, $M_y$, $M_z$ | Moment in $x/y/z$-direction | [N· m] |
| $Ma$ | Mach number | [-] |
| $p$ | Static Pressure | [Pa] |
| $p_{tot}$ | Total Pressure | [Pa] |
| $q$ | Dynamic pressure | [Pa] |
| $Re$ | Reynolds number | [-] |
| $R$ | Specific gas constant | [J/kg· K] |
| $T$ | Temperature | [K] |
| $U_\infty$ | Free stream velocity | [m/s] |
| $u$, $v$, $w$ | Velocity components in the $x/y/z$-direction | [m/s] |
| $u_c$ | Characteristic velocity | [m/s] |

# 1

# Introduction

With the increasing electrification of road vehicles, the automotive industry finds itself in the need to significantly reduce the drag produced by cars to enhance battery range and attract consumers. Moreover, governments in Europe are introducing regulations to compel car manufacturers to provide more reliable drag data. An example of these regulations is the Harmonised Light Vehicle Test Procedure (WLTP) [1], ensuring manufacturers provide emission values for every vehicle in every configuration, including tires and rims. This combination of new regulations and the increased relevance of drag underscores the necessity for Original Equipment Manufacturers (OEMs) to deliver precise drag results, meeting customer range expectations.

A critical factor influencing the drag of road vehicles is the interaction of the tires and their turbulent wake with the rest of the vehicle. Tires, as bluff rotating bodies positioned near the car's under body (an aerodynamically sensitive area due to its proximity to the ground) significantly affect the vehicle's overall drag. To achieve more precise drag results, optimising both experimental and numerical methodologies for aerodynamic prediction becomes crucial. Companies like Dassault Systemes® play a pivotal role providing accurate simulation technology with their fluid mechanics software PowerFLOW®. OEMs use PowerFLOW® for numerical simulations (that is, CFD simulations), comparing results with experimental data obtained in wind tunnels. A good correlation between wind tunnel and numerical simulation results is essential, as it increases confidence on the accuracy of the simulation results. However, the dynamic behaviour and technical difficulties to accurately measure tire deformation introduce discrepancies between the tire deformations existing in wind tunnels and the tire geometries used in numerical simulations. The current understanding on the aerodynamic implications of tire deformation is limited, especially in deformations involving multiple varying parameters, making it challenging to identify the key contributors to flow alteration and aerodynamic forces. Enhancing this understanding helps manufacturers and software developers create more robust simulation methodologies with a high potential for good correlation with experimental data.

The present project has been designed to address gaps in knowledge, identified by previous research discussed in Part I, concerning the impact of each geometrical parameter in a realistically deformed tire from a numerical standpoint. Utilising the digital environment facilitated by PowerDELTA® (the meshing tool for PowerFLOW®) permits the implementation of controlled deformations, wherein several geometrical parameters are isolated and systematically varied in magnitude. This presents an advantage over experimental methodologies, where it is notably challenging to isolate the geometrical parameters of tire deformation. The approach taken enhances the identification of each parameter's contribution to flow alteration. Through the undertaking of this project, insights are sought to be provided that will widen the understanding of the aerodynamic effects of tire deformation, contributing to the development of more accurate and reliable simulation methodologies.

## 1.1. Report Outline

Part I reviews and discusses the existing literature on tire aerodynamics, numerical modelling of rotating tires and useful analysis methodologies for such complex flow fields. From the discussion on the existing literature and the gaps identified, the research objective and research questions are proposed. Part II describes the parametrisation technique applied to create the parametric tire deformation tests, followed by the description of the numerical

method implemented in the simulations, together with its respective simulation setup description. The analysis methodologies and how they are implemented to the obtained simulation results are also covered in this part, going from the statistical approach of PCA, to the vortex identification method $\Gamma_2$ and the vortex centre identification algorithm. The simulation results are processed with these methodologies and discussed in Part III. Finally, Part IV addresses the research questions proposed in Part I with the discussion of results from Part III, giving recommendations for future work in the topic of this project.

# Part I

# Literature Review

# 2

# Previous Aerodynamics Studies

Although the flow topology over a wheel highly resembles the flow topology over a bluff body such as a cylinder due to the shape aspect ratio (width over height) of a tire's cross section, the presence of wheel related geometries and rotation introduce a higher degree of complexity to the flow over the tire with various separation points and vortex shedding. The aerodynamics of rotating wheels are a complex problem to study both experimentally and numerically, and over the years, advancements in modelling and flow analysis techniques have allowed to improve understanding of the flow topology of rotating wheels and the flow mechanisms that are relevant in the pressure distribution over the tire and the aerodynamic forces and coefficients.

Schütz [56] indicated that an important factor influencing the wheel's aerodynamic drag is the tire width, attributing 3 drag coefficient counts for every 5mm of width, assuming an unchanged front face and in the same incoming flow conditions. Wittmeier et al. [69] went further in the evaluation of the impact of geometric parameters of the tire on drag, where he concluded that the tire shoulder radius and the sidewall shape can significantly influence the flow around the tire, and eventually, the wheel's drag. Figure 2.1 below shows the aforementioned geometrical parameters in the cross section of the tire.

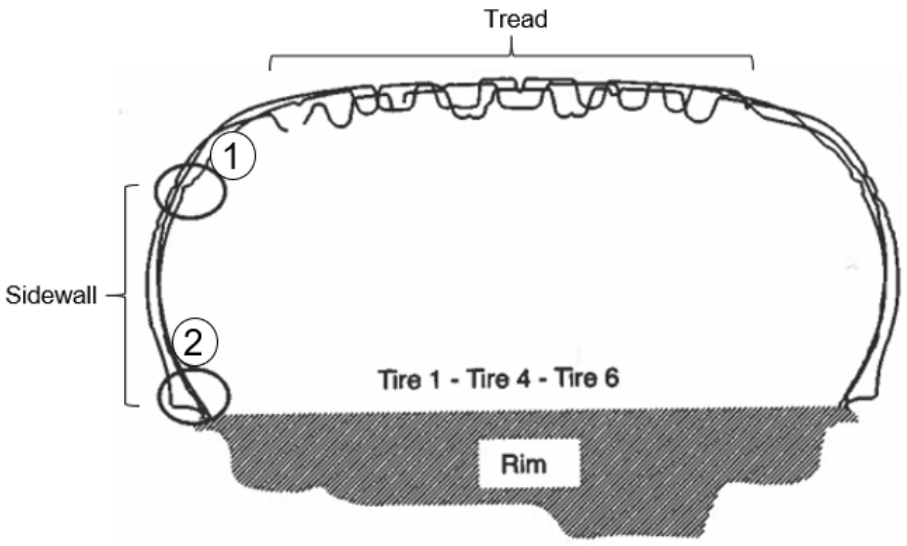


**Figure 2.1:** Cross-sections of 3 tires are superimposed. Circled region 1 refers to tire shoulder, circled region 2 referring to rim cover. Tread and sidewall extensions indicated. Image by Wittmeier et al. [69].

The wheel's mean flow topology can vary considerably depending on the surrounding geometric environment and wheel related geometries, which represent either the test setup, the vehicle on which the wheel is mounted,

or the wheel rim. These discrepancies have resulted in certain different conclusions on the resulting mean flow structures around wheels measured by researchers.

## 2.1. Isolated Rotating Wheel

Some of the earliest work on tire aerodynamics study was carried out by Fackrell et al. [23, 24, 25], focused on determining the forces and pressure distribution on the wheel through experimental tests. As stated previously, different conclusions on the mean flow structures were reported by researchers. However, Parfett et al. [46] found a general consensus of a schematic representation of the flow field around an isolated rotating wheel presented by Wäschle et al. [65, 67], who carried out numerical (referring to Computational Fluid Dynamics, CFD) and experimental studies, with measurements using Laser Doppler Anemometry (LDA) and oil-streak visualisation on the tire surface, on a set of tests for rotating and stationary wheels both in isolation and mounted on a vehicle.

Figure 2.6 shows the resulting mean flow obtained by Wäschle et al. [65, 67], where it is visible that the wake is dominated by counter rotating longitudinal trailing vortices (marked 2 in Figure 2.2), which are fed by the backflow close to the ground. This vortex pair is called the wake's horseshoe vortex, and is mainly responsible for the induced drag. These vortices generate a downwash behind the tire. However, this downwash is limited by transfer of momentum caused by the rotation of the tire and the viscosity effects, transporting air from the wheel wake against the inflow direction towards the front. This results in the separation of the flow at the tire's rear shoulders, forming the vortex ring (marked 3 in Figure 2.2) in the upper half of the wheel's immediate wake.

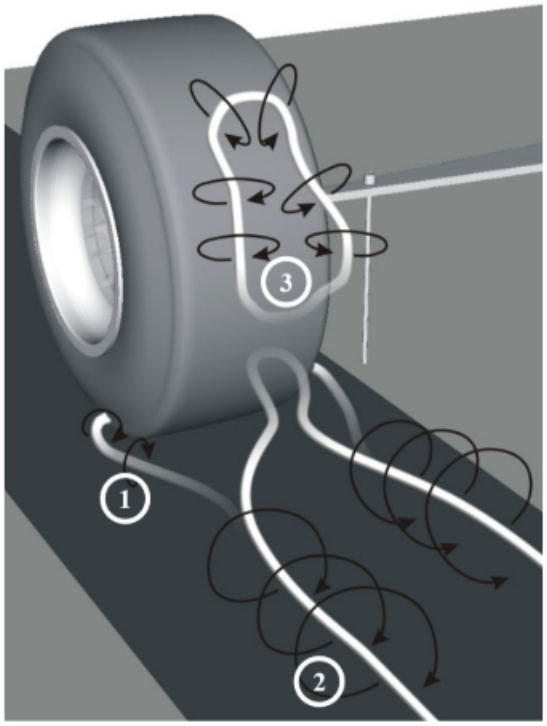


**Figure 2.2:** Vortex structures of an isolated rotating smooth tire by Wäschle et al. [65, 67].

Finally, at the very bottom, another vortex pair is formed at the contact patch (marked 1 in Figure 2.2), resulting from the front shoulders in the contact region of the tire with the ground, where air is transported from the bottom wake through the local separation occurring and mixes with the free-stream to originate these vortices. The contact patch counter rotating vortices cause the "jetting effect" of the flow around the tire contact patch.

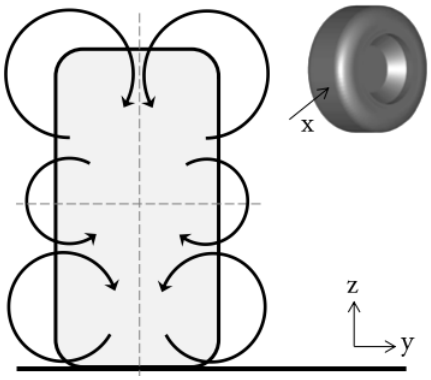


**Figure 2.3:** Vortex structures right behind an isolated rotating smooth tire by Diasinos et al. [20].

The vortical structure described by Wäschle et al. [65, 67] mostly agrees with the one described by Diasinos et al. [20], where as shown in Figure 2.3, three counter-rotating vortex pairs were observed, with the main wake horseshoe vortex generated at the tire base, while another vortex pair appeared at the wheel's mid-height, and the already discussed vortex pair at the top of the tire. As Wäschle et al. [67] described, at the top half of the wake of the wheel, in a rotating wheel, a vortex ring is formed. Therefore, it is possible that the mid-height vortices described by Diasinos et al. [20] actually belong within the vortex ring of the wake's upper half. However, these mid-height vortices could also be forming from the shoulder separation at the front mid-height, which is one of the flow topology discrepancies discussed at the beginning of this section, caused by the rim geometrical differences. These mid-height vortices, caused by the shoulder separation, were identified by Mercker and Berneburg [39] in their proposed vortex system of a rotating wheel, which can be seen in Figure 2.4, and they show in the absence of a rim geometry.

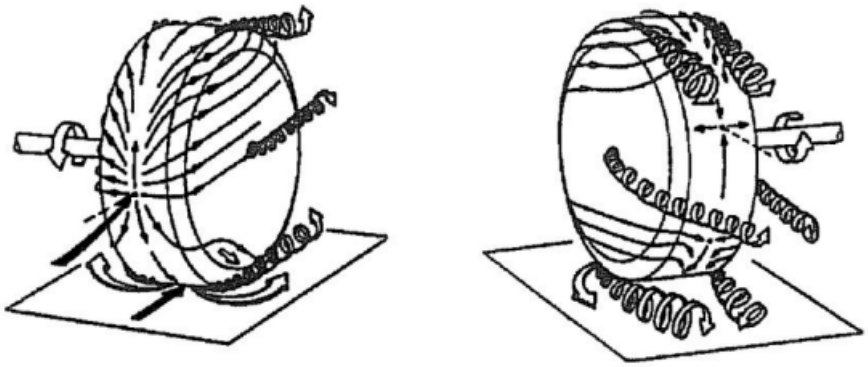

**Figure 2.4:** Vortex structures around an isolated rotating smooth tire by Mercker and Berneburg [39]. Front view on the right, rear view on the left.

Results obtained by Croner et al. [17][18], where experimental results and numerical results of an isolated rotating tire were compared with $\Gamma_2$ plots for an $x$-aligned plane right behind the wheel shows that the mid-height vortex pair and the upper wheel vortex pair seem to be merging, which would indicate a potential discrepancy with the topology described previously (Figure 2.5). The numerical results were obtained by implementing detailed time-resolved Unsteady-Reynolds Averaged Navier Stokes (URANS), solved by finite volume discretisation with the ONERA code *elsA*, with the ONERA *k-kL* two-equation turbulence model by Bézard and Daris [3].

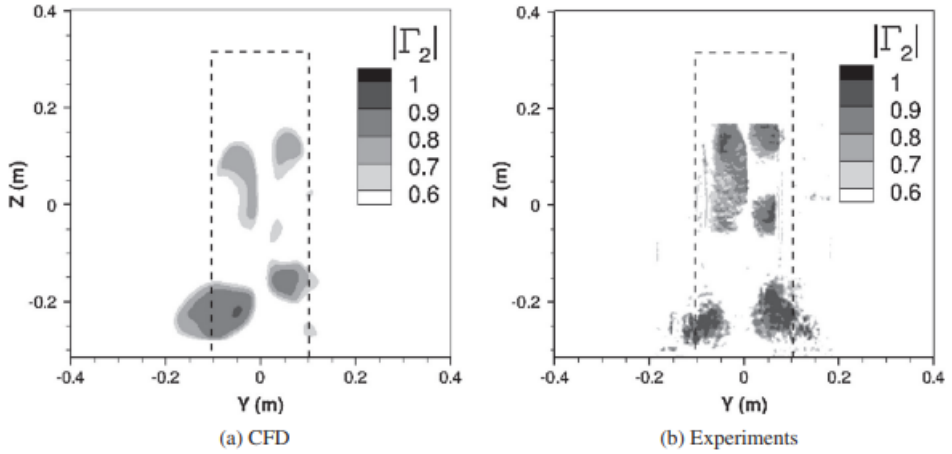


**Figure 2.5:** Vortex structures visible through $\Gamma_2$ contours (The $\Gamma_2$ criterion is described in Section 12), comparing numerical and experimental results in a slice at position $X = 0.66D$ (where $D$ is the diameter of the tire) behind the tire, by Croner et al. [18, 17].

Wäschle et al. [67] also addressed the flow topology of a stationary isolated wheel, where it was concluded that the boundary layer generated over the stationary ground was separating in front of the tire, producing a horseshoe vortex (marked 4 in Figure 2.6), which is deemed to be relatively weak, as it dissipated early in the tire wake. Another feature observed in the stationary isolated wheel is the increased strength of the trailing vortices (marked 2 in Figure 2.6), which refer to the wake horseshoe vortices. Finally, a large effect of the stationary wheel is the counter-rotating vortices produced at the top separation point (marked 3 in Figure 2.6).

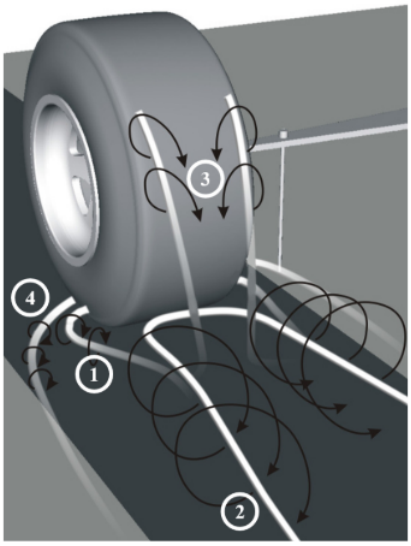


**Figure 2.6:** Vortex structures around an isolated stationary smooth tire by Wäschle et al. [65, 67].

These differences due to the effect of rotation are also reflected in the drag and lift results, as shown in Table 2.1, where the rotation of the wheel introduces significant reductions in lift and drag [66].

| **Wheel** | **Drag** | **Lift** |
|---|---|---|
| Stationary | $C_D \approx 0.50$ | $C_L \approx 0.30$ |
| Rotating | $\Delta C_D \approx -0.05$ | $\Delta C_L \approx -0.20$ |

**Table 2.1:** Drag and lift coefficient comparison for stationary and rotating isolated wheel by Wäschle et al. [66]. Drag and lift are non-dimenisonalised as in Section 7.

## 2.2. Rotating Wheel in Vehicle

When the wheel is mounted to a vehicle, the wheelhouse covers large part of the tire's frontal upper area and shoulders from incident flow, resulting in a different flow topology from the discussed in Section 2.1 in the top region, consequently reducing its relevance due to the wheel-arch enclosure. On the bottom end of the tire, Wäschle [65] identified the flow around tire to be affected by a change in the incident flow, which is effectively yawed by the displacement caused by the front of the vehicle. The main consequence of this oblique incidence on the front wheels is a shift in the location of stagnation point towards the inside of the wheel. As Wäschle [65] commented, this is also partly caused by the cooling air exiting from the engine bay. The overall effects of the stagnation point relocation are a reduced deflection of the flow, together with milder pressure gradients and a diminished separation region. As a result of this, looking at Figure 2.7, on the outer side of the wheel, earlier separation occurs in the region of contact of the wheel shoulder, resulting in a more pronounced outer contact patch vortex (B).

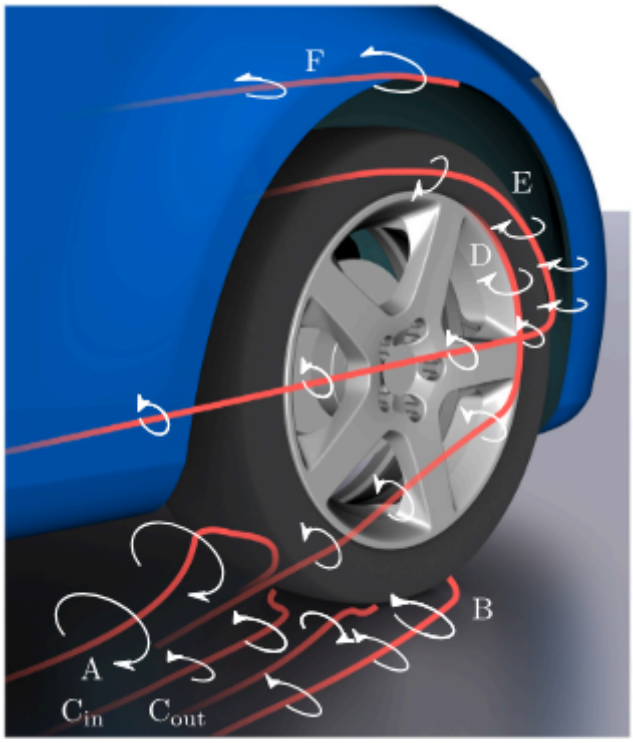


**Figure 2.7:** Vortex structures in a rotating smooth tire mounted in a vehicle by Wäschle et al. [65], extracted from [33].

The weakened contact patch vortex results in free flow reaching the rear of the tire and then separating around the base of the tire, on the shoulder location, originating a counter rotating vortex pair C. Because the incident flow is oblique, the inside of the tire receives higher energy air, corresponding to a larger separation around the shoulder, producing a stronger inner vortex in comparison to its outer counterpart ($C_{in}$ and $C_{out}$ respectively).

Another new vortex (A) is formed by the oblique flow approaching the inside of the wheel rim, which then separates at the shoulder area and leads to an inner vortex, significantly stronger than the C-vortex. On the outer lower side of the rim, the rim vortex is formed (D). The rotation of the wheel pushes the boundary layer on the tire wall against the incoming flow, producing backflow on the upper side of the tire, which impedes the development of an upper rim vortex. The rotation of the wheel also causes the presence of the so-called 'flank' vortex, which is located at the top of the tire and is originated when the air leaving the wheelhouse is opposed by the rotating wheel (Vortex E).

Finally, Wäschle [65] remarks that these results are obtained from a simplified vehicle model that resembles a sedan car and cannot be transferred to other types of vehicles, which would present flow features with certain variations from the ones discussed in this chapter.

In assessing the implication of wheel rotation on the overall forces of the vehicle, Wäschle [65] concluded that a

reduced area of losses behind the rear wheels is observed, which improves the flow incident to the lateral tail of the vehicle, increasing the rear base pressure. The result of this is an overall drag reduction in the vehicle. The rotation of the wheels also contributes to a cleaner underbody flow, providing the air travelling under the car with higher velocities and consequently, lower static pressure, creating lower lift.

## 2.3. Time-Dependency of Rotating Wheel Flow Features

The large majority of the studies discussed were based on the mean flow structure of the wake. Consequently, the averaging of measured data in flows containing vortices that have unsteady behaviour results in a loss of captured strength of the vortex and a unrealistic increase in size of the vortex structure. Understanding the transient behaviour of the wake adds value to the analysis and shows features that go overlooked in the mean flow. Croner et al. [17, 18] showed through simulation results (with the numerical model details given in Section 2.1 ) that the vortices generated near the ground are characterised by a highly unsteady behaviour, resulting in the contact patch vortices shedding at either side of the wheel due to the enhancement from the horseshoe vortices present in the wake behind the wheel. The vortex identification method used was the $Q$-criterion, described in Appendix D.3. As Figure 2.8 shows, this shedding makes the ground vortices move from side to side. Furthermore, Croner et al. [17, 18] also concluded that vorticity is shed on to the wake from the top of the tire downstream the top separation.

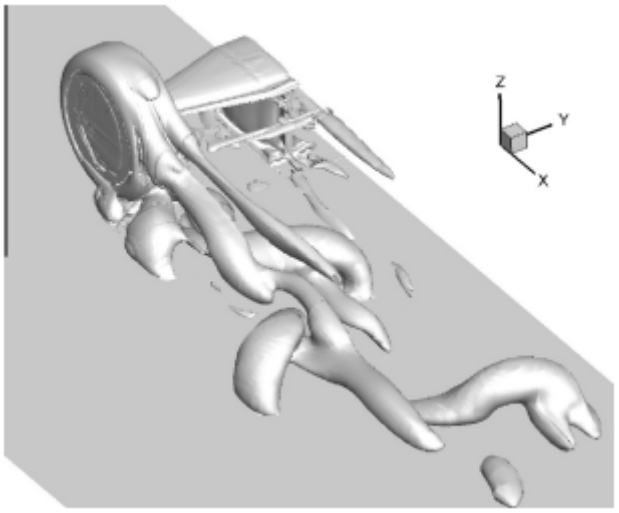


**Figure 2.8:** Iso-surface for $Q = 1000$ from URANS results by Croner et al. [17][18].

Parfett et al. [46] carried out experimental studies with PIV measurements of the flow of an isolated tire, where averaged data from 20 runs was compared to instantaneous data obtained with single-pass wake surveys. The averaged results showed good agreement with the flow filed described by Wäschle [65]. On the other hand, the instantaneous flow samples exhibit that the flow structures fluctuate significantly (see Figure 2.9), where the ground vortices to the right and left of the wheels vary in location for each sample, where the wake was dominated by the ground vortex on the left in a certain sample, then being dominated by the ground vortex on the right in a different sample, and a more balanced distribution in a third sample. Parfett et al. [46] remark that 20 tests are still a low number of samples to determine the frequency of the shedding accurately, which highlights the higher complexity of unsteady flow analysis, explaining why most researches focus on the study of mean flow for this problem.

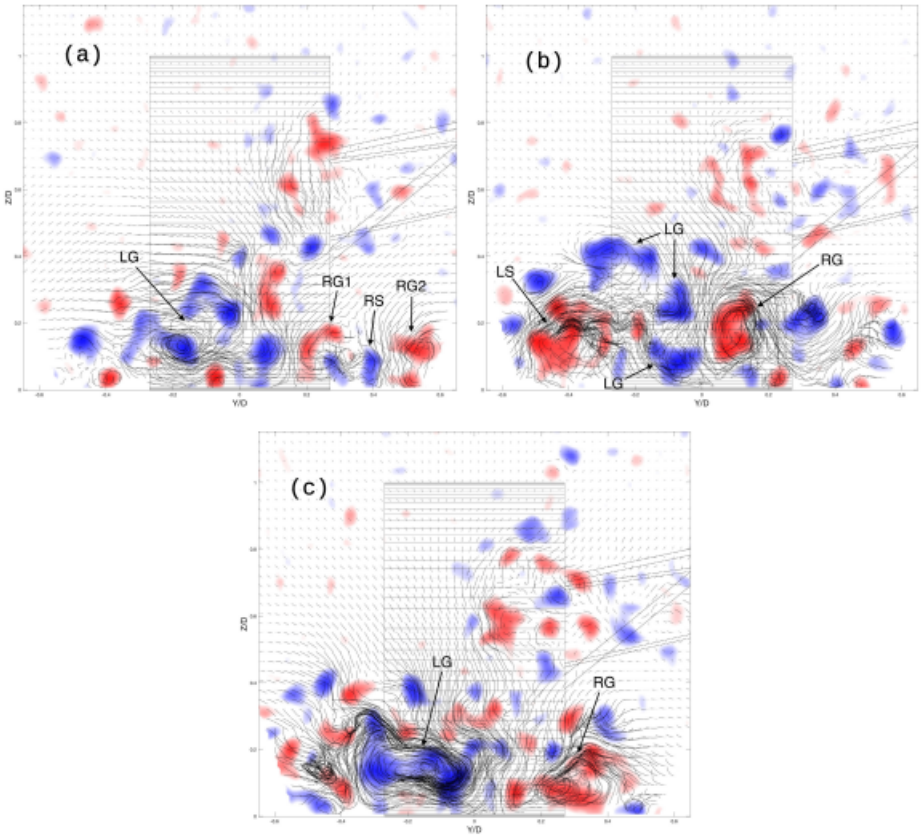


**Figure 2.9:** $\Gamma_2$ contours from instantaneous PIV measurements at a location $X = 1.6D$ (where $D$ is the wheel diameter) behind the wheel: (a) showing the left ground vortex $LG$ dominating; (b) showing the right ground vortex $RG$ dominating; and (c) showing a more balanced flow.

Parfett et al. [46] then used the single-shot PIV data to reconstruct the wake with wake surveys at different positions downstream, showing that, although the ground vortices propagating downstream show less smoothness as they develop downstream, the overall structure of the wake remains in agreement with the mean-flow described by Wäschle [65]. This means that, even though unsteady flow features may be overlooked in the averaged flow, valid conclusions of the wake structure can be drawn from the mean flow results.

## 2.4. Effect of Rim

Another wheel feature that has a significant impact on the overall vehicle aerodynamic forces is the rim geometry. Volvo [35] carried out tests to compare the aerodynamic drag resulting on a vehicle, testing with different tire geometries in wind tunnel experiments, where the drag was quantified and compared with the base pressure. The conclusion of this study was that a flat rim cover produced the largest drag reduction. Schütz [57] explained these results by arguing that the rims with openings produce a ventilation effect from the flow inside the wheelhouse, causing a lateral deflection of the flow, leading to a loss of momentum in the $x$-direction and its consequent increase in drag. It comes without saying that this effect can vary with rim opening geometries, where parameters such as profile and radii of the wheel spokes, as well as rim edge can be optimised to mitigate this loss of momentum. Nevertheless, the closed rim cover showed the lowest drag results by not introducing this deflection in the flow. These results were then supported by Duncan et al. [21] through experimental and numerical tests (with PowerFLOW® a solver based on the Lattice Boltzmann Method, LBM) of four rim geometries on the same tire, where the rim closed with a convex cover achieved the lowest drag. From the simulation results, a re-attachment of the flow in the lower half of the front wheel around the wheel cover and rear tire shoulder was observed, while without the cover, this behaviour was prevented by the flow coming from through the rim. Berg et al. [2] carried out a parametric investigation of the effect of rim geometry in drag, and confirmed that the main geometrical parameter is the rim coverage area, which has a linear effect on aerodynamic drag. These studies found that rims that weakened near-ground vortices produced less aerodynamic drag.

The resulting deflection can also be reduced with the incoming flow towards the wheel. As stated above, for wheels mounted inside the wheelhouse of a car, the incident flow is oblique, which leads to flow separation on the tire front shoulders, meaning that the rim finds itself inside the separation region, reducing its influence on the aerodynamics of the vehicle.

Modlinger et al. [42, 43] focused on studying how the ventilation effect of the rim could be optimised with rim geometry design to reduce drag. They found that the maximum pressure occurred at the outer end of the spokes (furthest point from the rim centre, where the spokes merge with the rim base), where the rotational speed is largest, generating the rim ventilation moment. It was then found that this ventilation moment could be minimised by designing the spokes with an aerodynamic profile instead of blunt geometries, as well as adding wedges on the outer radius to reduce the dam effect in the junction.

## 2.5. Effect of Wheelhouse

As discussed earlier, when the wheel is enclosed by the vehicle's wheelhouse, the flow around the upper half of the tire differs completely from the flow observed on an isolated wheel in free flow. According to studies carried out by Cogotti [13], the aerodynamic forces increase with wheelhouse volume (accounting for constant wheel size). In the front part of the wheelhouse, the flow moves upwards, while the cooling air flowing out of the engine bay into the wheelhouse is another inflow component in this region, as well as part of the underbody air flowing into the wheelhouse over the inner flank. The tread geometry of the tire transports air from the back towards the top of the tire, where it then vents outwards through the wheelhouse gap. Similarly to the deflection introduced by the rim, this exiting air also causes disturbances in the flow around the vehicle.

## 2.6. Effect of Tire Surface

The first investigation on the influence of tire surface on the pressure distribution over the tire was carried out by Fackrell and Harvey [24, 25], where a smooth tire surface was compared to a grooved tire surface in experimental tests. The resulting pressure distribution is given in Figure 2.10, where it can be seen that the addition of grooves results in a reduced pressure peak at the front of the tire, by ensuring pressure equalisation between the front and the rear through the grooved tires, hence reducing the "jetting effect" from the front stagnation to the rear of the tire.

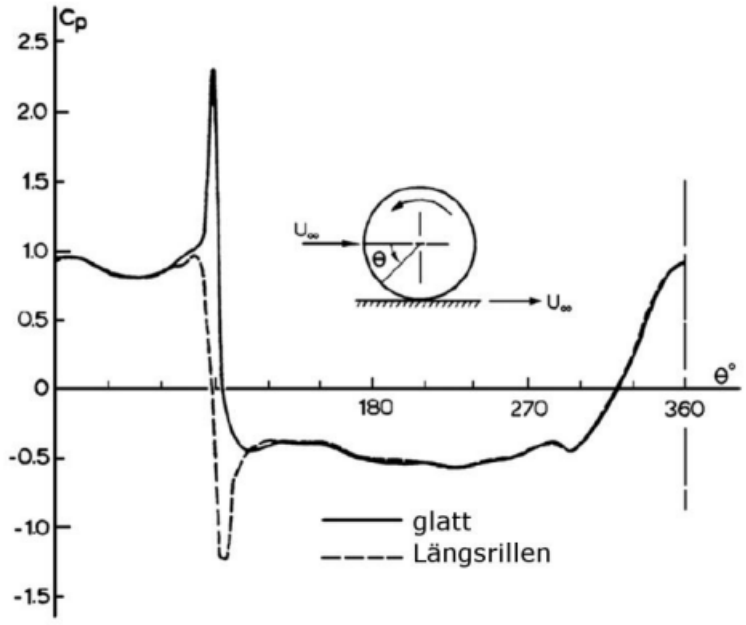


**Figure 2.10:** Pressure distribution over a rotating tire comparing two surfaces: *glatt* translates to smooth, and *Längsrillen* to longitudinal grooves, from German. Results obtained by Fackerll and Harvey [24] and plot extracted from [55].

The tire surface has a wide range of patterns that vary accordingly to their application. These patterns can go from a completely slick tire (no longitudinal or transversal grooves, also referred to as smooth tire) to a fully

treaded pattern. Josefsson et al. [30, 32] studied the effect of four different tire patterns: slick pattern (a); rain pattern (b), containing longitudinal grooves; lateral pattern (c), containing transversal grooves on the sides; and detailed pattern (d), which is a combination of the lateral and rain pattern, as an approximation of a treaded pattern. These different surfaces are depicted in Figure 2.11. Both closed rim and open rim geometries were tested for the deformed tires mounted on a full vehicle simulation.


**Figure 2.11:** Tire surface geometries tested by Josefsson et al. [30, 32] : (a) smooth tire surface; (b) longitudinal grooves tire surface; (c) lateral grooves tire surface; (d) lateral and longitudinal grooves, approximatingg a treaded tire surface.

With the closed rim, Josefsson et al. [30, 32] found overall drag reduction for all patterns with respect to the slick tire, with the largest reduction coming from the detailed pattern with 5 counts of drag coefficient less than the slick tire. The longitudinal grooves presented a reduction of 0.003 $C_D$, while the lateral grooves produced a reduction of 0.001 $C_D$. With the open rim geometry, similar trends were observed for drag coefficient, although the lateral grooves presented a larger reduction in drag than in the closed rim case, going from a 0.001 $C_D$ to a 0.003 $C_D$ reduction with respect to the slick tire. The flow mechanisms for these reductions were identified to be: contact patch separation, large separation from the upper half of the wheel, and a vortex from the front tire shoulder. These flow features presented very good agreement between experiment and simulation. Josefsson et al. [30, 32] then observed that the grooves produced smaller contact patch separation, resulting in smaller rear wheel wakes.

Further studies were performed by Alajbegovic et al. [36], where two tire surfaces were compared: fully treaded pattern, and grooved pattern (geometries can be seen in Figure 2.12). In these studies, numerical results were compared with experimental results for isolated tires by Schnepf et al. [55], where the fully treaded pattern was modelled with Immersed Boundary Method developed by Peskin [47], implemented within PowerFLOW® which will be explained in Section 3.5, while the grooved tire is modelled with rotating wall boundary condition.

**Figure 2.12:** Fully treaded tire surface (left) and grooved tire surface (right) by Alajbegovic et al. [36].

Comparing the results with experiment, the rotating treaded tire shows better agreement, with better representation of the bottom part of the wake, while the treaded tire presents a tighter wake than the grooved tire. Differences in the separation points can also be observed, where the treaded tire shows a smaller sidewall separation. On the top of the tire, the treaded tire presents a much earlier separation point than the grooved tire, which is a result of the momentum (negative in the streamwise direction) introduced by the tread blocks, pushing the air in the back of the tire upwards and forwards. This is shown by centreline planes of total pressure (Figure 2.13), which show the increase upwash caused by the treaded tire, matching better the experimental results.

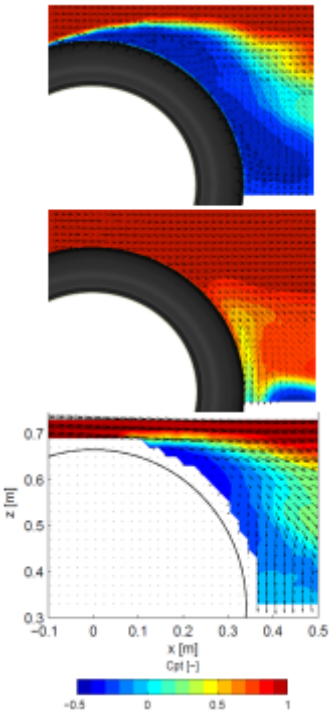


**Figure 2.13:** Total pressure coefficient plots at center plane ($y = 0.0$m). Numerical treaded surface (top), numerical grooved surface (middle), experimental by Schenpf et al. [55] (bottom). Numerical results by Alajbegovic et al. [36].

## 2.7. Effect of Tire Deformation

The weight of the vehicle on the tire produces a deformation of the bottom part of the tire's sidewall, generating a bulge shape and a contact patch. It comes without saying that higher loads will produce larger deformations, although the magnitude of these increments will vary for each tire geometry depending on its structural properties. Schnepf et al. [55] carried out experimental tests increasing the load on the tire, comparing results for a treaded and a smooth tire. While for the smooth tire, a very stable separation behaviour was noted with different loading conditions, in the case of the treaded tire, the size of the bottom wake increases with decreasing load. Replicating these results in numerical simulations presents several challenges, especially when it comes to the contact patch shape and size variations and the region around the contact patch. To reproduce the deformed tire tests numerically, Schnepf et al. [55] scanned the dynamically loaded tire using distance laser sensors with the resulting point cloud shown in Figure 2.14. The sampling frequency was 128Hz, with a spatial resolution of 0.5mm. As Schnepf et al. [55] remarks, this method presents limitations in the coverage of the lower slip area, as when measuring from the side, as reflection induced by the unfavourable angle impedes the sensor from determining the exact distance.

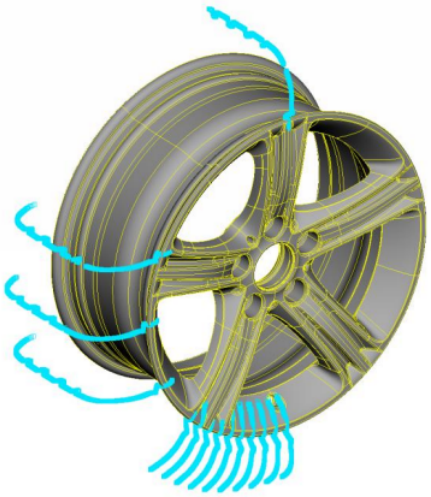

**Figure 2.14:** Scanned point cloud of dynamically loaded tire by Schnepf et al. [55].

Mortazawy et al. [44] made a numerical investigation on the effect of deformation using a lattice-Boltzmann based solver, where an undeformed rotating treaded tire and a deformed rotating treaded tire were simulated with immersed boundary method applied over the tire's tread, comparing the results with the experimental results obtained by Schnepf et al. [55] for the lowest load condition, which already produced a certain deformation. The deformation on the geometry used for the numerical simulation introduces a bulge in the bottom sidewall and an enlargement of the contact patch, as well as a change in curvature of the contact patch corners (see Figure 2.15).

**Figure 2.15:** Comparison of undeformed and deformed tire with fully treaded surface by Mortazawy et al. [44].

Comparing qualitatively the numerical results with the experiment, Mortazawy et al. [44] reported that the deformed tire presented much better agreement in the flow topology of the wake. Looking at iso-surfaces for total pressure coefficient equal to 0.0, in Figure 2.16, the differences in flow structures between the deformed and undeformed tire can be assessed.

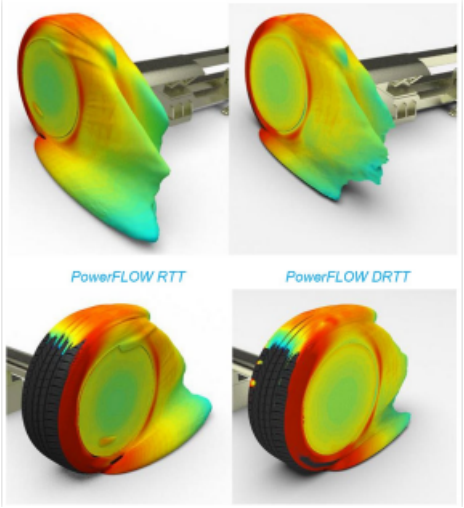


**Figure 2.16:** Iso-surfaces for $C_{p_{tot}} = 0.0$ coloured by velocity magnitude showing PowerFLOW® results for Rotating Tread Tire $RTT$ (left) and Deformed Rotating Tread Tire $DRTT$ (right). Imagees at the top show the ISO-view from a point of view behind the tire, while images at the bottom show the ISO-view from a point of viwe in front of the tire. Images by Mortazawy et al. [44].

The main differences occur at the floor structures, where although the wake deflection starts around the same point (where the tire geometry meets with the ground, represented by a moving belt), the bottom wake is much tighter in the deformed tire case. This is caused by differences in the wake deflection angle and height of the lobe vortex around the bottom of the tire. Looking at the flow around the contact patch with a total pressure slice (Figure 2.17), it is evident that the contact patch characteristics of the deformed tire produce a tighter wake thanks to better attachment around the corners in the inside of the tire. Since various parameters of the contact patch geometry are varied simultaneously, it is uncertain what the influence of the different geometrical parameters in the variations of the flow in this region is. A comparison with experiment on the flow at this location is not possible due to the challenges that this region near the ground and tire surfaces pose for PIV measurements.

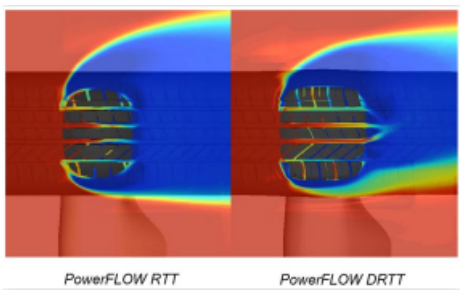


**Figure 2.17:** Slices of $C_{p_{tot}}$ at contact patch height for Rotating Tread Tire $RTT$ (left) and Deformed Rotating Tread Tire $DRTT$ (right) by Mortazawy et al. [44] (scales not available from source).

This is reflected on the $y$-velocity plots of slices at a y-location of $y$ = -0.15m, right on the outside of the tire, which show that the deformed tire shows better agreement with the $y$-velocity seen in the experiment, which has an increase of out-wash around the bottom rear of the tire (higher magnitudes). The numerical results show a region of in-wash around the bottom corner of the tire (lower magnitude), which the experimental results cannot confirm, due to the lack of measurements in this region. These regions of in-wash and out-wash at the bottom outer corner of the tire relate to the outer contact patch vortex, which, as shown in Figure 2.16, is larger for the undeformed case, hence resulting in a larger region with this velocity distribution. At a quantitative level, Mortazawy et al. [44] concluded that the deformed tire presented an increase of 14% in drag, which cannot be compared with Schnepf's results [55], since the drag was not quantified for this case study.

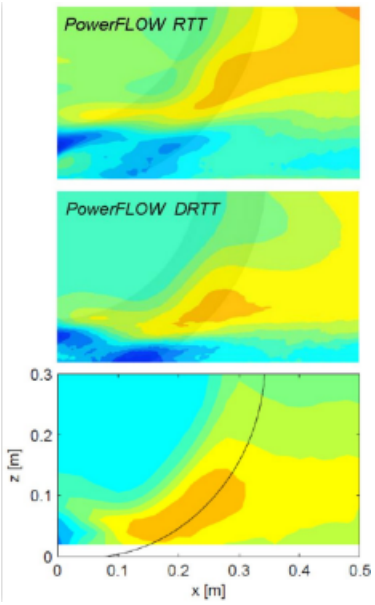


**Figure 2.18:** Slices of $y$-velocity: Rotating Tread Tire $RTT$ (top); Deformed Rotating Tread Tire $DRTT$ (middle); and experimental by Shcnepf et al. [55] (bottom). Numerical results by Mortazawy et al. [44] (scales not available from source).

Mortazawy et al. [44] attempted to replicate the study of the effect of increasing vertical loading on the tire, hence increasing the bulge deformation and contact patch size, on the wake of the tire. Three loading conditions were tested, where the behaviour observed in the experimental tests by Schnepf et al. [55, 54] was successfully replicated by the numerical studies, where Mortazawy et al. [44] captured a shrinking trend of the lobe horseshoe vortex both inboard and outboard of the tire (see Figure 2.19). These results suggest that the increased bulge size might be delaying the separation around the bottom of the tire, resulting in a "cleaner" separation for the heavier loaded tire. Mortazawy et al. [44] reported that for the medium loaded tire (3.5kN as defined in experiment), a bulge deformation increase of 5mm was produced in the geometry used in the numerical simulation. Nevertheless, other deformation parameters such as the contact patch and the bulge lateral and longitudinal curvatures remain uncertain, which leaves their influence on the results unknown.

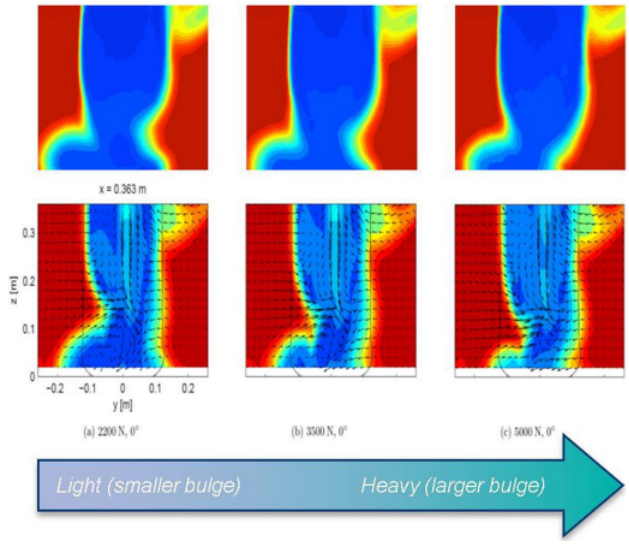


**Figure 2.19:** Increasing load from left to right. Numerical total pressure coefficient results by Mortazawy et al. [44] (top), experimental results by Shcnepf et al. [55] (bottom) (scales not available from source).

Numerical studies with Navier Stokes based solvers implement the contact patch in a different way as compared

to LBM based solvers [6, 8, 7, 61], where the contact patch is represented with a small step between the ground and the tire. This step is used to avoid skewness of the mesh cells around the contact line.

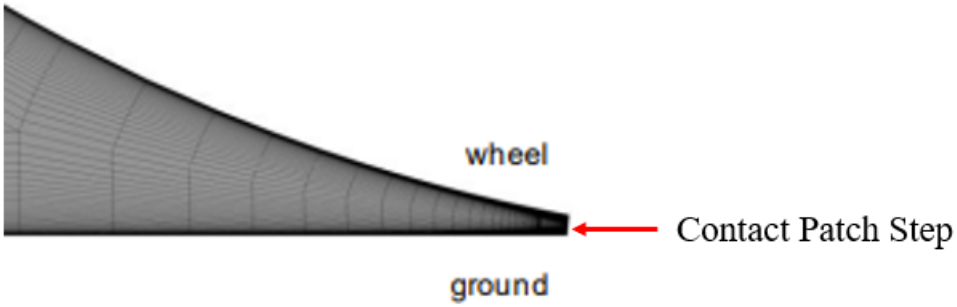


**Figure 2.20:** Contact patch step used in Navier Stokes based solvers to avoid skewness of the mesh cells. Image by Diasinos et al. [20]

Diasinos et al. [20] carried out studies to investigate the effect of changes in the contact patch size. The initial step height used was of $0.0028D$ (with $D$ being the wheel's diameter), representing the smallest step that was achieved without affecting the mesh around the contact patch. Diasinos et al. [20] then varied the contact patch size by increasing the step height to a maximum of $0.0085D$, always without varying the height of the top of the wheel. Diasinos et al. [20] observed that increasing the step height resulted in a reduction of the wheel wake width, where the separation point was displaced towards the rear of the wheel, delaying the lateral deflection angle of the flow jetting from the contact patch. It was indicated that this is caused by the change of aspect ratio of the contact patch, since increasing the step height results in a larger increase in the contact patch length with respect to the increase in the width. Diasinos et al. [20] point out that, delaying or reducing the contact patch separation results in a weakening and shrinking of the main wheel vortices. These vortices are responsible for the downwash in the central wake region. Therefore, reducing their strength results in a reduction of the central downwash, shifting the separation point at the top of the wheel tread forwards. This shift in the top separation point also produces reduction of drag coefficient of approximately 20%, while the lift coefficient is more sensitive to these variations, as it is reduced by 50%, since the forward migration of the top separation point reduces the peak low-pressure coefficient.

Josefsson et al. [33] carried out experimental studies testing tire geometries, as depicted in Figure 2.21. It is worth noting that the narrower tread results in a smaller contact patch, so in this case effects of contact patch size and shape variation can have an effect in this comparison.

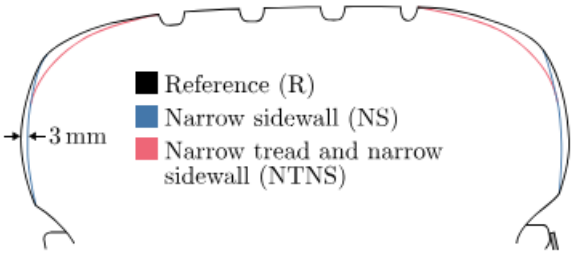


**Figure 2.21:** Tire profiles tested by Josefsson et al. [33].

These tire geometries were tested both with closed and open rims, and it was found that, for the case with closed rim, reducing the sidewall resulted in reduction of drag coefficient for both rim cases, while reducing both the sidewall and the tread resulted in an increase in drag coefficient for the case of closed rim, simultaneously, it resulted in a decrease in drag coefficient in the open rim case. Josefsson et al. [33] then went on to investigate the flow mechanisms producing these changes in drag coefficient. It was found that in the case of closed rim, the key differences were observed in the outer contact patch vortex. When the outer contact patch vortex was smaller, less outward deflection of the wake was captured, resulting in less drag. This was the case of the smaller sidewall, while for the smaller sidewall and smaller tread case, a larger outer contact patch vortex was observed, with its respective increased outward deflection, resulting in an increase in drag. In the case with open rim, that

same outer contact patch vortex trends were observed, but the drag coefficient differences were driven more by the changes in the wake produced by the rim.

# 3

# Numerical Modelling of Tire Rotation

To model rotating geometries in numerical simulations, there exist three main possible approaches: rotating wall boundary condition $RW$, moving reference frame $MRF$, and sliding mesh $SM$ and Immersed Boundary Method IBM. Alternative variations of these approaches have bee studied and are discussed in this section.

## 3.1. Rotating Wall Boundary Condition RW

For a simple case such as a smooth tire, the rotating wall boundary condition is an adequate way to prescribe the circumferential velocity from the rotation by implementing a surface boundary condition by imposing a tangential velocity component on the tire surface [56]. Nevertheless, the drawback that this approach presents is that regions of the geometry that are normal to the freestream velocity vector will not be modelled appropriately. This is due to the fact that its physical interpretation would be that of an inflow or outflow through a solid wall, as indicated by Hobeika and Sebben. [27]. Most wheel geometries present complex surfaces with treads that have different angles with respect to the incoming velocity vector. Therefore, more complex approaches are necessary.

## 3.2. Moving Reference Frame MRF

This approach allows for accounting for the Coriolis and centrifugal forces involved in rotation, although it is only applicable for axis-symmetric rotating geometries. These forces are calculated in a fluid region in a rotating frame of reference, without the region actually rotating. On the interface of the rotating fluid region and the stationary region, coupling takes place through appropriate transformations. This approach allows for the presence of geometries normal to the free stream velocity vector inside the fluid region with rotation. The main drawback of this approach is that, by not actually rotating the geometry, the results are highly dependent on the chosen position for the fluid region with rotation, especially when this region is in proximity of non-rotating parts. A solution to this is to apply circumferential averaging.

## 3.3. Sliding Mesh SM

This is the most complete and the most complex approach, as it involves the actual rotation of the geometry every time step, hence making the most suitable method for unsteady simulations. This means that this approach can only be implemented in an unsteady simulation, which implies a higher computational cost. The sliding mesh is applied to avoid re-discretisation for every time step. Unlike for MRF, averaging the sliding mesh results in losing the flow field-geometry correspondence. However, the most significant disadvantage of this approach is that it can only be implemented on axis-symmetric geometries, which excludes an undeformed tire intersecting with the ground or a deformed tire [31, 56].

## 3.4. Hybrid Approach MRFg

While the rims and their spokes are to be modelled with the moving reference frame (MRF) in the case of steady-state simulations, and sliding mesh in the case of unsteady simulations, as long as they are axis-symmetric geometries, tires intersecting with the ground and deformed tires require other modelling approaches that vary depending

on the complexity of their surface geometry. Figure 3.1 shows how these deformation effects produce the non axis-wise symmetry of the tire. Considering the tire surface options discussed in Section 2.6, simple geometries like the smooth tire and the tire with longitudinal grooves can be modelled with the rotating wall boundary condition, as they do not present any parts of the geometry that are normal to the free stream velocity vector.


**Figure 3.1:** Deformed tire with lateral and longitudinal grooves tested by Hobeika and Sebben [28].

The transversal (or lateral) grooves present in a treaded tire surface, see Figure 3.1, move in a direction normal to the surface. In this case, the rotating wall boundary condition cannot be applied (through a velocity component that is tangential to the surface), since mass conservation implies that the velocity cannot have a normal component to the surface, as its physical interpretation would be that of an inflow or outflow through a solid wall. While the sliding mesh approach would be able to provide an accurate model of the rotation of these complex geometries, as discussed earlier, due to the tire's intersection and deformation, the geometry is non axis-symmetric, which implies that the sliding mesh approach is not valid. Hobeika and Sebben [28] proposed a hybrid approach named MRFg, combining the rotating wall boundary condition and the moving reference frame approach. RW is used on the external tire area, and MRF is applied to the transversal grooves. This approach keeps the mesh fixed, which Hobeika and Sebben [28] argue does not have a large impact on the local flow differences and the results due to the small size and the many instances of these details around the tire. A depiction of how this approach is split into fluid regions is provided in Figure 3.2 below, where the moving reference frame is implemented in the grey region.

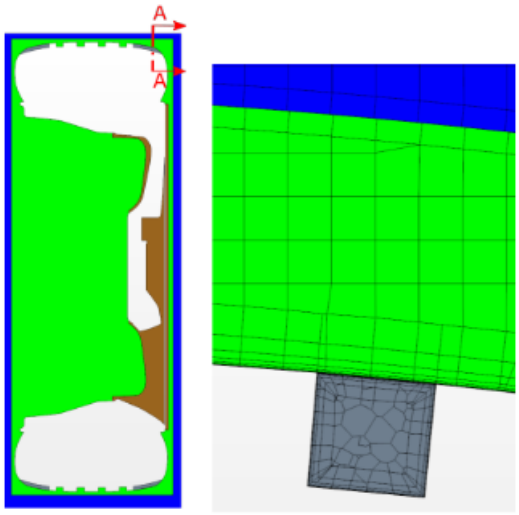


(a) Front view (b) A-A cross section

**Figure 3.2:** Region distribution for the $MRFg$ approach, where Region 0 (blue) is the majority of the computational domain, Region 1 (green) containing the whole wheel geometry, Region 2 (brown) isolating the rim spokes, and Region 3 (grey) for the lateral grooves, where moving reference frame is applied [28].

Hobeika and Sebben [28] validated this approach by comparing with an isolated axis-symmetric rotating wheel modelled with sliding mesh, which is the most accurate approach. The results showed that the MRFg produced a similar velocity distribution to the sliding mesh in the lateral grooves (see Figure 3.3).

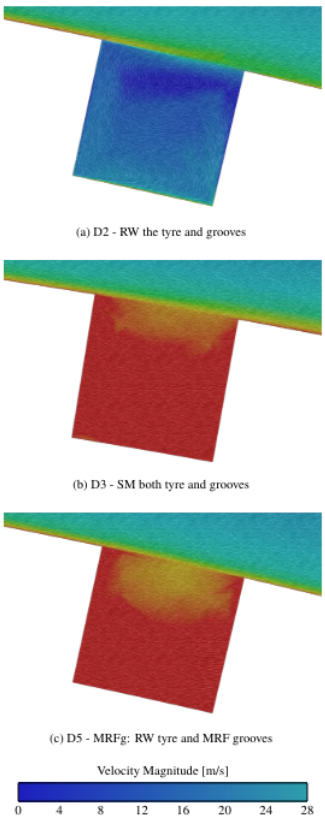


(a) D2 - RW the tyre and grooves

(b) D3 - SM both tyre and grooves

(c) D5 - MRFg: RW tyre and MRF grooves

**Figure 3.3:** Velocity field in a plane cutting through the lateral grooves. The tire rotates clockwise, hence flow moves from left to right along the surface. Rotating wall on the whole surface is represented at the top,sliding mesh at the middle, and *MRFg* (bottom) [28].

## 3.5. Immersed Boundary Method IBM

Immersed boundary is a fluid-structure interaction method for numerical simulations that was intended for biological fluid dynamics, developed by Peskin [47]. The method is useful for general fluid-structure interaction problems, such as modelling of treaded tires. This method is derived from the principle of least action, and is both a mathematical formulation and a numerical scheme, where the mathematical formulation works by a mixture of Eulerian and Lagrangian variables, related by interaction equations. These interaction equations involve a smoothed approximation of the Dirac delta function. When it comes to the numerical scheme, the Eulerian variables are defined on a Cartesian mesh that remains fixed, while the Lagrangian variables are defined on a curvilinear mesh to which free motion through the Cartesian mesh is applied. That means, this curvilinear mesh is not constrained by the fixed Cartesian mesh.

The Computational Fluid Dynamics (CFD) software that implements this method to model treaded tires is PowerFLOW® through the Rotating Treaded Tire (RTT) and Deformable Rotating Treaded Tire methodology (DRTT), which are for undeformed and deformed tires respectively [51, 50]. In this methodology, the treaded tire is split into carcass and tread, and on the carcass rotating wall boundary condition is applied, while the tread is modelled as a fluid region without permeability, keeping the tread region separated from the fluid domain. This approach allows for the modelling of actual tread rotation, without needing to implement a restricted approximation, as is the case on the detailed tire modelled by Hobeika with the MRFg approach [27]. Also, the IBM approach reduces the number of interfaces between differently modelled regions over the tire, hence reducing the error induced by these region interfaces, as well as providing a better representation of the tire deformation by ensuring that the tread follows the deformed geometry path.

## 3.6. Rotating Wall with Roughness

While the IBM approach presented above allows for more accurate representation of the tire geometry in CFD simulations, its computational cost tends to be higher than other approaches due to the need for higher fluid domain resolution to correctly model the tread motion. PowerFLOW® provides an alternative approach [51, 50]. In this approach, the tire geometry is a grooved tire, where only longitudinal grooves exist (such as the rain tire shown in Section 2.6). The rotation is then modelled by applying rotating wall boundary condition over the tire surface. However, to match the flow topology of the treaded tire, roughness is applied on the surface. The roughness values are derived from a calibration process in which the values are modified to match the flow field and separation points resulting from the treaded tire.

Sbeih et al [53] carried out a comparison study where several rotating tire modelling techniques were tested. The results showed that for a deformed tire, modelling with rotating wall and roughness presented a drag coefficient difference of 6 counts with respect to the treaded tire modelled with IBM. Although both approaches showed a drag coefficient difference of 3 counts with respect to experiment, they do show an improvement over modelling a grooved tire with only rotating wall boundary condition, as this approach showed a drag coefficient difference of 5 counts with respect to experiment. Therefore, for simulations where the flow topology around and downstream of the tire is a relevant factor, such as simulations where the tire is mounted on a full vehicle, the use of rotating wall boundary condition with roughness is justified when the computational resources do not allow for IBM implementation.

Additionally, Sbeih et al. [53] showed that the deformed tire modelled with the three approaches discussed in the previous paragraph presented an overall improvement of drag coefficient agreement with experiment when compared to undeformed rotating tire results, modelled with IBM and rotating wall boundary condition, which presented drag coefficient differences of 9 and 11 counts with respect to experiment, respectively.

# 4

# Analysis Methodologies

As described in Section 2, the flow around a rotating wheel and its wake is highly complex and largely dependent on multiple variables. The analysis of this flow field aims at identifying what are the flow mechanisms involved in the drag and wake variations caused by the parameters tested, and at providing answers into how these flow mechanisms relate to the geometries. To assess this, the analysis methodologies focus on a statistical overview that allows to identify the main trends over the whole spectrum of data points, with techniques such as Principal Component Analysis. Then, to gain understanding into how the wake develops, this section proposes an adequate methodology to identify and study the behaviour of the key vortex structures in the wake of a rotating wheel, as well as wake surveys that show where local momentum losses occur, hence relating these wake changes to the resulting drag variations. It comes without saying that the analysis could very well be carried out through a qualitative approach. However, this would require studying selected pieces of information at a time, while the statistical approach accounts for a larger set of data at once, whose results can then be used to select specific pieces of the data.

## 4.1. Principal Component Analysis

As Brunton et al. introduces in [5], Principal Component Analysis (PCA) is one of the main applications of the Singular Value Decomposition (SVD), and has been used for a long period of time, since it was developed by Pearson in 1901. In this implementation, from the data given as input, a hierarchical coordinate system is generated, representing high-dimensional correlated data, such that the directions of the coordinate system represent the principal components (PCs), which describe the largest variations in the data. The uncorrelated data results as directions of principal components that are orthogonal to each other. The input data is built by a matrix $\mathbf{X}$ with rows containing measurements from a single experiment, resulting in matrix $\mathbf{X}$ with size $n \times m$, where $n$ is the number of experiments, and $m$ is the number of measurements in a single experiment. As Brunton et al. [5] point out, it is important to apply to the data the necessary pre-processing steps, which involves normalising the data (by mean subtraction) to set the variance to unity before performing the SVD.

As Brunton et al. [5] describe, firstly the row-wise mean $\bar{x}_j$ is computed (Equation 4.1) and then it is subtracted from $\mathbf{X}$ (Equation 4.3).

$$\bar{x}_j = \frac{1}{n} \sum_{i=1}^{n} \mathbf{X}_{ij} \tag{4.1}$$

The mean matrix becomes:

$$\bar{\mathbf{X}} = \begin{bmatrix} 1 \\ \vdots \\ 1 \end{bmatrix} \bar{\mathbf{x}} \tag{4.2}$$

subtracting from **X**, resulting in **B**:

$$\mathbf{B} = \mathbf{X} - \bar{\mathbf{X}} \tag{4.3}$$

The covariance matrix of the rows in **B** is obtained by

$$\mathbf{C} = \frac{1}{n-1}\mathbf{B}^{\mathrm{T}}\mathbf{B} \tag{4.4}$$

Then, the first principal component $\mathrm{u}_1$ is expressed as

$$\mathbf{u}_1 = \underset{\|\mathbf{u}_1\|=1}{\operatorname{argmax}} \mathbf{u}_1^{\mathrm{T}}\mathbf{B}^{\mathrm{T}}\mathbf{B}\,\mathbf{u}_1 \tag{4.5}$$

Here, $\mathbf{u}_1$ is the eigenvector of $\mathbf{B}^{\mathrm{T}}\mathbf{B}$ of the largest eigenvalue. Therefore, Brunton shows that it is possible to compute the principal components by performing the eigen-decomposition of **C** (Equation 4.6). Since **C** is Hermitian, its eigen-decomposition exists.

$$\mathbf{C}\mathbf{Q} = \mathbf{Q}\mathbf{\Lambda} \tag{4.6}$$

where **Q** is the square $m \times m$ matrix whose $i^{th}$ column is the eigenvector of **C**, while $\mathbf{\Lambda}$ is the diagonal eigenvalue matrix whose diagonal elements are the corresponding eigenvalues $\Lambda_{ii} = \lambda_i$.

Applications of PCA for fluid mechanics with the purpose of being able to simultaneously investigate the major behaviour trends over large numbers of fluid measurement data have been previously tested. These applications go from signal processing, signal noise reduction, parametrisation of flow field attributes, reduction of dimensionality of the flow field, or flow feature extraction, among other things. An example of these applications can be found in Liu et al. [37], where they used PCA to perform a simplification of the flow field description in three-dimensional streamline field obtained numerically inside a reservoir. PCA enabled the parametrisation of streamline attributes and reduced the dimensionality of the flow field.

## 4.2. Vortex Identification Methodology

The description of the flow features generated by rotating tires in Chhapter 2 shows that vortex structures play major role in the drag coefficient resulting from the tire as they affect the wake development. Understanding the behaviour and characteristics of the vortices generated by the rotating tire is essential to identify the flow mechanisms that produce the changes in drag coefficient. Many systems to detect or identify vortices exist, but most procedures that rely on spatial derivatives of the velocity field fail to detect large-scale vortices superimposed on a turbulent velocity field. These characteristics may be encountered in flow fields with very noisy measurements caused by turbulence, such as the the flow field around or behind a rotating tire. To address this problem, two recent vortex identification functions were proposed by Michard et al. [26, 40], where the identification criteria of the vortex is based on topology of the velocity field, and not its magnitude.

The dimensionless scalar functions proposed by Michard et al. [26, 40] are $\Gamma_1$ and $\Gamma_2$. These remove the intermittency caused by small-scale turbulence, which is the factor that introduces the challenge of characterising the time-dependant variability of a large-scale vortex through a local quantity such as velocity gradient or vorticity. The definition of $\Gamma_1$ as defined by Michard et al. [26, 40] goes as follows:

$$\Gamma_1(P) = \frac{1}{N}\sum_{M\in S}\frac{(\overrightarrow{PM} \wedge \overrightarrow{v}_M)\cdot\hat{n}}{\|\overrightarrow{PM}\|\cdot\|\overrightarrow{v}_M\|} = \frac{1}{N}\sum_{M\in S} sin(\theta_M) \tag{4.7}$$

as shown in Figure 4.1, *P* is a fixed point in the measurement plane, *S* is a two-dimensional area enclosing *P* and *M*, and $\hat{n}$ is the unit vector normal to the measurement domain. The angle between the velocity vector at point

M, $\overrightarrow{v}_M$, and the radius $\overrightarrow{PM}$ is represented by $\theta_M$. $N$ denotes the number of measurement points M inside the area $S$. In contrast to $\Gamma_1$, $\Gamma_2$ is a Galilean invariant, which makes it suitable for vortex identification applications. $\Gamma_2$ is expressed as:

$$\Gamma_2(P) = \frac{1}{N} \sum_{M \in S} \frac{[\overrightarrow{PM} \wedge (\overrightarrow{v}_M - \overrightarrow{v}_P)] \cdot \hat{n}}{\|\overrightarrow{PM}\| \cdot \|\overrightarrow{v}_M - \overrightarrow{v}_P\|} = \frac{1}{N} \sum_{M \in S} sin(\theta_{PM}) \tag{4.8}$$

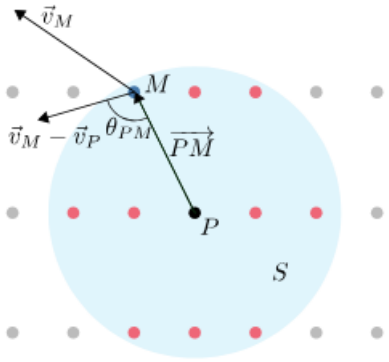


**Figure 4.1:** Illustration of the calculation of $\Gamma_2$ around a point $P$ in an area $S$. Image extracted from [33], inspired by Parfett et al. [46].

According to Michard et al. [26, 40] through Equation 4.8, the location of the vortex centre is determined by applying the location of maximum $|\Gamma_2|$, within a threshold of 0.9 to 1. In an effort to test the performance of the $\Gamma_2$ criterion, De Gregorio et al. [19, 16] carried out a comparison different vortex criteria and the $\Gamma_2$ criterion, by measuring the error in the vortex centre identification, defined by $(d_c)\% = \frac{\sqrt{\Delta x_c^2 + \Delta y_c^2}}{\sqrt{\Delta x^2 + \Delta y^2}}\%$, where $\Delta x_c$ and $\Delta y_c$ represent the Cartesian components of the identified centre distance to the theoretical centre, for a single synthetic normalised Vatistas vortex [63] with introduction of noise, as well as for a flow field measured in an experiment in a plane of one radius downstream of a rotor disk, which is a region characterised by high turbulent flow caused by the interaction of blade-tip vortices.

The other vortex identification criteria tested were: the $Q$-criterion, the $\Delta$-criterion, the maximum vorticity criterion ($\omega_z$), and the maximum circulation criterion ($\gamma$), all of them described by De Gregorio et al. [19, 16]. For the synthetic vortex comparison, Table 4.1 shows that the $\Gamma_2$ criterion gives the best results in identifying the centre of the vortex as the noise level increases from 20% to 90%. Figure 4.2 shows depicts the functions obtained from each criterion.

| | $\Gamma_2$ | $\Delta$ | $Q$ | $\omega_z$ | $\gamma$ |
|---|---|---|---|---|---|
| Noise: 20% | 0.5% | 43.8% | 17.9% | 51.7% | 10.6% |
| Noise: 50% | 10.1% | 149.1% | 507.6% | 38.4% | 80.4% |
| Noise: 70% | 30.0% | 6727.0% | 1563.8% | 7324.6% | 31.9% |
| Noise: 90% | 38.0% | 2637.0% | 6692.5% | 8163.8% | 6620.7% |

**Table 4.1:** Results of vortex centre identification error ($\varepsilon(d_c)\%$) comparing methods $\Gamma_2$-criterion, $\Delta$-criterion, $Q$-criterion, and $\omega_z$-criterion, with varying noise level. Results obtained by De Gregorio et al. [19, 16].

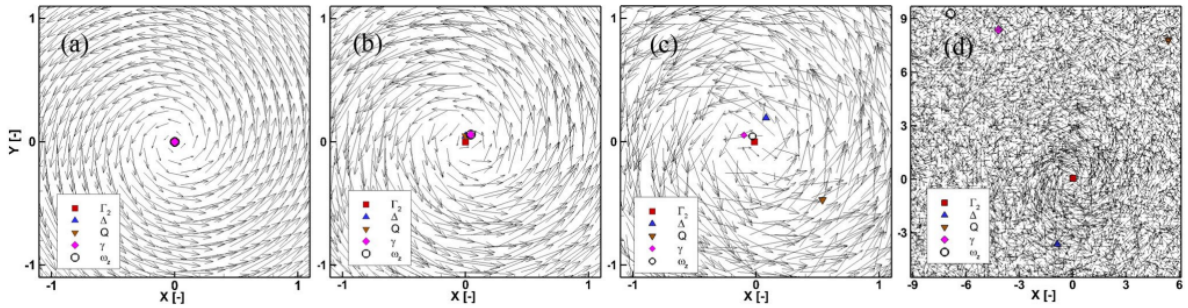


**Figure 4.2:** Velocity field plots with vortex centres detected by $\Gamma_2$-criterion, $\Delta$-criterion, $Q$-criterion, and $\omega_z$-criterion, with varying noise level: (a) noise 0%, (b) noise 20%, (c) noise 50%, and (d) noise 50%. Results obtained by De Gregorio et al. [19, 16].

In the second test case, with the experimental flow field of a rotor disk, De Gregorio et al. [19, 16] concluded that, although the $Q$-criterion is able to identify correctly the vortical structures, the peaks of the vortices are overpassed in intensity by peaks coming from the spurious regions, as shown in Figures 4.3 and 4.4. On the other hand, the $\Gamma_2$-criterion validates the main vortices, whose peak presents larger magnitude than the peaks in the spurious region, hence facilitating the identification of the key vortices.

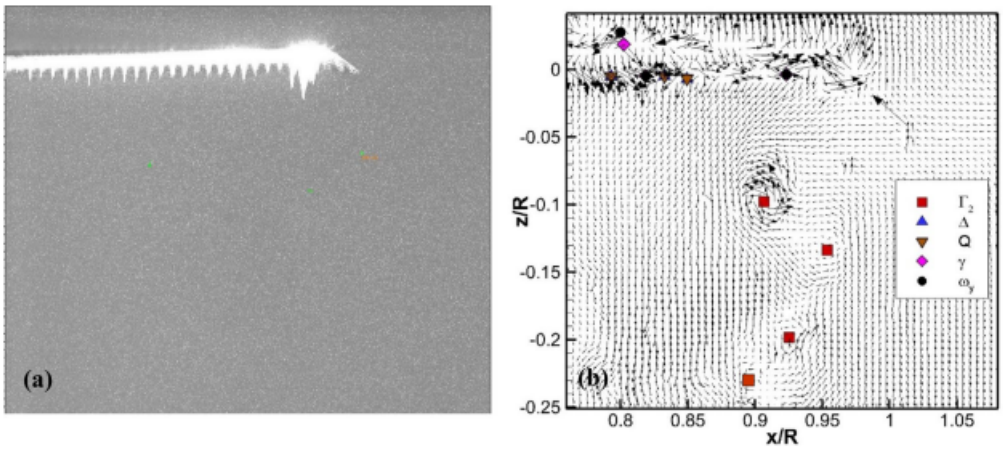


**Figure 4.3:** (a) PIV image with rotor blade; (b) resulting velocity field with detected vortex centres. Results by De Gregorio et al. [19, 16].

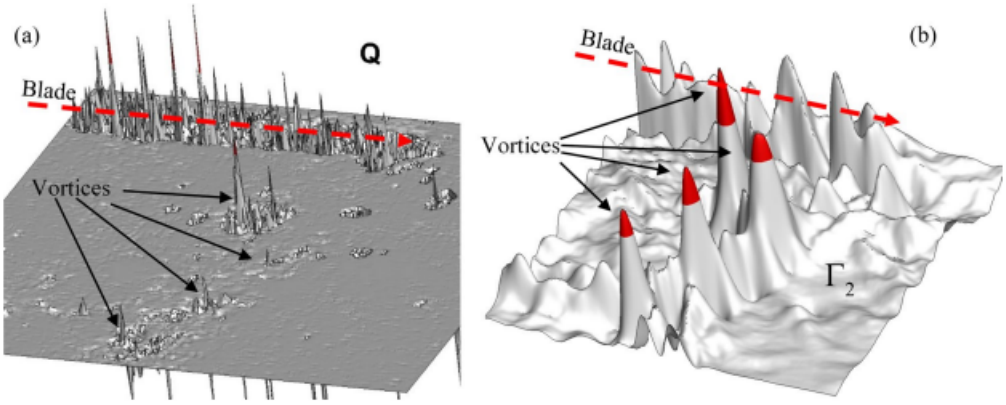


**Figure 4.4:** (a) $Q$-criterion applied over the resulting velocity field in Figure 27 with blade passage; (b) $\Gamma_2$-criterion applied to the aforementioned velocity field. Results obtained by De Gregorio et al. [19] [16].

## 4.3. Vortex Tracking Methodology

Implementations of the $\Gamma_2$-criterion in turbulent flow fields within the automotive industry, especially for experimentally measured flow fields, can be found in the work done by Croner et al. [17, 18], and by Josefsson et al. [33], to name a few. On the topic of calculating the vortex centre of measurements containing several vortices superimposed on a small-scale turbulent flow field, Sciacchitano and Stevens [60] developed a methodology to identify and track vortices spatially and temporaly by computing the exact location of their centres based on $\Gamma_2$ results. This methodology applies machine learning inspired algorithms to identify coherent structures. After calculating the $\Gamma_2$ distribution over each flow field measurement, hierarchical clustering is applied to determine vortex centres accurately; finally, the *Hungarian assignment* is used to enable labelling of vortices across flow field-slices, being able to account for different vortex behaviours such as merging or bursting.

Clustering aims at grouping coherent structures together by taking the centroids of $\Gamma_2$ contours in the fluid slice of measurements and classifying them within a same group based on similar properties. In this case, the property evaluated is the squared Eucledian distance of the centroids relative to each other. This approach is a version of the *single-link* hierarchical clustering defined by Sibson [58]. The linkage distance $D(A, B)$ is defined by Equation 4.9.

$$D_{Linkage}(A, B) = \min_{a \in A, b \in B} d(a, b) \tag{4.9}$$

where $a$ and $b$ are elements representing centroids of $\Gamma_2$ contours in each cluster $A$ and $B$. This *single-link* hierarchical clustering process as described by Sciacchitano and Stevens [60] is depicted in Figures 4.5 and 4.6 below.

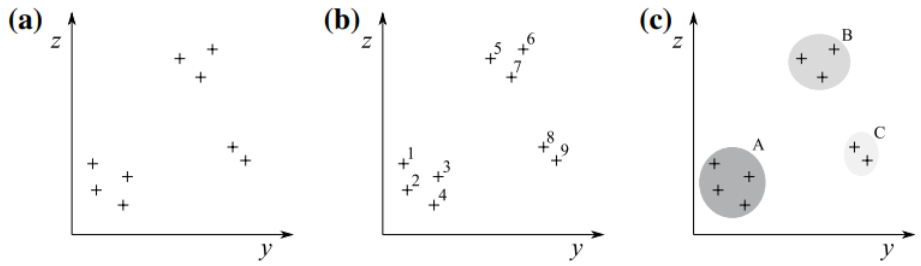


**Figure 4.5:** Hierarchical clustering process as described by Sciacchitano and Stevens [60]: (a) input data; (b) data labelling; (c) classifying data in clusters by similar properties.

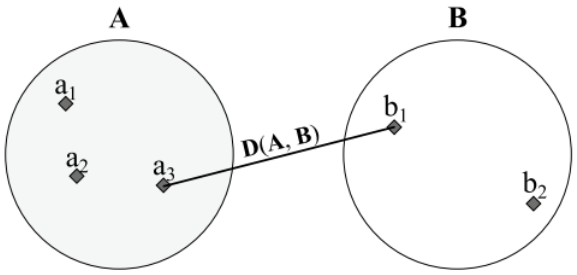


**Figure 4.6:** Linkage distance $D(A, B)$ for single-link clustering. Depicted by Manning et al. [38], adapted by Sciacchitano and Stevens [60].

As Sciacchitano and Stevens [60] point out, in practice the determination of the vortex core centroid includes plenty of noise in the data, for which Sciacchitano and Stevens [60] found as solution the process explained in this paragraph, consisting on clustering the centroids of contour levels, for which the effective vortex centre is represented by the mean of the points within a cluster. This does not represent the explicit physical position of the vortex core, but it is capable of detecting events such as vortex merging, where the mean centroid position would be shifted.

The implementation of the *Hungarian algorithm* derived by Kuhn [34] in an attempt to solve the *Assignment Problem*. Implementing the algorithm to track vortices temporally or spatially, Sciacchitano and Stevens [60] chose a *Hungarian* assignment formulation by Munkers [45], where it is assumed that the location of the vortices is known at time $t$ and $t+1$ from the $\Gamma_2$ results to which hierarchical clustering has been applied. Furthermore, a system of labelling of the vortices is used, while also a vortex at a time $t$ is selected as a hub. Then, the Eucledian distance relative to the hub coordinates is calculated, hence building up the so called cost matrix **M**, from which vortex pairings can be carried out after subtracting the row minima and resulting in null elements of the matrix. In this step, Sciacchitano and Stevens [60] highlight that the main assumption is that the time step $\Delta t$ is selected on the basis that no vortex travels more than half the minimum Eucledian distance with respect to its influencing vortex, $\delta/2$. This represents the vortex separation limit, depicted by Figure 4.7. Vortex behaviours such as bursting or leaving the domain of interest is addressed by modifications in the cost matrix.

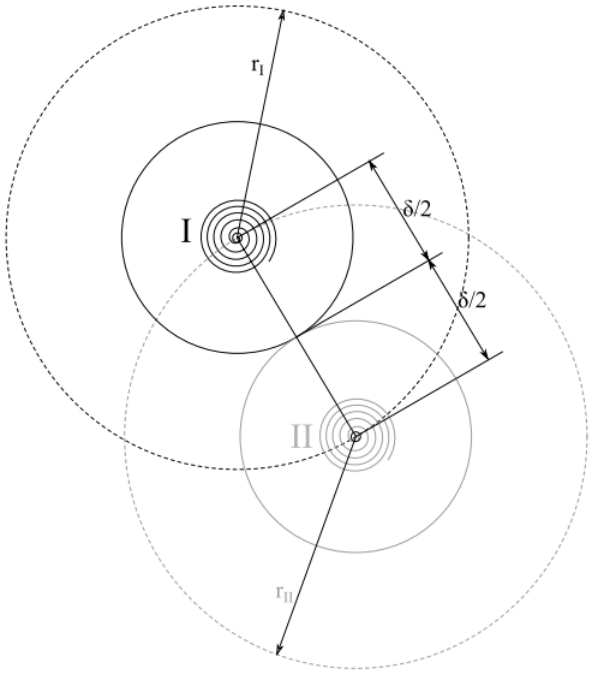


**Figure 4.7:** Vortex separation limit as defined by Sciacchitano and Stevens [60], where $4\delta/2$ is the minimum Euclidean separation distance between voritces.

Sciacchitano and Stevens [60] presented a discussion on the influence of the direction of the slicing of the 3D flow field, where it is remarked that the ideal slicing direction should be perfectly perpendicular to the vortex axis, although in practice this is challenging to achieve, especially if several vortices are being considered. Simpson et al. [59] investigated this problem through numerical simulation of an isolated Lamb-Oseen vortex, varying the axial velocity from null to a Gaussian distribution. Their conclusions were that these effects are relative small for angles up to 40° (between the slice and the vortex's axis).

## 4.4. Microdrag

To reach conclusions about the drag generated by isolated rotating tire tests, as well as full vehicle tests, it is useful to analyse the wake development. An approach widely used in the automotive industry to study the drag using momentum theorem is presented by Cogotti [11] [14] [12] [15], where a control volume C is defined enclosing the vehicle, and the distribution of pressures and velocities on the control volume rear boundary $S$, behind the vehicle, are measured, depicted by Figure 32.

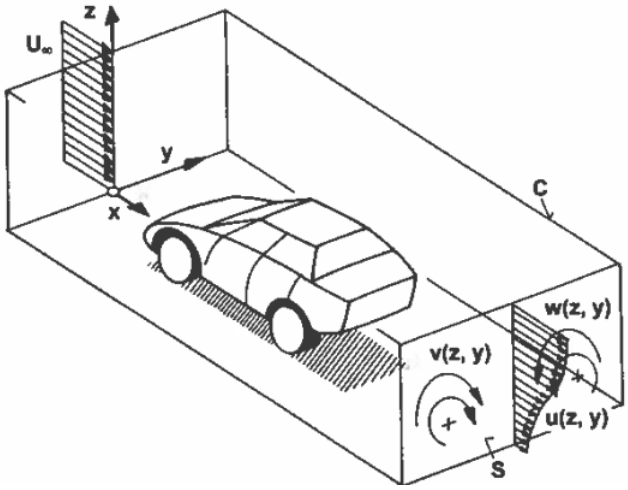


**Figure 4.8:** Depiction of control volume C for $C_{d_l}$ wake survey by Cogotti [11].

With the velocity components $u$, $v$ and $w$, the total pressure $p_{tot}$, and $A_x$ as the frontal reference area of the vehicle, using the momentum equation, the total drag results can be obtained with:

$$C_{D_l} \cdot A_x = \int_S (1 - C_{p_{tot}}) dS - \int_S \left(1 - \frac{u}{U_\infty}\right) dS + \int_S \left(\left(\frac{v}{U_\infty}\right)^2 + \left(\frac{w}{U_\infty}\right)^2\right) dS \tag{4.10}$$

where $C_{p_{tot}}$ is the total pressure coefficient and $U_\infty$ is the freestream velocity. Cogotti [11, 14, 12, 15] termed the sum of integrals in Equation 4.10 "Microdrag", $C_{D_l}$, and its distribution over the control surface S allows to draw conclusions about the points of drag generation. An example of performing a wake analysis with microdrag can be found in Windsors et al.'s [68] study of the effect of base bleed and rear cavities o the drag of an SUV, where a cavity is created at the rear face of the car (base), to bleed flow in this region. In the microdrag plots of the wake survey, conclusions of the regions where drag is generated can be drawn when comparing to the baseline vehicle. Furthermore, plotting $\Delta C_{D_l}$ shows the regions where the drag differences occur between the baseline case and the base bleed case (Figure 4.9).

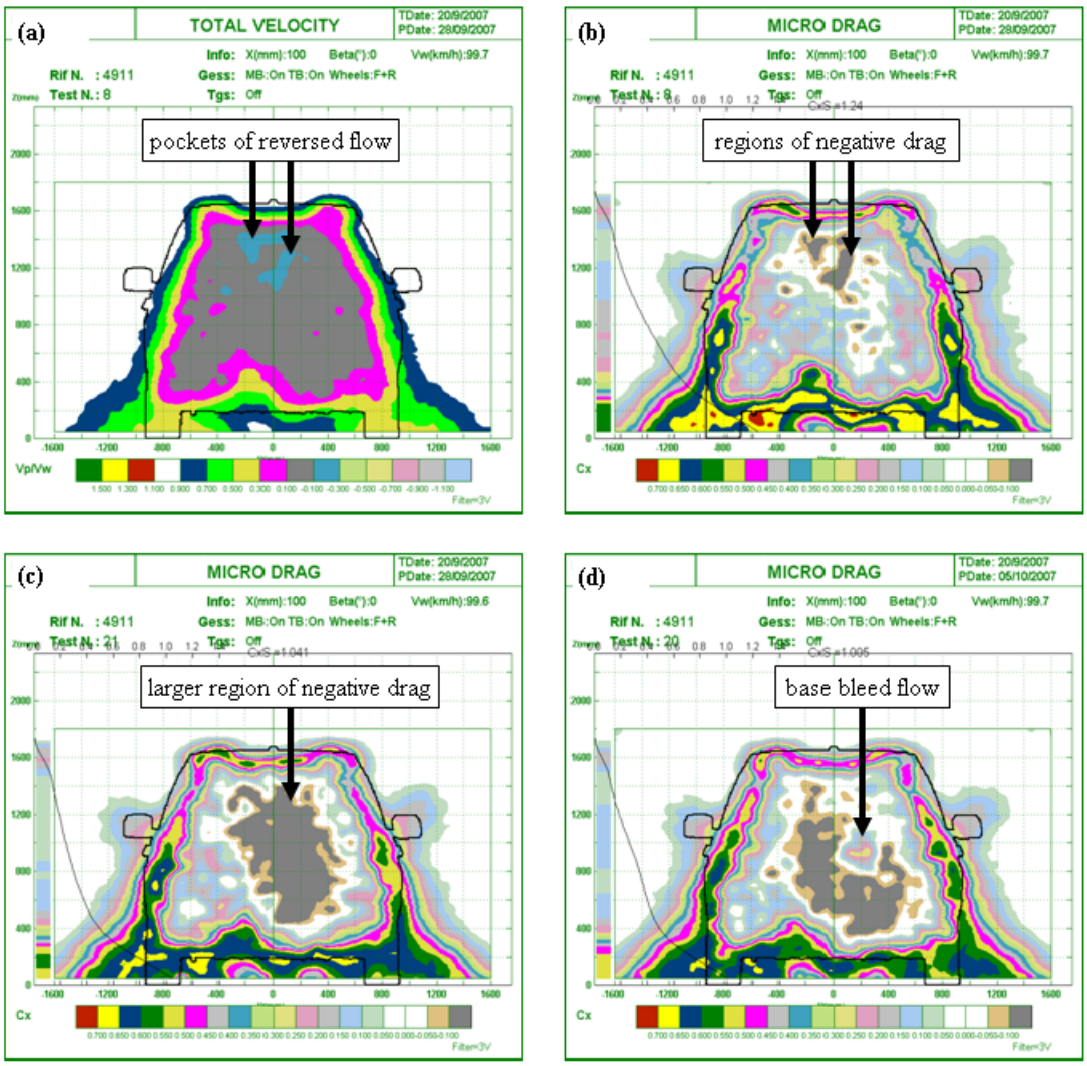


**Figure 4.9:** Wake survey plots in a $YZ$-plane. In (a), the velocity plot is given for the base vehicle; (b) microdrag plot for base vehicle; (c) microdrag plot for case with body cavity; and (d) microdrag plot for case with base bleed.

# 5

# Discussion

The previous sections have presented a review of the relevant topics in wheel aerodynamics, covering from a detailed description of the flow topology observed by previous studies and the different approaches to model a tire for aerodynamic numerical simulations, to useful analysis methodologies applicable to tire aerodynamic studies. Initial aerodynamic studies focused on understanding general aspects such as the pressure distribution and forces acting on the tire, while further research obtained understanding of the vortex structures and wake development. While the earliest research on tire aerodynamics was carried out experimentally, advancements in numerical modelling of rotating geometries have enabled further understanding of this complex aerodynamic problem. The complexity of this problem arises, not only from the complexity to accurately model a rotating tire, but also from the bluff nature of the geometry, which generates a highly turbulent flow field in its wake. To analyse how changes in the tire geometry affect this complex flow field, specific techniques are required, involving statistical analysis as well as vortex tracking methodologies adequate for turbulence-dominated measurements.

Fackrell and Harvey [24] presented the earliest study on the pressure distribution over an isolated rotating tire and an initial conclusion on the ”jetting effect” around the contact patch caused by the pressure difference front to rear, while conclusions on the vortex structures in the wake were drawn by Wäschle et al. [65, 66] and Diasinos et al. [20], which, although agreed mainly on the near-ground vortex structures, showed discrepancies on the mid and upper-half structures of the tire, which also were appreciated by other researchers. Investigations on the effects of geometries in or around the wheel showed that the use of different rims or wind tunnel set ups had an effect on the vortex structures, as well as in the symmetry of the wake, contributing to the flow topology discrepancies reported in Section 2. Rim geometries include a set of parameters that can be varied, and which, as concluded by Berg et al. [2], introduce a range of different flow behaviours to the wheel wake. These observations highlight the importance of understanding the interference of wheel and experiment setups in the results, especially when comparing with other references.

The considerable effect of rotation shown in the results obtained by Wäschle [65] indicates that for maximum accuracy, including tire rotation in experimental and numerical investigations is critical. Additionally, Wäschle [65] investigated the vortex structures generated by a rotating wheel mounted in a vehicle, indicating that the resulting flow topology is highly dependent on the rim geometry, as well as car-related geometries such as suspension, wheel arch and vehicle front, which alters the angle of the incident flow. Therefore, these conclusions may not always agree with other tests.

Section 2.3 opens a discussion on the time-dependence of the flow features of a rotating wheel. While the largest part of the literature reviewed presented conclusions based on the mean flow, Croner et al. [17, 18] showed that these features possess a highly unsteady behaviour that goes overlooked when analysing the mean flow. Parfett et al. [46] elaborated an experimental analysis of PIV instantaneous results. These instantaneous samples showed the unsteady nature of the near-ground vortices, although reconstructing the wake development turned out to show a certain amount of agreement with the vortex development concluded by Wäschle et al. [65] from mean-flow results. Therefore, it becomes clear that in the process of drawing conclusions from variations in the flow field of a rotating wheel, the unsteady behaviours need to be assessed, addressing the uncertainties derived from the unsteady behaviours that may no be captured.

Other geometrical parameters of the tire investigated englobe the tire surface and the tire deformation presented in Sections 2.6 and 2.7. Fackrell and Harvey [24] studied the differences on the pressure distribution caused by a smooth tire surface compared to a grooved tire surface with experimental studies, where it was proven that this geometrical aspect can have an effect in the overall behaviour of the flow over the tire. From a numerical point of view, modelling smooth and grooved tire surfaces has been possible with simple approaches such as rotating wall boundary condition, as thoroughly tested by Hobeika et al. [27]. However, modelling tread tire surfaces has posed a bigger challenge due to the presence of transversal grooves on the surface, which means that the tangential velocity component in this region would not provide a a physical result. While sliding mesh would be an appropiate solution to this problem, this approach is only applicable to axis-symmetric geometries, which deformed tires that intersect with the ground are not. To tackle this problem, Hobeika and Sebben [27] proposed the MRFg methodology. This approach involved a simplification of the tread surface and does not actually rotate the lateral grooves, while the recent DRTT methodology proposed by PowerFLOW® which implements IBM on the tread surface, allows for very accurate representation of the tread details.

The effect of vertical load translates into changes in the contact patch and the bulge protruding from the bottom of the sidewall simultaneously. An initial numerical investigation by Mortazawy et al. [44] on the effect of tire deformation showed large differences in the resulting wake, although it was not possible to attribute the cause of these variations to a specific deformation parameter. Tests to understand the effect of vertical load increase on the tire in the aerodynamic forces and wake development by Schnepf et al. [55] showed relevant changes in wake contraction. Mortazawy et al. [44] reproduced these loading tests numerically, agreeing on the trend of contracting wake with increasing loading. Since precise measurements of the deformed tire geometry in the experiment were not provided by Schnepf et al. [55] for the different loading cases, unknowns emerge as to how much the bulge and contact patch shapes were changing with increasing load. These unknowns also exist in the numerical test done by Schnepf et al. [55], as limitations on the tire scan procedure lead to inaccuracies in the geometry measurement. Joseffson et al. [33] tested an isolated bulge deformation without varying the contact patch, which resulted in a drag reduction in complete vehicle tests caused by a smaller deflection from the front tire wake due to a smaller outer contact patch vortex. This test provides some light into what contribution can be attributed to the bulge size parameter, but more tests with other isolated parameters would be necessary to gain a more complete understanding of all the contributions. Moreover, in the test scenarios where a full vehicle was tested, changes in the wake deflection, caused either by rim opening variations or by tire deformations that altered the vortex behaviour in the wake, showed a direct relation to the drag coefficient generated by the full vehicles tested, which was also appreciated in the base pressure of the vehicle. These relations indicate that the changes in drag caused by different deformations can be understood by studying how each deformation impacts its wake development.

In the likely case of not matching the deformed geometries in the numerical simulation, questions arise regarding the actual impact of these geometrical discrepancies in the results, then leading to questions on what deformation parameters have a larger impact on the flow variations observed by Schnepf et al. [55] and Mortazawy et al. [44].

Finally, the analysis methodologies presented in Section 4 define varied approaches to identify and understand the flow mechanisms involved in the complex problem of wheel aerodynamics. In particular, the vortex identification methodology proposed in the form of $\Gamma_2$ presents some particular advantages to identify large-scale vortices superimposed on a turbulent flow-field, as concluded by De Gregorio et al. [16]. This makes $\Gamma_2$ an adequate vortex identification method for the application of analysing vortex behaviours in the wake of a rotating wheel, which is characterised by being highly turbulent, as opposed to more traditional vortex identification methods.

# 6

# Research Objectives

The literature review presented in Chapters 2 and 3, and its pertinent discussion in Chapter 5 have outlined the major unknowns and uncertainties involved in the numerical modelling of rotating wheels, as well as the problems that derive from reproducing experimental tests. While the importance of maintaining fidelity in wheel-related and surrounding geometries has been stated and demonstrated, a gap in the literature is clearly identified when it comes to tire deformation and its effects. The analysis methodologies discussed in Section 4 present adequate methods to investigate the flow of rotating wheels in either standalone or full vehicle tests.

As stated in the previous sections, the deformation of the tire involves shape variations of the bulge and the contact patch. However, the individual impact of the majority of these variations has not been assessed and attributed (at the time of writing), therefore leaving open questions to which deformation effect is contributing the most to the wake development changes. Lack of knowledge on the impact of the deformation parameters may lead to poor correlation with experimental data, induced by the geometrical approximations that overlook relevant geometrical parameters and their impact in the resulting flow features.

These open questions regarding the impact of isolated tire deformation parameters promote interest in the study of these unknowns. As discussed at length previously, the physical tire deformation involves simultaneous variations of the bulge and contact patch shape. To be able to attribute the flow variation contribution of each deformation parameter, isolated parameter deformations are necessary. The structural nature of a rotating tire implies that isolating deformation parameters would require an extraordinarily large effort in experimental setups. Consequently, at the time of writing, this study is only feasible through numerical experiments, where digital tools enable the isolation and deformation of specific parameters in the tire's geometry.

This project is done in collaboration with Dassault Systèmes®, which means that the solver of choice is their Simulia® flagship solver for aerodynamic simulations: PowerFLOW®. As discussed previously, the high fidelity treaded tire modelling approach that PoweFLOW® offers is IBM through their DRTT methodology. Furthermore, LBM allows for a more accurate representation of the contact patch intersection with the ground, while Navier-Stokes based solvers need the implementation of a small step (depicted in Figure 2.20 in Section 2.7) that does not actually exist when the tire rotates on the road. Two case studies are evaluated: an isolated tire, reproducing the experimental setup given by Schnepf et al. [55]; and a complete vehicle case, where the tire geometries tested in the isolated wheel test are mounted to the *DrivAer*, an IP (Intellectual Property) free vehicle geometry developed by the Technical University of Munich [62]. The isolated tire case is intended to minimise the effect of surrounding geometries, while the complete vehicle case aims at showing the effect that wake variations resulting from different deformations have on the drag of the whole vehicle. In the following sections, the research objective of the thesis presented and its pertinent research questions are showcased.

## 6.1. Research Objective

The research objective of the thesis is:

**To identify and quantify which tire deformation parameters have the largest impact on drag coefficient and wake development variations.**

To facilitate the fulfilment of the defined research objective, a set of sub-objectives has been identified. These sub-objectives

- Perform an assessment of the time-dependence of results by studying the transient vortex behaviour in the wake.
- Define an analysis methodology to identify and quantify the flow features responsible for wake development variations.
- Identify the deformation parameters that have the highest impact on drag coefficient and wake variations.

## 6.2. Research Questions

Based on the research objective, a research question and its respective sub-questions are constructed. The research question is defined as:

**Which are the tire deformation parameters that produce the largest variations in drag coefficient and wake development?**

The areas of research are then broken down into:

- Aerodynamics of a Rotating Tire.
- Flow Analysis Methodologies.

The research sub-questions related to each research area are given below:

1. Aerodynamics of a Rotating Tire:
   (a) What are the most influential deformation parameters?
   (b) What are the flow features produced by the tire in the proposed tests and how do they relate to the deformation parameters tested?
2. Flow Analysis Methodologies:
   (a) How do the identified and quantified flow features influence the wake development?
   (b) How does the wake development relate to the drag coefficient variations?

# Part II

# Methodology

# 7

# Fluid Mechanics Definitions

In this chapter, basic fluid mechanics definitions are given, as they will be widely used along the next chapters of the present report. The first definitions to keep in mind are those that are essential for similarity analysis. These are the Reynolds number $Re$, which expresses a ratio of inertial forces over viscous forces, and the Mach number $Ma$, which expresses the ratio of kinetic energy over internal energy, see Equation 7.1.

$$Re_\infty = \frac{\rho_\infty U_\infty L_{ref}}{\mu_\infty}, \quad Ma = \frac{U}{a} = \frac{U_\infty}{\sqrt{\gamma R T_\infty}} \tag{7.1}$$

where $a$ is the speed of sound, $\gamma$ is the specific heat ratio ($\gamma = 1.4$ for standard air conditions), and $R$ is the specific gas constant $R = 287 J/(kg \cdot K)$.

The dynamic pressure of the fluid is described by:

$$q_\infty = \frac{\rho_\infty}{2} U_\infty^2 \tag{7.2}$$

PowerFLOW® uses a compressible formula to calculate the total pressure, as given by PowerFLOW®'s User's Guide [51]:

$$p_{tot} = p \left( \frac{T_{tot}}{T} \right)^{\gamma/(\gamma-1)} \tag{7.3}$$

where $p$ is the static pressure and $T_{tot}$ is defined as:

$$T_{tot} = T \left( 1 + \frac{\gamma - 1}{2} Ma^2 \right) \tag{7.4}$$

The pressure coefficient $C_p$ is defined as:

$$C_p = \frac{p - p_\infty}{q_\infty} \tag{7.5}$$

Hence, $C_p = 0$ denotes an undisturbed flow, while $C_p = 1$ denotes a stagnation point. For the total pressure $p_{tot}$, the total pressure coefficient is expressed as:

$$C_{p_{tot}} = \frac{p_{tot} - p_\infty}{q_\infty} \tag{7.6}$$

Finally, the aerodynamic forces (drag $F_x$, side force $F_y$, and lift $F_z$) are non-dimensionalised with the dynamic pressure and relating with the frontal area of the body $A_{ref}$, giving the forces coefficients:

$$C_{x/y/z} = \frac{F_{x/y/z}}{q_\infty A_{ref}} \tag{7.7}$$

Then, the moments correspondent to the aerodynamic forces are:

$$C_{Mx/My/Mz} = \frac{M_{x/y/z}}{q_\infty A_{ref} L_{ref}} \tag{7.8}$$

Regarding Equation 7.7, it is worth noting that in automotive aerodynamics, 1 aerodynamic count is equal to $C_{x/y/z} = 0.001$.

# 8

# Geometry Parametrisation

## 8.1. Geometry Overview

### 8.1.1. Standalone Tire

The geometrical setup of the project aims at replicating as close as possible the setup used by Schnepf et al. [55], as the standalone tire setup depiction in Figure 8.1 shows, where the arm and tire geometries replicated the experimental setup described by Schnepf et al. [55]. The undeformed tire has a base width of 254mm, with a side wall height of $\backsim$123mm. The wheel radius is 342.7mm (in the unloaded/undeformed case), and the rim geometry, as in the tests carried out by Schnepf et al. [55], counts with a flat cover to remove the influence of the flow effects characteristic of an open rim geometry caused by its rim spoke design. The tread channel gaps are measured to have a width of minimum of 2mm and maximum of 4mm.

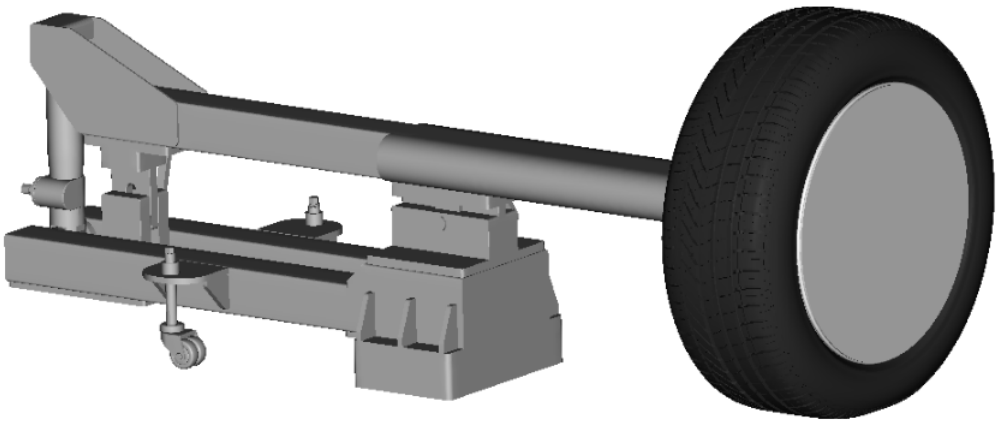

**Figure 8.1:** ISO-View of standalone tire setup, with arm and rim.

Figure 8.1 shows an Iso-view of the standalone tire, including arm, tire and rim, as setup in the standalone tire tests. The overall dimensions of the arm with the tire incorporated, are given in Figure 8.2 below. The total frontal area of the arm and the tire sums up to 0.444 $m^2$.

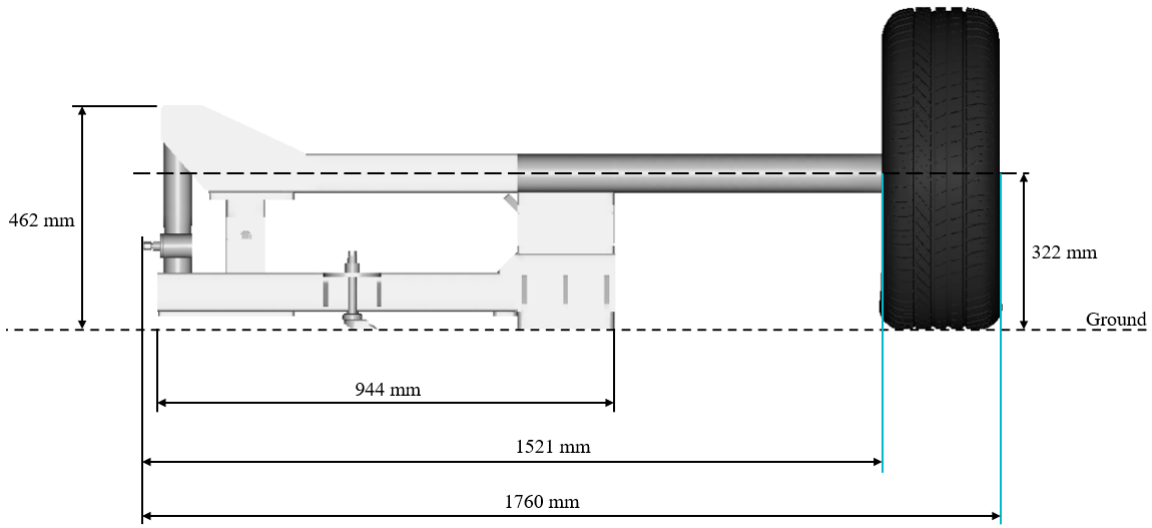


**Figure 8.2:** Overall dimensions of the standalone tire arm with the tire incorporated (front view).

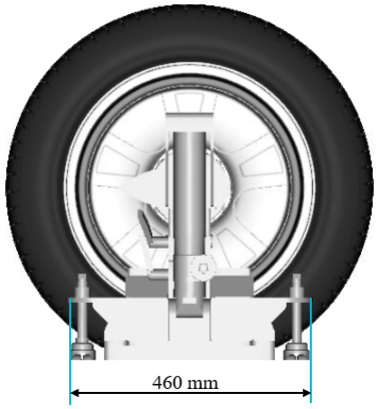


**Figure 8.3:** Overall dimensions of the standalone tire arm with the tire incorporated (side view).

### 8.1.2. Full Vehicle Geometry

As stated previously, for the full vehicle tets, the *DrivAer* model, developed by the Technical University of Munich [62], is used in the detailed under-body configuration, which includes a realistic representation of the under-body geometry of a sedan car. The rear-end geometry configuration is 'Notchback'. The frontal area of the vehicle, including the wheels, results in 2.172 $m^2$. An Iso-view of the described vehicle can be seen below in Figure 8.4.

**Figure 8.4:** ISO-View of *DrivAer* model used for the full vehicle tests.

It can be seen in Figure 8.4 that the wheels are fitted with the same rim cover used in the standalone tire setup to replicate the rim-flow conditions of the standalone test. The detailed underbody geometry can be appreciated in the bottom-view of the *DrivAer* provided below in Figure 8.5.

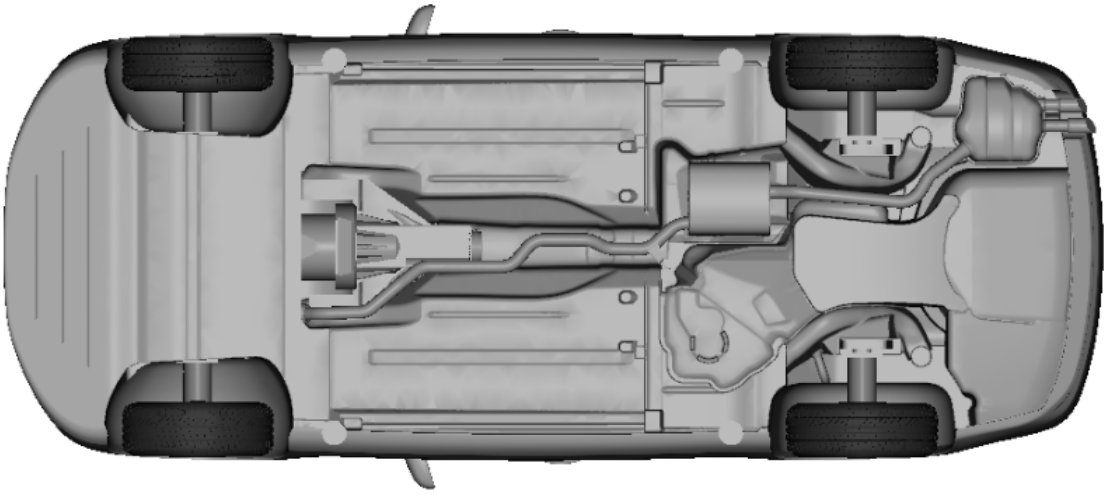

**Figure 8.5:** *DrivAer* bottom view, showing the 'Detailed Underbody' configuration used for the full vehicle tests.

The overall dimensions of the $DrivAer$ model are given in Figures 8.6 and 8.7.

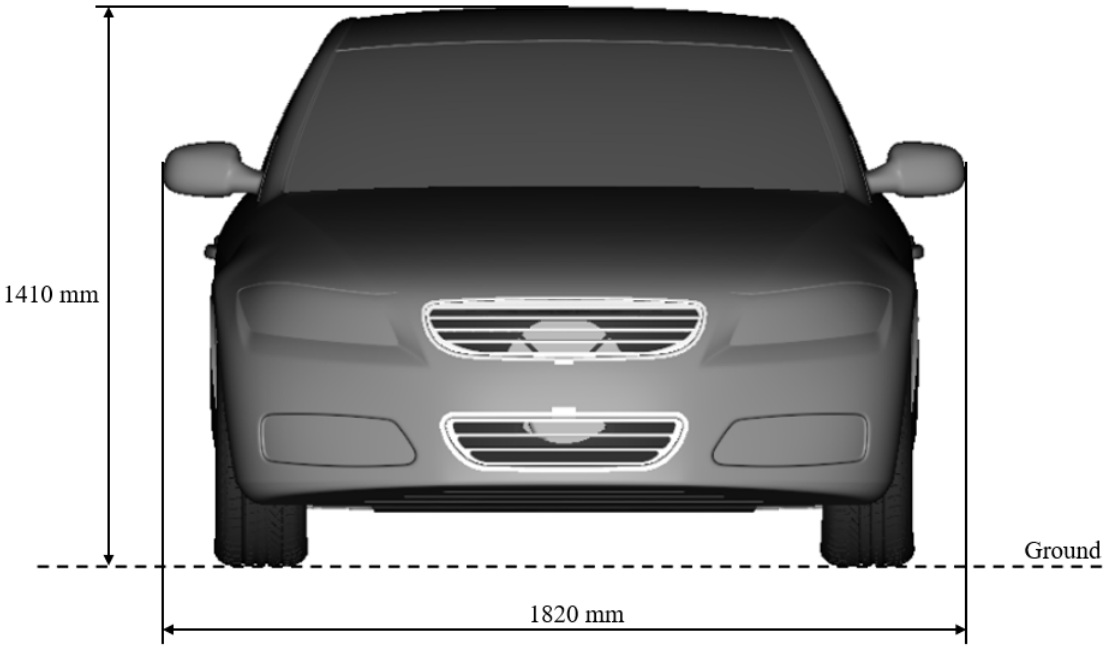


**Figure 8.6:** *DrivAer* front view, showing dimensions.

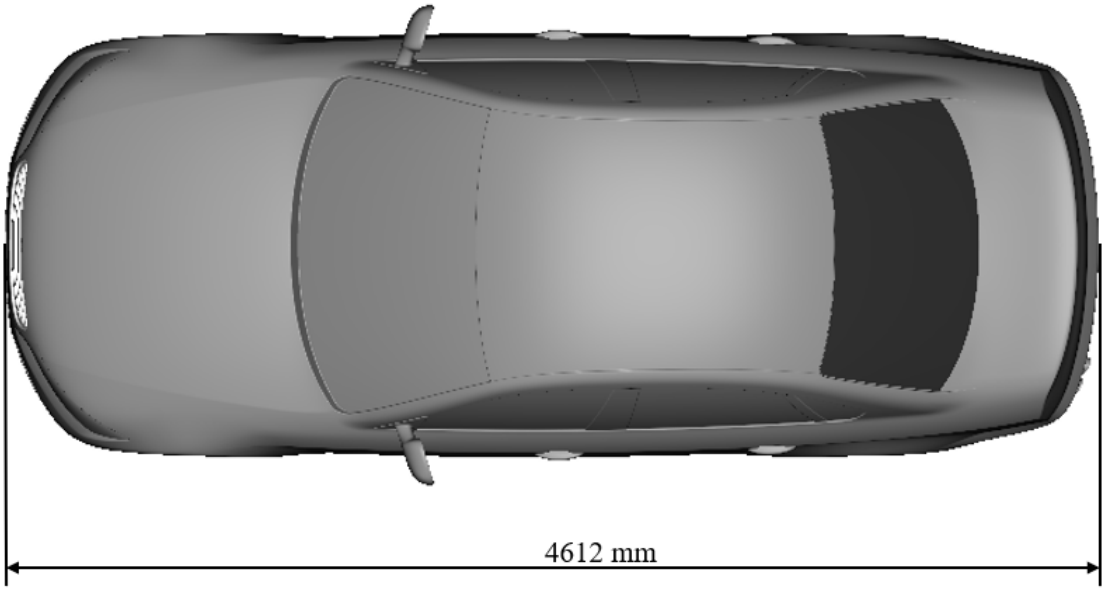


**Figure 8.7:** *DrivAer* top view, showing dimensions.

## 8.2. Tire Deformation Parametrisation

In Section 2.7 it was described that when vertical load is applied to a tire, mainly two parts of the tire geometry are affected: the bulge and the contact patch. The bulge is the region of the sidewall and corresponding tread on the lower end of the tire that surrounds the contact patch and gets deformed as a consequence of the load acting on the ground through the tire. Therefore, to alter parameters of the deformation in isolation, the deformation effect is broken down into several variables that are grouped into bulge deformations and contact patch deformations.

### 8.2.1. Bulge Deformations

Deformations over the bulge involve protrusions transversely and longitudinally. As Figure 8.8 depicts, these protrusions are accounted for through the Bulge Size $B$, the Lateral Insertion Angle $\alpha$, and the Longitudinal Insertion Angle $\beta$. While $B$ represents a uniform increase of the bulge outwards sideways, $\alpha$ represents an sharpening of the shoulder region (only in the bulge area) without increasing the bulge size. Finally, $\beta$ provides an increment of the bulge protrusion in the longitudinal direction. Note that a reduction of $\alpha$ and $\beta$ will result in a larger bulge protrusion.

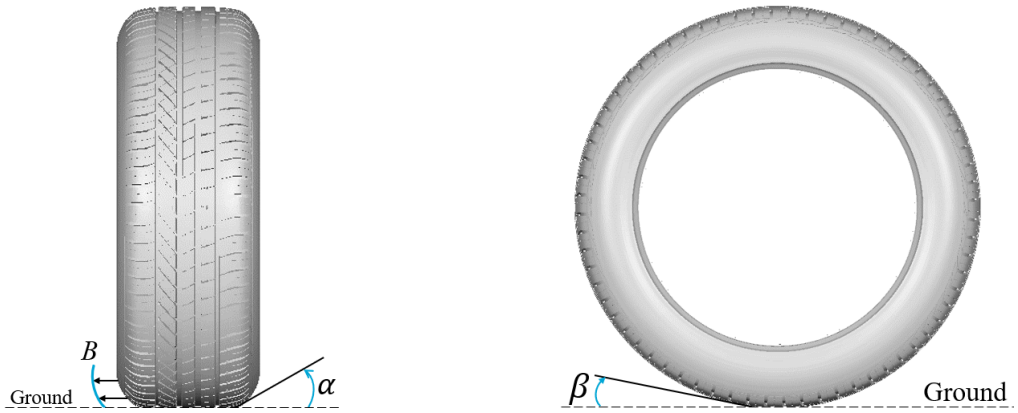


(a) Tire front view, with parameters Bulge Size *B* and Lateral Insertion Angle $\alpha$.

(b) Tire side view, with parameter Longitudinal Insertion Angle $\beta$.

**Figure 8.8:** Tire bulge-related parameters, where the discontinuous lines represent the ground.

### 8.2.2. Contact Patch Deformations

When it comes to the contact patch, deformations have been broken down into eight main parameters: width $W$; inside, outside and central lengths ($L_{inside}$, $L_{outside}$ and $L_0$ respectively); and the curvature of the corners of the contact patch at the four different positions through their radius (Front Inside Corner $R_{FIC}$, Rear Inside Corner $R_{RIC}$, Front Outside Corner $R_{FOC}$, and Rear Outside Corner $R_{ROC}$), see Figures 8.9 and 8.10.

These parameters can be varied simultaneously in certain orders to generate specific contact patch shapes, such as the shape resulting from a cambered tire (when angle is applied over the tire to tilt it inwards or outwards), or an 'H-Style' shape, referred to as 'H-Shape', which results from a low pressure tire, or very large tires.

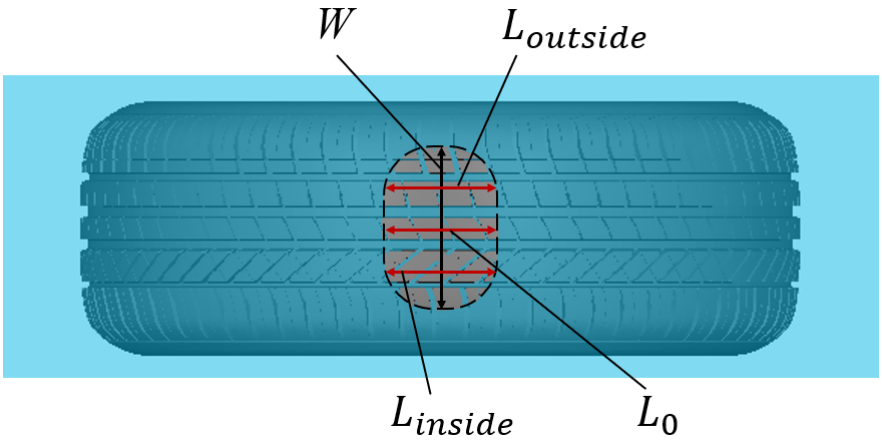


**Figure 8.9:** Tire bottom view, with parameters Contact Patch Width *W*, and Contact Patch Lengths $L_{outside}$, $L_0$ and $L_{inside}$, where the blue screen represents the ground.

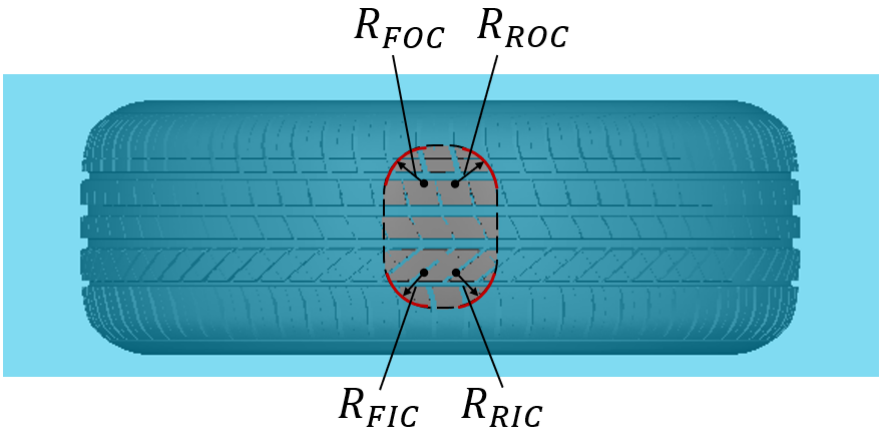


**Figure 8.10:** Tire bottom view, with parameter Contact Patch Curvature, given by the radius at each corner $R_{FOC}$, $R_{ROC}$, $R_{FIC}$ and $R_{RIC}$, where *FOC* is the Front Outside Corner; *ROC* is Rear Outside Corner; *FIC* is Front Inside Corner; and *RIC* is Rear Inside Corner. The blue screen represents the ground.

### 8.2.3. Deformation Implementation

As thoroughly covered in Section 2.7, the effect of the deformation as compared to an undeformed tire is well investigated and documented. Therefore, to continue the work carried out by Mortazawy et al. [44] where the impact of deformation parameters is assessed, the baseline geometry of the current study is defined as a baseline deformed tire, generated with the Tire Morph Lattice tool in PowerDELTA®, the meshing tool offered by Simulia®. The deformation inputs provided were:

- Tire Loaded Radius *TLR*: 327 mm.
- Tire Pressure: 2.3 bar.
- Tire Sink: -1 mm.

The tool then produces a lattice structure around the tire mesh that is morphed accordingly to the inputs given. The lattice generated can be seen in Images 8.11 (a) and 8.11 (b) below. For the purpose of displacing nodes relevant to the tire bulge and the contact patch, a higher density of node sections are concentrated around the bulge and contact patch area.

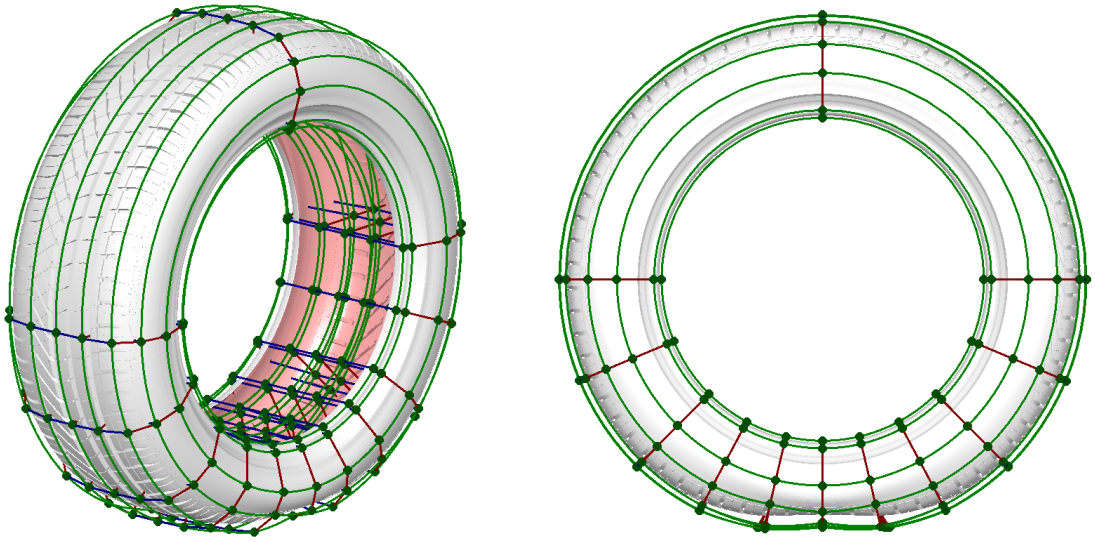

(a) Tire lattice Iso-view.

(b) Tire lattice side view.

**Figure 8.11:** Lattice structure created around the tire surface mesh.

A comparison between the undeformed geometry and the deformed geometry resulting from the Tire Morph Lattice tool is given in Figure 8.12, where shape changes can be recognised in the bulge area. Similarly, Figure 8.13 shows the variations generated in the contact patch shape and size through the implementation of the deformation.


**Figure 8.12:** Undeformed tire (left) versus Deformed tire (right).

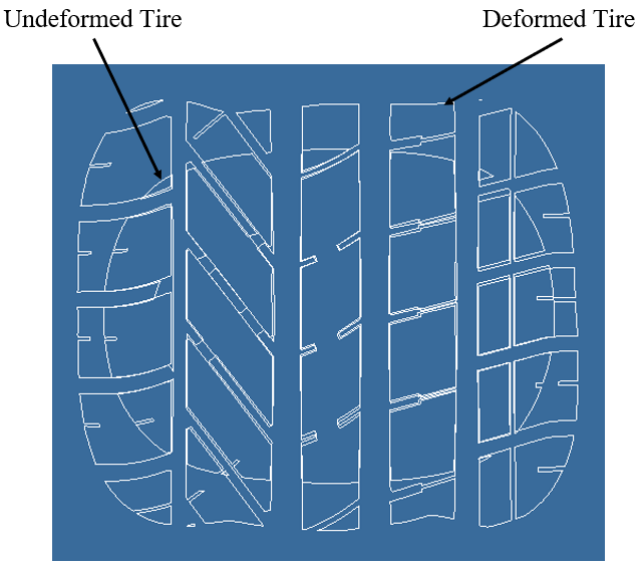


**Figure 8.13:** Contact patch comparison between undeformed and deformed tire.

The implementation of the deformation parameters described in Section 8.2 on the tire geometry described in Section 8.1 is done by adjusting the lattice nodes. Figure 8.14 below shows how each node has an area of influence over the tire mesh, which will be morphed accordingly to the nodes displacement. This area of influence can be shrunk or expanded in the Morphing Tool within PowerDELTA®, as well as by varying the number of nodes across each lattice frame, both in the angular-direction frame, and over the cross section frame. These variations of the lattice became useful in the process of varying deformation parameters while minimising the impact on the other parameters.

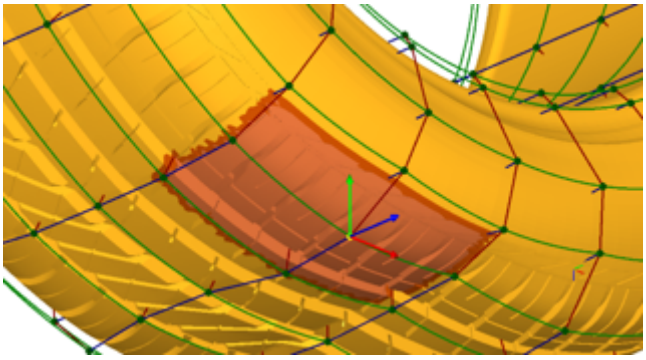

**Figure 8.14:** Domain of influence (reddened area) relative to selected point in the lattice.

### 8.2.4. Deformation Parameter Matrices

Even though the procedure described above in Section 8.2.3 allows for very low interference with parameters excluded through each parameter-specific deformation, the limitations of this procedure show that for certain deformations, especially contact patch deformations, inadvertent interference occurs. To address this, specific deformations studies were carried out, as will be explained later in this chapter. Two variations with respect to the baseline deformation are introduced for each parameter, where the deformation is implemented to a qualitative observation of the desired parameter, and a posterior measurement of the parameters in question, since the nature of the lattice structure imposes great difficulties to modify shape variations in a discrete fashion.

Table 8.1 shows the measured parameters for the baseline deformation, as well as the measured parameters on the resulting isolated bulge deformations with respect to the baseline measurements. In the implementation of these deformations, the contact patch size and shape remained unaltered, and introducing restricted variations to the desired isolated parameter was carried out with little to no interference with other bulge deformation parameters.

| **Parameter** | Baseline | Test 1 | Test 2 | Test 3 | Test 4 | Test 5 | Test 6 |
|---|---|---|---|---|---|---|---|
| $B$ [mm] | 6 | +5 | +10 | - | - | - | - |
| $\alpha$ [deg] | 17 | - | - | 15* | 6* | - | - |
| $\beta$ [deg] | 30 | - | - | - | - | 12.6* | 5.4* |
| $L_{in}$ [mm] | 150 | - | - | - | - | - | - |
| $L_0$ [mm] | 153 | - | - | - | - | - | - |
| $L_{out}$ [mm] | 150 | - | - | - | - | - | - |
| $W$ [mm] | 180 | - | - | - | - | - | - |
| $R_{FOC}$ [mm] | 31.7 | - | - | - | - | - | - |
| $R_{FIC}$ [mm] | 31.7 | - | - | - | - | - | - |
| $R_{ROC}$ [mm] | 31.7 | - | - | - | - | - | - |
| $R_{RIC}$ [mm] | 31.7 | - | - | - | - | - | - |

**Table 8.1:** Bulge Deformation Tests.

*Not given as difference to baseline, but as absolute measurements.

Restricted deformations on the contact patch proved more difficult, and Table 8.2 shows that increasing the length and the width resulted in a slight smoothing (curvature radius increase) of the corners. The three relevant parameters for the length deformation ($L_{inside}$, $L_{outside}$ and $L_0$) are modified uniformly.

| **Parameter** | Baseline | Test 7 | Test 8 | Test 9 | Test 10 |
|---|---|---|---|---|---|
| $B$ [mm] | 6 | - | - | - | - |
| $\alpha$ [deg] | 17 | - | - | - | - |
| $\beta$ [deg] | 30 | - | - | - | - |
| $L_{in}$ [mm] | 150 | +7.3 | +15 | - | - |
| $L_0$ [mm] | 153 | +7.3 | +15 | - | - |
| $L_{out}$ [mm] | 150 | +7.3 | +15 | - | - |
| $W$ [mm] | 180 | - | - | +4.6 | +8.4 |
| $R_{FOC}$ [mm] | 31.7 | +2 | +6 | +12 | +8 |
| $R_{FIC}$ [mm] | 31.7 | +2 | +6 | +12 | +8 |
| $R_{ROC}$ [mm] | 31.7 | +2 | +6 | +12 | +8 |
| $R_{RIC}$ [mm] | 31.7 | +2 | +6 | +12 | +8 |

**Table 8.2:** Contact Patch Deformation Tests.

Finally, to derive the effect of the curvature changes from the length and width, tests with varying curvature based on the largest length and width deformations were performed. Since more than one parameter is being purposely varied in these tests, they are presented together with the multi-parameter deformations matrix, which aims at investigating the effect of the contact patch shapes described in earlier (Camber shape and H-shape) in Table 8.3.

| **Parameter** | Baseline | Test 11 | Test 12 | Test 13 | Test 14 | Test 15 | Test 16 | Test 17 | Test 18 |
|---|---|---|---|---|---|---|---|---|---|
| $B$ [mm] | 6 | - | - | - | - | - | - | | |
| $\alpha$ [deg] | 17 | - | - | - | - | - | - | | |
| $\beta$ [deg] | 30 | - | - | - | - | - | - | | |
| $L_{in}$ [mm] | 150 | +15 | +15 | - | - | +20 | +34 | - | 12.6 |
| $L_0$ [mm] | 153 | +15 | +15 | - | - | - | +14.5 | -23 | -13 |
| $L_{out}$ [mm] | 150 | +15 | +15 | - | - | +14 | +5 | - | +12.6 |
| $W$ [mm] | 180 | - | - | +8.4 | +8.4 | - | - | - | - |
| $R_{FOC}$ [mm] | 31.7 | +1 | +17 | +14.3 | +26.2 | +41 | +43 | -2.4 | -7.3 |
| $R_{FIC}$ [mm] | 31.7 | +1 | +17 | +14.3 | +26.2 | -1 | -2 | -2.4 | -7.3 |
| $R_{ROC}$ [mm] | 31.7 | +1 | +17 | +14.3 | +26.2 | +19 | +25 | -2.4 | -7.3 |
| $R_{RIC}$ [mm] | 31.7 | +1 | +17 | +14.3 | +26.2 | 5.5 | +3.3 | -2.4 | -7.3 |

**Table 8.3:** Multi-parameter Deformation Tests.

The resulting deformed geometries for each of these tests are depicted in Appendix B.

# 9

# Numerical Method

As part of the collaboration with Dassault Systèmes® for this thesis, the commercial solver PowerFLOW® was used for the numerical studies. PowerFLOW® is based on the Lattice-Boltzmann method, which derives from kinetic theory. Kinetic theory-based methods require the use of "lattice" grids to discretise the computational domain. These grids are characterised by being regular and non-surface-oriented. This chapter presents an overview of Kinetic Theory, as well as a description of the Lattice-Boltzmann method, also referred to as *LBM*.

## 9.1. Kinetic Theory Overview

The existing approaches to describe gaseous flows are characterised by the Knudsen number, which represents the ratio between the mean free path $\lambda$ between molecule collisions and the reference length $L$, as given by Equation 9.1.

$$Kn = \frac{\lambda}{L} \tag{9.1}$$

$Kn >> 1$ corresponds to free molecular flow, while for $Kn << 1$ the flow is continuum. The latter one is a considered a valid assumption for ground vehicle aerodynamics. Kinetic theory can describe flows contained within the $Kn$ range $1 << Kn << 1$, hence discrete lattice methods based on kinetic theory present the more widespread approach to model fluids. For flows characterised by $Kn << 1$, Navier Stokes can be used, as it is valid exclusively for continuum Newtonian fluids, while further modelling simplifications are constituted by the Euler equations, where the flow is assumed to be inviscid; and potential theory, where the flow is assumed to be irrotational and inviscid.

In automotive aerodynamics, the flow is assumed to be subsonic with temperatures of around 20°C. Therefore, the air is assumed to behave like an ideal gas, where the relation between pressure $p$, density $\rho$, and temperature $T$.

$$p = \rho RT \tag{9.2}$$

where the dry air specific gas constant is $R = 287 J/(kg \cdot K)$.

Kinetic theory presents a statistical description of molecular motion on a mesoscopic level, which is more feasible than the microscopic level at which individual molecules move and collide. The mesoscopic level of kinetic theory is still well below the macroscopic level of Navier-Stokes equations. In this approach, the motion of many particles in a volume with speed $\mathbf{c}$, position $\mathbf{x}$ and time $t$ is specified by a velocity distribution function $f(\mathbf{x}, \mathbf{c}, t)$. The Boltzmann equation (Equation 9.3) expresses the rate of change of the velocity function distribution $f(\mathbf{x}, \mathbf{c}, t)$,

where the first term on the left-hand side is the time evolution, the second term is the convection, and the right-hand side term is known as the "collision operator" $\Omega$, through which equilibrium is achieved, see Chen et al. [9].

$$\frac{d}{dt}f(\mathbf{x},\mathbf{c},t) = \frac{\partial}{\partial t}f(\mathbf{x},\mathbf{c},t) + \mathbf{c}\cdot\nabla f(\mathbf{x},\mathbf{c},t) = \Omega(f(\mathbf{x},\mathbf{c},t)) \tag{9.3}$$

In the Boltzmann equation, a physically correct solution is achieved when the collision operator satisfies conservation of mass, momentum and energy. The tendency towards equilibrium is accounted for by the collision operator $\Omega$ through viscosity. An approximation of the collision operator is achieved with a modified *BGK* (Bhatnagar, Gross and Krook) model [4]:

$$\Omega(\mathbf{x},\mathbf{c},t) = \frac{1}{\tau}[f^{eq}(\mathbf{x},\mathbf{c},t) - f_i(\mathbf{x},\mathbf{c},t)] \tag{9.4}$$

Equation 9.4 gives the relaxation through the difference between the current local state $f_i$ and and the local equilibrium distribution $f^{eq}$. The relaxation time $\tau$ represents a collision frequency. Through the Chapman-Enskog expansion, the relaxation parameter is related to the kinematic viscosity $\nu$ by

$$\frac{\nu}{T} = \tau - \frac{1}{2} \tag{9.5}$$

Integrating over all possible particle speeds $\mathbf{c}$ gives the macroscopic quantities

$$\text{Density:} \quad \rho(\mathbf{x},t) = \int f(\mathbf{x},\mathbf{c},t)d\mathbf{c} \tag{9.6}$$

$$\text{Momentum:} \quad \rho(\mathbf{x},t)\cdot u(\mathbf{x},t) = \int f(\mathbf{x},\mathbf{c},t)\mathbf{c}d\mathbf{c} \tag{9.7}$$

$$\text{Energy:} \quad E(\mathbf{c},t) = \int f(\mathbf{x},\mathbf{c},t)\cdot(\mathbf{c}-\mathbf{v})^2 d\mathbf{c} \tag{9.8}$$

with the static pressure being obtained through the equation of state (Equation 9.2).

Substituting the collision operator into the Boltzmann equation (9.3), where $f_c = f(\mathbf{x},\mathbf{c},t)$, gives the equation of motion of the fluid particle distribution function to describe the macroscopic behaviour of the fluid:

$$\frac{\partial}{\partial t}f_c + \mathbf{c}\cdot\nabla f_c = \frac{1}{\tau}[f_c^{eq} - f_c] \tag{9.9}$$

where the equilibrium distribution $f^{eq}$ represents the function resultant in a thermodynamically relaxed distribution, given by Maxwell form:

$$f^{eq} = \frac{\rho}{(2\pi RT)^{3/2}}\exp\left[-\frac{(\mathbf{c}-\mathbf{u})^2}{2RT}\right] \tag{9.10}$$

From the equation of motion (9.9) for the fluid particle distribution function (also referred to as PDF) at kinetic theory level, equations of motion for the macroscopic behaviour of the fluid can be derived. This procedure is carried out by performing a Taylor expansion of the derivative terms of Equation 9.9, subsequently followed by integration of the microscopic velocities, recovering in the Navier-Stokes equations.

## 9.2. The Lattice-Boltzmann Method

Lattice Methods are denoted as *DjQm*, where *j* is the dimensionality, and *m* the finite number of discrete particle velocities, with PowerFLOW® implementing *D3Q19*. Hence, the phase space is three-dimensional with 19 discrete velocities. The lattice system provides the discrete spatial locations, and the time step $\Delta t$ provides discrete time. The method is of second order in space and time. The equation of motion of the PDF for the discrete lattice system is expressed as:

$$\frac{\partial}{\partial t} f_i + \mathbf{c}_i \cdot \nabla f_i = \frac{1}{\tau}[f_i^{eq} - f_i] \tag{9.11}$$

where $f_i$ is the PDF for state $i$, and the continuum velocity $\mathbf{c}$ is replaced by the discrete particle velocity $\mathbf{c}_i$. Substituting the gradients for the discrete quantities gives:

$$f_i(x + \mathbf{c}_i \Delta t, t + \Delta t) - f_i(x, t) = \frac{1}{\tau}[f_i^{eq} - f_i] \tag{9.12}$$

Equation 9.12 updates across time steps, hence generating an inherently time-dependent flow field solution. As given by Kinetic Theory, the macroscopic quantities are obtained by integrating the particle distribution function, this time as summations of the lattice states:

$$\rho = \sum_i^N f_i, \qquad \rho u = \sum_i^N f_i \mathbf{c}_i, \qquad P + \rho \mathbf{u}\mathbf{u} = \sum_i^N f_i \mathbf{c}_i \mathbf{c}_i \tag{9.13}$$

where *N* is the number of lattice states.

## 9.3. Spatial Discretization

The fluid domain is discretised into a Cartesian grid composed of cubic cells, hence composing the lattice. These cubic cells are referred to as voxels, and have an aspect ratio of 1. As mentioned previously, PowerFLOW® implements a *D3Q19* method, meaning that each voxel posses 19 discrete particle velocities, as depicted in Figure 9.1.

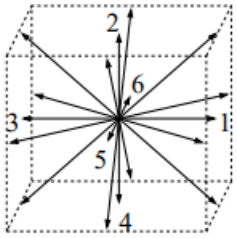


**Figure 9.1:** Voxel with discrete particle velocities, extracted from Wagner [64].

The geometry is represented by a surface triangulation with the main requirement being that the solid faces composing the geometry constitute closed facetisations, so that the exterior and interior face are clearly separated, resulting in the exterior face bounding the fluid domain, while the interior face has no interface with the fluid domain. Although voxels have a regular structure, the surface of the geometry may be of any arbitrary shape. In PowerFLOW® this is enabled by the generation of surfels, explained in more detail in Section 9.5. When the discretisation of the computational domain is carried by dividing the domain with lattice planes, the geometry facets are intersected by these planes, resulting in the aforementioned surfels. As it is observable in Figure 9.2, surfels generally make up to a fraction of the geometry's facets. Only when a facet is completely enclosed within a voxel will it become a single surfel.

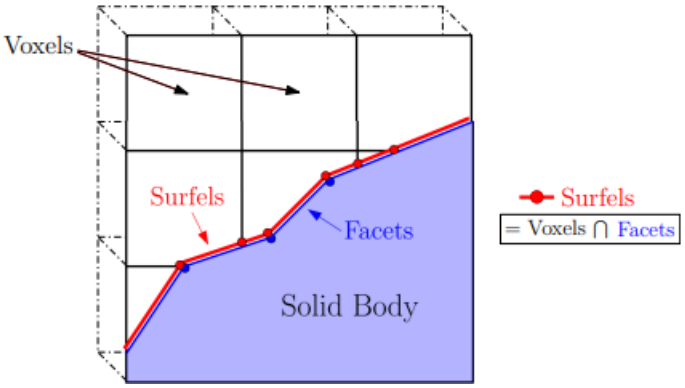


**Figure 9.2:** Generation of surfels through the geometry's facets intersecting with the Cartesian planes, extracted from Pestana [48].

## 9.4. Temporal Discretisation

During simulation time, particles move from one voxel to another, and interact with each other within each time step. Consequently, each time step is composed of two phases: particle advection and particle collision. In the discrete Lattice-Boltzmann Equation 9.12, the advection is represented by the left-hand side, while the right-hand side refers to the collision phase.

- **Particle Advection Phase:** Particles move one discrete step from one voxel to another at each time step. However, PowerFLOW® tracks particle density distributions rather than the movement of individual particles. Therefore, each particle distribution function $f_i(\mathbf{x}, t)$ propagates with according to its microscopic velocity $\mathbf{c}_i$ to the neighbouring lattice $\mathbf{x} + \mathbf{c}_i$. Consequently, while individual particle densities can only shift in a discrete direction, the macroscopic flow velocity can be continuous in any direction.
- **Particle Collision Phase:** As mentioned in Section 9.1, the collision operator has the objective to bring thermodynamic equilibrium to provide a physically correct solution. Therefore, after the advection phase, at each voxel, all the microscopic velocity states are summed to calculate $\rho$ and $\mathbf{u}$. Next, the equilibrium distributions $f^{eq}$ are computed. Finally, the new particle distribution function $f_i^{new}$ is obtained through the collision operator:

$$f_i^{new} = f_i + \frac{1}{\tau}[f_i^{eq} - f_i] \tag{9.14}$$

The timestep $\Delta t$ is given by [57]:

$$\Delta t = c_{lattice} \cdot \frac{\Delta x}{v_\infty} \tag{9.15}$$

where $c_{lattice}$ is the speed of sound, $\Delta x$ is the voxel size, and $v_\infty$ is the free stream velocity.

## 9.5. Wall Boundary Conditions

As introduced in Section 9.3, by intersecting the lattice planes with the facets composing the geometry, the resulting surface elements are the so-called "surfels", while the voxels intersecting the surfels are called "partial voxels". As described by Chen et al. [10], this means that a curved smooth surface is approximated via piece wise-planar elements, where the resulting surface acquires a polygonal shape consisting of planar facets ($S^\alpha; \alpha = 1, ..., \alpha_m$), each one of them being tangential to the original smooth surface, with each of their surface normal pointing towards the fluid domain $\mathbf{n}^\alpha$ ($|\mathbf{n}^\alpha| = 1$), and an area $A^\alpha$. For each facet, a parallelepiped is extruded in the direction of $-\mathbf{c}_i$, with volume defined by $V_i^\alpha = |\mathbf{c}_i \cdot \mathbf{n}^\alpha| A^\alpha \Delta t$. Then, the PDF's are redistributed to the near-wall voxels according to the volumetric overlap existing between each voxel with the parallelepiped for each state.

On the surface, the in-going particles $\Gamma_i^{in,\alpha}(t) \equiv \sum_{\mathbf{x}} P_i^\alpha(\mathbf{x}) N_i(\mathbf{x}, t)$; $\forall\, \mathbf{c}_i \cdot \mathbf{n}^\alpha \leq 0$ are converted into the outcoming particles $\Gamma_i^{in,\alpha}(t) \equiv \sum_{\mathbf{x}} P_i^\alpha(\mathbf{x}) N_i(\mathbf{x}, t)$; $\forall \mathbf{c}_i \cdot \mathbf{n}^\alpha \geq 0$, where $N_i(\mathbf{x}, t) (\equiv f_i(\mathbf{x}, t) \Delta V)$. Hence, analogous to the continuous Boltzmann situation, the fluxes across a surface can be defined exactly by integrating the PDF's crossing the surface. The mass flux is given by:

$$\jmath_m^\alpha(t) \equiv \frac{1}{A^\alpha \Delta t}\ [\ \sum_{i,\mathbf{c}_i\cdot\geq 0} \Gamma_i^{out,\alpha}(t) - \sum_{i,\mathbf{c}_i\cdot\leq 0} \Gamma_i^{in,\alpha}(t)] \tag{9.16}$$

And the momentum flux given by:

$$J_m^\alpha(t) \equiv \mathbf{F}^\alpha \equiv \frac{1}{A^\alpha \Delta t}\ [\ \sum_{i,\mathbf{c}_i\cdot\geq 0} \mathbf{c}_i\Gamma_i^{out,\alpha}(t) - \sum_{i,\mathbf{c}_i\cdot\leq 0} \mathbf{c}_i\Gamma_i^{in,\alpha}(t)] \tag{9.17}$$

Satisifying $\jmath_m^\alpha = 0$, the slip condition is yielded by specular reflection of the particles, where the momentum balance results in a normal force only ($F_n = p$), such as in a frictionless wall [57]. The no-slip condition however, is represented by bounce-back reflection of the particles colliding with the wall, inverting the velocity components, consequently generating a tangential force on the wall: $F_t = -\mu(\partial u_t/\partial x_n)$. However, this no-slip condition only applies only to Direct Numerical Simulations. For a more detailed explanation on the implementation of boundary conditions in LBM, see [10].

## 9.6. Turbulence Model

PowerFLOW® uses a VLES approach (Very Large Eddy Simulation), which models the isotropic turbulence with a set of RNG $k-\epsilon$ equations. Large-scale turbulent structures are resolved within the grid resolution, while the structures that cannot be resolved within the grid are modelled. The scale separation of the calculated structures and the modelled structures is achieved identifying the intrinsic length/time scales. No spatial filtering is performed over the flow equations as is performed in LES.

As described by Chen et al. [8], in the BGK model the Knudsen number $Kn$ represents the ratio of characteristic collisional time-scale $\tau_{turb}$ corresponding to turbulent eddy interactions, and the flow advective time-scale corresponding to the dissociation from local equilibrium caused by a non-homogenous main flow.

$$Kn = \tau_{turb}\frac{Df/Dt}{f} << 1 \tag{9.18}$$

Then, the effective turbulent relaxation time $\tau_{turb}$ is defined through a systematic renormalisation-group (RNG) procedure resulting in:

$$\tau_{turb} = \tau_0 + C_\mu \frac{k^2/\epsilon}{T\sqrt{1+\eta^2}} \tag{9.19}$$

where $C_\mu = 0.085$, $\eta = Sk/\epsilon$, $\tau_0$ is the bare molecular relaxation time, $T$ is the temperature, $S$ is a measure of the local velocity gradient. The turbulent kinetic energy $k$ and the turbulent dissipation rate $\epsilon$ are determined according to the RNG $k-\epsilon$ transport equations, which contain proprietary extensions to achieve VLES time-accuracy physics [51].

## 9.7. Wall Model

Turbulent boundary layers present high resolution requirements due to the high-velocity gradients at the wall, which present a strong relation with the skin friction. The dimensionless wall distance of the first node is calculated with Equation 9.20 below. Equation 9.21 is the dimensionless velocity $u^+$.

$$\text{Dimensionless Wall Distance:}\quad y^+ = \frac{y\sqrt{\tau_w/\rho}}{\nu} \tag{9.20}$$

$$\text{Dimensionless Velocity:}\quad u^+ = \frac{u}{\sqrt{\tau_w/\rho}} \tag{9.21}$$

In order to save computational cost, the region nearest to the wall is modelled using a hybrid wall function called "Logarithmic Law of the Wall", described by Pope [49]:

- $y^+ \leq 5$, Laminar Sublayer: $u^+ = y^+$.
- $5 < y^+ \leq 30$, Buffer Zone: since $u^+ \neq y^+$ and $u^+ \neq \frac{1}{\kappa} \ln y^+ + b$, this zone requires empirical modelling for accurate prediction of $u^+$.
- $y^+ > 30$, Turbulent (or Logarithmic) Zone, given by the logarithmic function:

$$u^+ = \frac{1}{\kappa} \ln y^+ + B \tag{9.22}$$

where $\kappa$ is the von Kármán constant $\kappa \approx 0.41$ and the constant $B \approx 5.0$ to $5.5$.

# 10

# Simulation Setup

## 10.1. Standalone Tire

### 10.1.1. Deformed Rotating Treaded Tire Modelling: Immersed Boundary Method

In Chapter 3 it was established that the methodology implemented by PowerFLOW® with version 6-2021-R7, to model a deformable rotating treaded tire is through the Immersed Boundary Method (IBM), which was briefly introduced in Section 3.5. Figure 10.1 shows that the tire mesh is split into two regions: the IBM-region, that covers the tread geometry; and the rotating wall region, which is applied on the sidewall.

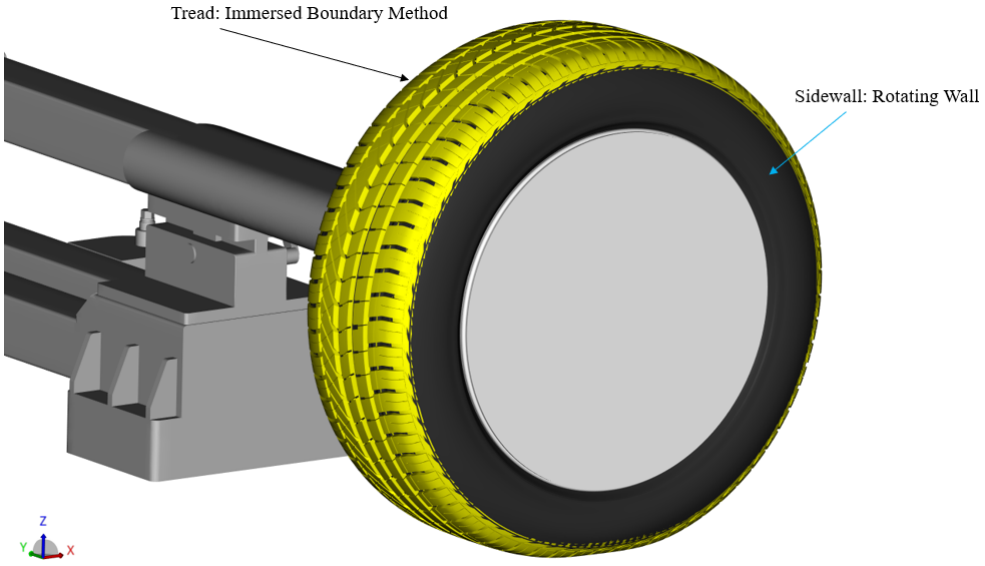


**Figure 10.1:** Tread-Sidewall split of tire geometry to implement boundary conditions: immersed boundary method on tread and rotating wall on sidewall.

The tread-sidewall split is done by PowerCASE® (which is the simulation setup tool for PowerFLOW® based on the inputs measured on the tire geometry, such as the shoulder depth, the maximum tread depth and maximum grove angle. These inputs are given below, with the shoulder depth and maximum tread depth measurements depicted in Figures 10.2 and 10.3, while the maximum groove angle was set to 15 degrees.

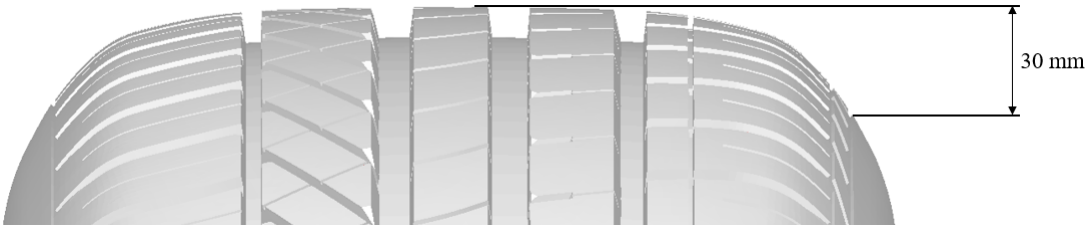


**Figure 10.2:** Measured shoulder depth.


**Figure 10.3:** Measured maximum tread depth.

In the Immersed Boundary Method, the flexible structure is represented by a set of discrete points that compose the Lagrangian variables, which interact with the fluid (Eulerian variables) through an exchange of forces. The key to couple the Lagrangian grid with the Eulerian grid, as described by Peskin [47], is the use of the delta functions, which deals with the spatial discrepancy between the boundary and the grid. The fluid is described in the Eulerian reference frame with fixed points, governed by the Navier-Stokes equations, yielded from the evolution of the PDF's:

$$\rho\left(\frac{\partial \mathbf{u}}{\partial t} + \mathbf{u}\cdot\nabla\mathbf{u}\right) = -\nabla p + \mu\nabla^2\mathbf{u} + \mathbf{f}_{\text{IB}} \tag{10.1}$$

$$\nabla\cdot\mathbf{u} = 0 \tag{10.2}$$

where $\mathbf{u}(\mathbf{x},t)$ is the Eulerian velocity field of the fluid at point $\mathbf{x}$, $p$ is the pressure field of the fluid, with $\rho$ being the density, $\mu$ the viscosity and $\mathbf{f}_{\text{IB}}(\mathbf{x},t)$ is the force per unit volume exerted by the immersed boundary on the fluid, which is spread from the Lagrangian force density $\mathbf{F}(s,t)$, calculated at the boundary points from the boundary's elastic properties, using the Dirac delta function $\delta(\mathbf{x}-\mathbf{X}(s,t))$. Here, $s$ represents the position along the boundary for a simplified 1D case used in this explanation:

$$\mathbf{f}_{\text{IB}}(\mathbf{x},t) = \int \mathbf{F}(s,t)\delta(\mathbf{x}-\mathbf{X}(s,t))ds \tag{10.3}$$

As described by Peskin [47], the Dirac delta function is approximated via a smooth approximation that spreads the force over several grid points near the boundary:

$$\delta_h(\mathbf{x}) = \frac{1}{h^3}\phi\left(\frac{x_1}{h}\right)\phi\left(\frac{x_2}{h}\right)\phi\left(\frac{x_3}{h}\right) \tag{10.4}$$

where $x_1$, $x_2$ and $x_3$ are the Cartesian components of $\mathbf{x}$, $\phi(r)$ is a smooth function continuous for all real $r$, where $r$ denotes $x_1/h$, $x_2/h$ and $x_3/h$, and $h$ refers to the grid spacing.

The position of the immersed boundary is updated through the interpolation of the velocity of the boundary points (in the Lagrangian grid) from the fluid velocity field (in the Eulerian grid), as given by Equation 10.5 below, again using the Dirac delta function.

$$\frac{\partial \mathbf{X}(s,t)}{\partial t} = \mathbf{U}(\mathbf{X}(s,t),t) = \int \mathbf{u}(\mathbf{x},t)\delta(\mathbf{x}-\mathbf{X}(s,t))d\mathbf{x} \tag{10.5}$$

with $\mathbf{U}(\mathbf{X}(s,t),t)$ representing the velocity at the boundary points $\mathbf{X}(s,t)$. A more detailed explanation of the method can be found in Peskin [47].

### 10.1.2. Global Parameters

The simulation parameters of the standalone tire test case were set to replicate the test conditions given by Schnepf et al. [55], where the inflow velocity (also referred to as characteristic velocity) was set to 140 km/h (38.89 m/s), hence the wheel's angular velocity was 113.813 rad/sec. The reference area of the tire alone is measured as 0.1590111 $m^2$, while the reference area together with the arm becomes 0.444181 $m^2$. Table 10.1 below provides the properties of air, as they were implemented in the PowerFLOW® simulations.

| **Air Properties** | |
|---|---|
| Reference Pressure | 101325 Pa |
| Characteristic Temperature | 293.1 deg $K$ |
| Gas Molecular Weight | 28.997 kg/kmol |
| Gas Specific Heat Ratio | 1.4 [-] |
| Constant-pressure Specific Heat | 1007 J/(kg · deg K) |
| Turbulence Intensity | 0.001 [-] |
| Turbulence Length Scale | 5 mm |

**Table 10.1:** Air properties and turbulence settings.

### 10.1.3. Domain and Boundary Conditions

Figure 10.4 below shows the Wind Tunnel Domain used for the standalone tire tests, which reproduces the size used by Schenpf et al. [54]. The wind tunnel dimensions are 37 metres in the $x$-direction, 19 metres in the $y$-direction, and 10 metres in the $z$-direction. The centre of the tire is set at the centre of the wind tunnel in the $x$ and $y$-directions. The tire centre height is $z$: 0.335703 metres.

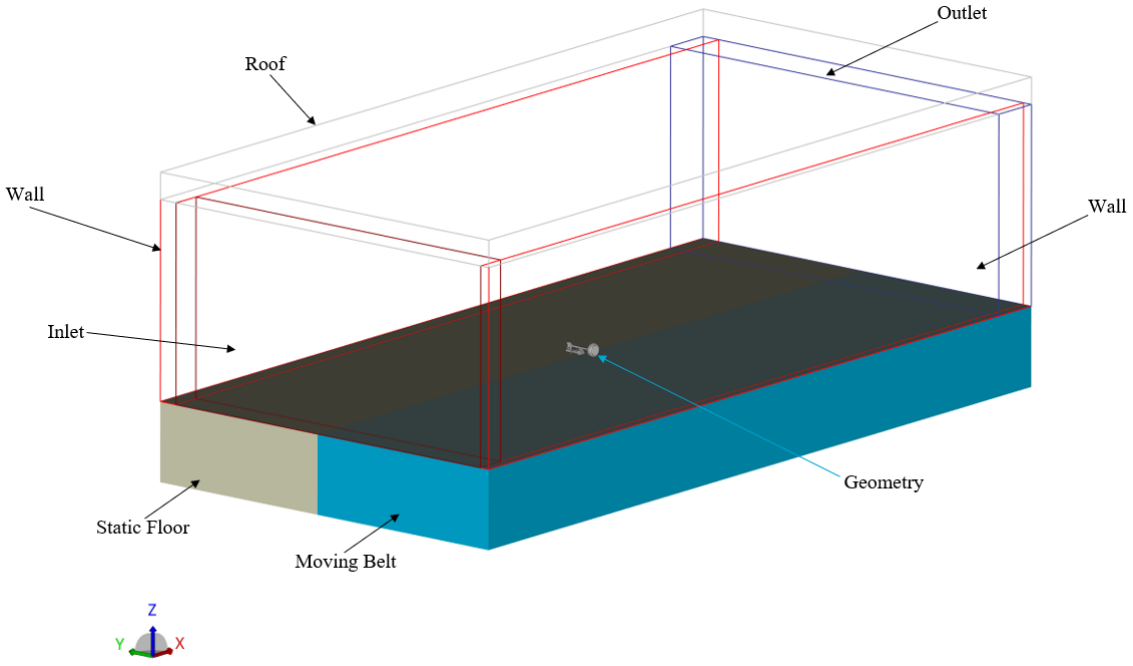


**Figure 10.4:** Boundaries of standalone tire test domain.

The boundaries off the simulation domain, visible in Figure 10.4, are applied as:

- **Inlet:** Characteristic velocity in $x$-direction, with the predefined turbulence intensity.
- **Outlet:** Static pressure (set to reference pressure), free flow direction and reflection damping.
- **Walls and Roof:** set as friction-less wall.
- **Static floor, arm geometry and rim cover:** set as standard wall.

- **Moving belt:** sliding wall with $x$-velocity set as characteristic velocity.

The floor split between the static floor and the moving belt, which is done at $y$: 0.66 metres from the tire centre, which is at position $y$: 0.0 metres. A top view of the split is presented in Figure 10.5 below.

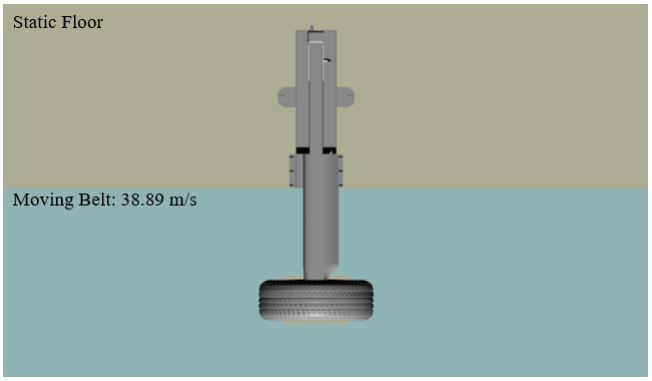


**Figure 10.5:** Top view of ground split: static floor and moving belt.

### 10.1.4. Surface Mesh

The surface mesh used for the tire geometry remains the same in standalone tire tests and full vehicle tests, for the sake of comparison. The surface mesh chosen was based on the good agreement with the experimental results achieved by Schnepf et al. [54], a validation that is covered in detail in Section 10.1.8. The surface mesh used facets with a longest edge of 15 mm (found on the sidewall, which as Figure 10.6 (b) shows, is the coarser region of the mesh due to the simplicity of this part of the geometry), and a shortest average edge length of of 3.5 mm over the tread region, where the geometry acquires more complexity, as it can be appreciated in Figure 10.6 (a). The total number of elements becomes 304876 facets.

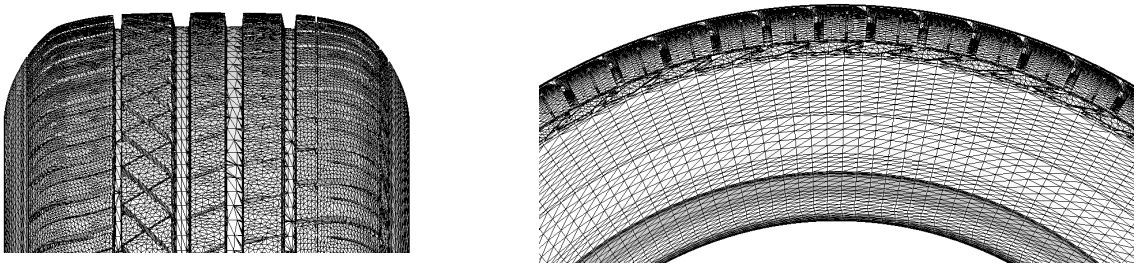

(a) Front view of the tire's surface mesh.

(b) Side view of the tire's surface mesh.

**Figure 10.6:** Surface mesh of tire geometry.

A finer mesh is tested to verify that the used mesh in the tests (original mesh) has sufficient resolution, a simulation is performed with a finer mesh where the maximum edge size is set to the voxel size of the finest Variable Resolution region (0.625mm), described in more detail in the next section. Figure 10.7 below shows the original mesh in (a), with the finer mesh in (b).

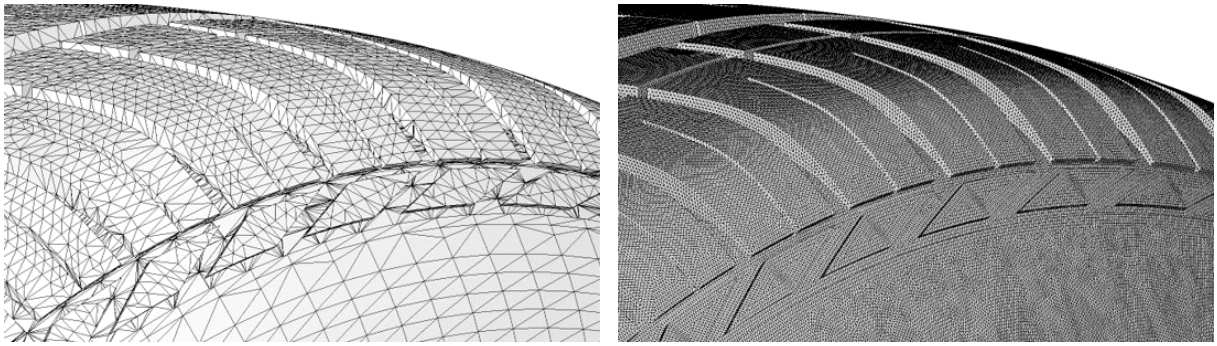

(a) Iso-view of original mesh.

(b) Iso-view of fine mesh.

**Figure 10.7:** Surface mesh comparison: original and fine mesh.

The results of the comparison of $C_D$ in Table 10.2 show that a difference below 1 count is obtained. Looking at the flow field comparison, it can be observed in Figures 10.8 to 10.10 that the resulting flow is essentially the same. Therefore, for efficiency purposes, the original mesh is considered sufficiently fine to accurately resolve the flow field in this problem.

| | Cumulative Running Average $C_D$ [-] | Confidence Interval [-] |
|---|---|---|
| Original Mesh | 0.18646 | +/- 0.00070 |
| Fine Mesh | 0.187567 | +/- 0.00061 |

**Table 10.2:** Cumulative running average $C_D$ comparison for original and fine mesh.

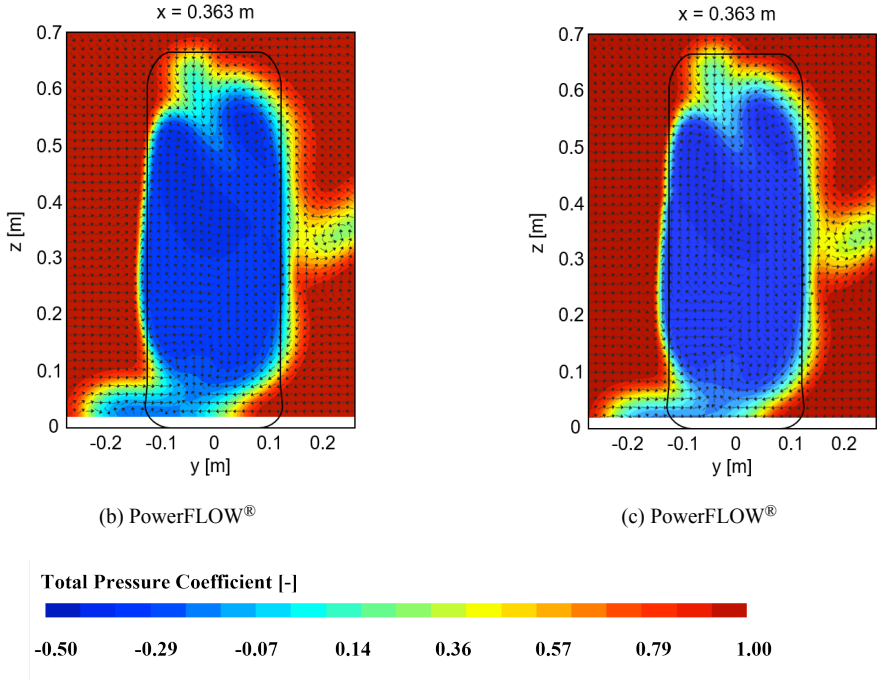


(b) PowerFLOW®

(c) PowerFLOW®

**Figure 10.8:** $x$: 0.363 m comparison with experiment.

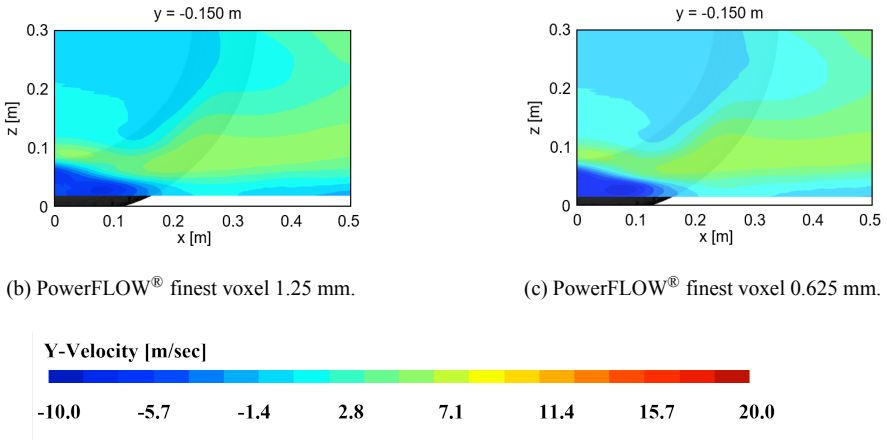


(b) PowerFLOW® finest voxel 1.25 mm. (c) PowerFLOW® finest voxel 0.625 mm.

**Figure 10.9:** $x$: 0.363 m comparison with experiment.

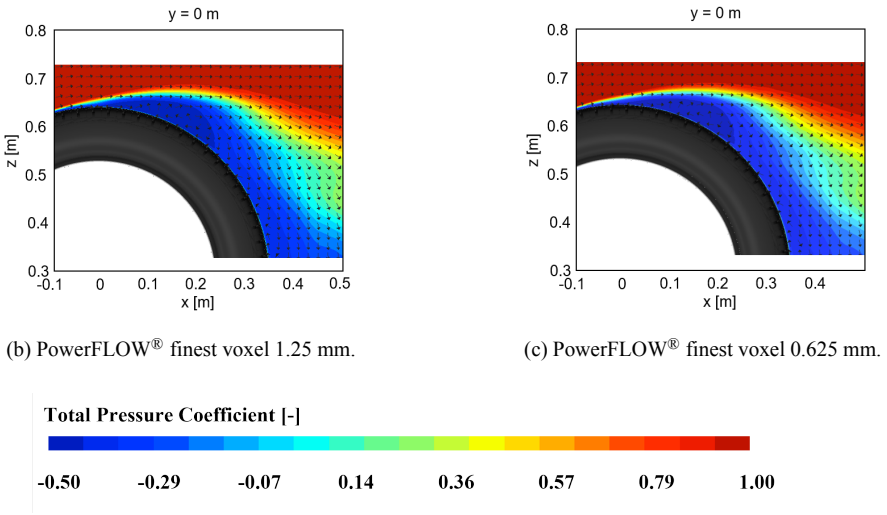


(b) PowerFLOW® finest voxel 1.25 mm. (c) PowerFLOW® finest voxel 0.625 mm.

**Figure 10.10:** $x$: 0.363 m comparison with experiment.

### 10.1.5. Volume Mesh

As described in Chapter 9, the volume of the fluid domain is discretised in voxels. The voxel size is then varied according to a scale hierarchy implemented through Variable Resolution regions, VR regions. The smallest voxel size is kept in the region closest to the geometry, from where the voxel edge length increases by a factor of 2. The definition of the finest VR region was done through a validation process that is further explained in latter Section 10.1.8. The validation resulted in 11 VR regions and the regions are numbered from the coarser region (VR 1) to the finest region (VR 11). Table 10.3 below shows the voxel size increase across scales.

| Scale | Voxel Size [m] | Update Frequency [Hz] |
|---|---|---|
| 1 | 0.640 | 642.6 |
| 2 | 0.320 | 1285 |
| 3 | 0.160 | 2570 |
| 5 | 0.080 | 5141 |
| 5 | 0.040 | $1.028{\cdot}10^{+3}$ |
| 6 | 0.020 | $2.056{\cdot}10^{+3}$ |
| 7 | 0.010 | $4.113{\cdot}10^{+3}$ |
| 8 | $5{\cdot}10^{-3}$ | $8.225{\cdot}10^{+3}$ |
| 9 | $2.5{\cdot}10^{-3}$ | $1.645{\cdot}10^{+4}$ |
| 10 | $1.25{\cdot}10^{-3}$ | $3.29{\cdot}10^{+4}$ |
| 11 | $6.25{\cdot}10^{-4}$ | $6.58{\cdot}10^{+4}$ |

**Table 10.3:** VR scales, voxel size and update frequency.

The five finest regions can be seen in Figure 10.11, from which the following observations can be made: VR 11 is a 10 mm offset of the carcass of the tire; VR 10 are two boxes created around the bulge and contact patch region, where relevant vortices develop; VR 9 and VR 8 are volumes of revolution around the tire, where VR 8 has a larger diameter than VR 9; and VR 7 is a box that englobes the whole geometry of the tire, rim and arm together. While the solution in the finest region (VR 11) is updated every time step, as the voxel size increases for each scale with a factor of 2, its update frequency varies by a factor of 1/2. The resulting number of voxels and surfels from this resolution scheme is 91,043,777 and 4,160,551 respectively.

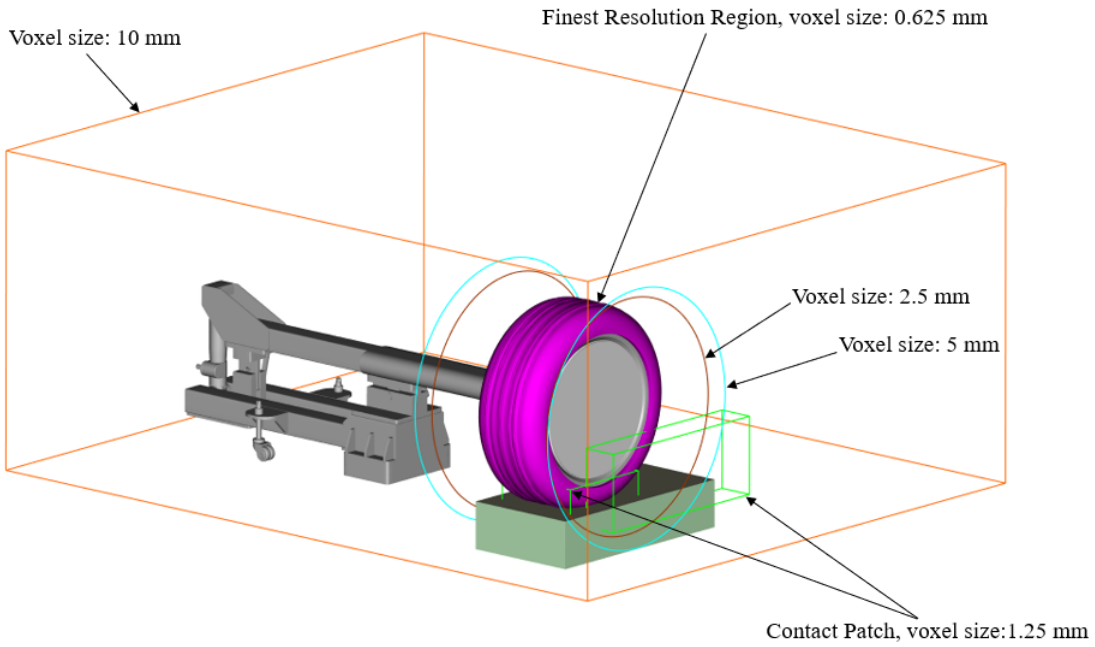


**Figure 10.11:** VR's 11 to 5 in standalone tire setup.

The resulting Cartesian grid can be seen in Figure 10.13, where in certain it can be seen that a minimum number of voxels is ensured before transitioning to a larger voxel size scale.

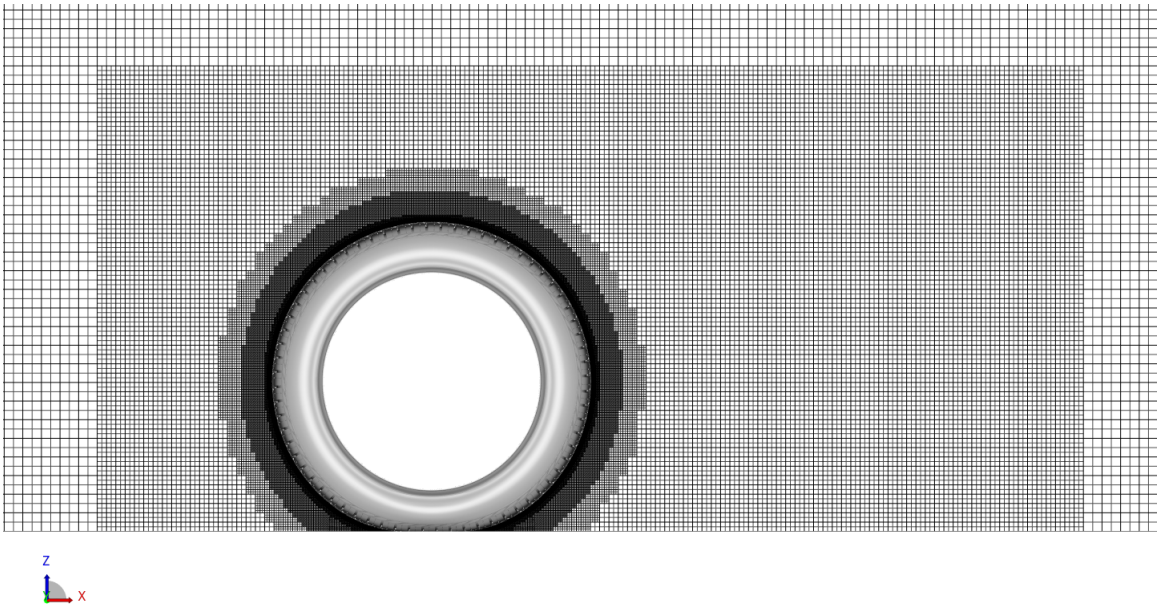


**Figure 10.12:** Cartesian grid standalone tire, side view.

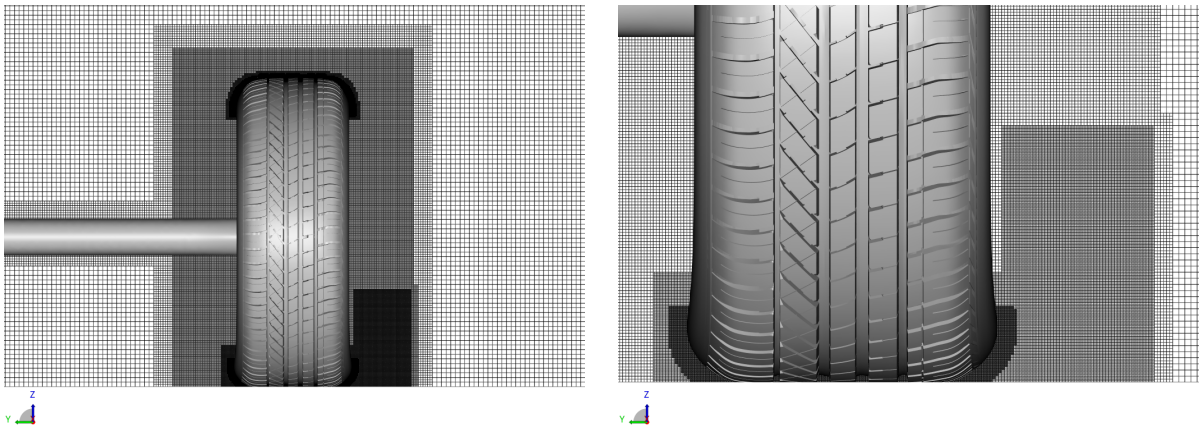


(a) Front view of Cartesian grid.

(b) Cartesian grid tire bottom close up.

**Figure 10.13:** Tire bulge-related parameters, where the discontinuous lines represent the ground.

In the voxel distribution it can be observed that VR 11 does not reach up to the end of the sidewall. This is purposely done to avoid intersection with the Local Reference Frame (LRF) region (sliding mesh for rim rotation), as it must not have more than one VR scale intersection. This is clearly depicted in Figure 10.14.

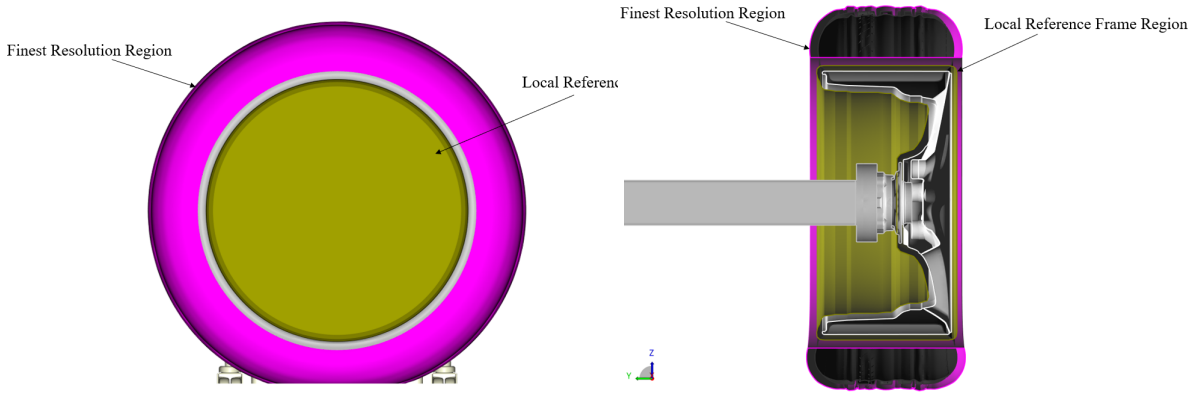


(a) VR11 and LRF region (side view).

(b) VR11 and LRF region (cross-section).

**Figure 10.14:** VR 11 radially cut to avoid intersection with LRF region.

### 10.1.6. Simulation Time

To determine the minimum running time that the standalone tire simulations required, an initial long run was performed on the Baseline deformaation, from which different averaging windows were extracted and compared. Following from the work done by Mortazawy et al. [44], where a 2.2-second run time was selected, the long run duration was set to last for slightly longer than twice the original time, hence a 5-second run was determined. From this long run, the shortest averaging window was defined from the original simulation length (2.2 seconds). From there, a small increment was chosen for the second averaging window (2.5 seconds), finally setting two other averaging windows of 3 and 4 seconds. The cumulative running average of the drag coefficient value was compared across averaging windows to assess the deviation from the reference value, which was defined as the cumulative running average of the drag coefficient in the 5-second average ($C_{D_{5sec}}$). Table 10.4 shows the differences of each averaging window with respect to the 5-second reference, together with the confidence interval of the $C_D$ cumulative running average.

| Running Time | Cumulative Running Average $C_D$ [-] | $\Delta C_D$ to $C_{D_{5sec}}$ | Confidence Interval [-] |
|---|---|---|---|
| 0 to 2.2 seconds | 0.187615 | 0.00081 | +/- 0.00085 |
| 0 to 2.5 seconds | 0.186756 | -0.00045 | +/- 0.00075 |
| 0 to 3 seconds | 0.186461 | -0.00034 | +/- 0.00070 |
| 0 to 4 seconds | 0.186418 | -0.00038 | +/- 0.00060 |
| 0 to 5 seconds | 0.186680 | - | +/- 0.00060 |

**Table 10.4:** Cumulative running average $C_D$ of several averaing windows.

From the results shown in Table 10.4, it can be concluded that, while all the differences with respect to the baseline are smaller than their correspondent confidence interval, which is calculated with a statistical analysis methodology that PowerFLOW® includes in the simulation force monitors to retrieve the cumulative running average with an estimation of the confidence interval at any simulation time. This methodology is inspired by Mockett et al.'s work [41]. As is expected, the overall trend is that for longer simulation time, the cumulative running $C_D$ average gets closer to the 5-second value, with the exception that the 3-second value is actually closer than the 4-second value. With the 3-second and 4-second averages presenting a difference to the 5-second average that is more than half of the difference obtained in the original averaging, it is concluded that sufficient accuracy is achieved from the 3-second averaging onwards.

Further comparisons of the different averaging windows is necessary to confirm the $C_D$ results, and that involves a study of the flow topology. The vortices at the bottom of the tire have been widely regarded as highly relevant in the present report. Therefore, the area of focus in the flow topology comparison is the vortices in the wake at an $x$-location of $0.6D$ behind the tire, where $D$ is the diameter of the tire. The vortex identification method of choice is the $\Gamma_2$-Criterion, which in Section 4.2 it was initially posed as an adequate method for vortex identification in highly turbulent flow fields. A further discussion on the applicability of the $\Gamma_2$-Criterion is described Chapter 12. Note that, as stated later in Chapter 12, a positive value of $\Gamma_2$ represents clockwise rotating vortices, while a

negative value of $\Gamma_2$ represents counter-clockwise rotating vortices.

Comparing $\Gamma_2$ plots of the other windows with respect to the 5-second topology in Figure 10.15 (e), where the tire is being looked at from behind, and the arm then lays on the right of the tire (although not visible in this image), it can be appreciated that the flow topology remains consistent across windows: a large vortex pair of counter-rotating vortices on the upper region (vortices 1 and 4), which are the trailing vortices; a small vortex pair of counter-rotating vortices at the base of the tire in proximity with the ground, which seem to be the contact patch vortices (vortices 3 and 5). These vortex pairs agree with those identified at the bottom part of the wake by Wäschle el al. [65] and Diasinos et al. [20], although the low $\Gamma_2$ magnitude of vortex 5 could be due to its proximity to the ground and the related boundary effects, further discussed in Chapter 12. Finally, to the left of the bulge (outer side of the tire), another vortex pair of counter-rotating vortices seems to be forming (vortices 2 and 6). When comparing these structures across the different averaging windows, it can be observed that, while the first two vortex pairs (pair 1-4 and pair 3-5) can be observed across different averaging windows, vortex 6 only seems to be a proper vortex in the 5-second window, while in the other windows it shows as a region of turbulence without a strongly identified vortex core. This could indicate that vortex 6, as appreciated in the 5-second window, is simply a consequence of the averaging time, and not an actual vortex, hence emphasising the need for a deeper time-dependent analysis of the vortex structures identified in the averaged data. This analysis is carried out in Section 10.1.7.

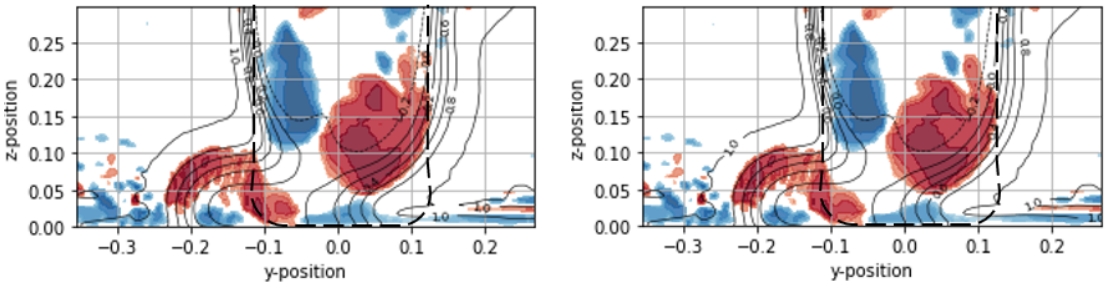


(a) 0.0 to 2.2 seconds.




(b) 0.0 to 2.5 seconds.

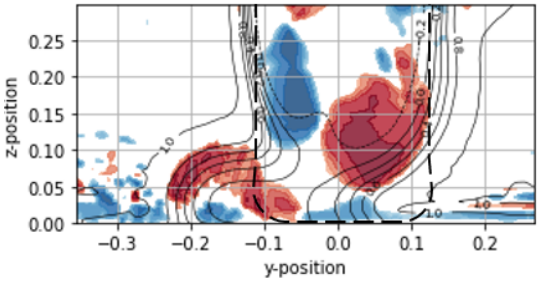


(c) 0.0 to 3.0 seconds.

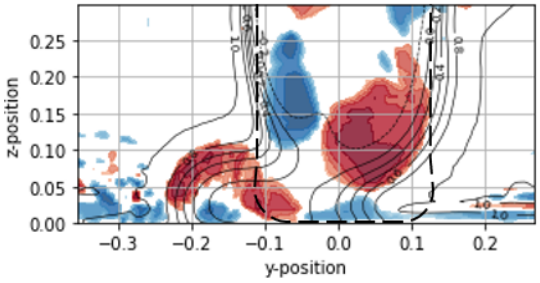


(d) 0.0 to 4.0 seconds.

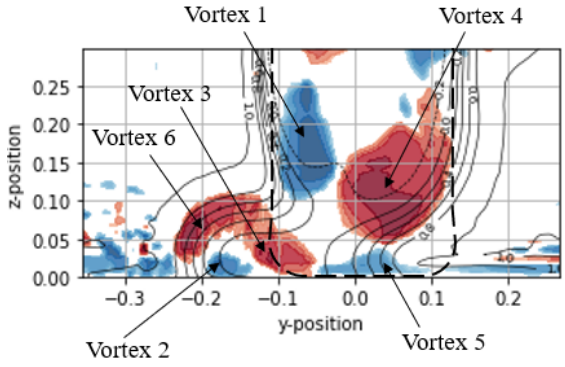


(e) 0.0 to 5.0 seconds.

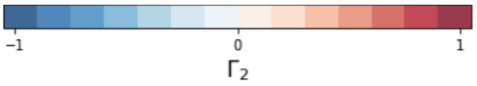


**Figure 10.15:** $\Gamma_2$ plots for the various averaging windows looking at the tire from rear view. Comparison with 5-second average applying a low threshold filter of $\Gamma_2 = 0.6$.

Regarding the main 4 vortices that are consistently observed, an evolution towards a more concentrated core is captured as the averaging time approaches 5 seconds. Within these marginal differences, it can be stated that it is from the 3-second average that the topology presents good agreement with the 5-second average. This statement goes well with the conclusions drawn from the $C_D$ cumulative running average result.

A more specific evaluation of the vortex identification evolution is done by implementing the vortex identification methodology to be described in Chapter 13. Figure 10.16 shows that vortex centres identified by the algorithm upon the definition of what a vortex core is ($\Gamma_2 \in (-1, 0.9) \cup (0.9, 1)$, by Michard et al. [40]) result in vortices 1, 2, 3 and 4, hence vortices 5 and 6, although qualitatively identified, do not meet the vortex identification criteria.

In Figure 10.16 the black dots refer to the reference positions of the identified vortices in the 5-second averaging window. It is therefore visible that the vortex locations for the 3-second averaging window are closest overall to the reference locations.

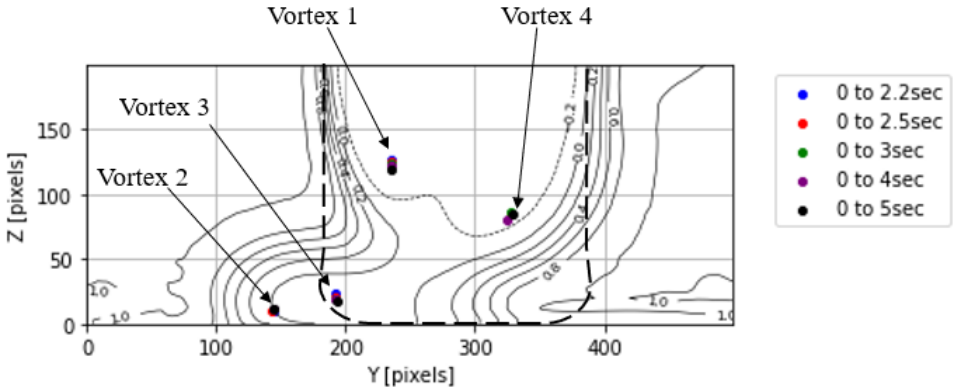


**Figure 10.16:** Comparison of vortex locations for the different averaging windows with respect to the 5-second average.

The accuracy of the vortex locations is quantified by measuring the percentage error $\%\epsilon(d_c)$ of the vortex position with respect to the reference location $x_{i,5_{sec}}$, $y_{i,5_{sec}}$. The Eucledian distance between the vortex with respect to its reference location is then normalised with the finest local voxel size, which in the area of focus at $x$-location $0.6D$ is 1.25 mm, corresponding to VR 10, see Equation 10.6.

$$\varepsilon(d_c) = \frac{\sqrt{(x_i - x_{i,5_{sec}})^2 + (y_i - y_{i,5_{sec}})^2}}{d_{ref}} \tag{10.6}$$

The results of Equation 10.6 are given in Table 10.5, where it can be appreciated that the trend confirms the overall pattern observed in the previous comparisons, where the 3-second average provides sufficient accuracy with respect to the 5-second average, in this case by giving the lowest mean error among the different windows compared. Therefore, it was concluded that the adequate simulation time was 3 seconds, with a slight increase to 3.1 seconds to ensure a 3-second average after the end of the initial transient, which is the simulation time that ellapses until the initial flow settles from the initial conditions to a periodic state. The initial transient is detected by the signal analysis performed by PowerFLOW® based on the force signal. For the chosen physical simulation time, the resulting CPU hours were approximately 35,555 hours.

| Running Time | $\%\varepsilon(d_c)$ Vortex 1 | $\%\varepsilon(d_c)$ Vortex 2 | $\%\varepsilon(d_c)$ Vortex 3 | $\%\varepsilon(d_c)$ Vortex 4 | Mean $\%\varepsilon(d_c)$ |
|---|---|---|---|---|---|
| 0 to 2.2 sec | 262.16 | 56.86 | 218.64 | 31.59 | 142.31 |
| 0 to 2.5 sec | 234.61 | 65.32 | 101.90 | 35.72 | 109.39 |
| 0 to 3 sec | 1966.09 | 38.75 | 80.41 | 61.19 | 94.11 |
| 0 to 4 sec | 114.999 | 30.48 | 103.37 | 226.15 | 118.75 |

**Table 10.5:** Percentage error $\%\varepsilon(d_c)$ of vortex location with respect to the 5-second average. Normalised with local finest voxel size (1.25 mm).

### 10.1.7. Time-dependence of results

As mentioned in the previous chapter, it is necessary to make an evaluation of the time-dependence of the results. This involves a study of the flow topology of the Baseline deformation evolution at different frames of the transient flow. The frames are selected in the second part of the 3-second averaging window (after 1.5 seconds) to ensure the absence initial transient effects that could affect the flow topology. Six continuous frames are taken, which due to the sampling period of the fluid measurement region being $1/8^{th}$ of a revolution, correspond to the instances: $t_1 = 1.505$ seconds, $t_2 = 1.512$ seconds, $t_3 = 1.519$ seconds, $t_4 = 1.526$ seconds, $t_5 = 1.533$ seconds and $t_6 = 1.539$ seconds, see Figure 10.17 below.

In frame $t_1$ two main regions of vorticity can be distinguished: Region Vortex 1 and Region Vortex 2, where the balance of the wake seems even between these two regions. As the flow evolves to $t_2$, Region Vortex 2 clearly becomes the dominant region in the wake, while Region Vortex 1 seems to dissipate. It is then in $t_3$ that Region Vortex 1 reappears, at the same time that Region Vortex 3 shows up. Then in $t_4$, it is Region Vortex 3 that dominates the wake, highlighting the oscillatory nature of the flow in this region. In $t_5$ Region Vortex 4 shows up,

and all four regions show to be in balance within the wake. This distribution goes on into $t_6$, where each vortex regions seem to converge into its own concentrated vortex core.

It is concluded then that the time-dependent behaviour of the vortices consists of an oscillatory behaviour where periods of dominance of the wake change from Region Vortex 2 to 1, and to equilibrium. It is in the instances where equilibrium shows between the main two regions that Regions Vortex 3 and 4 start to show. In contrast to Regions 1 and 2, which for certain instances appear to be a scatter of vortices, Regions 3 and 4 show more consistently concentrated into one vortex core. Finally, it can be concluded from this transient analysis that the vortices 2 and 3, identified in Figure 10.16, are simply a region of constant turbulence, where no coherent structures form at any of the time instances observed.

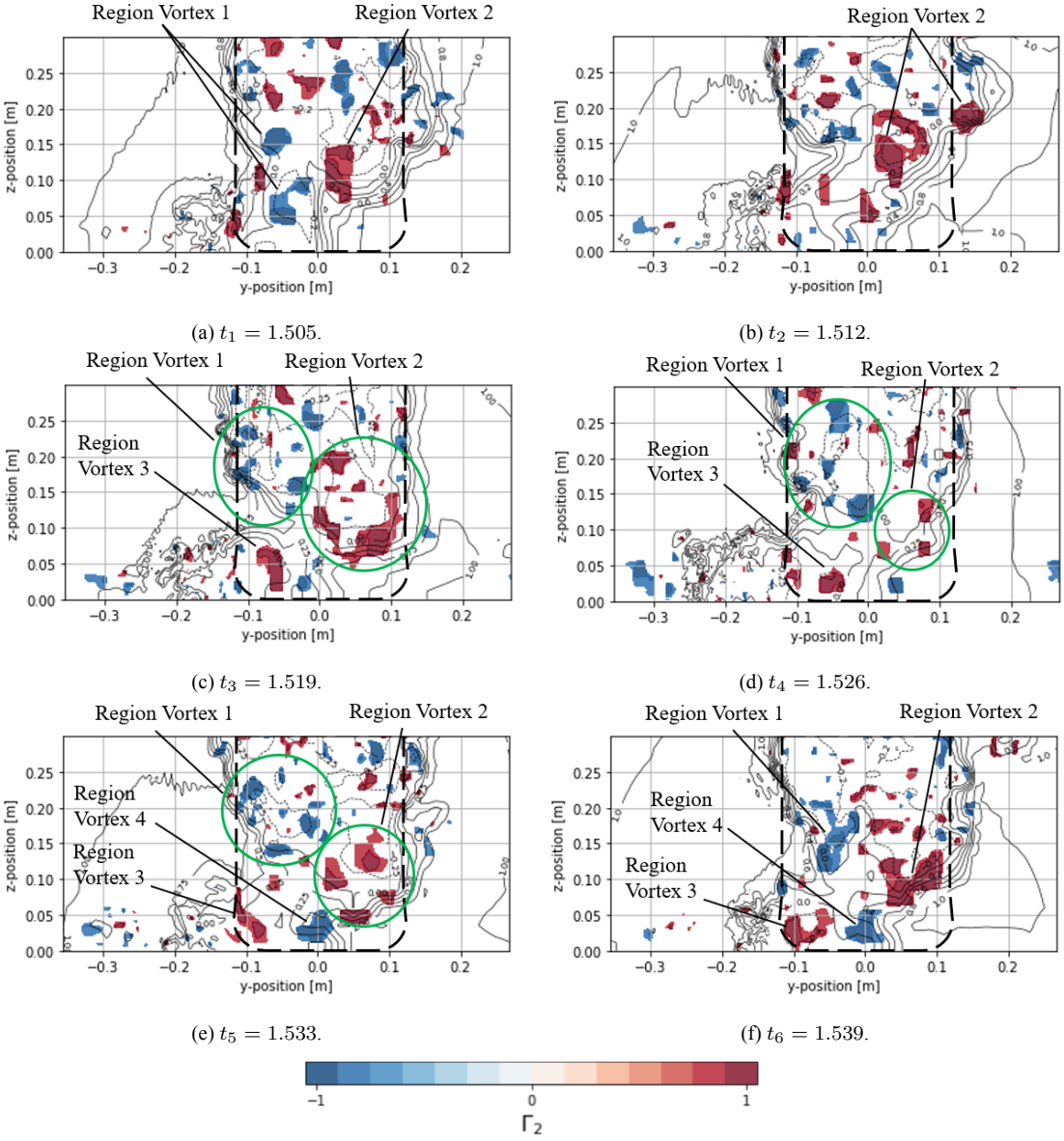


(a) $t_1 = 1.505$.

(b) $t_2 = 1.512$.

(c) $t_3 = 1.519$.

(d) $t_4 = 1.526$.

(e) $t_5 = 1.533$.

(f) $t_6 = 1.539$.

**Figure 10.17:** $\Gamma_2$ plots for different flow instances in transient flow analysis.

## 10.1.8. Setup Validation

The standalone tire simulation setup described throughout the current Section 10.1 was validated by comparing the flow field results with the experimental results obtained by Schnepf et al. [54]. Two resolution schemes are compared: the validated scheme by Mortazawy et al. [44], with a finest voxel size of 0.625 mm (VR 11); and a coarser scheme with 1.25 mm as finest voxel size (VR 10). The flow field comparison is done with respect to

12-hole probe measurements of the wake and the flow around the tire, with slices: $x$-aligned slice at $x$: 0.363 m, covering the whole cross section of the tire; $y$-aligned slice at $y$: -0.15 m, focusing on the rear corner of the contact patch at the outside of the tire; and a $y$-aligned slice at $y$: 0.0 m, which shows the flow at the centreline on the top separation point. As Schnepf et al. [54] describe, measurements in the vicinity of the boundaries was not possible due to the 12-hole probe being unable to take measurements in a distance lower than 20 mm to the boundary.

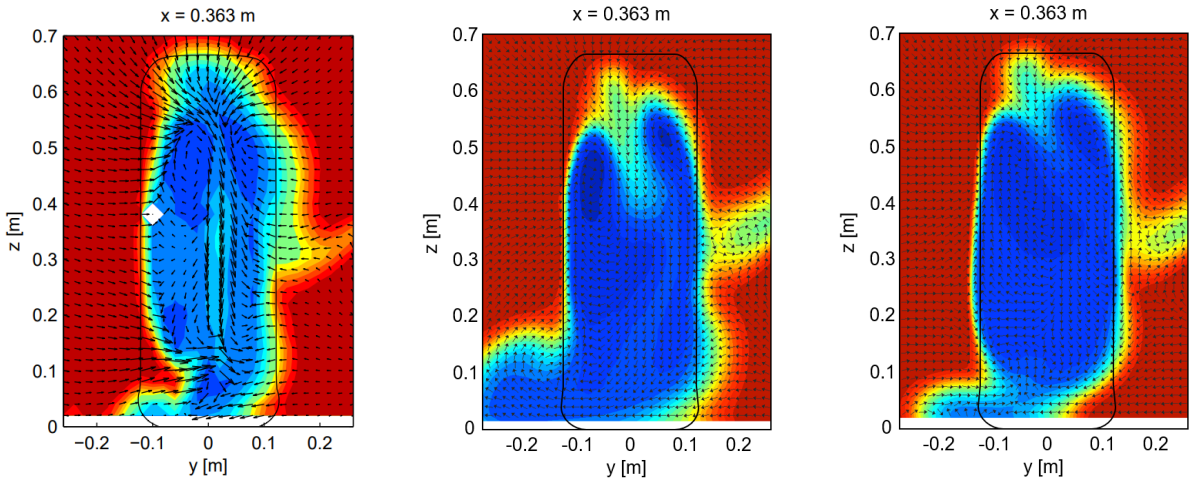


(a) Experiment, Schnepf et al. [55]. (b) PowerFLOW® finest voxel 1.25 mm. (c) PowerFLOW® finest voxel 0.625 mm.

**Figure 10.18:** $x$: 0.363 m comparison with experiment of total pressure coefficient.

Figure 10.18 above shows the comparison in the $x$: 0.363 m slice, where it can be observed that the finer resolution scheme achieves a better match with the experiment in the wake of the tire, as the bottom of the wake is tighter than the VR 10 wake, while at the top of the wake the VR 10 overpredicts the downwash induced by the two counter-rotating vortices at the top of the tire. VR 11 achieves a better prediction of the downwash in this area. Both resolution schemes agree on the region of losses concentrated on the outside bottom corner.

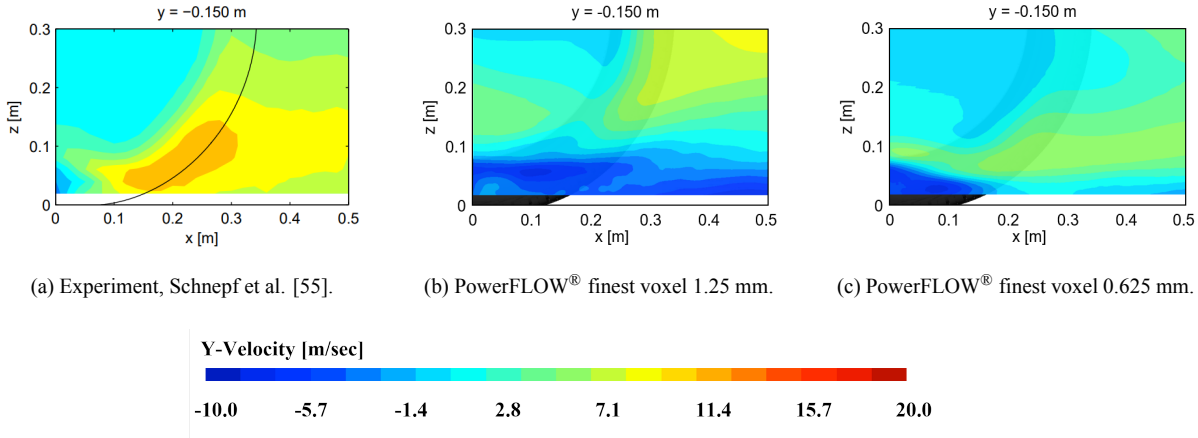


(a) Experiment, Schnepf et al. [55]. (b) PowerFLOW® finest voxel 1.25 mm. (c) PowerFLOW® finest voxel 0.625 mm.

**Figure 10.19:** $y$: -0.15 m comparison with experiment of $y$-velocity.

Looking at the $y$:-0.15 m slices, a confirmation of the comparison made on the outside bottom corner of the tire is given, where the wake given by the VR 10 scheme was much bigger in this region than in the experiment. This

can be seen with the larger region of outwash at the bottom of the slice in Figure 10.19 (b), while the VR 11 scheme attains a more similar outwash region to the experiment.

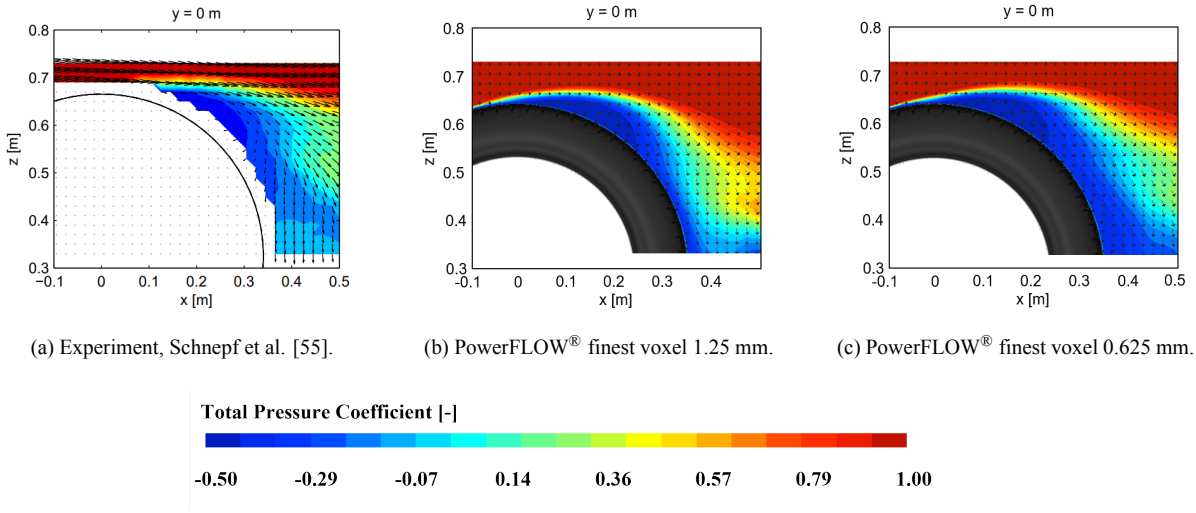


(a) Experiment, Schnepf et al. [55].

(b) PowerFLOW® finest voxel 1.25 mm.

(c) PowerFLOW® finest voxel 0.625 mm.

**Figure 10.20:** $y$: 0.0 m comparison with experiment of total pressure coefficient.

Finally, at the $y$-aligned slice at the top centreline is compared the stronger downwash predicted by the VR 10 scheme is seen in a smaller wake. Overall, it is concluded that the VR 11 scheme attains a more accurate flow field with respect to the experimental results, which justifies its selection for the studies carried out.

## 10.2. Full Vehicle: DrivAer Model

### 10.2.1. Global Parameters

Since no experimental data was available to compare with the full vehicle results, the setup choice was made based on PowerFLOW®s best practices for full vehicle external aerodynamics [50], as this setup proved to be adequate to accurately predict drag coefficient in a multitude of automotive studies, such as the studies carried out by Sbeih et al. [53]. The characteristic velocity was set to 100 km/h (27.78 m/s), which results in the same Reynolds number as the standalone tire test case (ca. $2.6 \cdot 10^6$). The reference area of the vehicle is measured as 2.172 $m^2$. The wheel's angular velocity was set to 86.94 rad/sec. The air properties and turbulence settings are the same as the ones given in Table 10.1. The simulation duration for the full vehicles tests is determined, as recommended by PowerFLOW®s best practices [50], by the 'autostop' implemented by PowerINSIGHT® [52], where the simulation is automatically stopped once the stability and accuracy criteria of 1 count are met byb the cumulative running avergae. Nevertheless, a maximum simulation duration of 5 seconds is given as input. For the baseline deformation case, 1 count accuracy convergence was achieved at approximately 14,415 CPU hours.

### 10.2.2. Boundary Conditions

The wind tunnel dimensions for this case are automatically generated by PowerCASE® through the *Wind Tunnel Controls* described in [51]. For open-jet wind tunnel conditions, the walls and the ceiling are placed such that the area blockage ratio remains at 0.1%, while the inlet and outlet are placed as far as possible from the vehicle. This results in the dimensions: 114.32 metres in the $x$-direction, 55.864 metres in the $y$-direction, and 38.8745 metres in the $z$-direction. Figure 10.21 presents a depiction of this domain.

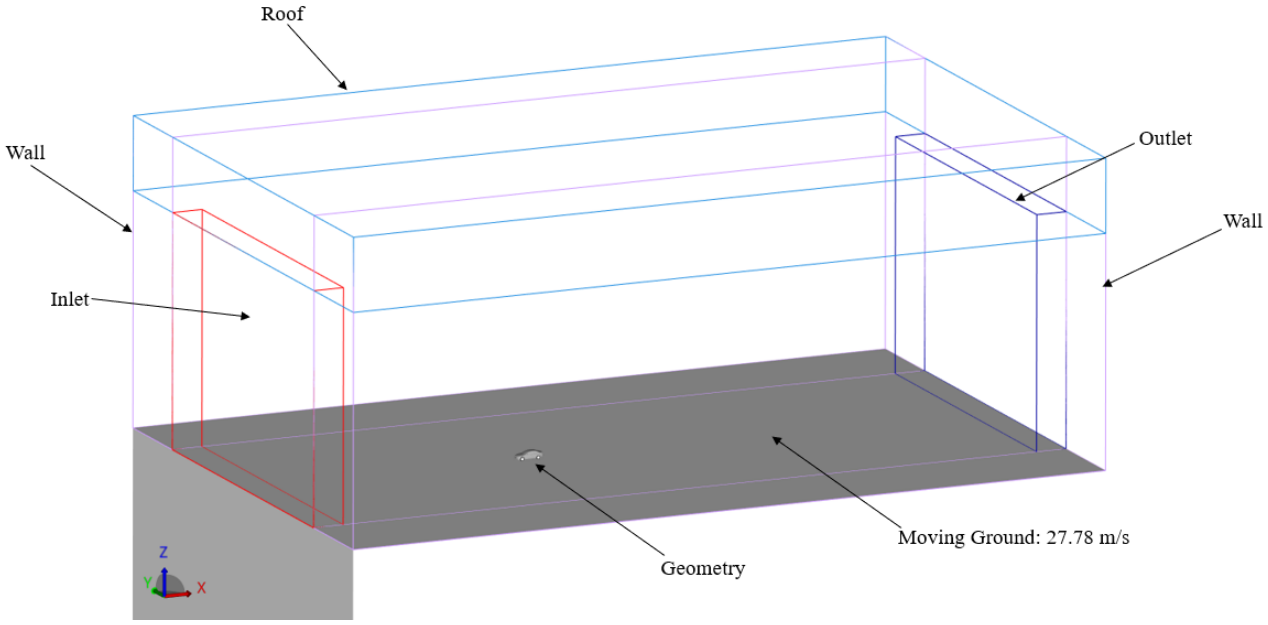


**Figure 10.21:** Full vehicle simulation domain boundaries.

Similarly to the standalone tire setup, the roof and walls were set as slip surfaces so that a boundary layer does not develop on them, since that would compromise the blockage ratio and create buoyancy. The inlet was given characteristic velocity in $x$-direction, while the outlet was set as static pressure with the characteristic pressure and free flow direction. In the case of the floor, this setup intends to reproduce open road conditions, for which the whole floor was set as sliding wall with $x$-velocity set to characteristic velocity. The $DrivAer$ model configuration used for this analysis has open grills, which means that a porous medium has to be setup in the radiator of the engine. The porous medium settings were set with initial $x$-velocity of 5 m/sec, and viscous and inertial resistance in the $x$-direction of 400 1/sec and 100 1/m respectively, which are the standard settings in the best practices case template. When it comes to the tire modelling, the same the same boundary conditions described in Section 10.1.1 are applied to the tire geometries in the full vehicle case, also applying the LRF region to the region containing the rim geometry, as shown in Figure 10.14.

## 10.2.3. Surface Mesh

The *DrivAer* geometry was meshed following the recommendations of PowerFLOW®s best practices for automotve external aerodynamics [50]. Different settings are applied to upper body and under body surfaces, as the flow conditions over these surfaces tend to differ dramatically, especially if the vehicle model contains a detailed under body geometry. For the upper body mesh, three parameters are instructed: surface tolerance, which refers to the maximum distance between the facets of the mesh and their underlying CAD surface; normal tolerance, which is the maximum angular difference between the planar facets the underlying CAD surface; and maximum edge length, described as the maximum length of the edges within the mesh. According to [50], these parameters must be set as: surface tolerance $\leq$ 0.05 mm, with recommended 0.01 mm for regions with large pressure gradients; normal tolerance $\leq$ 25 deg; and no specific settings for the maximum edge length, provided that a value of 0 mm will let the other two parameters produce a ”fine” mesh quality.

## 10.2.4. Volume Mesh

The spatial resolution of the fluid domain was set according to PowerFLOW®s best practices for external aerodynamics, where in contrast to the standalone tire, previous studies such as the ones carried out by Sbeih et al. [53] and Duncan et al. [22] validated a finest voxel size of 1.25 mm for accurate drag coefficient prediction. Therefore, the VR scales used in the full vehicle tests is as given by Table 10.6.

| Scale | Voxel Size [m] | Update Frequency [Hz] |
|---|---|---|
| 0 | 1.280 | 119.3 |
| 1 | 0.640 | 238.7 |
| 2 | 0.320 | 477.44 |
| 3 | 0.160 | 954.77 |
| 5 | 0.080 | 1909 |
| 5 | 0.040 | 3819 |
| 6 | 0.020 | 76388 |
| 7 | 0.010 | $1.528 \cdot 10^{+4}$ |
| 8 | $5 \cdot 10^{-3}$ | $3.055 \cdot 10^{+4}$ |
| 9 | $2.5 \cdot 10^{-3}$ | $6.11 \cdot 10^{+4}$ |
| 10 | $1.25 \cdot 10^{-3}$ | $1.222 \cdot 10^{+5}$ |

**Table 10.6:** Full vehicle setup VR scales, voxel size and update frequency.

Figure 10.22 shows the finest voxel region, and Figure 10.23 shows the Cartesian grid resulting from the VR distribution, where the progression through the resolution scales can be appreciated. The VR 9, 8, 7 and 6 regions are shown in Appendix C. For the provided resolution scheme, the resulting number of voxels and surfels is 201,288,966 and 16,717,314 respectively.


**Figure 10.22:** VR 10 region, voxel size 1.25 mm.

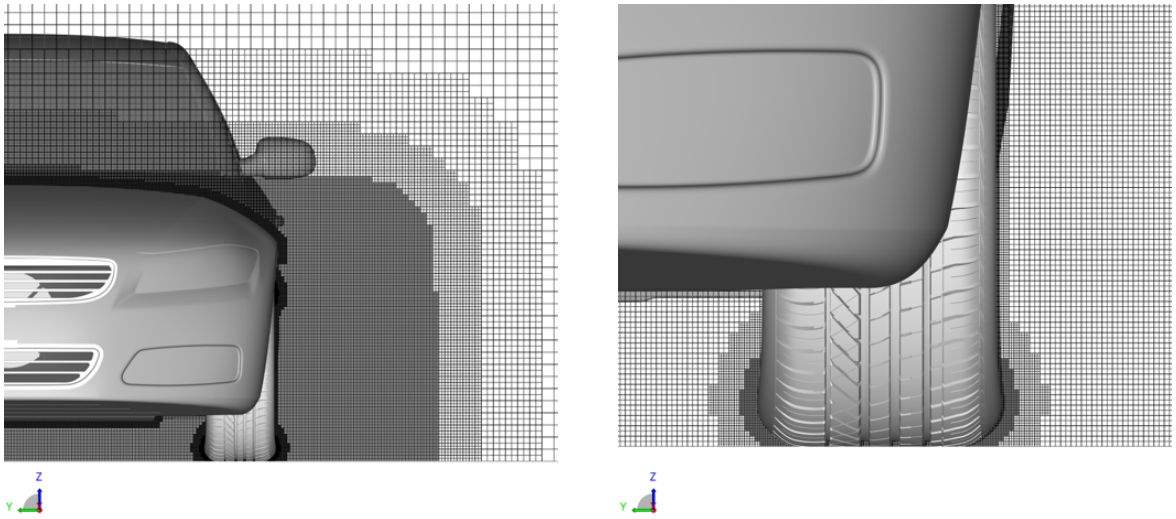

(a) Full vehicle Cartesian grid front view.

(b) Full vehicle Cartesian grid front view close up.

**Figure 10.23:** Full vehicle Cartesian grid.

# 11

# Principal Components Analysis

The implementation of Principal Components Analysis has been deeply described in Section 4.1, showing its utility for representing high-dimensional correlated data to observe the main trends of variations in a set of measurements across several experiments. For the current application, the measurements to be taken are a set of variables in the flow field of the tire wake, over different $x$-locations downstream the tire, covering the areas of the flow relevant to the bottom wake, where the variations induced by the deformation tests are introduced.

Figure 11.1 depicts the panels where average measurements of relevant flow variables are taken at each $x$-location. Each panel has a size of $0.045\text{m}\times0.36\text{m}$. The variables of which the average value over each panel is taken are: total pressure, static pressure, microdrag (which was explained in Chapter 4.4), $x$-vorticity, $x$-velocity, $y$-velocity, and $z$-velocity.

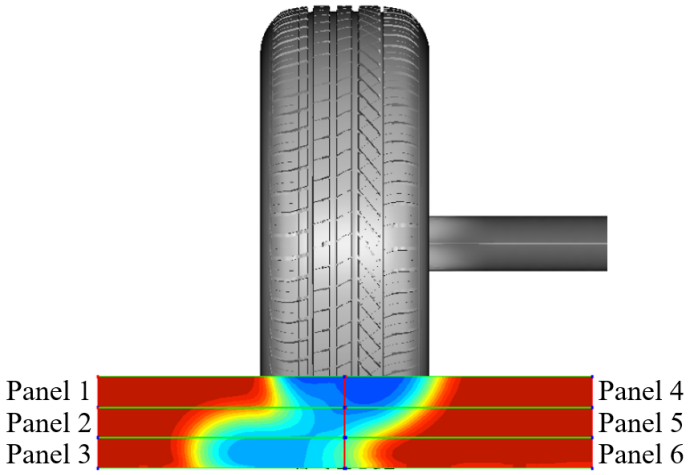


**Figure 11.1:** Measurement panels.

The set of $x$-locations where the measurements are taken are shown in Figure 11.2 for the case of the standalone tire, where it can be seen that the locations are taken with respect to the tire's diameter $D$. Measurements are taken in a position right in front of the tire ($x_1$) to capture flow variations right upstream, in the tire's centreline ($x_2$), and three locations downstream of the tire ($x_3$, $x_4$ and $x_5$).

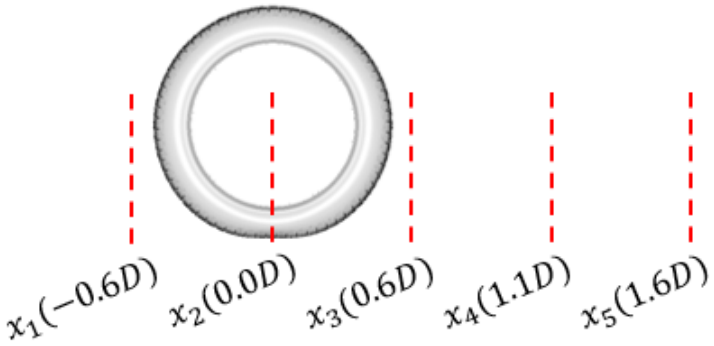


**Figure 11.2:** Standalone tire $x$-locations.

From the measurements taken for each deformation test, the difference to the baseline measurement is calculated. Therefore, the measurement data matrix is composed as specified in Matrix $\mathbf{X}$ (49), where each row is a deformation test, and each column is a measurement.

$$\mathbf{X} = \begin{bmatrix} \text{Deformation Test 1} \\ \text{Deformation Test 2} \\ \vdots \\ \text{Deformation Test } N \end{bmatrix} \tag{11.1}$$

The hierarchy of the columns is defined with variables arranged as groups of columns, composed of sub-columns containing all the $x$-locations, and where each column represents a panel-measurement of Variable $N$. Therefore, matrix $X$ adopts size $r \times c$, where $r$ are the number of deformation tests, and $c$ is given by:

$$c = N_{variables} \times N_{x-locations} \times N_{panels} \tag{11.2}$$

Since seven variables are taken ($V = V_1, ..., V_7$), at five $x$-locations ($L = L_1, ..., L_5$) containing six panels ($P = P_1, ..., P_6$): $c = 7 \times 5 \times 6 = 210$. Hence, each row of the $X$ matrix is structured as:

$$\text{Deformation Test } N = [(V_1, L_1, P_1) \ \cdots \ (V_1, L_5, P_6) \ (V_2, L_1, P_1) \cdots (V_7, L_5, P_6)] \tag{11.3}$$

# 12

# Vortex Identification Method

## 12.1. Method Verification

In Section 4.2 the advantages of using the $\Gamma_2$-Criterion over other vortex identification methods for noisy flow fields were covered. For a 2D incompressible velocity field, $\Gamma_2$ is given by Equation 12.1, which was described in detail in Section 4.2.

$$\Gamma_2(P) = \frac{1}{N} \sum_{M \in S} \frac{[\overrightarrow{PM} \wedge (\overrightarrow{v}_M - \overrightarrow{v}_P)] \cdot \hat{n}}{\|\overrightarrow{PM}\| \cdot \|\overrightarrow{v}_M - \overrightarrow{v}_P\|} = \frac{1}{N} \sum_{M \in S} sin(\theta_{PM}) \tag{12.1}$$

To ensure a proper implementation of the method, a verification is needed through a synthetic flow field. For this exercise, the synthetic vortex of choice is the Rankine vortex, given by:

$$V_\theta(r) = \begin{cases} \frac{\Gamma}{2\pi} \frac{r}{r_c^2} & r \leq r_c \\ \frac{\Gamma}{2\pi r} & r > r_c \end{cases} \tag{12.2}$$

Two parameters were varied to carry out sensitivity tests: the vortex radius $R_c$ and the $\Gamma_2$ disk radius $r_{disk}$. The 2D computation domain is size 4 metres $\times$ 4 metres, and the vortex centre is positioned at $(0, 0)$ metres with a circulation maginutde of $\Gamma = -10\text{m}^2/\text{sec}$. The different vortex radii tested are: $R_{c_1} = 1.0$ m, $R_{c_2} = 0.5$ m and $R_{c_3} = 0.25$ m. The disk radii tested were based on a fraction of the maximum distance calculated in the computation domain $d_{max}$, which for the current case is $4\sqrt{2}$ m. Starting from a maximum disk size of $r_{disk,1} = 0.25 d_{max}$, from which incremental reductions are applied for the next disk sizes: $r_{disk,2} = 0.125 d_{max}$ and $r_{disk,3} = 0.0625 d_{max}$. Finally, a much smaller disk size is tested in $r_{disk,4} = 0.0105 d_{max}$.

Figure 12.1 shows a grid of $\Gamma_2$ plots, where each column shows a vortex radius of the three tested, while each row is a different disk radius. Therefore, the size of this image matrix is ($N$ Disk radius $\times$ $N$ Vortex radius), where the left-most column is the largest vortex radius, and the right-most column is the smallest vortex radius. On the rows, the upper-most row is the largest disk radius, while the lower-most row is the smallest disk radius.

From the plots given in Figure 12.1, two main observations can be made on the two sensitivity parameters considered: there exists a boundary effect and the extension of the transition region (from the vortex region $r \leq r_c$ to the outside-of-vortex region $r > r_c$). While no effect on these two features can be seen coming from the varying vortex radius, reducing the disk radius does have an impact on the boundary effects and the transition region: reducing the disk radius results in a reduction of both effects. Therefore, it becomes clear that for the computation of $\Gamma_2$ in the simulation domain (with focus in a specific area of interest) the boundary effects need to be accounted for, as well as implementing the smallest disk size tested for optimum accuracy of the $\Gamma_2$ flow field results.

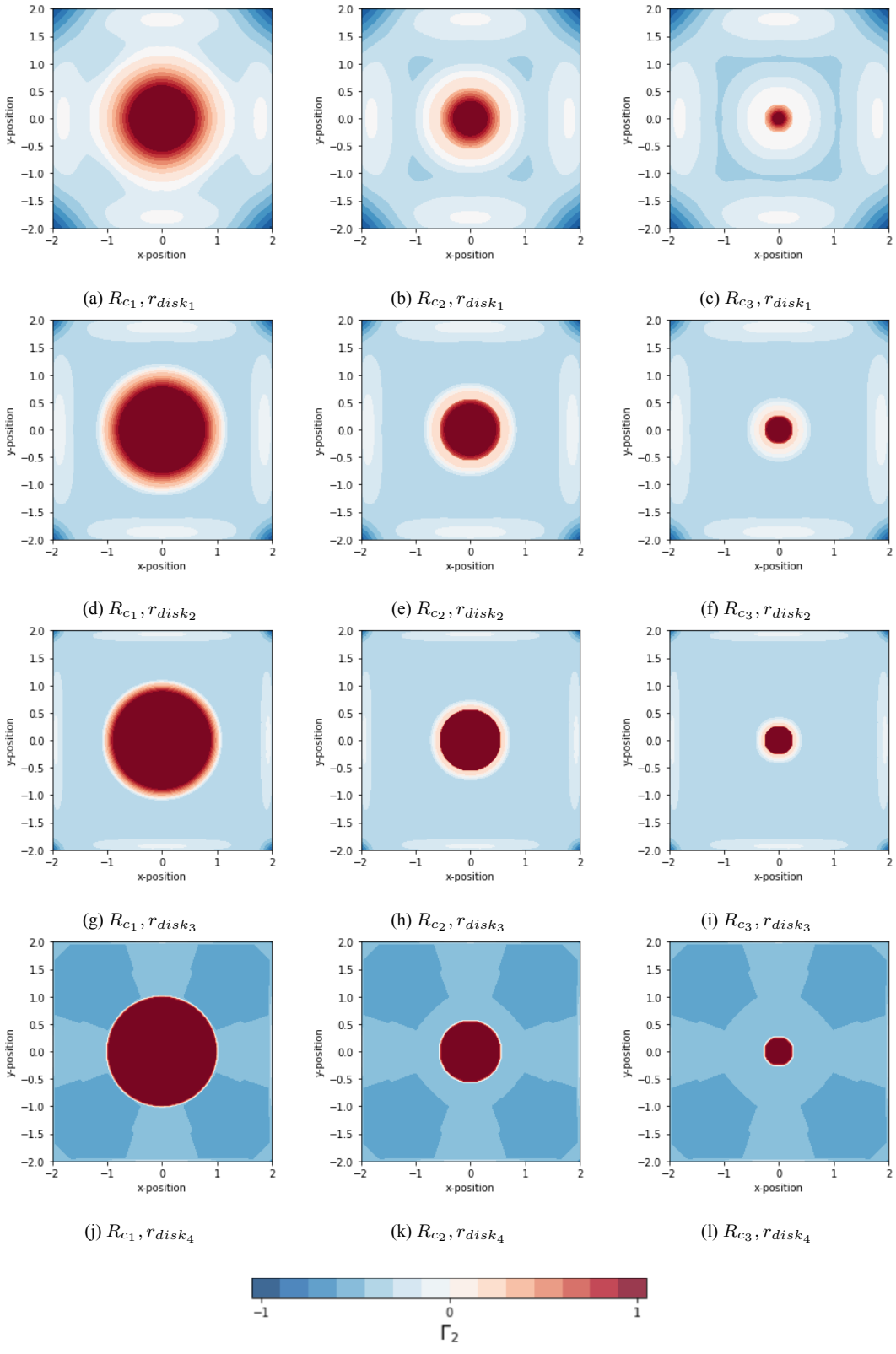


(a) $R_{c_1}, r_{disk_1}$ (b) $R_{c_2}, r_{disk_1}$ (c) $R_{c_3}, r_{disk_1}$

(d) $R_{c_1}, r_{disk_2}$ (e) $R_{c_2}, r_{disk_2}$ (f) $R_{c_3}, r_{disk_2}$

(g) $R_{c_1}, r_{disk_3}$ (h) $R_{c_2}, r_{disk_3}$ (i) $R_{c_3}, r_{disk_3}$

(j) $R_{c_1}, r_{disk_4}$ (k) $R_{c_2}, r_{disk_4}$ (l) $R_{c_3}, r_{disk_4}$

**Figure 12.1:** $\Gamma_2$ plots for Rankine Vortex, with varying $R_c$ and $r_{disk}$.

The magnitude of $\Gamma_2$ and the direction of rotation of the vortex are verified by Figure 12.2, where a clockwise rotation of the vortex, as given by $\Gamma = -10m^2/\text{sec}$ in (a) results in positive $\Gamma_2$ values in the vortex, while a counter-clockwise rotation of the vortex ($\Gamma = 10m^2/\text{sec}$) results in negative $\Gamma_2$ values in the vortex.

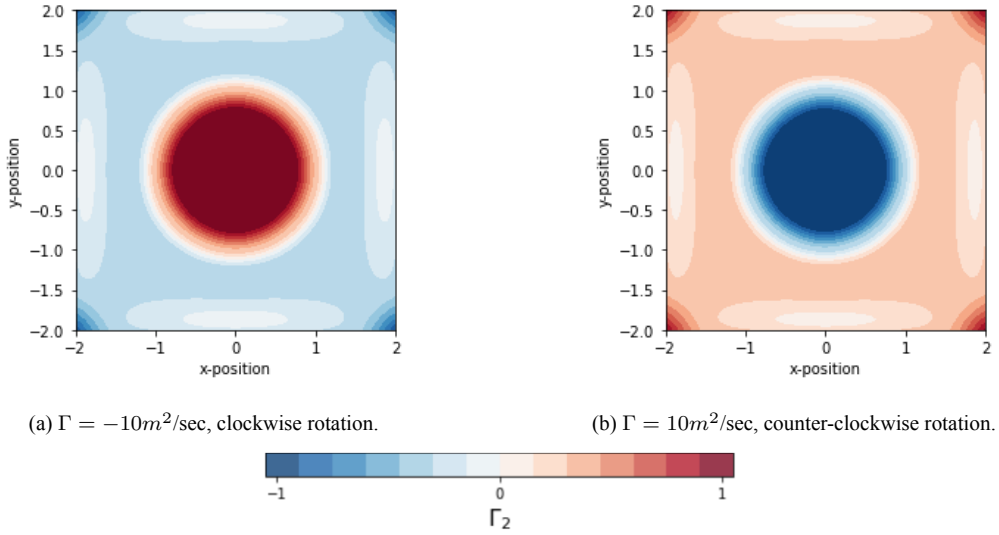


(a) $\Gamma = -10m^2$/sec, clockwise rotation.

(b) $\Gamma = 10m^2$/sec, counter-clockwise rotation.

**Figure 12.2:** Comparison of $\Gamma_2$ magnitude distribution for a clockwise rotating vortex (Γ=-10) and a counter-clockwise rotating vortex (Γ=10).

## 12.2. Method comparison in simulation domain

Figure 12.3 displays the solution implemented in the simulation fluid domain to account for the boundary effects identified in the previous chapter. The area of interest for the vortex analysis methodologies is the bottom part of the wake behind the tire, given by the 'Visualisation Domain', taken from the larger fluid slice size (1500,1005) mm at $x = 0.6D$. The manner in which the boundary effects are considered in the $\Gamma_2$ computation is by extending the actual computation domain to a larger region than the visualised region, hence hiding the boundary effects in the visualisation domain. This extension is given by $E$, which is calculated as the disk radius $r_{disk} = 0.0625 d_{max}$, where $d_{max}$ is only considered over the visualisation domain, hence giving $E = 0.043266$ m. However, the bottom edge of the visualisation domain lays over the ground, where no extension can be applied for the computation domain. To account for this, the results of $\Gamma_2$ are filtered by a threshold $\Gamma_2 \in (-1, -0.85) \cup (0.85, 1)$. The effect of this filtering can be appreciated in Figure 12.4.

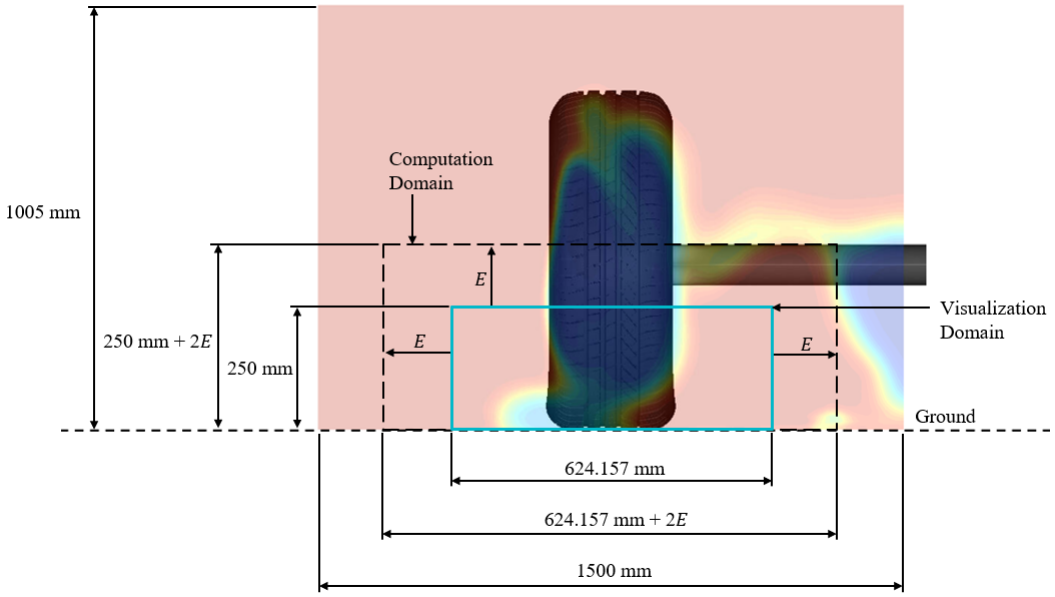


**Figure 12.3:** $\Gamma_2$ Computation and visualisation domains for simulation results.

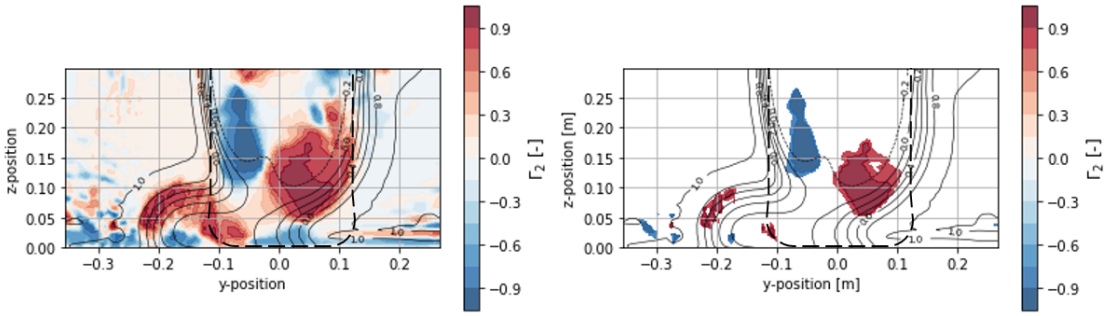


(a) $\Gamma_2$ distribution without filtering.

(b) $\Gamma_2$ distribution filtered by threshold $\Gamma_2 = 0.85$.

**Figure 12.4:** Depiction of effect of $\Gamma_2$ filtering.

After computation of $\Gamma_2$ following the considerations mentioned in the previous paragraph, several vortex identification methods are compared to the $\Gamma_2$-Criterion for the simulation results (restricted to the baseline deformation). The other vortex identification methods are: $X$-Vorticity, Swirl, $Q$-Criterion, and $\lambda_2$. The formulation of these methods is given in Appendix D. These are methods that, contrary to the $\Gamma_2$ criteria, rely on $\nabla u$. Figure 12.5 includes the comparison made for the standalone tire results, where a qualitative observation highlights that significant differences in the vortex cores identified across methods. In the standalone tire case, the vortices identified by $X$-Vorticity and Swirl are also captured by $\Gamma_2$, although $X$-Vorticity shows a smaller vortex C (as compared to $\Gamma_2$), while Swirl does not show vortex C at all. On the other hand, $Q$-Criterion and $\lambda_2$ show agreement with the other methods in vortex A, although vortex B is seemingly very shallow, while a new vortex core that is not seen in any of the other methods appears (vortex E).

The flow topologies presented by $\Gamma_2$ for $r_{disk_1} = 0.0625 d_{max}$ and $r_{disk_2} = 0.0105 d_{max}$ evidence a few discrepancies that are caused by the effect of the disk radius discussed earlier. The larger disk radius captures vortex F, which in the smaller disk radius it cannot be identified as a coherent vortex core, and thanks to the time-dependence analysis carried out in Section 10.1.7 it can be identified as a region of turbulence. Two vortices in the vicinity of the ground (vortices G and D) that are resolved in the smaller disk radius results are not present in the larger radius plot, which is a consequence of the boundary effect, emphasised by the larger disk radius. Nevertheless, it became clear through the short-average flow analysis that actually vortex G, identified in the averaged results, is not a coherent vortex core in time.

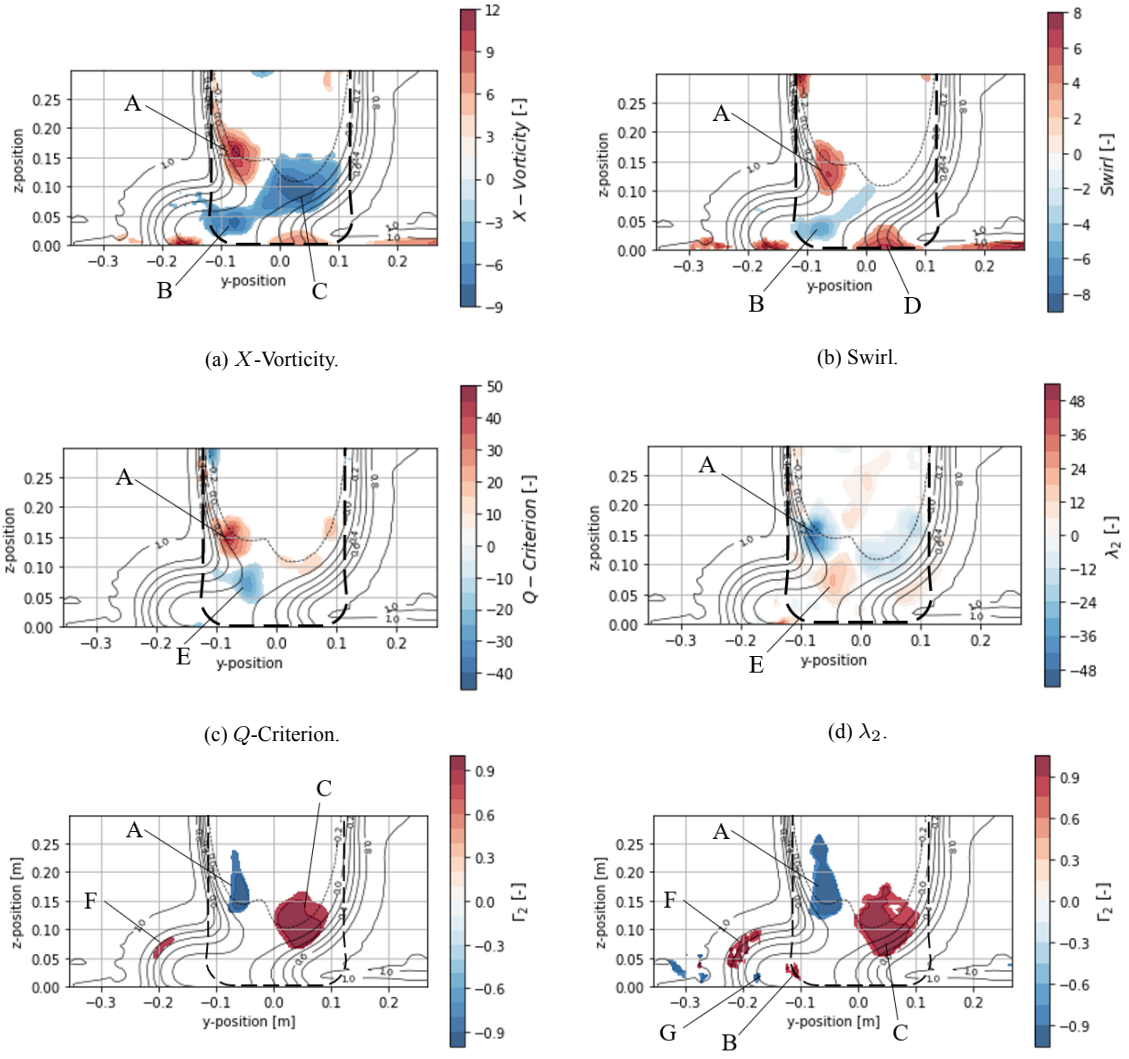


(a) $X$-Vorticity.

(b) Swirl.

(c) $Q$-Criterion.

(d) $\lambda_2$.

(e) $\Gamma_2, r_{disk_1}$.

(f) $\Gamma_2, r_{disk_2}$

**Figure 12.5:** Comparison of vortex identification methods for standalone tire case.

The method comparison with the full vehicle results highlights the main advantage of the $\Gamma_2$-Criterion over the other methods, as the vortex cores become much more evident and clear, while the increased noise in the flow field (as a consequence of the surrounding rough geometries of the $DrivAer$ model) results makes the vortices identified in the $\Gamma_2$ plots much less noticeable in the other methods.

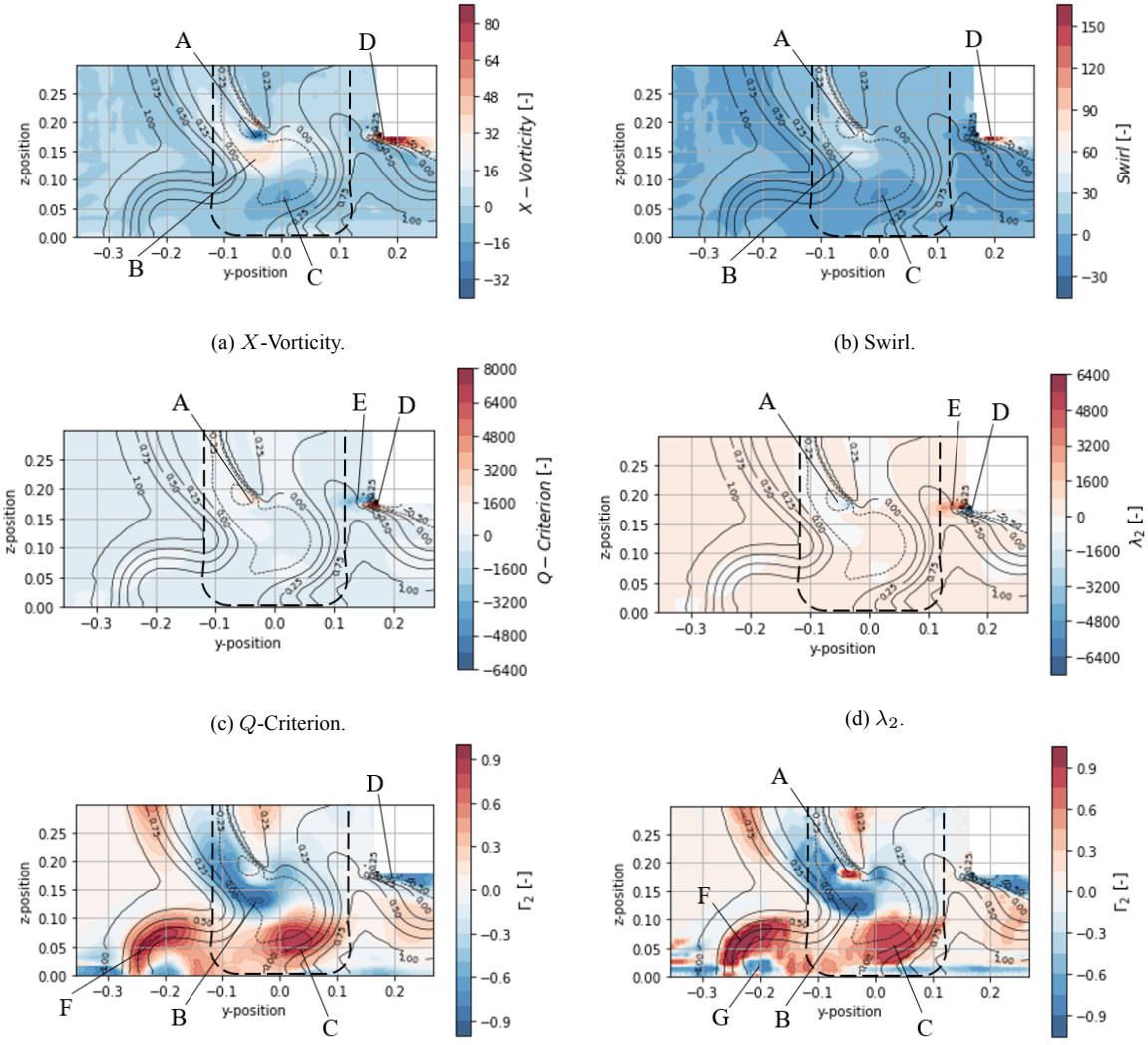


(a) $X$-Vorticity.

(b) Swirl.

(c) $Q$-Criterion.

(d) $\lambda_2$.

(e) $\Gamma_2$, $r_{disk_3}$ (unfiltered).

(f) $\Gamma_2$, $r_{disk_4}$ (unfiltered).

**Figure 12.6:** Comparison of vortex identification methods for the full vehicle case.

# 13

# Vortex Centre Identification Algorithm

In Section 4.3 the algorithm developed by Stevens and Sciacchitano [60] to track vortices was discussed. This algorithm consists of two main parts: vortex centre identification, and vortex tracking in time or space. The first part of the algorithm was carried out by implementing hierarchical clustering, while the second part is based on the Hungarian algorithm. For the scope of this project, the part of interest is the hierarchical clustering, since a complete tracking algorithm was not the main purpose of the whole body of work. Furthermore, given the small number of relevant vortices, these are tracked in space manually for the limited cases in which it became necessary. Therefore, the algorithm implemented to identify the vortex centres in the flow topology of study is entirely inspired by the first part of the algorithm put together by Stevens and Sciacchitano [60].

The hierarchical clustering algorithm, as thoroughly discussed in Section 4.3 consists of grouping coherent structures together from an input of unclassified objects based on similar properties. This is done through the single-link hierarchical cluster analysis by Sibson et al. [58]. For the current application of this algorithm, the objects to cluster are centroids of $\Gamma_2$ contours. The clustering of these centroids is done based on a linkage distance $D_{Linkage}(A, B)$ (Equation 13.1), which defines the minimum distance between two centroids $a$ and $b$ to belong to the same cluster of centroids ($A$ and $B$, respectively), see Stevens and Sciacchitano [60].

$$D_{Linkage}(A, B) = \min_{a \in A, b \in B} d(a, b) \tag{13.1}$$

The diagram presented laid out in Figure13.1 describes the whole workflow of the algorithm:

- **Inputs:** Y and Z-Velocity fields, and linkage distance $D_{Linkage}$.
- **Calculation of $\Gamma_2$:** From the input velocity fields, $\Gamma_2$ is computed over the domain of interest, following the formulation described in Chapter 12.
- **Filter $\Gamma_2$ results:** The $\Gamma_2$ are filtered by $\Gamma_2 \in (-1, -0.85) \cup (0.85, 1)$ according to the reasons given Chapter 12.
- **Calculation of centroid of $\Gamma_2$ contours:** The centroid of the filtered $\Gamma_2$ contours is calculated as the centre of mass of each closed contour. This proves another utility of implementing the smallest disk radius possible in the computation of $\Gamma_2$, as provides a larger number of closed contours, hence improving the accuracy of the vortex centre identification algorithm. The centroids are filtered by a total pressure coefficient band ($C_{p_{tot}}$: -0.5 , 0.2), which is the region of the wake where the relevant vortices are located. To remove the centroids identified in the turbulent region at the bottom left of the tire, a height filter $z > 0.075$m is also applied.
- **Centroid clustering:** In this final step, the input linkage distance is used to perform the clustering of the calculated centroids. The effective centre of the vortex is taken as the mean of the clustered points.

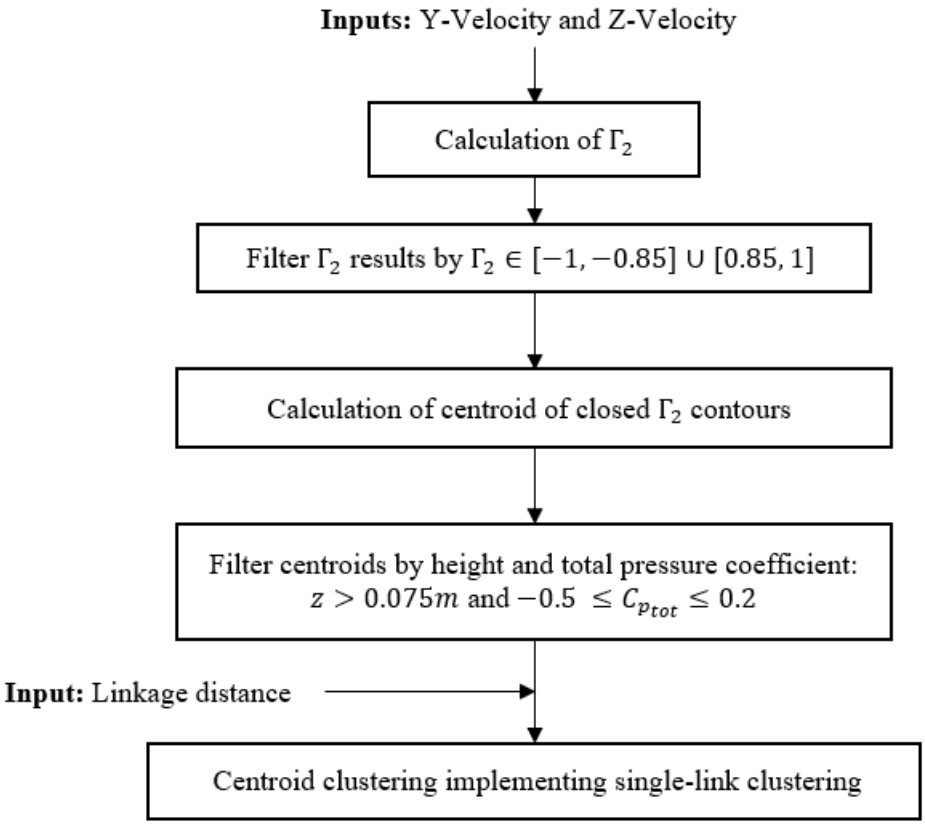


**Figure 13.1:** Vortex centre identification algorithm diagram.

Figure 13.2 (a) shows the calculated centroids (black stars) for a given calculation of $\Gamma_2$. Then, Figure 13.2 (b) shows the computed means of each cluster, representing the centre of the vortices. Comparing with Image 10.15 (e), the algorithm is able to identify the centre of the qualitatively assessed as 'relevant vortices' successfully. This definition of relevant vortices is based on the results from the transient analysis on the Baseline deformation, where Region Vortex 1 and 2 (also referred to as vortex A and C in the averaged results), in Figure 13.2 (b) represented as *P1* and *P2* were the more consistent structures in the topology.

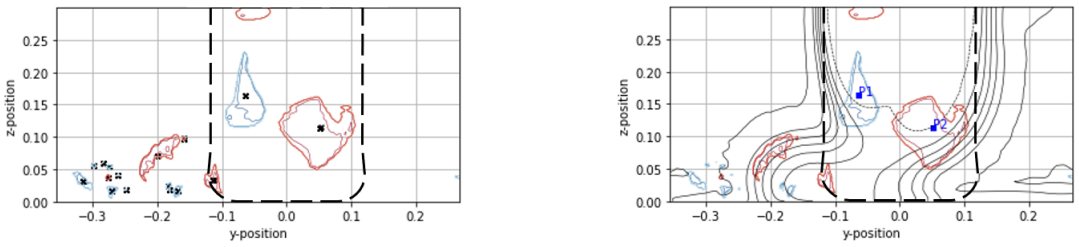


(a) Computed centroids of $\Gamma_2$.

(b) Means of computed clusters.

**Figure 13.2:** Centroids of $\Gamma_2$ and mean of clusters (effective vortex centres).

To determine the adequate linkage distance, a sensitivity analysis was carried out in which the linkage distance was increased from the starting distance 0.02m, with the aim of finding the minimum linkage distance that is able to identify the relevant vortices. Figure 13.3 shows that up to a linkage distance of 0.05m, two vortices are identified in the region of vortex C (as identified qualitatively in the previous sections). It is then with a linkage distance of 0.1m that one vortex core is identified in this region.

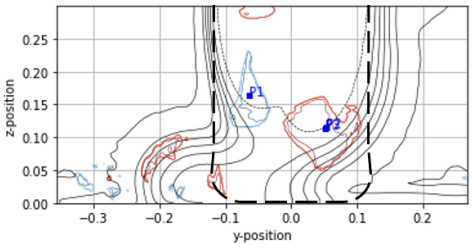


(a) $D_{Linkage} = 0.02$m.

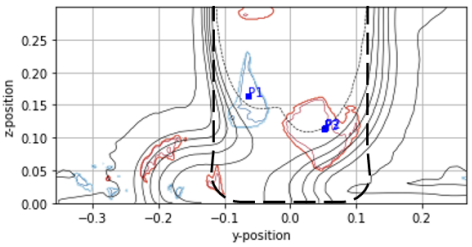


(b) $D_{Linkage} = 0.05$m.

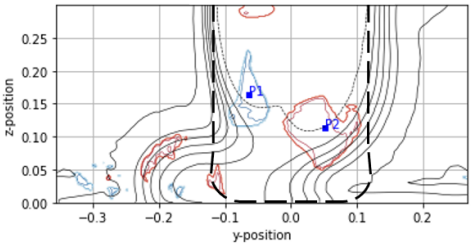


(c) $D_{Linkage} = 0.1$m.

**Figure 13.3:** Sensitivity study of linkage distance.

# Part III

# Results

For the sake of simplicity and easier referencing to each parameter test, the nomenclature used to refer to the different tests in the following sections is as given in Table 13.1 below.

| **Bulge Deformations** | | **Contact Patch Size Deformations** | | **Multi-Parameter Deformations** | |
|---|---|---|---|---|---|
| Test 1: | Bulge: +5mm | Test 7: | L: +7.3mm | Test 11: | R + L, Sharp |
| Test 2: | Bulge: +10mm | Test 8: | L: +15mm | Test 12: | R + L, Smooth |
| Test 3: | $\alpha$: 15deg | Test 9: | W: +4.6mm | Test 13: | R + W, Smooth 1 |
| Test 4: | $\alpha$: 6 deg | Test 10: | W: +8.4mm | Test 14: | R + W, Smooth 2 |
| Test 5: | $\beta$: 12.6deg | | | Test 15: | Cambered: Base |
| Test 6: | $\beta$: 5.4deg | | | Test 16: | Cambered, Offset: +8mm |
| | | | | Test 17: | H-Shape: Base |
| | | | | Test 18: | H-Shape, Offset: +8mm |

**Table 13.1:** Parameter test nomenclature.

Given that for certain deformations the reference area varies with respect to the Baseline deformation, the drag coefficient definition in Equation 7.7 is rearranged to $C_xA$ for the standalone tire force comparison, to remove the effect of the varying areas of the tire:

$$C_xA = \frac{F_x}{q_\infty} \ [m^2] \tag{13.2}$$

# 14

# Standalone Tire

The resulting $C_xA$ from the deformation tests is given in Figure 14.1 as the difference of each deformation test with respect to the baseline deformation. Note that, as indicated in Section 8.2, the curvature test difference is calculated with their respective baselines, which are *L: + 15mm* for the *R + L* curvature tests, and *W: + 8.4 mm* for the *R + W* curvature tests. This allows for the correct extraction of the contribution from the curvature parameter deformation. From Figure 14.1 the main conclusions that can be derived are that bulge deformations produce an increase in drag with respect to baseline, while reductions in drag are only found in contact patch deformations. The largest variations in these trends are found in the *Bulge: + 10 mm* deformation for the largest drag increase, and in *R + L: Sharp* and contact patch shape offsets, which include a sharpening of the corner curvature on the contact patch, for the largest drag reductions. The error bars given in Figure 14.1 represent the confidence intervals calculated for each simulation. The deltas observed are in most cases larger than this interval, hence any transient uncertainty is considered non-relevant.

While some deformation parameters show a linear trend between the increase of the deformation with the drag coefficient variation, such as the bulge size and the bulge lateral insertion, other deformation parameters present highly non-linear trends, like the contact patch size deformations (Length and Width), where the parameter deformation increases show first an increase in drag, followed by a significant reduction in drag for the larger deformation.

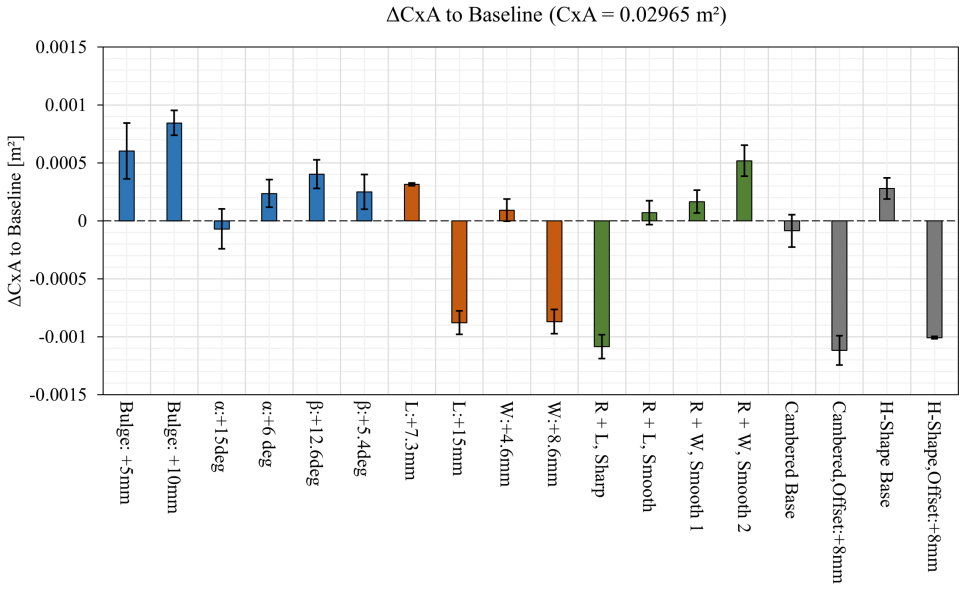


**Figure 14.1:** Standalone Tire $\Delta C_x$ to Baseline with confidence interval.

## 14.1. Initial Qualitative Analysis

To understand how the flow is behaving around the tire and the deformation areas for the standalone tire case, as well as to get an overview of what the flow trends are, an initial qualitative analysis is carried out. Firstly, a comparison to the loaded tire study by Schnepf at al. [55] is done in Figure 14.2. In the experimental flow field results, it can be observed that, increasing the vertical load on the tire results in an incrementally narrower wake at the bottom, together with a reduction of the area of total pressure losses localised in the bottom left part of the wake (outboard).

The deformation parameters with the most significant variations in the lower wake have been included in Figure 14.2 to provide an overview of how different parameters capture different parts of the wake changes observed in the experiment. These parameters consist of: Bulge Size $B$, Lateral Insertion Angle $\alpha$, and Contact Patch Width $W$. Looking at the effect of increasing $B$, it is noted that the inboard part of the wake becomes tighter, right underneath the arm, while non-linear variations are found in the reduction of the total pressure losses in the outboard bottom part. On the other hand, the increments of the lateral insertion angle (where reducing $\alpha$ produces a larger bulge protrusion in this region), results in a linear reduction of the localised losses at the outboard part of the lower wake, as seen in the experimental results, while no changes can be observed on the inboard part of the wake. Finally, increasing the contact patch width generates certain variations on the outboard region of losses, together with an inboard tightening of the wake, a behaviour that is captured in the experimental results.

Looking at the flow field from other points of view, for which comparison to experiment by Schnepf et al. [55] does not exist, further insight into how the wake is being affected by the deformation applied can be obtained. Plots of velocity magnitude are given in Figure 14.3, with a $z$-aligned slice at height $-0.47D$, which lies between the contact patch ($-0.49D$) and the bulge's mid height ($-0.45D$). It can then be appreciated that variations of the velocity magnitude are produced at the four corners of the contact patch and bulge. While the first increment of $B$ (*B: + 5 mm*) produces a seemingly increase in velocity around the rear corners, both outside (top of the image) and inside (bottom of the image), these then reduce again for *B: + 10 mm*. This results in different out-wash angles of the wake, where the larger velocities at the rear corners clearly show a reduction in out-wash together with a narrower wake.

Figure 14.4 shows the $y$-velocity in the same slice, where it can be seen that while the out-wash on the rear inside corner increases linearly with the increase of $B$, it is the in-wash at the rear that introduces the non-linear wake behaviour previously discussed, as it increases for *B: + 5mm*, but then decreases for *B: + 10mm*. How these trends show on the bulge surface is presented in Figure 14.5. Here the inboard part of the bulge is depicted with the velocity magnitude on its surface. The trend previously discussed is confirmed, where the velocity on the rear corner increases to its largest extent over most of the bulge area for *B: + 5mm*.

Overall, from the qualitative analysis covered in this section, it is concluded that the trends of variation for several parameters tested has a non-linear behaviour that needs more complex and detailed descriptions of the flow field for its understanding.

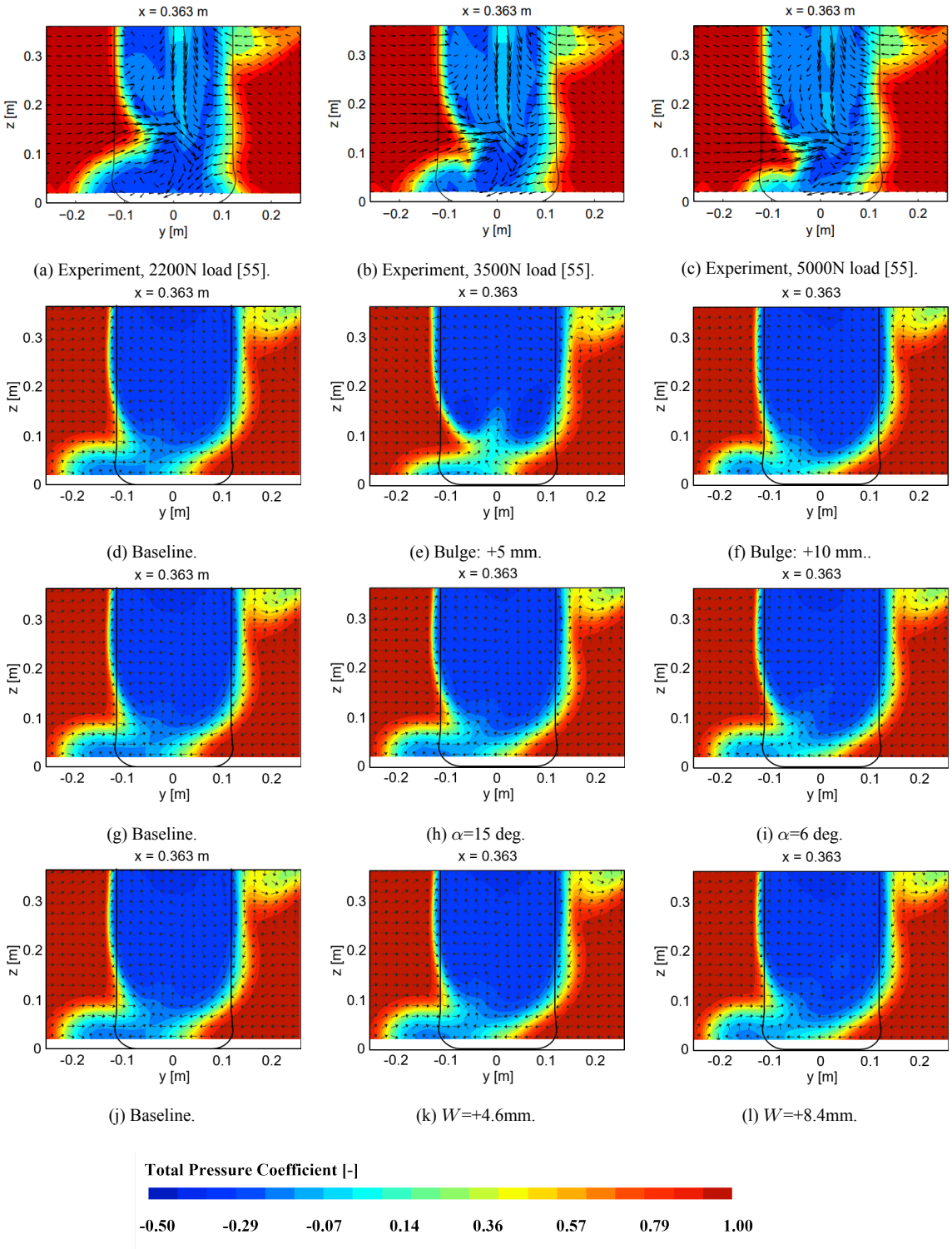


(a) Experiment, 2200N load [55]. (b) Experiment, 3500N load [55]. (c) Experiment, 5000N load [55].

(d) Baseline. (e) Bulge: +5 mm. (f) Bulge: +10 mm..

(g) Baseline. (h) $\alpha$=15 deg. (i) $\alpha$=6 deg.

(j) Baseline. (k) $W$=+4.6mm. (l) $W$=+8.4mm.

**Figure 14.2:** Total Pressure coefficient comparison with loaded tire study experimental results by Schenpf et al. [55], with an $x$-slice at $x$ : 0.363m behind the tire.

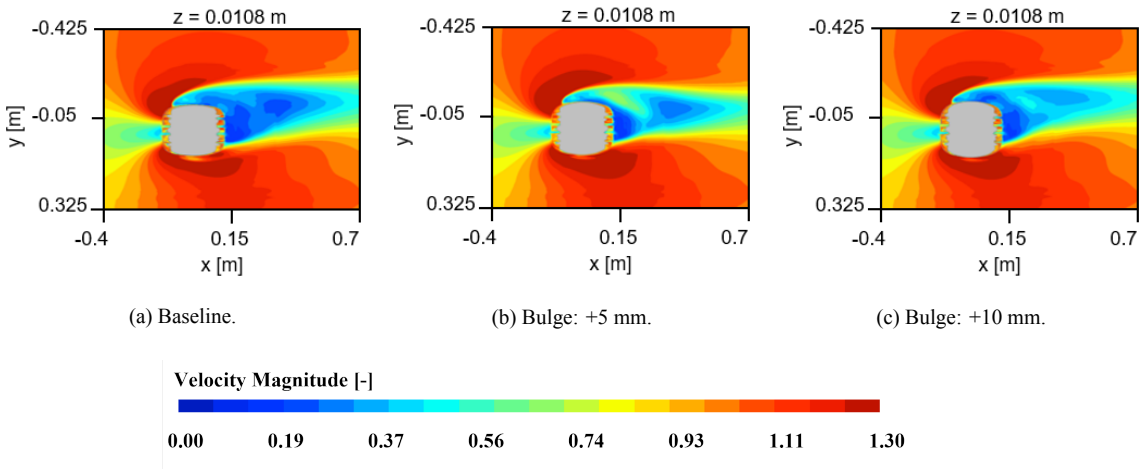


(a) Baseline. (b) Bulge: +5 mm. (c) Bulge: +10 mm.

**Figure 14.3:** Velocity magnitude plots for bulge size tests on a $z$-slice at h:$-0.47D$.

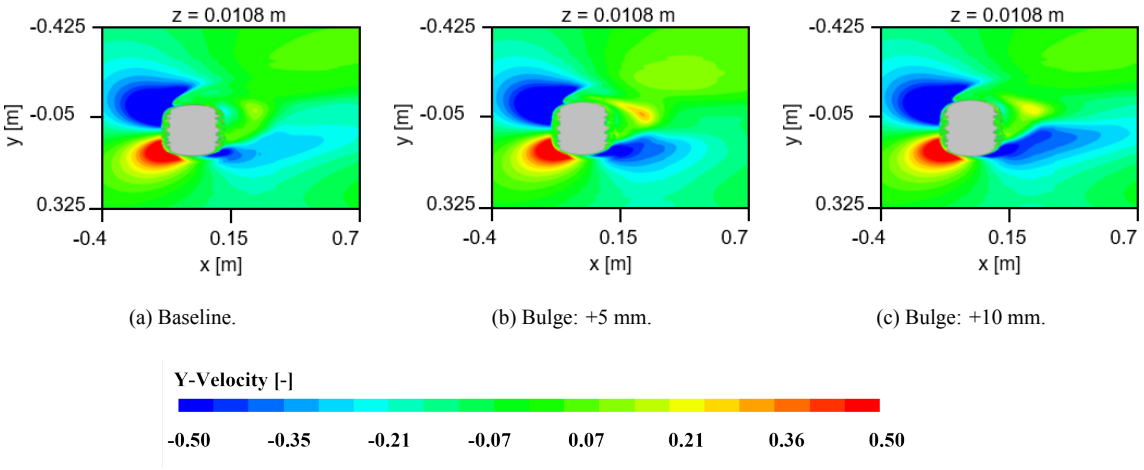


(a) Baseline. (b) Bulge: +5 mm. (c) Bulge: +10 mm.

**Figure 14.4:** Y-Velocity plots for bulge size tests on a $z$-slice at h:$-0.47D$..

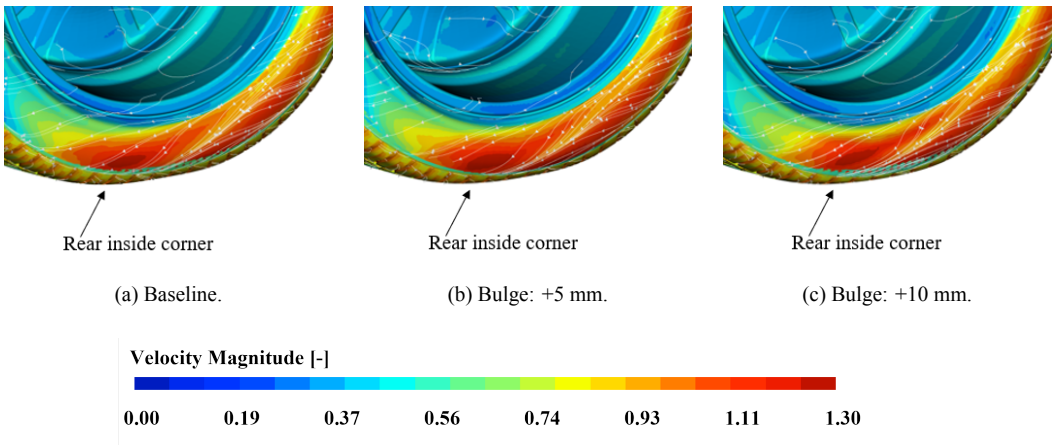


(a) Baseline. (b) Bulge: +5 mm. (c) Bulge: +10 mm.

**Figure 14.5:** Velocity magnitude plots on bulge sureface.

## 14.2. Principal Components Analysis

Principal Component Analysis has been widely covered in Sections 4.1 and 11. Figure 14.6 shows the distribution of the data for principal component 1 (PC1) and principal component 2 (PC2), which capture 70% of the variance. The largest part of the variation is captured by PC1, although it is clear that most of the deformations lay in one cluster of points, meaning that the wake variations due to the different deformations cannot be classified in clear groups or categories, with only a few outliers of the main cluster, among which lay *B: + 5mm* and *R + L: Sharp*, which, as described previously in Figure 14.1, are among the tests that produced the largest variation in $C_x A$.

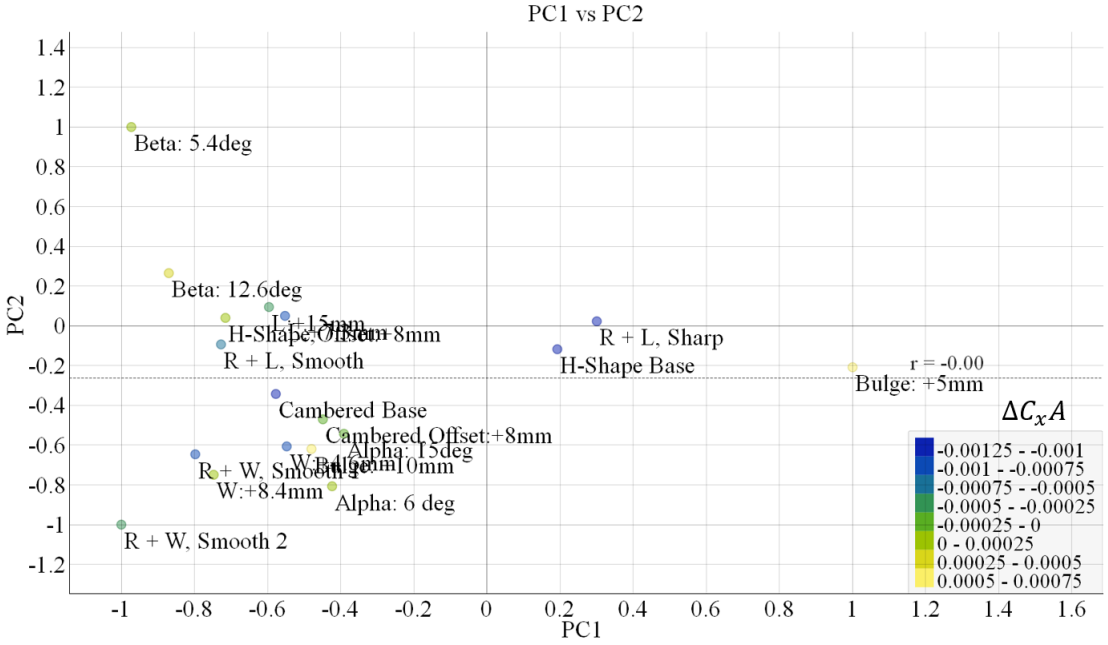


**Figure 14.6:** Principal Components 1 and 2 distribution.

To assess the capabilities of the measured flow variations to predict the drag coefficient variation, a linear regression model is carried out, with $\Delta C_x A$ as target. Figure 14.7 shows that the resulting model produced with the input measurements described in Section 11, the behaviour of the drag variation is not properly captured. Since the measurements are taken from flow variables describing the wake development, that lack of correlation with the drag coefficient evolution across deformations can be concluded to be more dependent of local effects on the tire surface.

On the other hand, when the target of the regression model is set to be the Microdrag Delta $\Delta C_{D_l}$ (described in Section 4.4) calculated for the entire tire wake in a location $x : 2.5D$ (as is depicted in Figure 14.8, with a zoomed view on the main cluster in Figure 14.9), a better correlation is found between the measurements and the momentum losses in the wake (as described by the Microdrag $C_{D_l}$), as they are calculated in Equation 4.10.

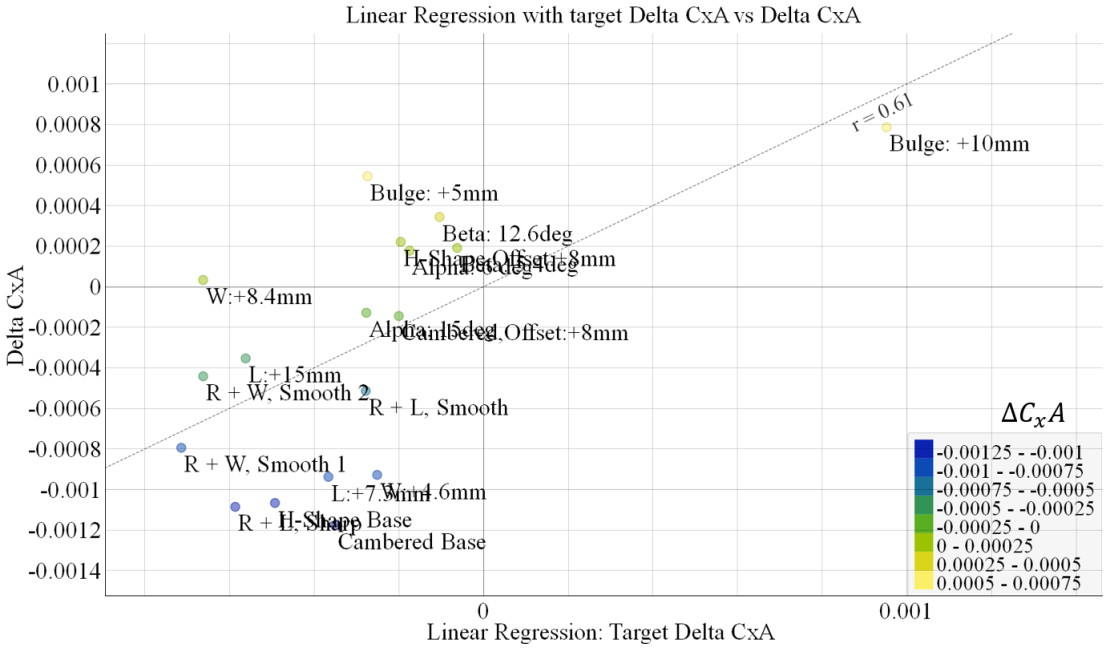


**Figure 14.7:** Linear regression model with target: $C_x$ versus standalone tire $C_x$.

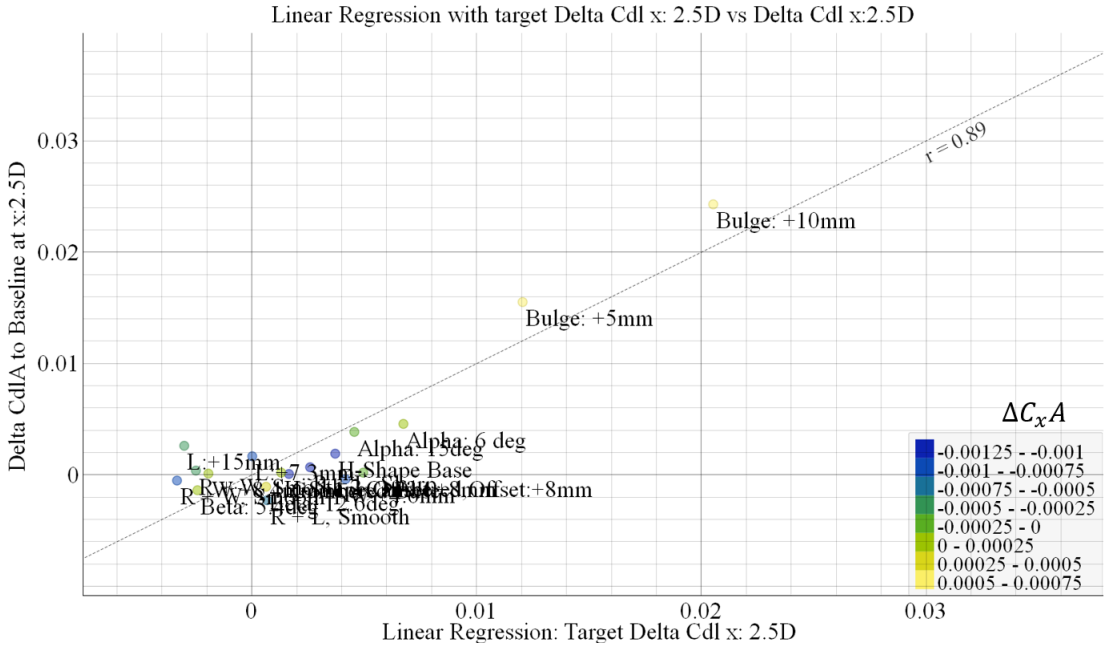


**Figure 14.8:** Linear regression model with target: $C_{D_l}$ at $x : 2.5D$ versus standalone tire $C_{D_l}$ at $x : 2.5D$.

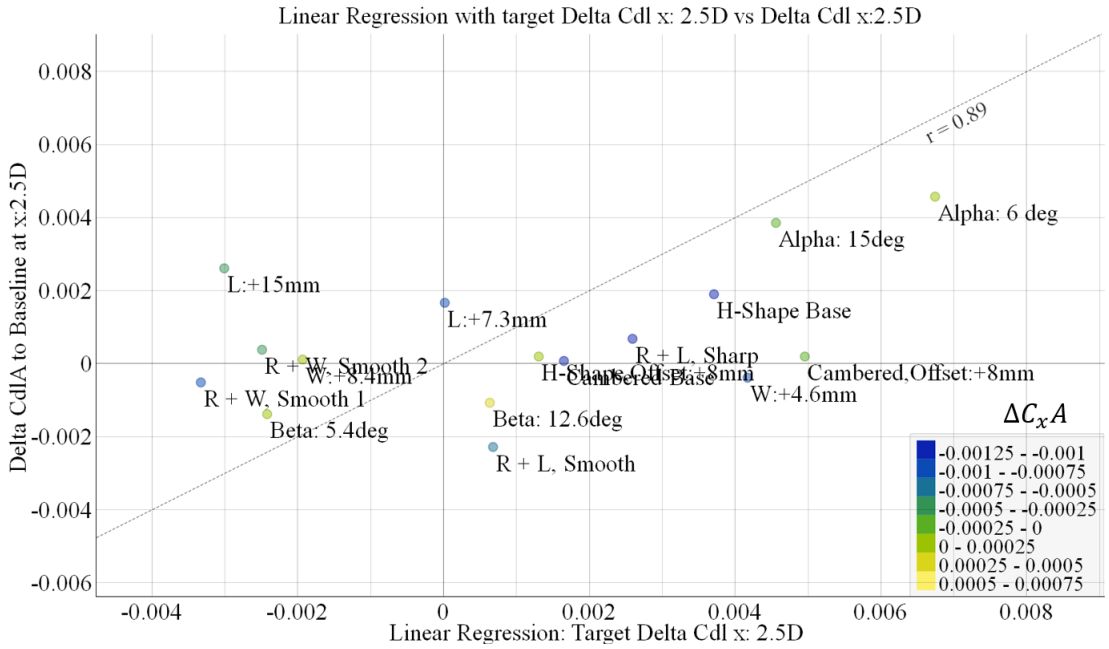


**Figure 14.9:** Zoomed view on cluster of Linear regression model with target: $C_{D_l}$ at $x : 2.5D$ versus standalone tire $C_{D_l}$ at $x : 2.5D$.

For the regression model, the first four principal components have been accounted for, as they represented about 80% of the variance in the data. Ultimately, although the PCA analysis has generated a few useful conclusions −mainly that the measurements used as input work better to describe and predict the wake but not the $C_xA$ variation for each deformation test− this analysis approach fails to classify the data in clearly separated clusters that could bring light into how the wake is behaving differently depending on each deformation, which would have simplified the non-linear behaviours overviewed in the qualitative analysis.

## 14.3. Vortex Behaviour and Wake Development

Given the discussed challenges to simplify the non-linear behaviours observed in the wake of the standalone tire, an approach focused on the analysis of the behaviour of the vortices relevant for the tire wake evolution and its changes across deformations is implemented. To do that, the wake width is measured at different $x$-locations downstream of the tire ($x : 0.6D, 0.7D, 0.8D, 0.9D, 1.0D$). The width is measured by finding the distance between the minimum and maximum $y$-location of the envelope of a total pressure coefficient of 0.5 at each $x$-location at a height $z : 0.075$ m and taking the difference. Then, plotting the $y$-min and $y$-max of the envelope shows on which side of the tire wake (inboard or outboard, respectively) the width variations are produced.

With the implementation of the vortex identification algorithm at $x : 0.6D$, it is then possible to correlate the changes in wake width with the changes of the vortex positions in the wake, hence being able to understand what drives the evolution of the wake across deformations. For the current application, from the vortices identified in Figure 12.5, the quantified approach is applied to vortices A and C, since they present a more consistent presence across deformation test results, while vortex B is evaluated in a qualitative manner.

### 14.3.1. Bulge Size

Figure 14.10 (a) shows that *Bulge: + 5mm* produces a drastic reduction in the wake width, which in Figure 14.10 (b) can be seen coming from both inboard and outboard of the wake, although the dominant part remains the outboard part. On the other hand, *Bulge: + 10mm* experiences a slight reduction in wake width, which comes mostly from the inboard part of the wake.

Looking at the vortex plots in Figure 14.11, when it comes to vortices A and C, inverse trends are visible for *Bulge: + 5mm* and *Bulge: + 10mm* with respect to Baseline, where for *Bulge: + 5mm* the centre of both vortices move upwards, while for *Bulge: + 10mm* they move downwards. Nevertheless, on the outboard part of the lower wake vortex B appears dissipated for *Bulge: + 5mm*, while it seems to be stronger for *Bulge: + 10mm*. This explains the drastic difference in wake width observed on the outboard for *Bulge: + 5mm*, while the downwards movement of vortex C explains the slightly tighter inboard part of the wake. For the case *Bulge: + 10mm*, it is the slight outwards movement of vortex C that causes a small contraction of the inboard wake with respect to Baseline.

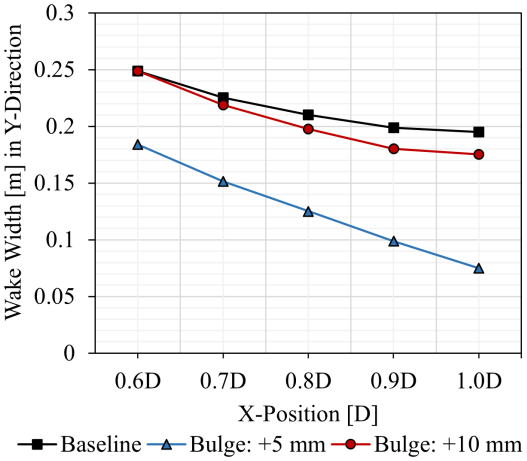


(a) Overall wake width.

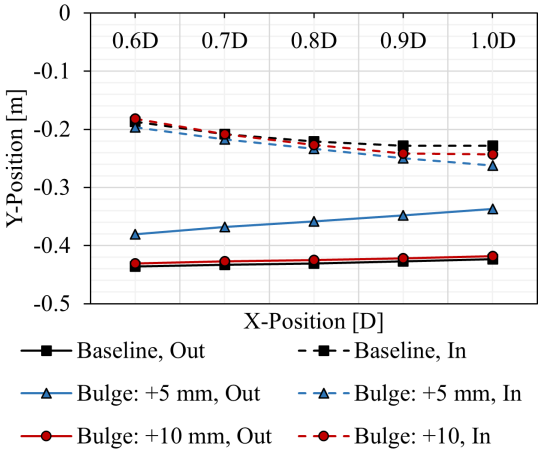


(b) Wake limits: inboard and outboard.

**Figure 14.10:** Wake width development for $B$.

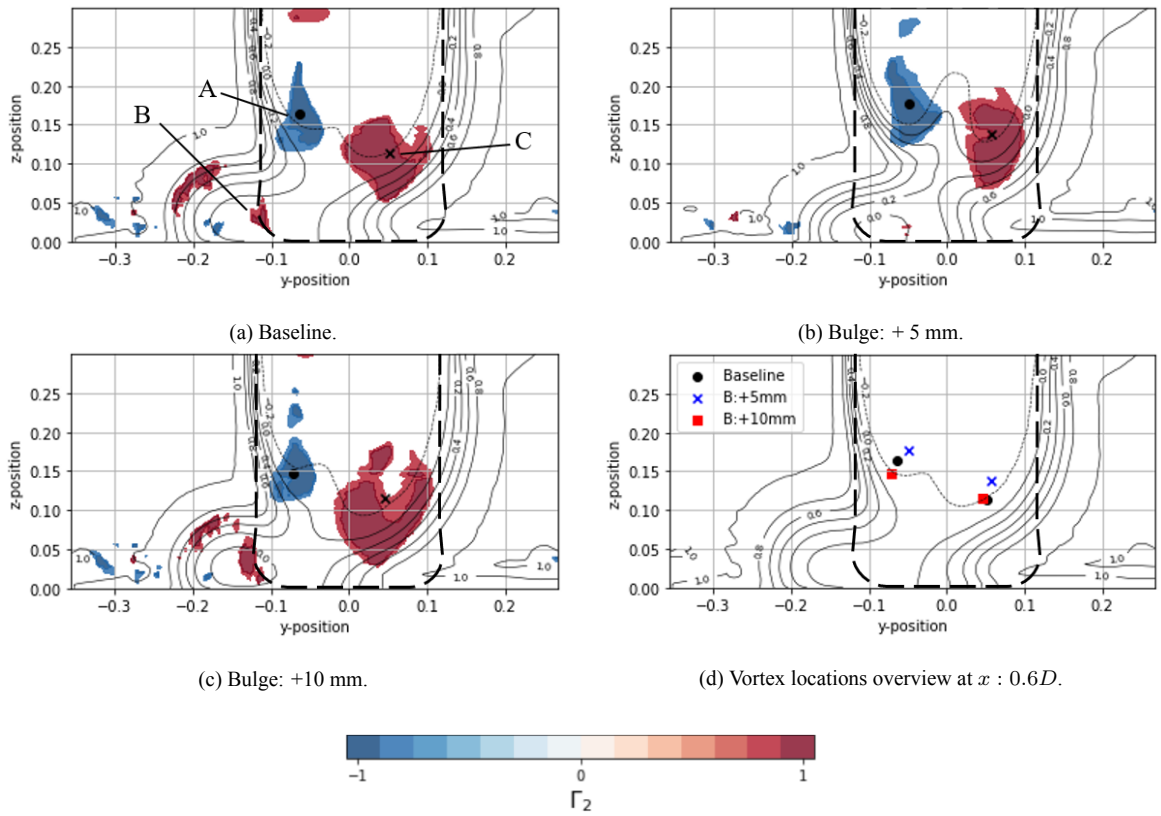


(a) Baseline.

(b) Bulge: + 5 mm.

(c) Bulge: +10 mm.

(d) Vortex locations overview at $x : 0.6D$.




**Figure 14.11:** $\Gamma_2$ flow topologies for $B$ tests and their respective identified vortex centre positions.

## 14.3.2. Lateral Insertion Angle

Although some differences in the behaviour of vortex B can be appreciated between Baseline, $\alpha : 15deg$ and $\alpha : 6deg$ (Figure 14.12), only a small contraction is appreciated on the inboard part of the wake, which at $x : 0.6D$ is equal for both deformation tests, although the contraction becomes slightly larger for $\alpha : 15deg$ in downstream locations of the wake. While vortex C does show a downwards displacement for both tests with respect to baseline (see Figure 14.13 (d)), it is difficult to attribute the wake contraction to this movement (as it follows an opposite trend to that observed in the Bulge Size study), which could be caused by differences in the transient behaviour of the very turbulent region around the centre line at the bottom of the wake, observed in previous transient analysis in Section 10.1.7. This region shows clear differences in Figure 14.13 (a) to (c).

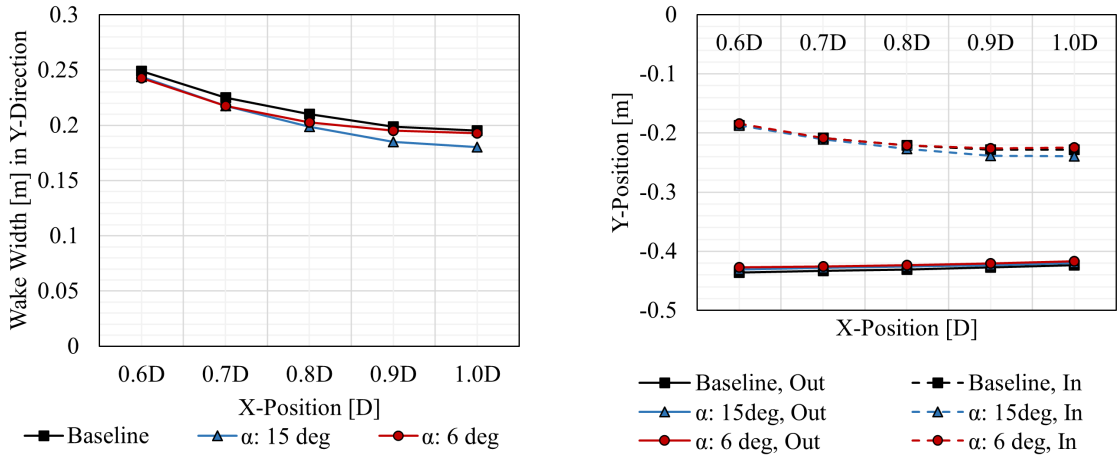


(a) Overall wake width.

(b) Wake limits: inboard and outboard.

**Figure 14.12:** Wake width development for $\alpha$.

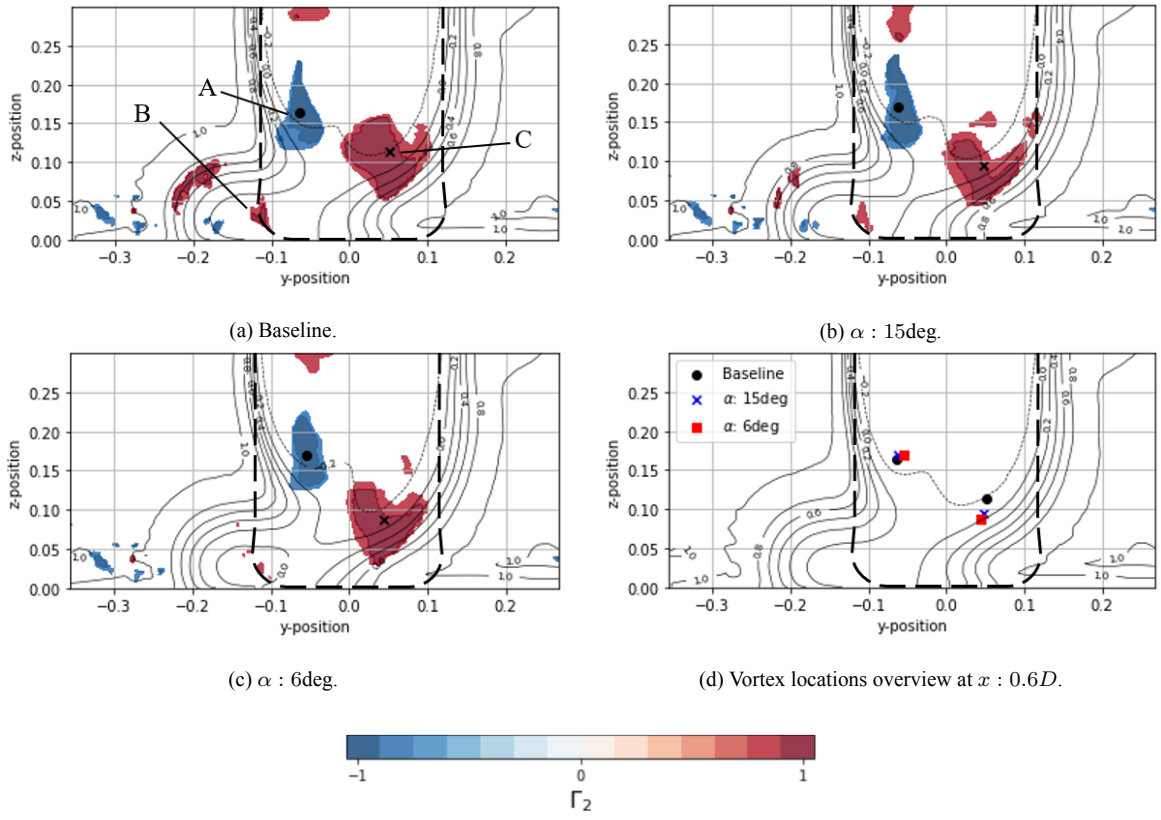


(a) Baseline.

(b) $\alpha$ : 15deg.

(c) $\alpha$ : 6deg.

(d) Vortex locations overview at $x$ : $0.6D$.

**Figure 14.13:** $\Gamma_2$ flow topologies for $\alpha$ tests and their respective identified vortex centre positions.

### 14.3.3. Longitudinal Insertion Angle

A consistent trend of wake expansion that becomes larger downstream is clearly appreciated for both deformation tests ($\beta$ : 12.6*deg* and $\beta$ : 5.4*deg*) in Figure 14.14, with contributions from both sides of the wake. Contemplating Figure 14.15 (d), the centre of both vortex A and C seems to be moving downwards with respect to Baseline. On the outer end of the wake at the bottom, the differences seem negligible in the vortex B region. However, where the vortex behaviour differences become more drastic are in vortex C, which seemingly splits into two cores,

although the algorithm identifies one core due to the lower $\Gamma_2$ contour englobing both cores. This behaviour is analysed in more detail in the transient analysis provided in Section 14.4.

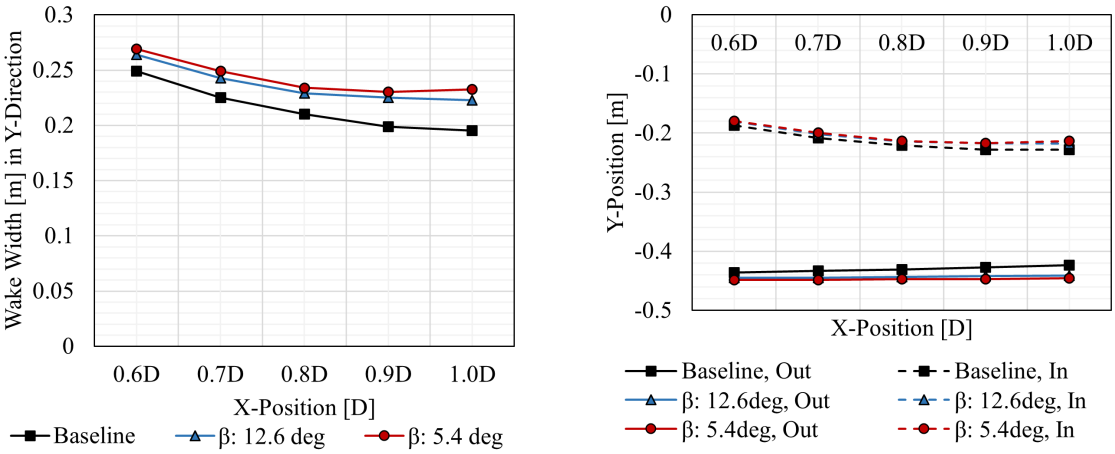


(a) Overall wake width.

(b) Wake limits: inboard and outboard.

**Figure 14.14:** Wake width development for $\beta$.

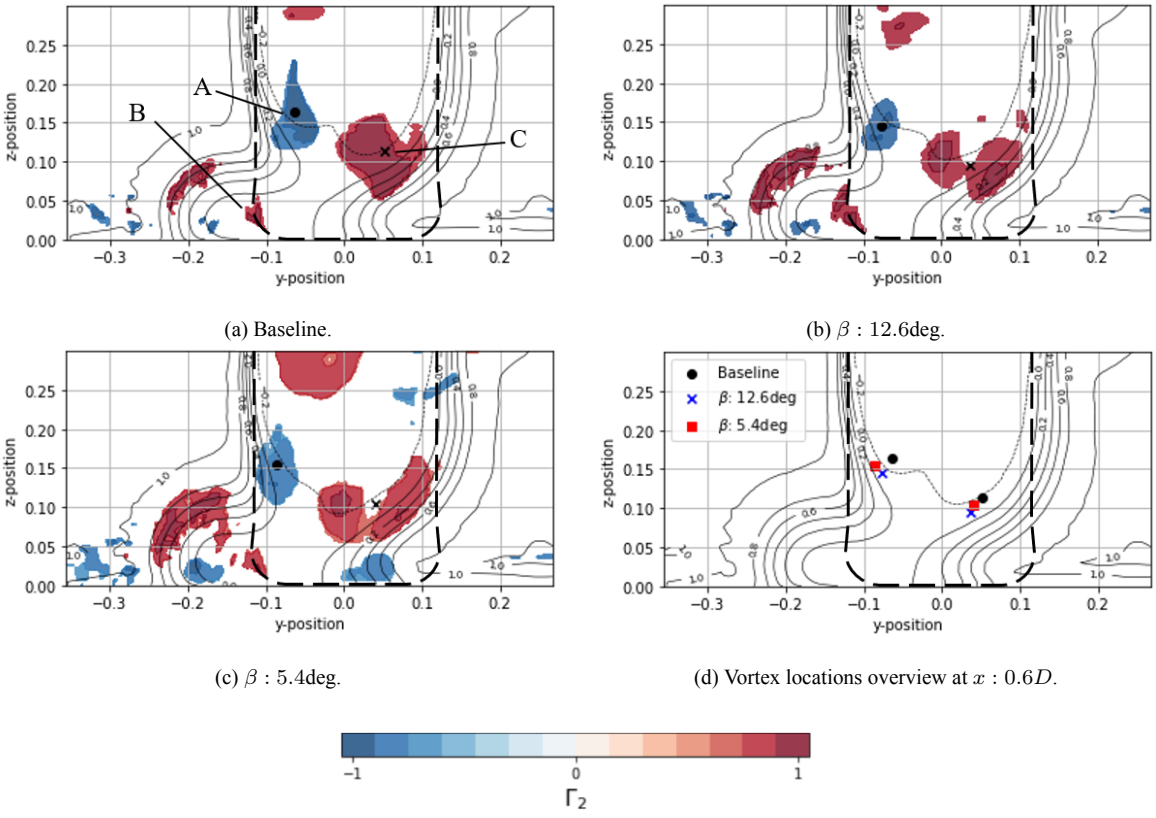


(a) Baseline.

(b) $\beta$ : 12.6deg.

(c) $\beta$ : 5.4deg.

(d) Vortex locations overview at $x$ : $0.6D$.

**Figure 14.15:** $\Gamma_2$ flow topologies for $\beta$ tests and their respective identified vortex centre positions.

## 14.3.4. Contact Patch Length

When it comes to the Contact Patch Length tests, as Figure 14.16, no significant contractions or expansions can be appreciated neither at the outboard nor the inboard part of the wake. This finding correlates well with the

lack of displacement from vortices A and C, visible in Figure 14.17, while vortex B also presents a very similar behaviour for both deformation tests.

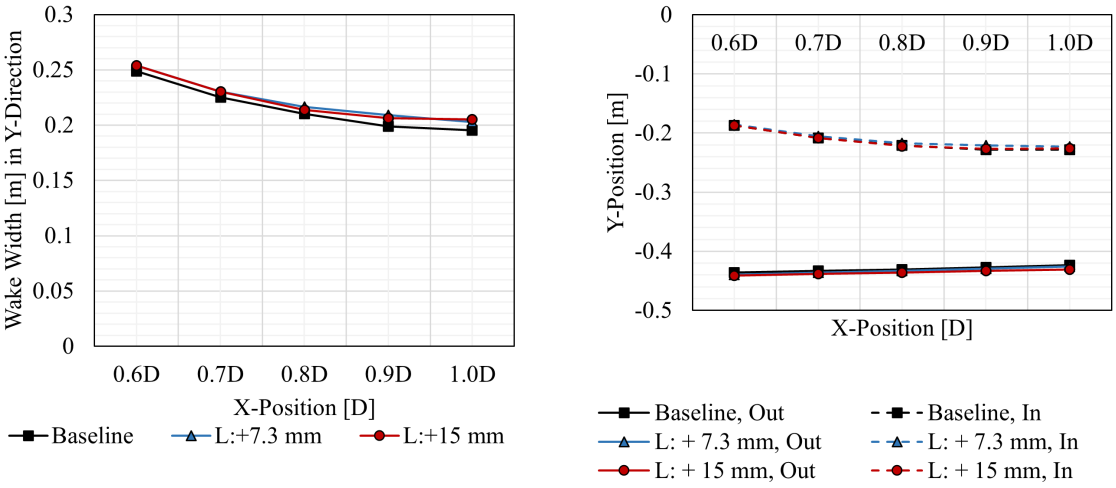


(a) Overall wake width.

(b) Wake limits: inboard and outboard.

**Figure 14.16:** Wake width development for $L$.

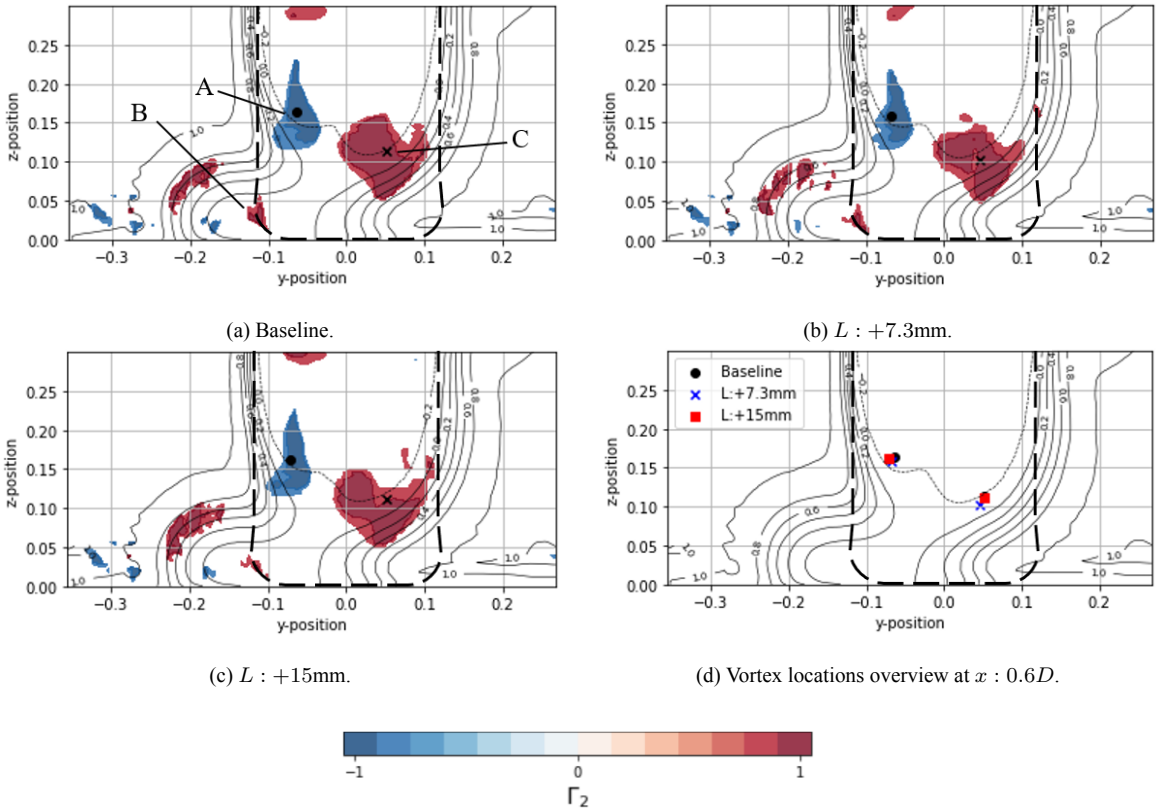


(a) Baseline.

(b) $L$ : +7.3mm.

(c) $L$ : +15mm.

(d) Vortex locations overview at $x$ : $0.6D$.

**Figure 14.17:** $\Gamma_2$ flow topologies for $L$ tests and their respective identified vortex centre positions.

## 14.3.5. Contact Patch Width

While at the beginning of the wake $x$ : $0.6D$ no significant differences in the wake width are observed, the width development downstream clearly shows a very different behaviour for the test *W: +8.4 mm*, with a drastic expansion with respect to Baseline and *W: +4.6 mm*. Figure 14.18 (b) shows that the wake expansion experienced

in *W: +8.4 mm* has its origin predominantly in the evolution of the inboard part of the wake. This can be confirmed with the behaviour of vortex C in Figure 14.19, where again it splits into two cores, while the centre identified by the algorithm shows insignificant displacement with respect to Baseline and *W: +8.4 mm*, as it captures the centre of the englobing contour. From Figure 14.18 (b), it becomes clear that it is the behaviour of this vortex split downstream that makes the difference in the wake width development for *W: +8.4 mm*.

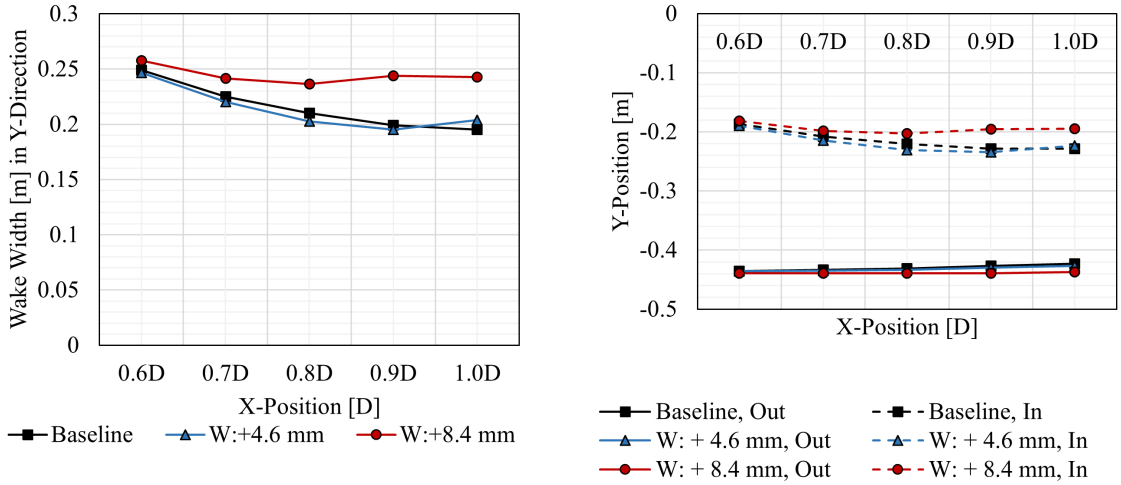


(a) Overall wake width.

(b) Wake limits: inboard and outboard.

**Figure 14.18:** Wake width development for $W$.

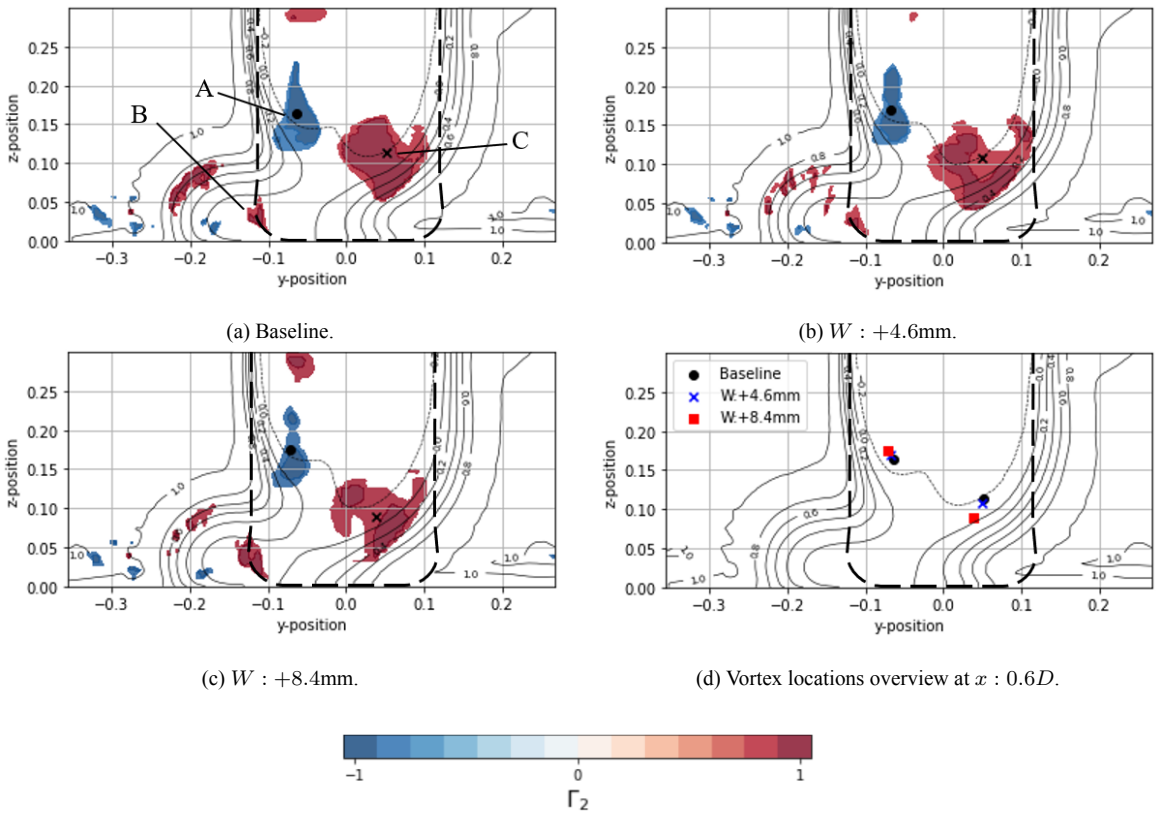


(a) Baseline.

(b) $W$ : +4.6mm.

(c) $W$ : +8.4mm.

(d) Vortex locations overview at $x$ : $0.6D$.

**Figure 14.19:** $\Gamma_2$ flow topologies for $W$ tests and their respective identified vortex centre positions.

### 14.3.6. Contact Patch Length Curvature

As Figure 14.20 shows, a sharper curvature presents a considerable contraction of the wake on both sides, while a smoother curvature presents the opposite trend, with a slight expansion of the wake. Figure 14.21 shows that in *R + L: Sharp* both vortex A and C are more clearly defined, with a displacement upwards with respect to the respective baseline in this test case, which is *L: +15mm*, similar to the behaviour seen in *Bulge: +5mm* where the wake contraction was similar to *R + L: Sharp*. Furthermore, for *R + L: Smooth* a core split occurs in vortex C, implying possible differences in the transient behaviour of vorticity in this region, which could be leading to its wake thickening.

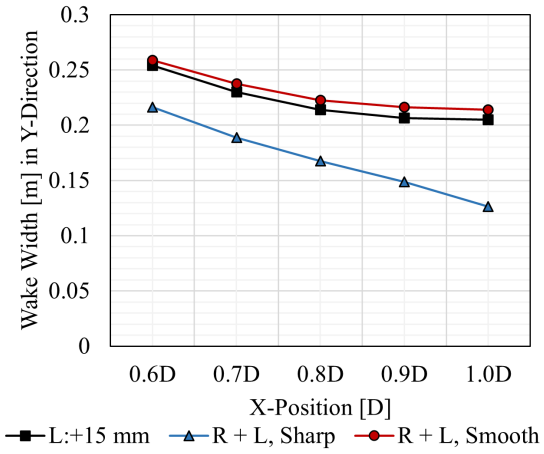


(a) Overall wake width.

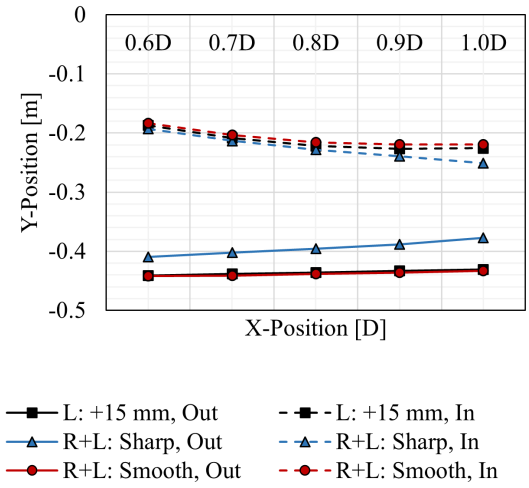


(b) Wake limits: inboard and outboard.

**Figure 14.20:** Wake width development for $R + L$.

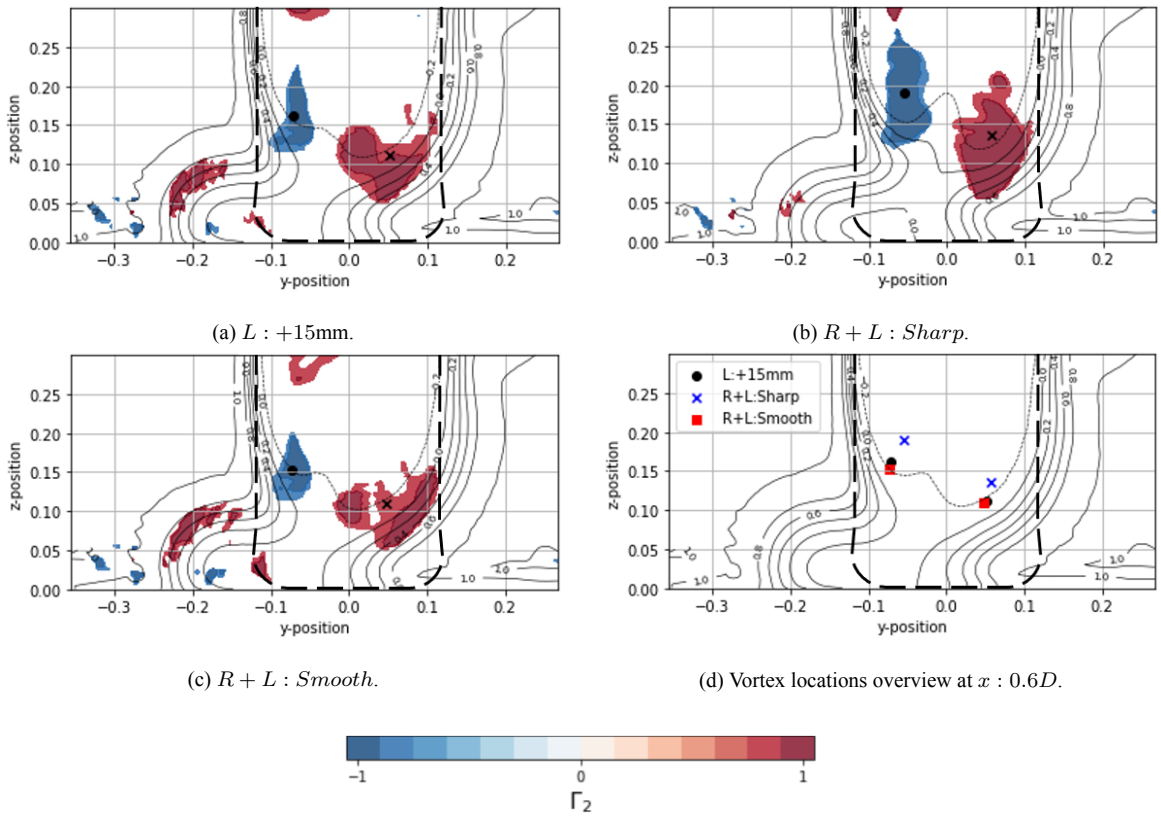


(a) $L$ : +15mm.

(b) $R + L$ : *Sharp*.

(c) $R + L$ : *Smooth*.

(d) Vortex locations overview at $x$ : $0.6D$.

**Figure 14.21:** $\Gamma_2$ flow topologies for $R + L$ tests and their respective identified vortex centre positions.

## 14.3.7. Contact Patch Width Curvature

The behaviour observed in the wake development in Figure 14.22 strongly resembles the wake evolution found in Figure 14.18 for *W: +8.4 mm*. In this case this evolution occurs for both tests, where the curvature increasingly becomes smoother with respect to the respective baseline *W: +8.4 mm*. Like in *W: +8.4 mm*, the test cases present a core split for vortex C, which becomes more pronounced for *R+W: Smooth 2*. These similarities in behaviour for different curvatures suggest that the dominant parameter in this vortex and wake behaviour is the contact patch width.

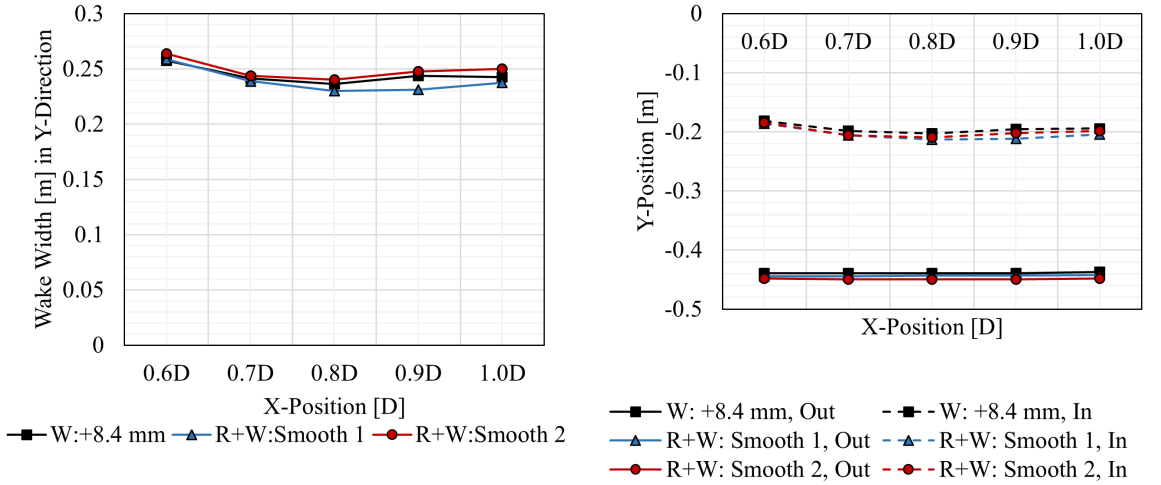


(a) Overall wake width.

(b) Wake limits: inboard and outboard.

**Figure 14.22:** Wake width development for $R + W$.

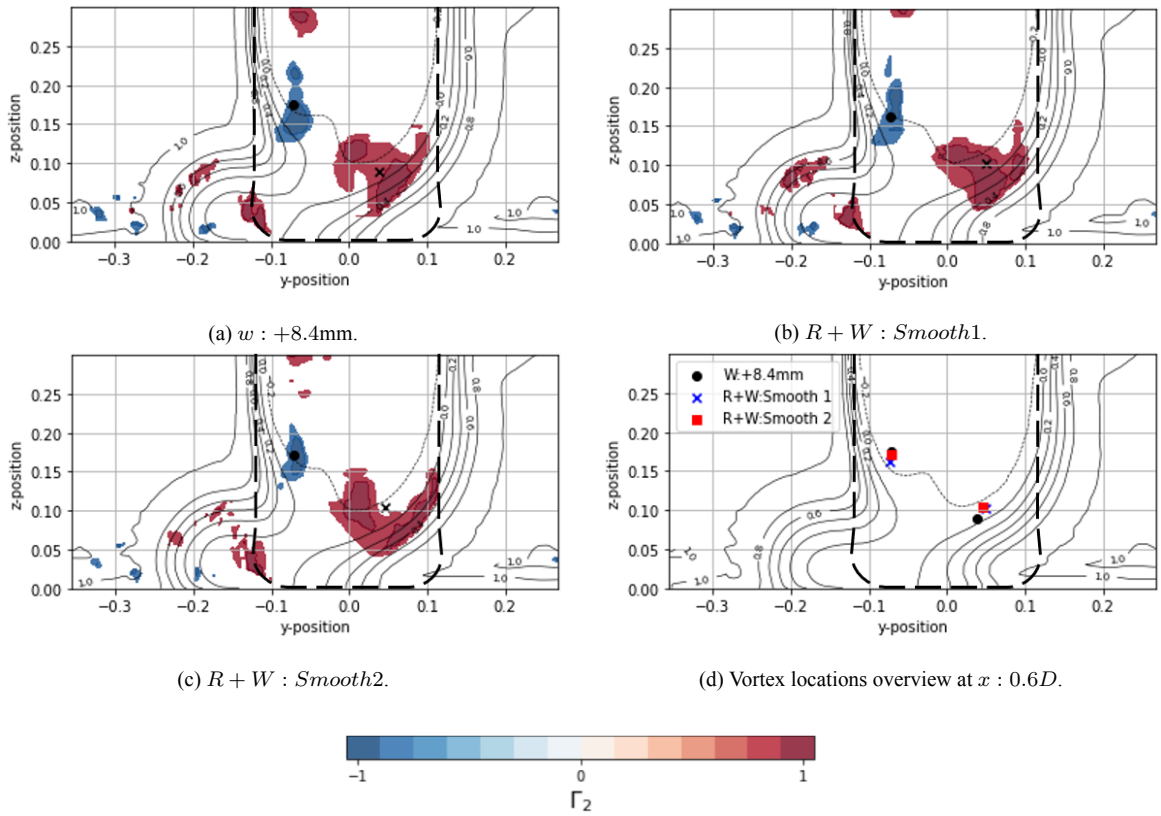


(a) $w$ : +8.4mm.

(b) $R + W$ : $Smooth1$.

(c) $R + W$ : $Smooth2$.

(d) Vortex locations overview at $x$ : $0.6D$.

**Figure 14.23:** $\Gamma_2$ flow topologies for $R + W$ tests and their respective identified vortex centre positions.

## 14.3.8. Cambered Shaped Contact Patch

The differences in the wake for this test case only become significant downstream, where the base shape produces a reduction in width, while the shape offset goes in the opposite direction and slightly increases the width. Figure 14.24 (b) shows that the contribution to the wake width differences is predominantly from inboard. Comparing with the behaviour of vortex C in this part of the wake, no significant differences can be observed at $x$ : $0.6D$ in Figure 14.25. Therefore, it seems that it could be differences in the transient behaviour of this vorticity region downstream that causes the discrepancies observed in the wake development, as it is a characteristic that has been appreciated in the transient effects found previously.

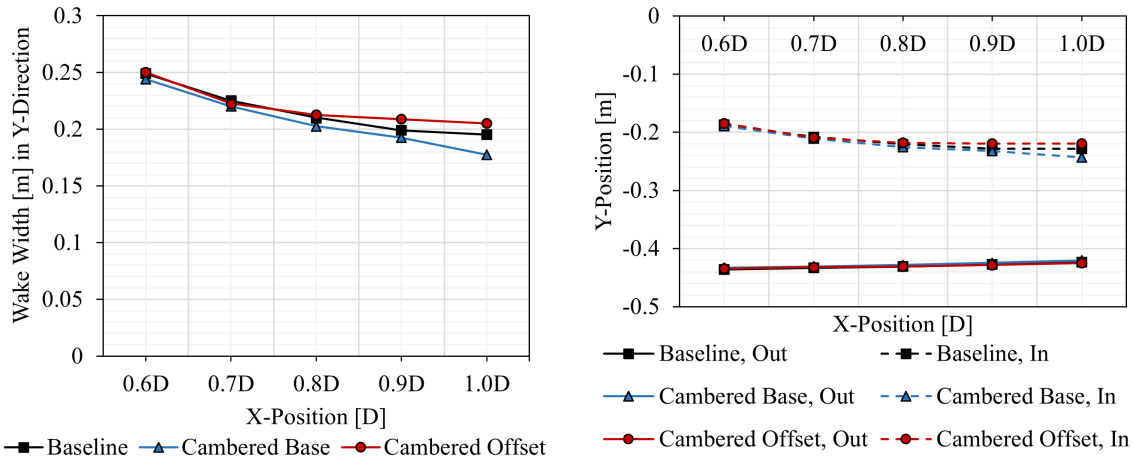


(a) Overall wake width.

(b) Wake limits: inboard and outboard.

**Figure 14.24:** Wake width development for cambered shape.

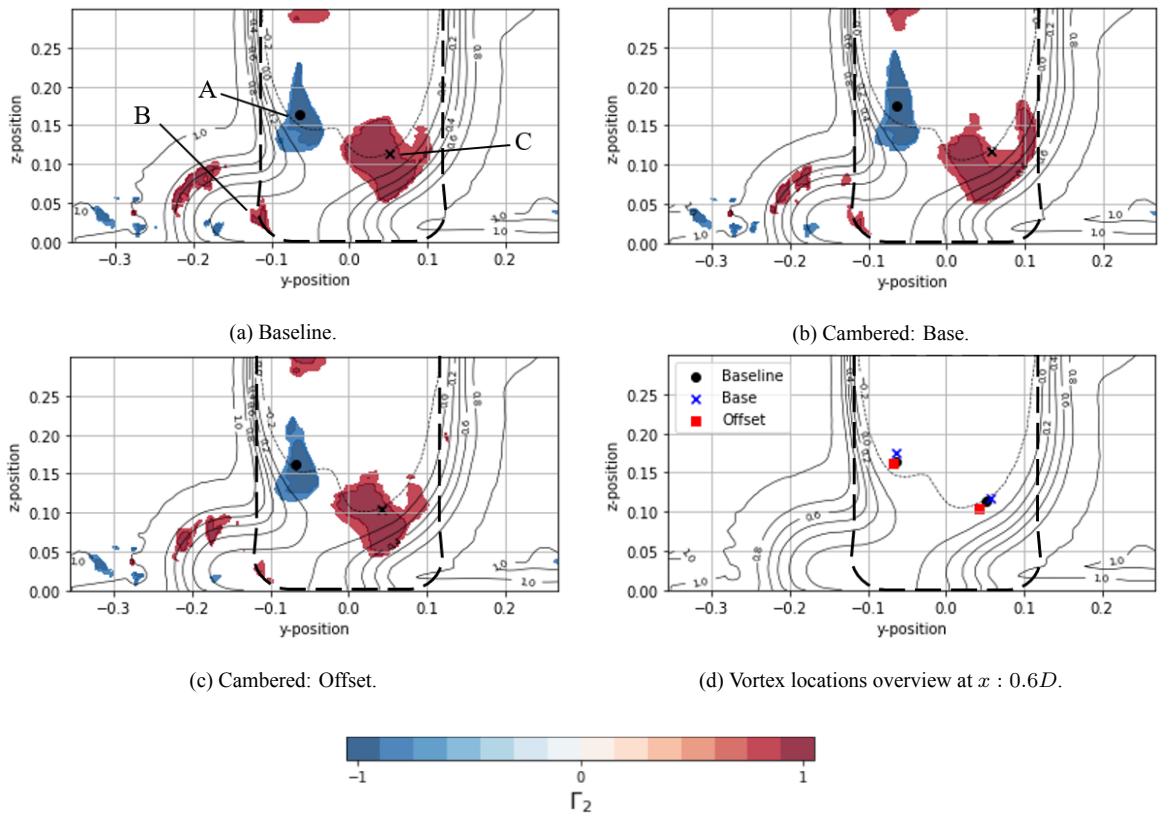


(a) Baseline.

(b) Cambered: Base.

(c) Cambered: Offset.

(d) Vortex locations overview at $x : 0.6D$.




**Figure 14.25:** $\Gamma_2$ flow topologies for cambered shape tests and their respective identified vortex centre positions.

## 14.3.9. H-Shaped Contact Patch

As Figure 14.26 shows, the base and the offset of the H-Shape contact patch shape produce opposite trends early in the wake. While in the early wake the width differences focus on the outboard part for the offset test, as they originate from the inboard part in the base case, further downstream the inboard contributions grow for the offset case. This seems associated with the vortex core split observed for vortex C in Figure 14.27 (c). The trend for the offset presents a strong similarity with the *R + L: Sharp* test, since both have a sharper corner curvature than their respective baselines.

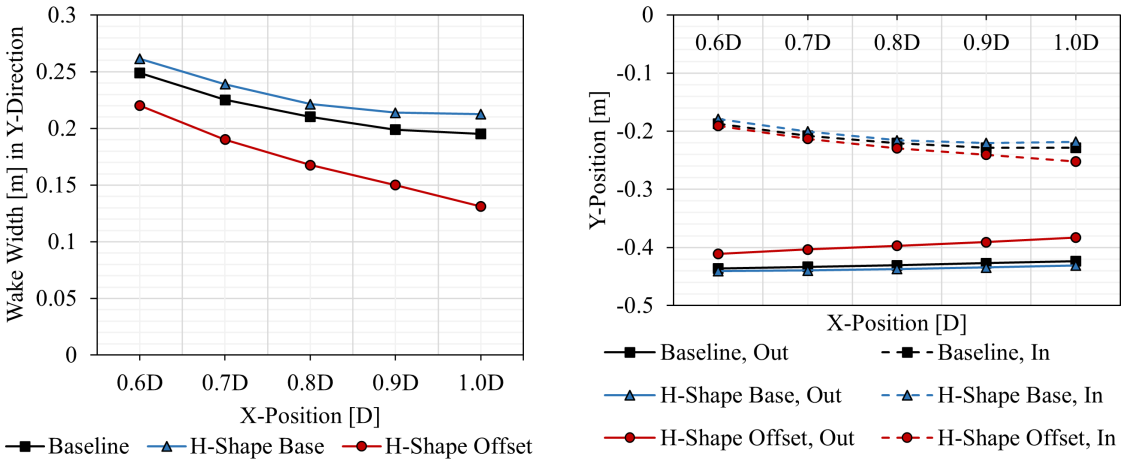


(a) Overall wake width.

(b) Wake limits: inboard and outboard.

**Figure 14.26:** Wake width development for H-shape.

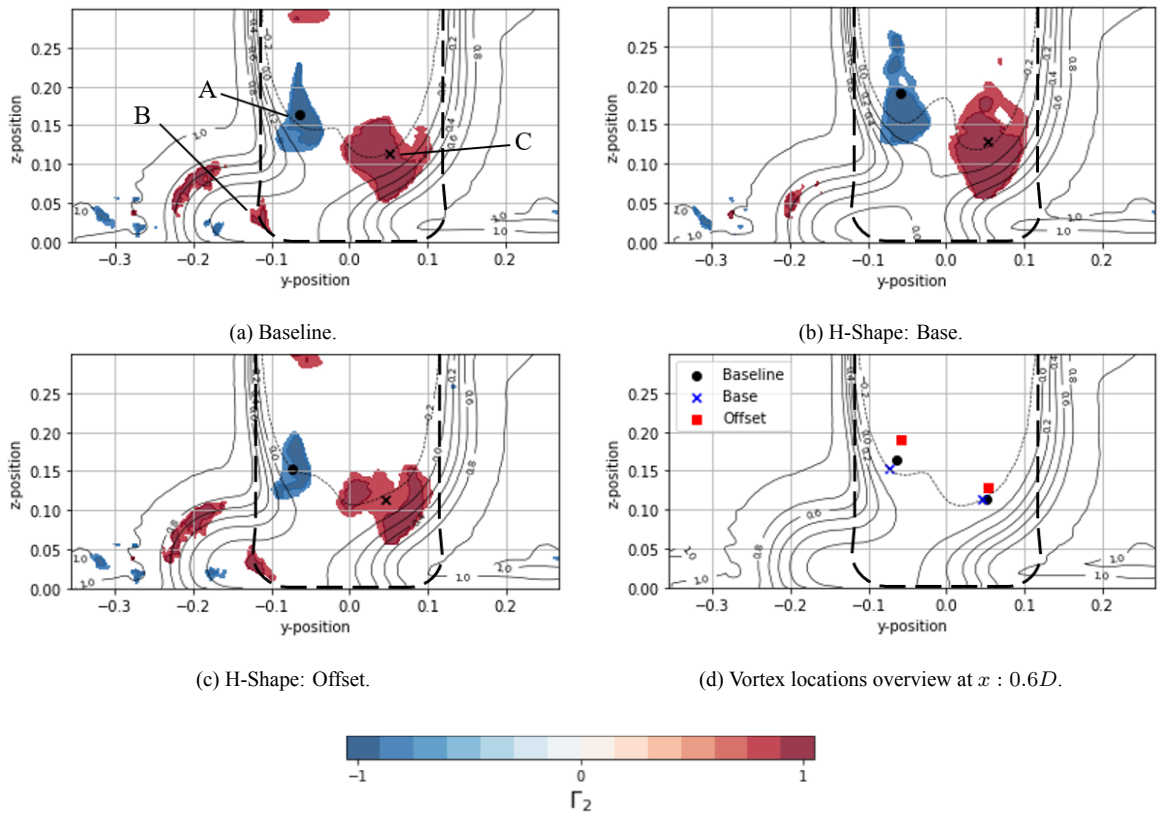


(a) Baseline.

(b) H-Shape: Base.

(c) H-Shape: Offset.

(d) Vortex locations overview at $x : 0.6D$.




**Figure 14.27:** $\Gamma_2$ flow topologies for H-shape tests and their respective identified vortex centre positions.

## 14.4. Wake Transient Behaviour

As highlighted in the previous sections, the vortex core split that occurs in vortex C for certain tests suggests that a drastic change in the transient behaviour of the vortices that are defined within the region of vortex C in the 3-second average. The current section includes a series of continuous frames taken from an averaging period of $1/8^{th}$ of a revolution for the two different wake behaviour types: expansion and contraction, just as it was performed for the Baseline case in Section 10.1.7. Here the aim is to study the differences in the transient behaviour that result in the topology variations observed in the full average results. Although it is difficult to obtain a full picture of the transient behaviour with only six frames in a very short period of time, some behaviour trends can still be extracted.

An analysis of the wake expansion behaviour found in the $\beta : 12.6$ *deg* case is given in Figure 14.28. While observing the vortices scattered in Region Vortex 1, which then becomes vortex A, shows a continuous presence over most frames, it can be seen that for Region Vortex 2 a pattern where several regions of strong vorticity is found to alternate across frames: at $t = 1.505$ seconds, several vortices composing Region 2 are visible, which then become one large vortex core at $t = 1.512$ seconds; subsequently, at $t = 1.519$ seconds, this region loses coherence again and the vortices scatter; in the next instance ($t = 1.526$ seconds), three vortices gain strength; at $t = 1.533$ seconds two strong vortex cores are present in this region, while finally at $t = 1.539$ seconds the vortices become more scattered.

It is then this alternating presence of multiple vortex cores in the region composing vortex C (Region Vortex 2) that over time shows the two cores in the full average results, contrasting with the transient behaviour studied for the Baseline deformation in Section 10.1.7, where although scattering of vortices in this region also was observed, the presence of a centralised strong vortex core was more consistent over the same time instances.

The other behaviour discussed in the previous section, which refers to the wake contraction behaviour found in deformations such as *B: +5mm*, is shown in Figure 14.29 for the same time instances as in the wake contraction case. Here, it can be observed that Region Vortex 1 and 2 are more consistently coherent in time, where they seem to be in equilibrium, in contrast to the more scattered and imbalanced vortex regions given by $\beta : 12.6$ *deg*.

It then seems that the upward trajectory that characterised these vortex regions in the 3-second average analysis is the presence of vertical coherence, such as the one visible at $t = 1.526$ seconds. Furthermore, Vortex Regions 3 and 4 are more pronounced and stable.

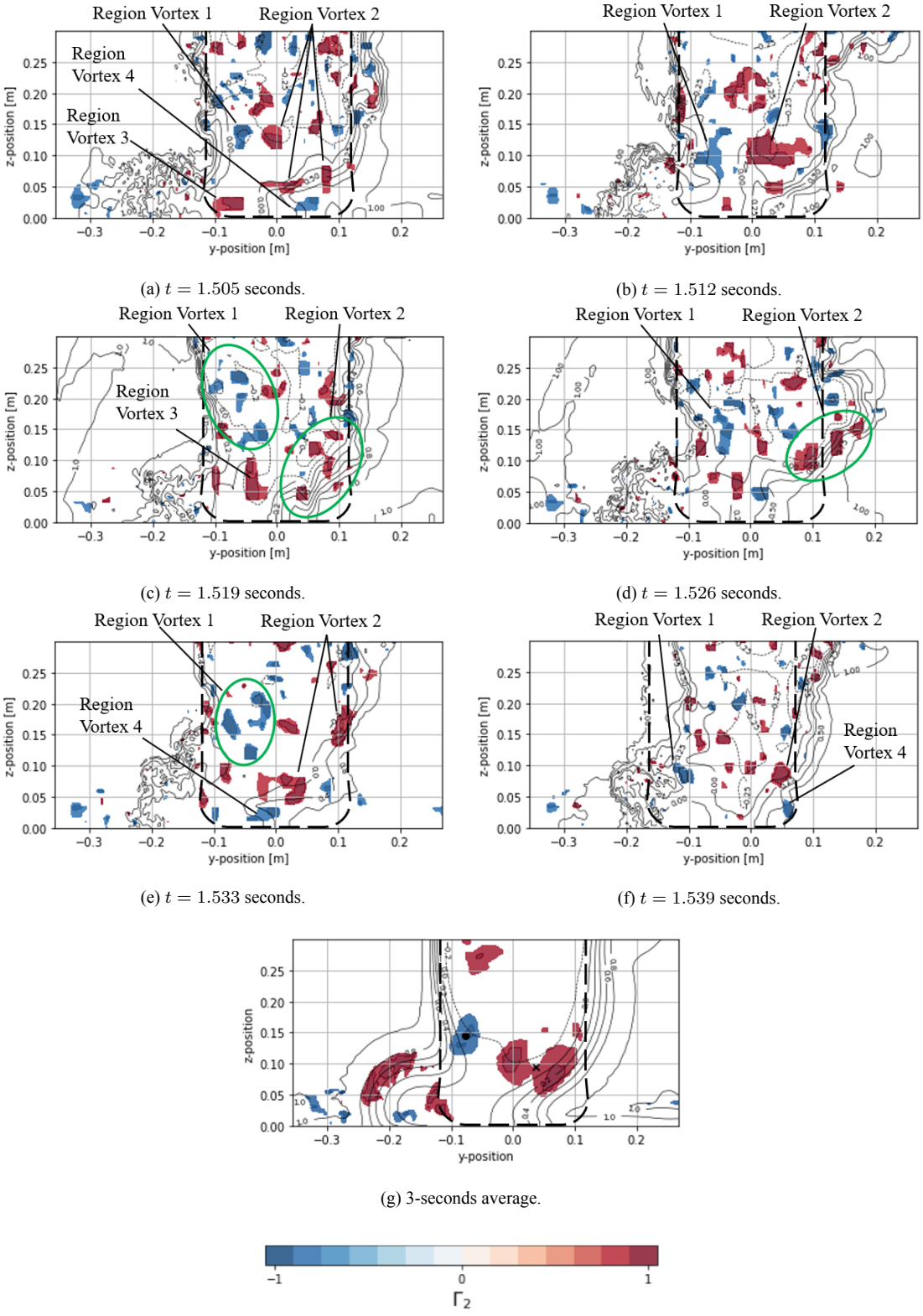


(a) $t = 1.505$ seconds.

(b) $t = 1.512$ seconds.

(c) $t = 1.519$ seconds.

(d) $t = 1.526$ seconds.

(e) $t = 1.533$ seconds.

(f) $t = 1.539$ seconds.

(g) 3-seconds average.




**Figure 14.28:** Transient $\Gamma_2$ plots for the various instances of taken from averages of $1/8^{th}$ of a revolution for the $\beta : 12.6deg$ test.

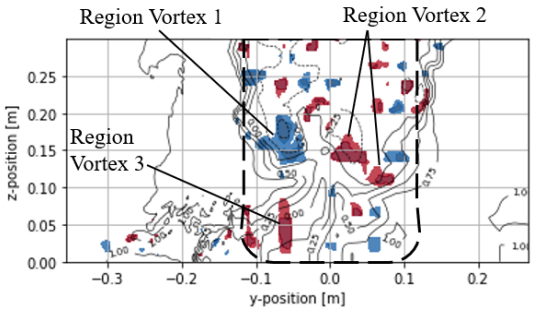


(a) $t = 1.505$ seconds.

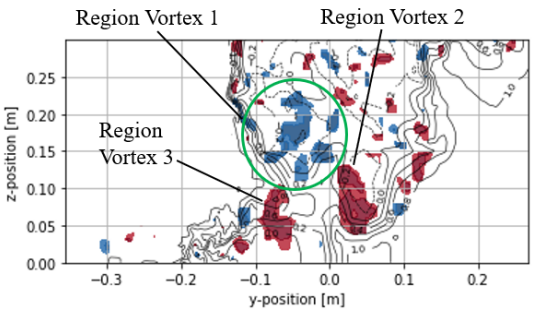


(b) $t = 1.512$ seconds.

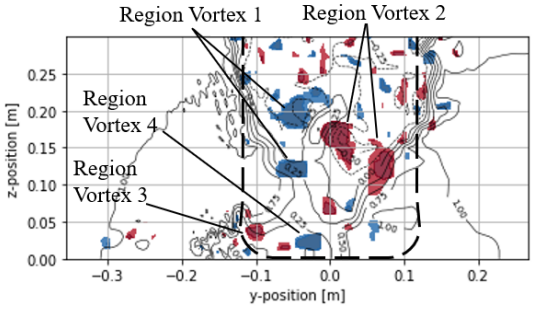


(c) $t = 1.519$ seconds.

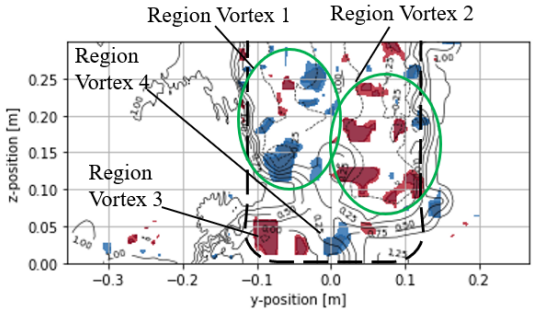


(d) $t = 1.526$ seconds.

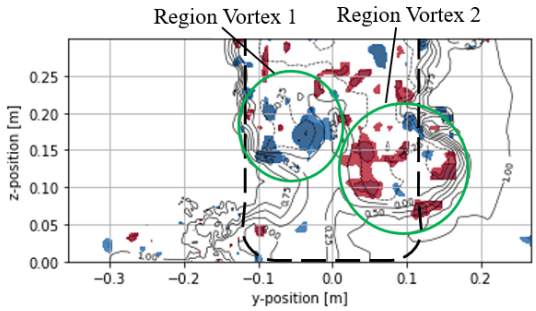


(e) $t = 1.533$ seconds.

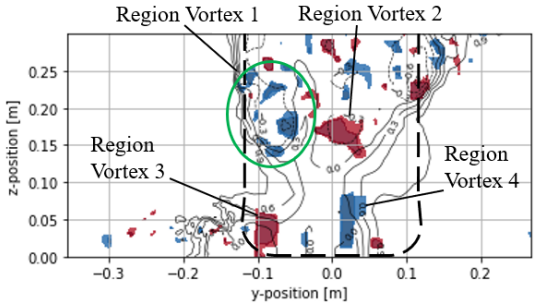


(f) $t = 1.539$ seconds.

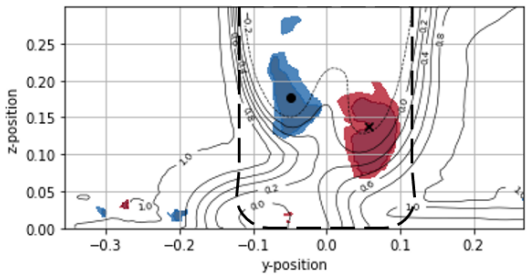


(g) 3-seconds average.

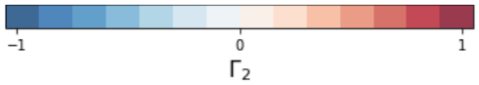


**Figure 14.29:** Transient $\Gamma_2$ plots for the various instances of taken from averages of $1/8^{th}$ of a revolution for the *B: +5mm* test.

## 14.5. Wake Downstream Development

The results presented from section 14.3.1 to 14.3.9 above showed that for some cases, considerable wake contractions and expansions were built up downstream in the wake. This case shows at its clearest for the Contact Patch

Width and Contact Patch Width Curvature tests. Therefore, a study of the evolution of relevant vortices at downstream locations in the wake is necessary to understand how the wake width differences occur. The pronounced displacements of the vortex cores across total pressure envelopes meant that the total pressure filters defined in Chapter 13 were removed from the vortex centre identification algorithm.

Table 14.1 shows the evolution of the wake from $x : 0.6D$ to $x : 1.0D$ for the Contact Patch Width tests, where on the top row an overview of the centres of vortex A and C can be found, with the $\Gamma_2$ flow topology for the different $x$-locations provided in the 5 lower rows. From the vortex position overview, two main conclusions can be drawn: vortex A presents a general displacement trend upwards, with some discrepancies in the pace of this upwards movement across tests; vortex C experiences a pronounced outwards displacement (towards the left of the domain) for *W: + 8.4 mm*, while for the Baseline case and *W: + 4.6 mm* it remains more static downstream.

On a qualitative level, some differences in the topology can also be found, where vortex C becomes a scatter of vortices from $x : 0.9D$ for *W: + 8.4 mm*, while it remains a well defined single core for the other two cases. Furthermore, vortex A experiences a more rapid upwards travel for *W: + 8.4 mm*, as it disappears from the visualisation domain in $x : 0.9D$, while for the other two cases this occurs in $x : 1.0D$. It can then be concluded that it is the transient behaviour differences of vortex C that result in a more turbulent wake evolution, giving it its increased thickness downstream.

Table 14.2 includes the same plot layout described for Table 14.1 for the Contact Patch Width Curvature (*R + W*) tests. Here, the same overall behaviour is displayed, where vortex A travels upwards, while vortex C tends to travel outwards. The vortex position overview in the first row shows that making the corner curvature smoother presents a trend for an increased outwards displacement of vortex C, together with a more pronounced upwards displacement of vortex A. This observation is consistent with the behaviour described from Table 14.1. The $\Gamma_2$ flow topology displayed in the lower rows gives an indication of vortex C becoming a more turbulent region in the actual transient flow, hence explaining the increased wake width downstream, consistent with the findings described in the previous paragraph for the Contact Patch Width tests.

Finally, the wake contraction behaviour downstream in the wake is studied in Table 14.3, where both vortex B and C present an upward moving trajectory in the downstream locations. While this is clear for vortex B, for the case of vortex C this seems to be the effect of the merging of the vorticity region represented by vortex C with a vorticity region developed above it. This merging is not achieved in the Baseline case, resulting in the more apparently static behaviour of vortex C in this case.

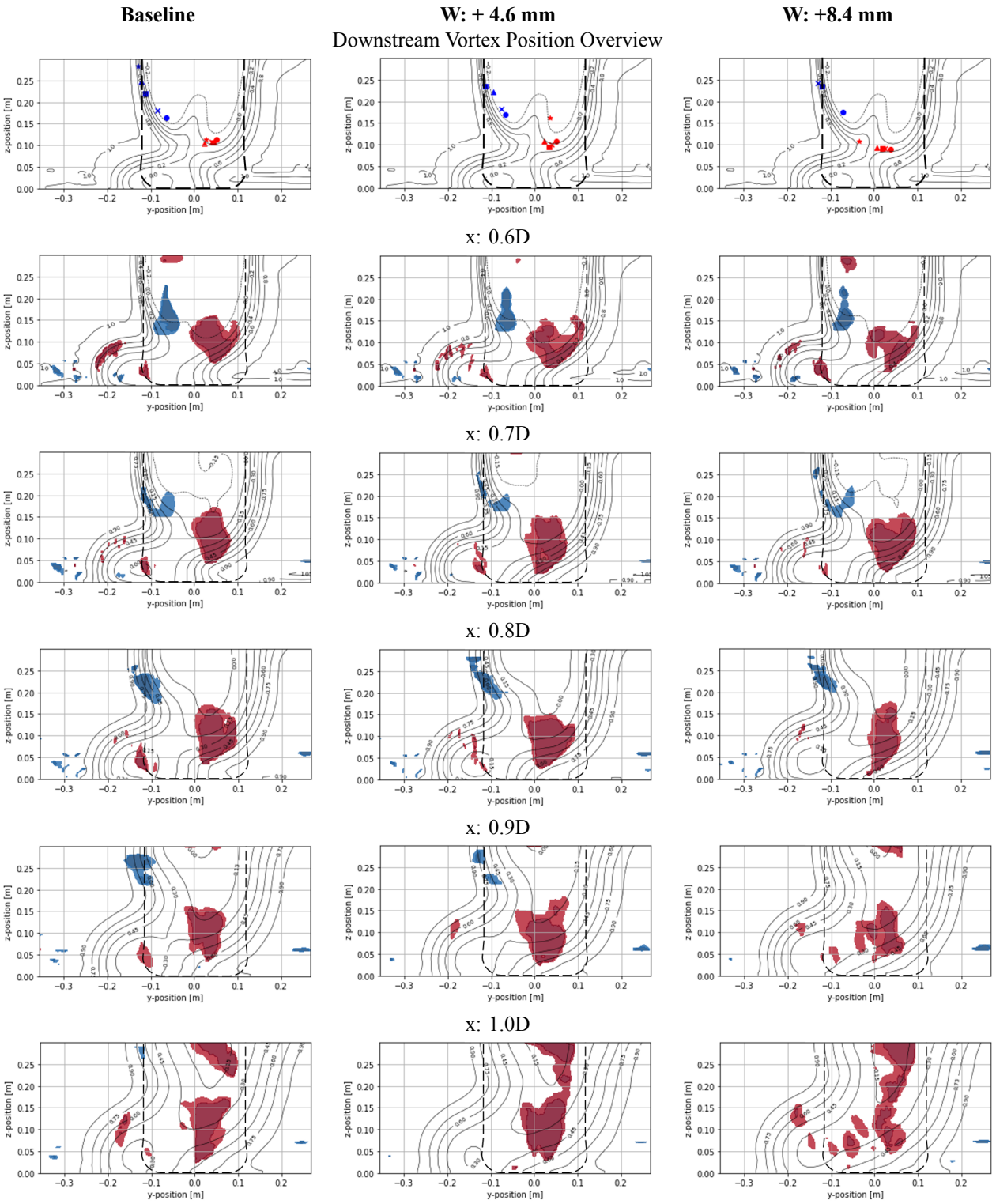


**Table 14.1:** Wake Development for Contact Patch Width tests. Top: overview of vortex positions in downstream locations; Legend: blue refers to vortex A, red refers to vortex C; circle: $x : 0.6D$, cross: $x : 0.7D$, square: $x : 0.8D$, triangle: $x : 0.9D$, and star: $x : 1.0D$. Lower rows show $\Gamma_2$ topology at the different $x$-locations.

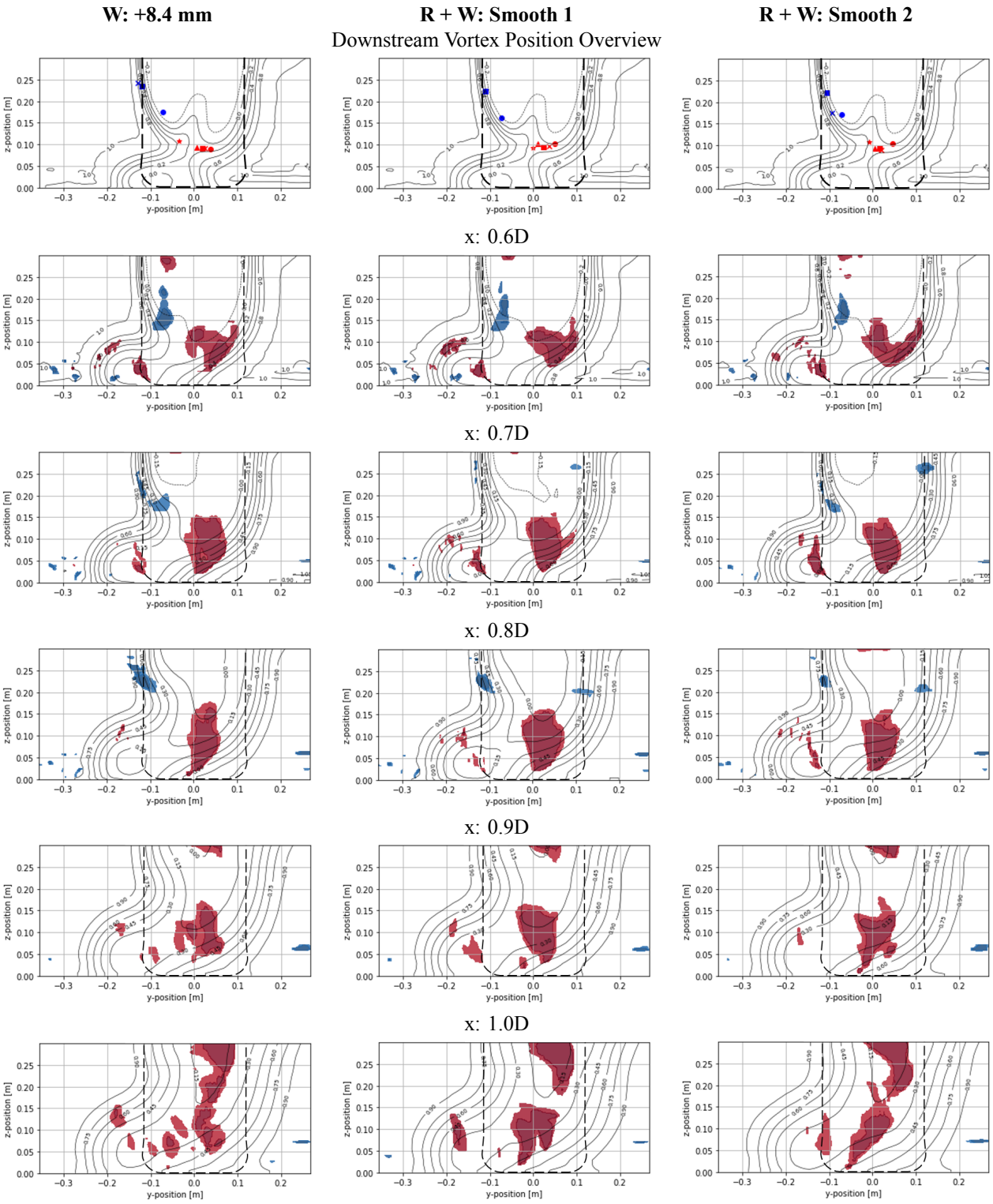


**Table 14.2:** Wake Development for Contact Patch Width Curvature tests. Top: overview of vortex positions in downstream locations; Legend: blue refers to vortex A, red refers to vortex C; circle: $x : 0.6D$, cross: $x : 0.7D$, square: $x : 0.8D$, triangle: $x : 0.9D$, and star: $x : 1.0D$. Lower rows show $\Gamma_2$ topology at the different $x$-locations.

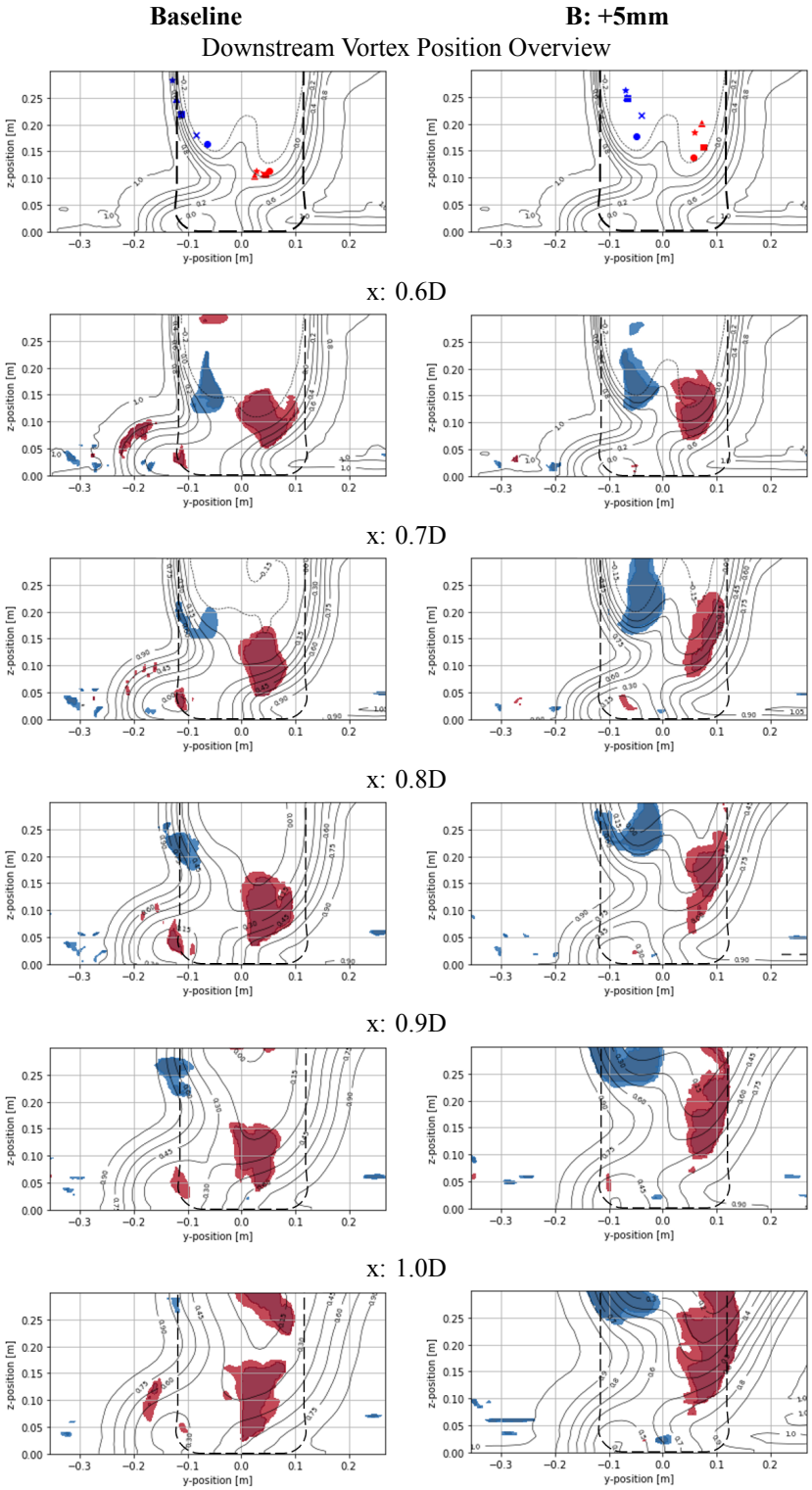


**Table 14.3:** Wake Development comparison for $B : +5$mm. Top: overview of vortex positions in downstream locations; Legend: blue refers to vortex A, red refers to vortex C; circle: $x : 0.6D$, cross: $x : 0.7D$, square: $x : 0.8D$, triangle: $x : 0.9D$, and star: $x : 1.0D$. Lower rows show $\Gamma_2$ topology at the different $x$-locations.

# 15

# Full Vehicle

## 15.1. Vehicle Forces

Comparing the drag coefficient of the standalone tire case with the full vehicle case, as is laid out in Figure 15.1, it can be observed that drag variation trends across deformations differ due to the presence of the vehicle, which as discussed in Section 2.2, results in a more oblique incident flow at the bottom, whit large differences on the top parts due to the area covered by the wheel-arch. Some examples of this can be found in the Bulge Size deformations, where for the standalone case, increasing the Bulge Size results in an increase in drag, while the opposite trend is produced in the full vehicle case (*DrivAer*).

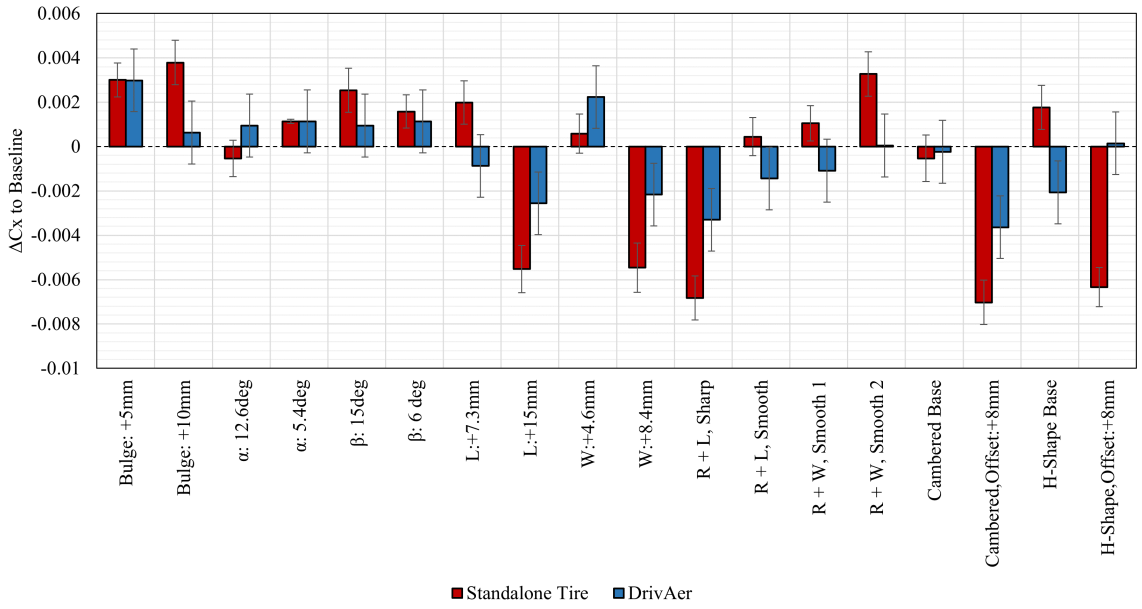


**Figure 15.1:** Standalone Tire $\Delta C_x$ compared with *DrivAer* $\Delta C_x$.

An approach to discern if the drag of the vehicle is related to interaction with the wake coming from the front axle or a local effect on the tire is by comparing the drag coefficient of the vehicle together with the drag coefficient of the front and rear axles, as is given in Figure 15.2. From this comparison, it is possible to separate the deformations whose impact on the vehicle's drag is due to the wake interaction and which may be due to changes locally on the pressure distribution around the tire. Keeping in mind that when both the front and the rear axle's $\Delta C_x$ build up to about the total variation of the *DrivAer*'s $\Delta C_x$, the drag changes can be attributed to local effects on the tire. On the other hand, when the drag generated by the front and rear axles do not add up to the *DrivAer*'s $\Delta C_x$ variation, the $C_x$ variations are then attributed to variations in the interaction with the wake coming from the

front axle. From Figure 15.2 it can be concluded that the parameters that show a more clear local effect are the Contact Patch Width *W*, the Contact Patch Curvature over Length *R* + *L* and the contact patch curvature over width *R* + *W*. The cases with more pronounced wake interaction are found for the Bulge Size *B* and Longitudinal Insertion Angle $\beta$, where the $\Delta C_x$ from the front and rear axle present large variations that do not show on the total variation of the *DrivAer*'s $\Delta C_x$. The remaining deformation parameters ($\alpha$, *L* and contact path shapes, Cambered and H-Shape) exhibit variations that are more difficult to classify, and suggest that more complex interactions are occurring.

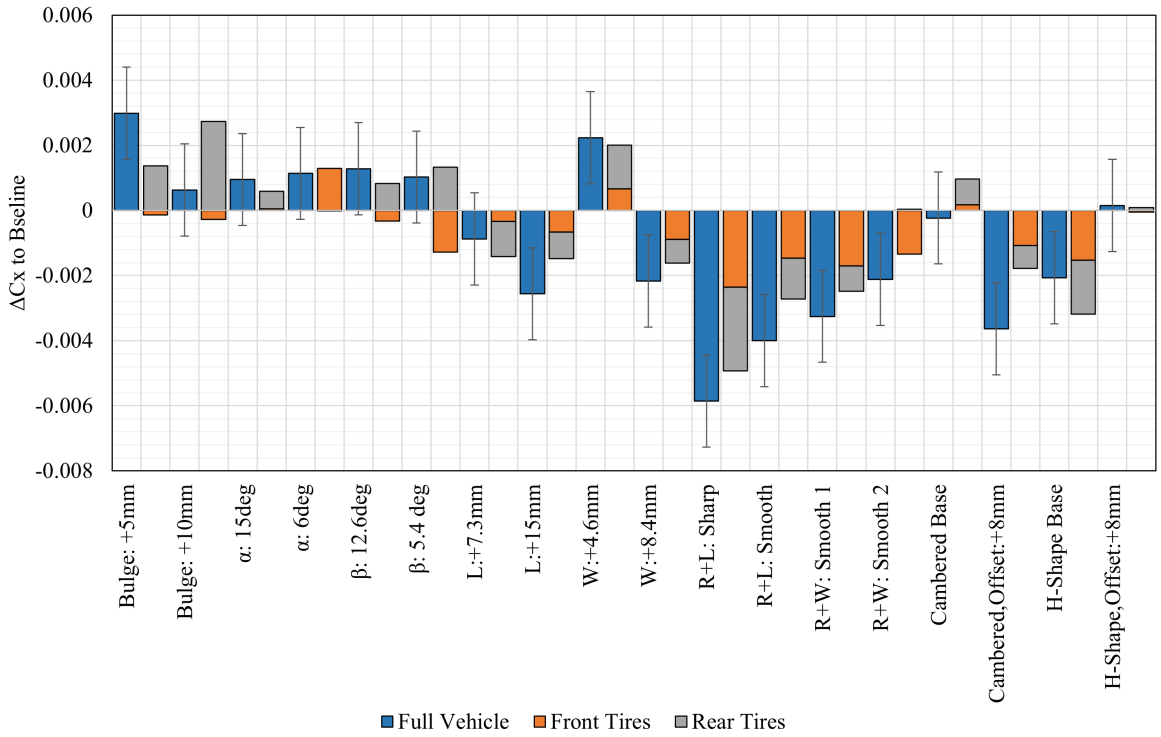


**Figure 15.2:** Full vehicle $\Delta C_x$ compared to Front Axle and Rear Axle $\Delta C_x$ to Baseline.

## 15.2. Vortex Behaviour Analysis

To confirm the trends discussed in Section 15.1, the analysis methodology implemented for the standalone tire case is also used for the *DrivAer*. In this occasion, only two deformation cases are chosen for study based on the two different trends observed in Figure 15.2, where the Bulge Size deformations show an effect of wake interaction, while curvature studies show a local effect trend.

### 15.2.1. Bulge Size

Differences in the wake for Bulge Size tests become evident looking at Figure 15.3, where increasing the Bulge Size results in a linear trend of the wake becoming narrower due to effects in the flow field on the outboard part of the wake. Looking at the variations of vortices B and C in Figure 15.4, as identified in Section 12, a trend can be appreciated where vortex C moves upwards as the Bulge Size increases, while vortex B tends to move outwards. these variations do not seem to affect the wake width, since the changes seem to be predominantly driven by the turbulent region on the bottom left corner of the tire, although an interaction between the highly turbulent region and the displacement of vortices B and C may exist. In any case, these variations of the vortex positions area strong indicator that 3D flow presents large variations for bulge deformations.

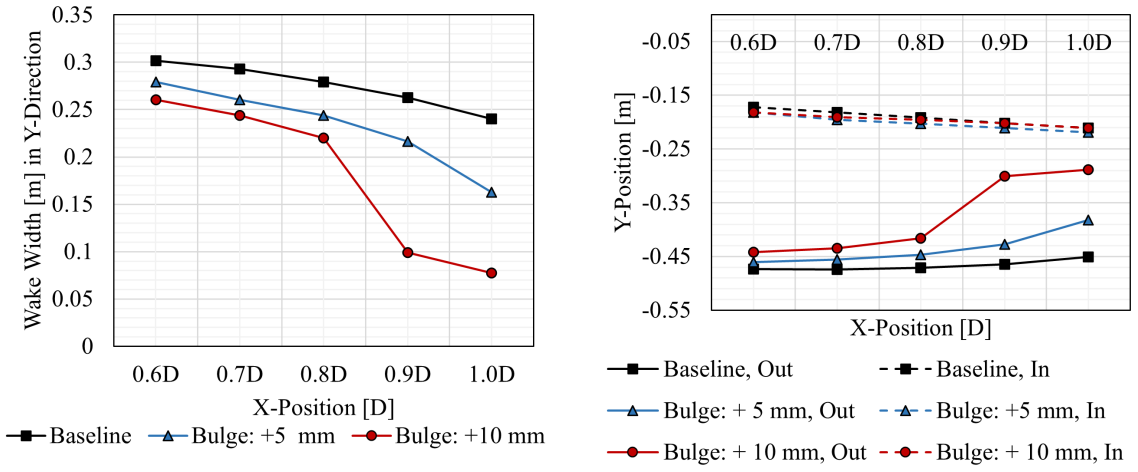


(a) Overall wake width.

(b) Wake limits: inboard and outboard.

**Figure 15.3:** Wake width development for $B$.

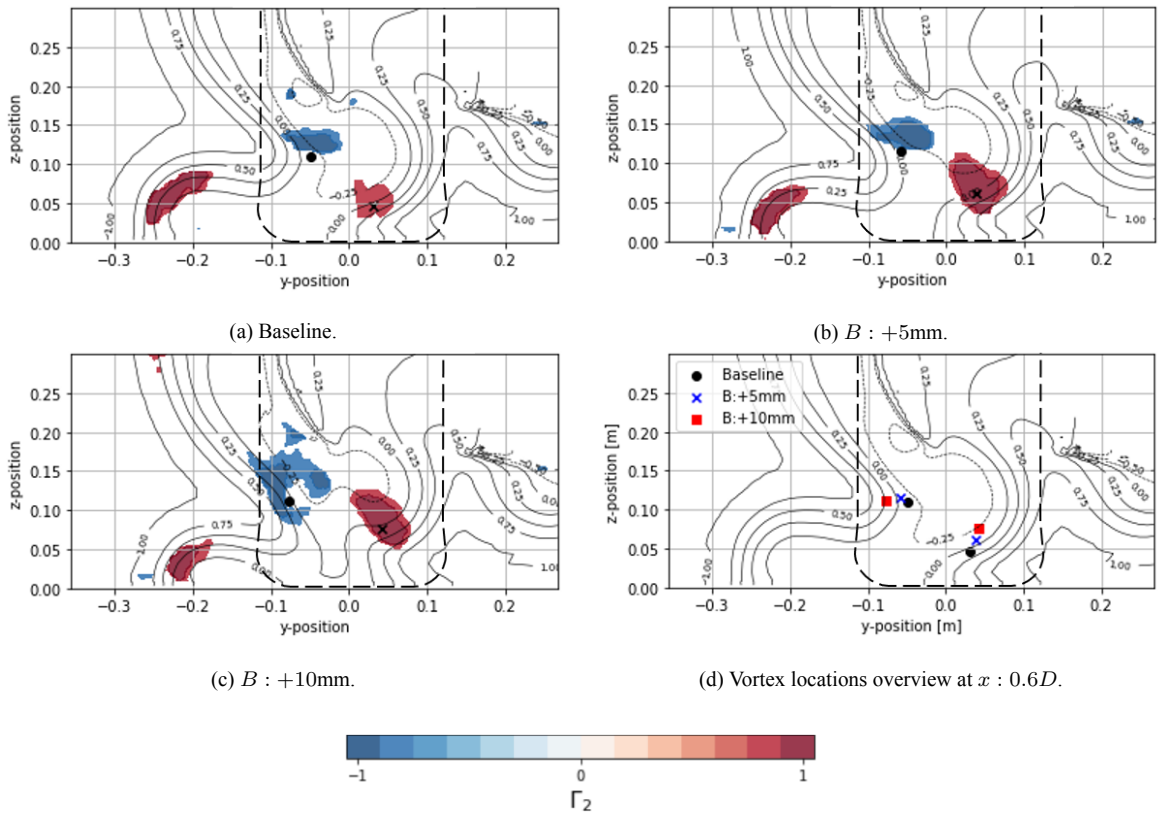


(a) Baseline.

(b) $B$ : +5mm.

(c) $B$ : +10mm.

(d) Vortex locations overview at $x$ : $0.6D$.

**Figure 15.4:** $\Gamma_2$ flow topologies for $B$ tests and their respective identified vortex centre positions.

## 15.2.2. Contact Patch Length Curvature

The $R$ + $L$ deformations were classified in the trend of drag coefficient varying due to local effects on the tire due to pressure distribution changes on the surface caused by the contact patch deformations, and no involvement from wake interaction. Figure 15.5 shows insignificant variations in the wake as a result of changes of the corner curvature at the contact patch, hence confirming that, since no wake variations are produced, no changes in the wake interactions seem to be involved in the drag coefficient variations resulting from these tests. The lack of changes of wake width is confirmed by the no quantified displacement of vortices B and C, visible in Figure 15.6.

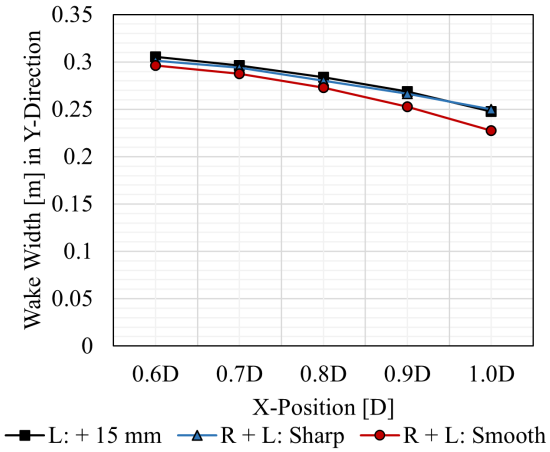


(a) Overall wake width.

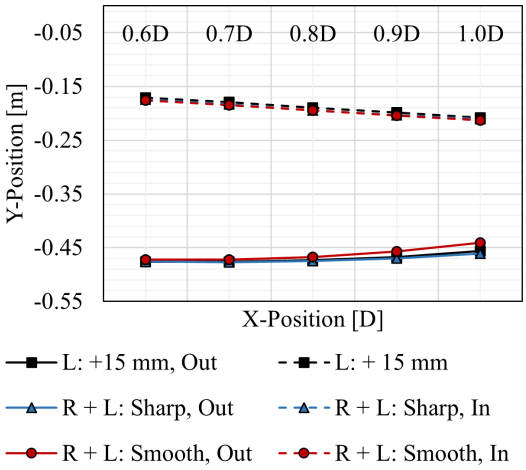


(b) Wake limits: inboard and outboard.

**Figure 15.5:** Wake width development for $R + L$.

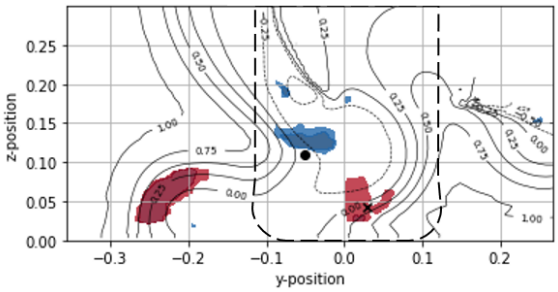


(a) Baseline.

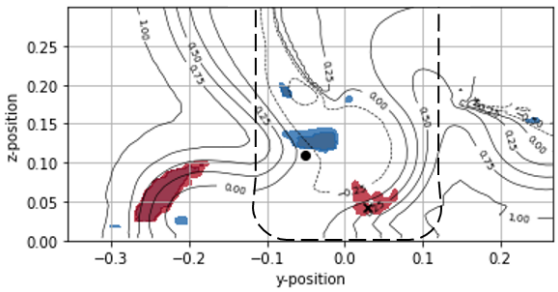


(b) $R + L : Sharp$.

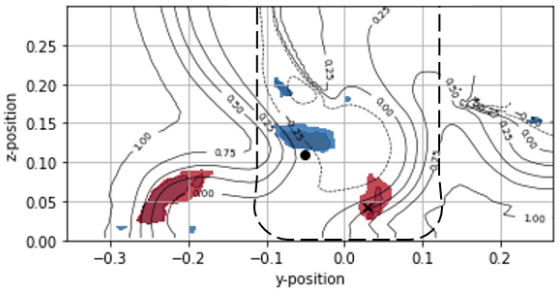


(c) $R + L : Smooth$.

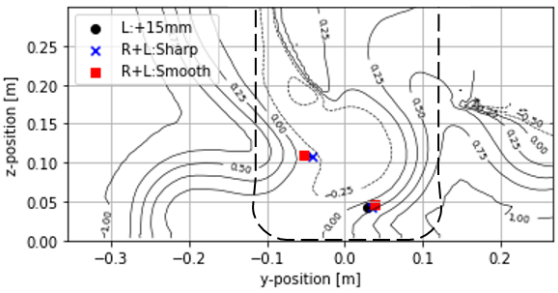


(d) Vortex locations overview at $x : 0.6D$.

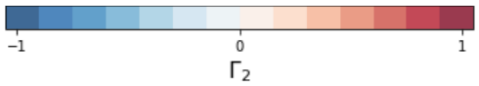


**Figure 15.6:** $\Gamma_2$ flow topologies for $R + L$ tests and their respective identified vortex centre positions.

# Part IV

# Conclusions

The work performed in this project has been directed to methodically investigate the aerodynamic impact of parametric tire deformations in a standalone tire case and a full vehicle case. The primary objective was to identify the deformation parameters with the highest impact in drag coefficient and wake variations. To carry out this investigation, an analysis methodology was developed with the aim of quantifying flow variations in the wake and identifying the flow features involved. Given the unsteady behaviour of the tire wake, a study of the transient behaviour of the wake was required to understand how the changes captured in the averaged results were representing changes in the transient behaviour of the wake.

## 15.3. Research Questions

### 15.3.1. What are the most influential deformation parameters?

The overview of drag coefficient variations for the standalone tire case and the full vehicle case already show that the Bulge Size deformation and Sharp Corner Curvatures are the most influential parameters in terms of force coefficients, as the Bulge Size produces the largest increase in drag coefficient, while the Sharp Contact Patch Curvatures, also present on the contact patch shape offsets, produce the most significant drag coefficient reduction.

In the the analysis of vortex behaviour and wake development, the deformation parameters that showed the strongest influence on the wake development as a result of changes in the transient behaviour of the flow caused by the deformation were the Bulge Size, sharp curvatures, Longitudinal Insertion Angle and the Contact Patch Width.

### 15.3.2. What are the flow features produced by the tire in the proposed tests and how do they relate to the deformation parameters tested?

An initial qualitative analysis showed that non-linear behaviours for each deformation parameter test could occur, hence emphasising the need for complex analysis methodologies in order to understand how the flow features around the tire influence the wake development and how they relate to the deformation parameters. With the first approach being a statistical method in Principal Components Analysis, it was found that, although the measurements used as input data for the eigen-decomposition showed certain correlation with the Microdrag in the far wake of the standalone tire, the PCA approach failed to classify the measurements and deformations in the different ways that the wake can develop depending on the flow features related to the different deformations.

The second approach was based on studying the vortex behaviour in the wake and correlating with the wake width development. This method proved more useful in classifying the deformations and how they affect the flow field, as well as showing that the relevant flow features were identified as regions of vorticity representing the horseshoe trailing vortices of the wake, as well as the highly turbulent region at the outside part of the bottom of the wake, which were the areas where changes originated for the deformations with the largest influence on the wake, identified in the previous section as: Bulge Size, sharp curvatures, Longitudinal Insertion angle and the Contact Patch Width.

### 15.3.3. How do the identified and quantified flow features influence the wake development?

The analysis in the second approach then coupled the identified flow features and their influence in the wake development, where tighter wakes relate to more coherent vorticity regions, which in the averaged data showed as a stronger vortex core, while thicker wakes are strongly linked to a phenomenon where, in the full averaged results, the inboard vortex core C would split into two cores, resulting in a thicker wake. These behaviors were classified as wake contraction behaviour, and wake expansion behaviour respectively. The transient analysis of this behaviour gave a small insight that showed a relation with an increased vorticity region coherence (for the wake contraction behaviour) and increased unsteadiness of the vorticity (for the wake expansion behaviour) in the inboard region. The parameters related with the wake contraction effect were Bulge Size and sharp curvatures. The wake expansion effect was found for parameters such as the Longitudinal Insertion Angle and the contact patch width, although it was found to be more pronounced in the width case downstream in the wake, while for the Longitudinal Insertion Angle case, wake width differences were already appreciated in the early wake. For the more pronounced cases, further investigation into the wake development downstream was carried out, where it was concluded that the increased small-scale turbulence would result in an expanding wake downstream of the tire, in contrast to the less turbulent wake observed in the wake contraction case.

### 15.3.4. How does the wake development relate to the drag coefficient variations?

A correlation between the wake development changes and the drag was not found for the standalone tire case with the regions of the wake analysed, as the PCA results showed. The statistical approach did not show a correlation between wake variations and the drag of the standalone tire. The presence of wake development variations presented a stronger influence on the changes in drag coefficient in the full vehicle case, since these wake variations introduce a complex interaction with the rest of the vehicle. In the context of a full vehicle, the results showed that the drag variations can be classified into three main groups: those generated by clear local effects on the tires, those generated by clear wake interactions with the rest of the vehicle, and those were a more complex interaction seems to take place. Analysis of the vortex behaviour and wake width development confirmed that bulge deformations are responsible for drag coefficient variations caused by pronounced interactions with the wake, while contact patch deformations were linked to local drag variations on the tire. However, it is worth noting that certain parameters presented complex wake interactions both for bulge and contact patch deformations. It then follows that the effect of deformations on the wake differed from the standalone tire case to the full vehicle case.

## 15.4. Recommendations for future work

Finally, some open topics derived from the work carried out in this thesis are outlined for possible future work on the current subject. Firstly, further adjustments can be done on the PCA approach, where by introducing measurements of variables on the tire surface, such as pressure, velocity or skin friction, could improve the correlation of the data with the drag coefficient variations. Secondly, it has been observed that the wake development variations are strongly linked to variations in the transient behaviour of the vortices generated by the tire due to deformation changes. However, with the difficulties outlined on the transient behaviour analysis, alternative ways of studying the transient nature of the tire wake are proposed, with them being Proper Orthogonal Decomposition (POD), or Dynamic Mode Decomposition (DMD). These methodologies offer ways of studying oscillatory behaviours of the wake, where the flow behaviour can be decomposed in modes, hence enabling a simplification of a complex flow field, such as that of the tire wake. Lastly, in the full vehicle case, the existence of a relation between certain deformation parameters and the interaction of the tire wake with the rest of the vehicle, affecting its drag coefficient, have been identified. However, these interactions are complex and require deeper analysis specific to automotive aerodynamics to be fully understood.

# References


[1] Sept. 2017. URL: https://www.wltpfacts.eu/.

[2] H. Berg and A. Brandt. “Investigation of Aerodynamic Wheel Design”. PhD thesis. Department of Mechanics and Maritime Sciences, 2018.

[3] H. Bézard and T. Daris. “Calibrating the length scale equation with an explicit algebraic Reynolds stress constitutive relation”. In: *Engineering Turbulence Modelling and Experiments 6* (2005), pp. 77–86. DOI: 10.1016/b978-008044544-1/50006-6.

[4] P. L. Bhatnagar, E. P. Gross, and M. Krook. “A model for collision processes in gases. I. Small amplitude processes in charged and neutral one-component systems”. In: *Physical Review* 94.3 (May 1954), pp. 511–525. DOI: 10.1103/physrev.94.511.

[5] S. L. Brunton and J. N. Kutz. *Data-Driven Science and Engineering: Machine Learning, Dynamical Systems, and Control*. Cambridge University Press, 2022.

[6] H. Chen. “Volumetric formulation of the lattice Boltzmann method for fluid dynamics: Basic concept”. In: *Physical Review E* 58.3 (1998), pp. 3955–3963. DOI: 10.1103/physreve.58.3955.

[7] H. Chen et al. “Expanded analogy between Boltzmann kinetic theory of fluids and turbulence”. In: *Journal of Fluid Mechanics* 519 (2004), pp. 301–314. DOI: 10.1017/s0022112004001211.

[8] H. Chen et al. “Extended boltzmann kinetic equation for turbulent flows”. In: *Science* 301.5633 (2003), pp. 633–636. DOI: 10.1126/science.1085048.

[9] Hudong Chen, Chris Teixeira, and Kim Molvig. “Digital Physics Approach to computational fluid dynamics: Some basic theoretical features”. In: *International Journal of Modern Physics C* 08.04 (Aug. 1997), pp. 675–684. DOI: 10.1142/s0129183197000576.

[10] Hudong Chen, Chris Teixeira, and Kim Molvig. “Realization of fluid boundary conditions via discrete boltzmann dynamics”. In: *International Journal of Modern Physics C* 09.08 (Dec. 1998), pp. 1281–1292. DOI: 10.1142/s0129183198001151.

[11] A. Cogotti. In: *Generation of a Controlled Turbulent Flow in an Automobile Wind Tunnel and its Effect on Car Aerodynamics and Acoustics* ().

[12] A. Cogotti. “A strategy for optimum surveys of passenger-car flow fields”. In: *SAE Technical Paper Series* (1989). DOI: 10.4271/890374.

[13] A. Cogotti. “Aerodynamic Characteristics of Car Wheels”. In: *International Journal of Vehicle Design, SP3, Impact of Aerodynamics on Vehicle Design* (1983), pp. 173–196.

[14] A. Cogotti. “Flow-field surveys behind three Squareback car models using a new “fourteen-hole” probe”. In: *SAE Technical Paper Series* (1987). DOI: 10.4271/870243.

[15] A. Cogotti. “XXIII FISITA Congress”. In: *Paper 905149*. 1990.

[16] M. Coletta et al. “13th International Symposium on Particle Image Velocimetry - ISPIV 2019”. In: 2019.

[17] E. Croner et al. “Aerodynamic characterization of the wake of an isolated rolling wheel”. In: *International Journal of Heat and Fluid Flow* 43 (2013), pp. 233–243. DOI: 10.1016/j.ijheatfluidflow.2013.04.008.

[18] E. Croner et al. “Conference on Modelling Fluid Flow (CMFF’12)”. In: *The 15th International Conference on Fluid Flow Technologies*. 2012.

[19] F. De Gregorio and A. Visingardi. “Vortex Detection Criteria Assessment for PIV data in Rotorcraft Applications”. In: *Experiments in Fluids* 61.8 (2020). DOI: 10.1007/s00348-020-03012-7.

[20] S. Diasinos, T. J. Barber, and G. Doig. “The effects of simplifications on isolated wheel aerodynamics”. In: *Journal of Wind Engineering and Industrial Aerodynamics* 146 (2015), pp. 90–101. DOI: 10.1016/j.jweia.2015.08.004.

[21] B. D. Duncan et al. “Further CFD studies for detailed tires using aerodynamics simulation with Rolling Road Conditions”. In: *SAE Technical Paper Series* (2010). DOI: 10.4271/2010-01-0756.

[22] Bradley D. Duncan, Axel Fischer, and Satheesh Kandasamy. “Validation of lattice-boltzmann aerodynamics simulation for vehicle lift prediction”. In: *ASME 2010 3rd Joint US-European Fluids Engineering Summer Meeting: Volume 1, Symposia – Parts A, B, and C* (Jan. 2010), pp. 2705–2716. DOI: 10.1115/fedsm-icnmm2010-30891.

[23] J. E. Fackrell. PhD thesis. Imperial College London (University of London), 1972.

[24] J. E. Fackrell and J. K. Harvey. “Advances in Road Vehicle Aerodynamics”. In: 1973.

[25] J. E. Fackrell and J. K. Harvey. “AIAA”. In: *2nd Symposium on Aerodynamic of Sport and Competition Automobiles*. 1975.

[26] L. Graftieaux, M. Michard, and N. Grosjean. “Combining piv, pod and Vortex Identification Algorithms for the study of unsteady turbulent swirling flows”. In: *Measurement Science and Technology* 12.9 (2001). DOI: 10.1088/0957-0233/12/9/307.

[27] T. Hobeika and S. Sebben. “Tyre pattern features and their effects on Passenger Vehicle Drag”. In: *SAE International Journal of Passenger Cars - Mechanical Systems* 11.5 (2018), pp. 401–413. DOI: 10.4271/2018-01-0710.

[28] Teddy Hobeika and Simone Sebben. “CFD investigation on Wheel Rotation Modelling”. In: *Journal of Wind Engineering and Industrial Aerodynamics* 174 (Mar. 2018), pp. 241–251. DOI: 10.1016/j.jweia.2018.01.005.

[29] J .C.R. Hunt, A.A. Wray, and P Moin. “Eddies, Streams, and Convergence Zones in Turbulent Flows”. In: *Center for Turbulence Research Report* (1988). DOI: CTR-S88:193-208.

[30] E. Josefsson. PhD thesis. Department of Mechanics and Maritime Sciences, Chalmers University of Technology, 2022.

[31] E. Josefsson. *Methods for wheel roation modelling*. Ed. by H.Editor Nilsson. 2020.

[32] E. Josefsson, T. Hobeika, and S. Sebben. “Evaluation of wind tunnel interference on numerical prediction of Wheel Aerodynamics”. In: *Journal of Wind Engineering and Industrial Aerodynamics* 224 (2022), p. 104945. DOI: 10.1016/j.jweia.2022.104945.

[33] E. Josefsson, S. Sebben, and M. Urquhart. “Characterisation of the flow around passenger vehicle wheels with varying tyre profiles”. In: *International Journal of Heat and Fluid Flow* 103 (2023), p. 109191. DOI: 10.1016/j.ijheatfluidflow.2023.109191.

[34] H. W. Kuhn. “The Hungarian method for the assignment problem”. In: *Naval Research Logistics Quarterly* 2.1–2 (1955), pp. 83–97. DOI: 10.1002/nav.3800020109.

[35] C. Landström et al. “An Experimental Investigation of Wheel Design Parameters with Respect to Aerodynamic Drag. In: Progress in Vehice Aerodynamics and THermal Management”. In: 2011.

[36] C. Lew et al. “Aerodynamic simulation of a standalone rotating treaded tire”. In: *SAE Technical Paper Series* (2017). DOI: 10.4271/2017-01-1551.

[37] F. Liu et al. “Flow field description and simplification based on principal component analysis downscaling and clustering algorithms”. In: *Frontiers in Earth Science* 9 (2022). DOI: 10.3389/feart.2021.804617.

[38] Christopher D. Manning, Prabhakar Raghavan, and Hinrich Schuetze. *An introduction to information retrieval*. Cambridge University Press, 2022.

[39] E. Mercker and H. Berneburg. “Innovation and Reliability in Automotive Design and Testing”. In: *Lecture at the Third International Conference*. 1992.

[40] M. Michard et al. “Turbulent Shear Flows”. In: *11th Proceeding*.

[41] Charles Mockett, Frank H. Thiele, and Thilo Knacke. “8th International Symposium on Engineering Turbulence Modelling and Measurements - ETMM8”. In: 2010.

[42] F. Modlinger, R. Demuth, and N. Adams. “Investigations on the Realistic Modeling of the Flow around Wheels and Wheel Arches by CFD”. In: *JSAE* (2007). DOI: 20075195.

[43] F. Modlinger, R. Demuth, and N. Adams. “New Directions in the Optimization of the Flow around Wheels and Wheel Arches”. In: 2008.

[44] M. Mortazawy et al. “Aerodynamic simulation of a standalone round and deforming treaded tire”. In: *SAE International Journal of Advances and Current Practices in Mobility* 3.5 (2021), pp. 2227–2235. DOI: 10.4271/2021-01-0948.

[45] J. Munkers. “Algortihms for the assignment and transportaion problems”. In: *J Soc Ind Appl Math* (1957), 5:32–38.

[46] A. Parfett, H. Babinsky, and J. K. Harvey. “A Study of the Time-Resolved Structure of the Vortices Shed into the Wake of an Isolated F1 Car Wheel”. PhD thesis.

[47] C. S. Peskin. “The immersed boundary method”. PhD thesis. 2002.

[48] Miguel Pestana. “Effets d’un stator Hétérogène sur le bruit d’interaction rotor-stator: étude analytique, Expérimentale et Numérique”. PhD thesis. Université de Sherbrooke, 2020.

[49] Stephen B. Pope. “Mean velocity profiles”. In: *Turbulent Flows*. Cambridge University Press, 2000, pp. 272–274.

[50] *PowerFLOW Best Practices Guide for External Aerodynamics, PF202-R3-BP*. 2021.

[51] *PowerFLOW User’s Guide*. 2024.

[52] *PowerINSIGHT User’s Guide*. 2014.

[53] K. Sbeih et al. “Accurate automotive spinning wheel predictions via deformed treaded tire on a full vehicle compared to full width moving belt wind tunnel results”. In: *SAE Technical Paper Series* (2023). DOI: 10.4271/2023-01-0843.

[54] B. Schnepf, T. Schütz, and T. Indinger. “Further investigations on the flow around a rotating, isolated wheel with detailed tread pattern”. In: *SAE International Journal of Passenger Cars - Mechanical Systems* 8.1 (2015), pp. 261–274. DOI: 10.4271/2015-01-1554.

[55] B. H. Schnepf et al. “Untersuchung von Einflussfaktoren auf die umströmung eines PKW-Rades in simulation und experiment”. PhD thesis. Universitätsbibliothek der TU München, 2016.

[56] T. Schütz. *Aerodynamics of Road Vehicles*. Society of Automotive Engineers, 2016.

[57] T. Schütz. “Ein Beitrag zur Berechnung der Bremsenkühlung an Kraftfahrzeugen”. PhD thesis. Universität Stuttgart, 2009.

[58] R. Sibson. “Slink: An optimally efficient algorithm for the single-link cluster method”. In: *The Computer Journal* 16.1 (1973), pp. 30–34. DOI: 10.1093/comjnl/16.1.30.

[59] C. E. Simpson et al. “Detecting vortices within unsteady flows when using single-shot piv”. In: *Experiments in Fluids* 59.8 (2018). DOI: 10.1007/s00348-018-2575-3.

[60] P. R. Stevens and A. Sciacchitano. “Application of clustering and the Hungarian algorithm to the problem of consistent vortex tracking in incompressible flowfields”. In: *Experiments in Fluids* 62.8 (2021). DOI: 10.1007/s00348-021-03265-w.

[61] C. M. Teixeira. “Incorporating turbulence models into the lattice-boltzmann method”. In: *International Journal of Modern Physics C* 09.08 (1998), pp. 1159–1175.

[62] TUM. *Geometrie*. URL: https://www.epc.ed.tum.de/aer/forschungsgruppen/automobilaerodynamik/drivaer/geometrie/.

[63] G. H. Vatistas. “New model for intense self-similar vortices”. In: *Journal of Propulsion and Power* 14.4 (1998), pp. 462–469. DOI: 10.2514/2.5323.

[64] Alexander J. Wagner. “Chapter 4 - Lattice Boltzmann”. In: *North Dakota State University*. 2008, pp. 17–22.

[65] A. Wäschle. “Numerische und experimentelle Untersuchung des Einflusses von drehenden Radern auf die Fahrzeugaerodynamik”. PhD thesis. 2006.

[66] A. Wäschle and J. Wiedemann. “Numerische Simulation der Radumströmung zur Untersuchung des Radeinflusses auf die Fahrzeugaerodynamik”. In: *Berechnung und Simulation im Fahrzeugbau* VDI-Bericht 1701 (2002), pp. 325–352.

[67] A. Wäschle et al. “Flow around an isolated wheel - experimental and numerical comparison of two CFD codes”. In: *SAE Technical Paper Series* (2004). DOI: 10.4271/2004-01-0445.

[68] S. Windsor and A. Gaylard. “The Effect of Base Bleed and Rear Bleed and Rear Cavities on the Drag of an SUV”. In: SAE, 2010.

[69] F. Wittmeier et al. “Reifenentwicklung unter aerodynamischen Aspekten”. In: *ATZ - Automobiltechnische Zeitschrift* 115.2 (2013), pp. 144–150. DOI: 10.1007/s35148-013-0038-y.

# Part V

# Appendices

# A

# Appendix A - Geometry Orthogonal Views

## A.1. Standalone Tire

Orthogonal views that have not been used in the main body of the report of the standalone tire geometry (tire and arm).

**Figure A.1:** Inside side view of standalone tire geometry.

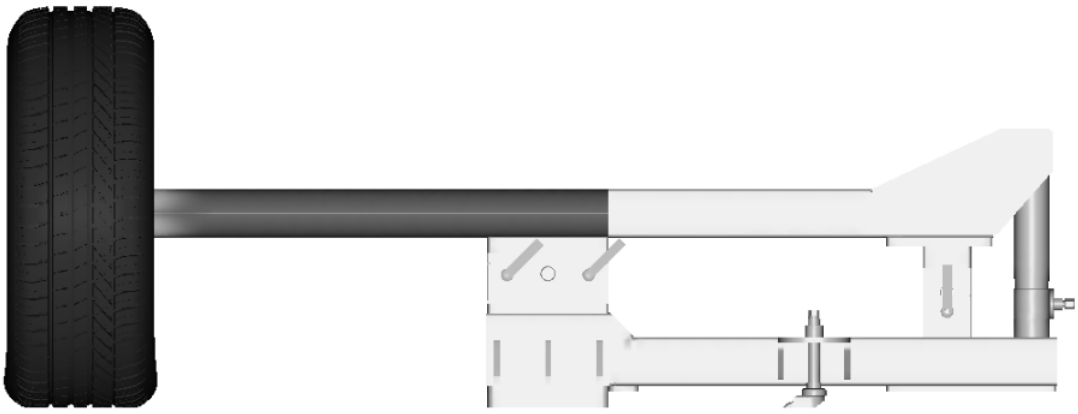

**Figure A.2:** Rear view of standalone tire geometry.

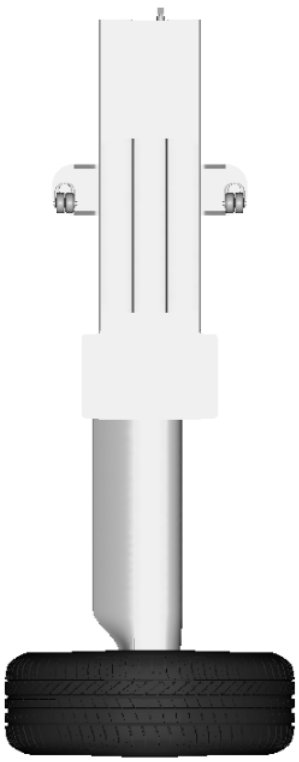

**Figure A.3:** Bottom view of standalone tire geometry.

## A.2. Full Vehicle:DrivAer Model

Orthogonal views that have not been used in the main body of the report of the *DrivAer* model.

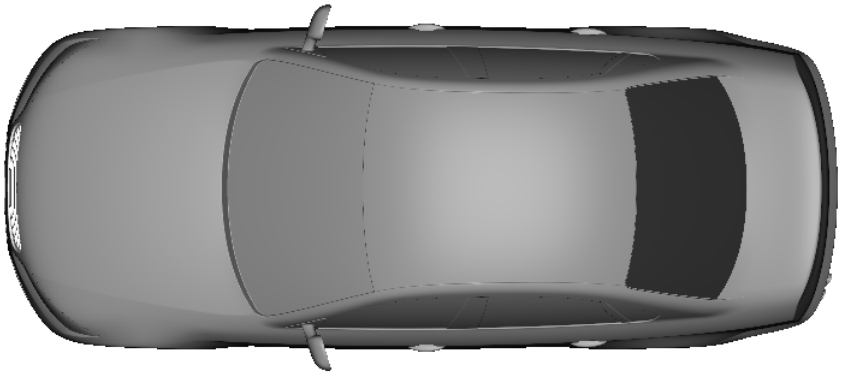

**Figure A.4:** Top view of *DrivAer* model.

**Figure A.5:** Rear view of *DrivAer* model.

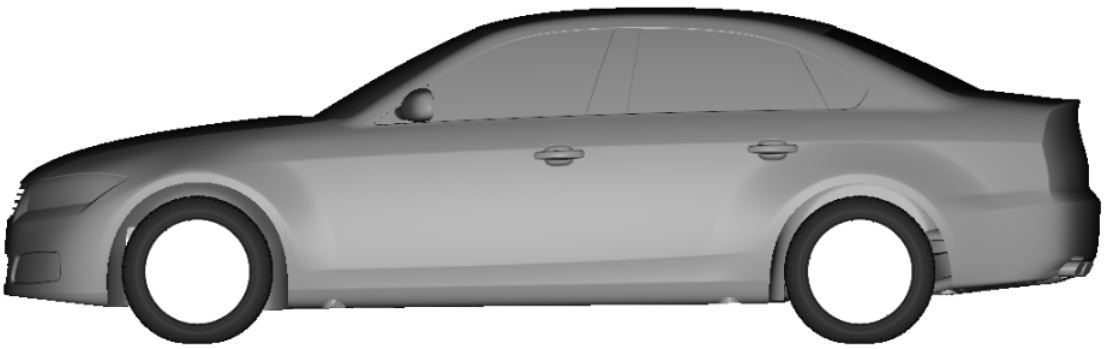

**Figure A.6:** Side view of *DrivAer* model.

# B

# Appendix B - Parametric Deformations

This Appendix offers a depiction of the resulting geometry from the implementation of the parametrisation described in Chapter 8.

## B.1. Bulge Deformations

### B.1.1. Bulge Size

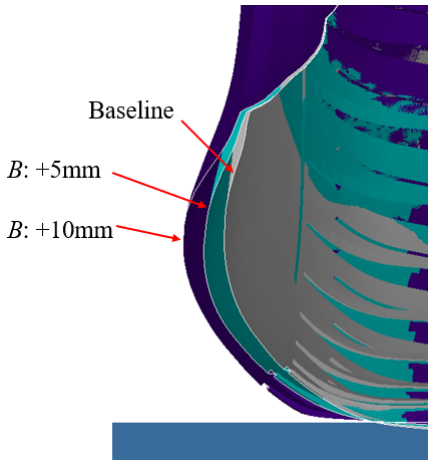


**Figure B.1:** Bulge Size *B* deformations, front view with plane cutting cross section.

### B.1.2. Lateral Insertion Angle $\alpha$

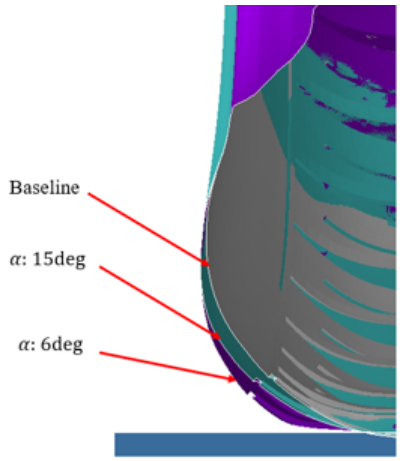


**Figure B.2:** Lateral Insertion Angle $\alpha$ deformations, front view with plane cutting cross section.

### B.1.3. Longitudinal Insertion Angle $\beta$

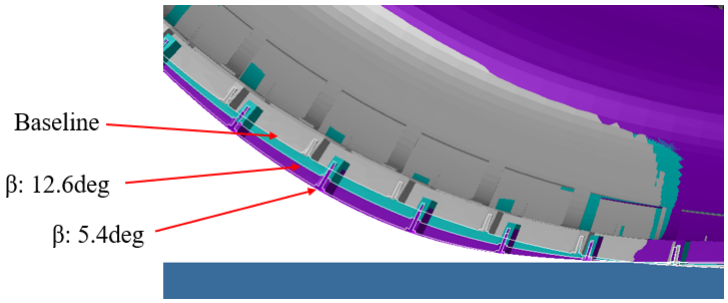


**Figure B.3:** Longitudinal Insertion Angle $\beta$ deformations, side view with plane cutting cross section.

# B.2. Contact Patch Deformations

## B.2.1. Contact Patch Length L

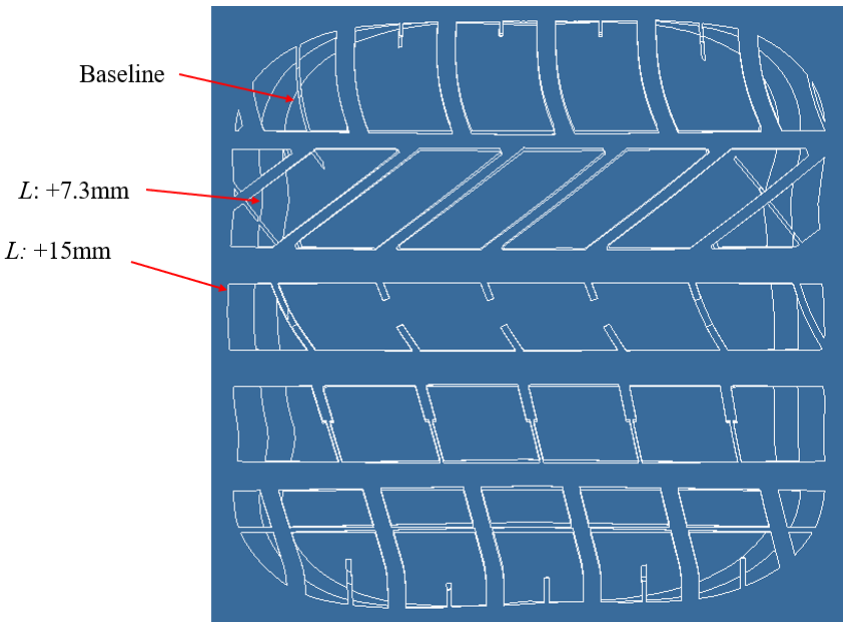


**Figure B.4:** Contact Patch Length *L* deformations. Bottom view where right is front, and bottom is outside. The arm is on the top, to the inside of the tire.

## B.2.2. Contact Patch Width W

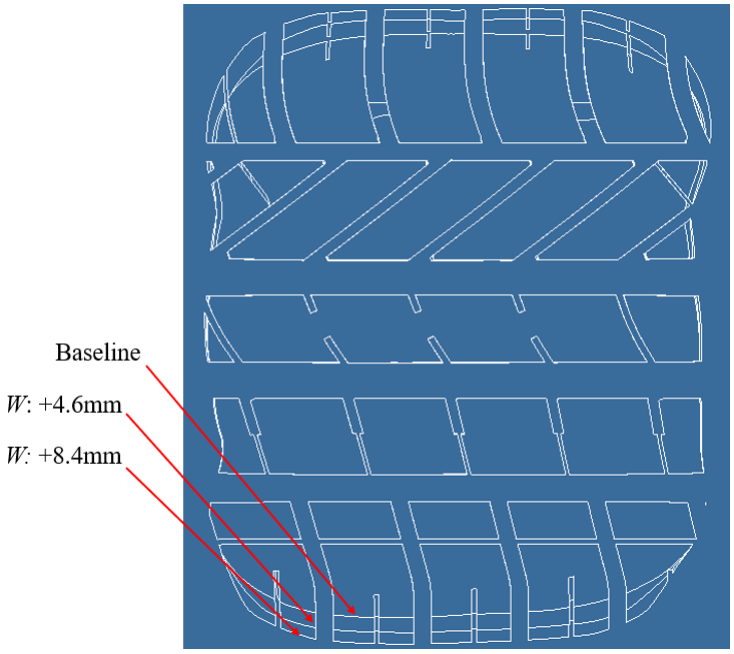


**Figure B.5:** Contact Patch Width *W* deformations.

### B.2.3. Contact Patch Curvature over Length R+L

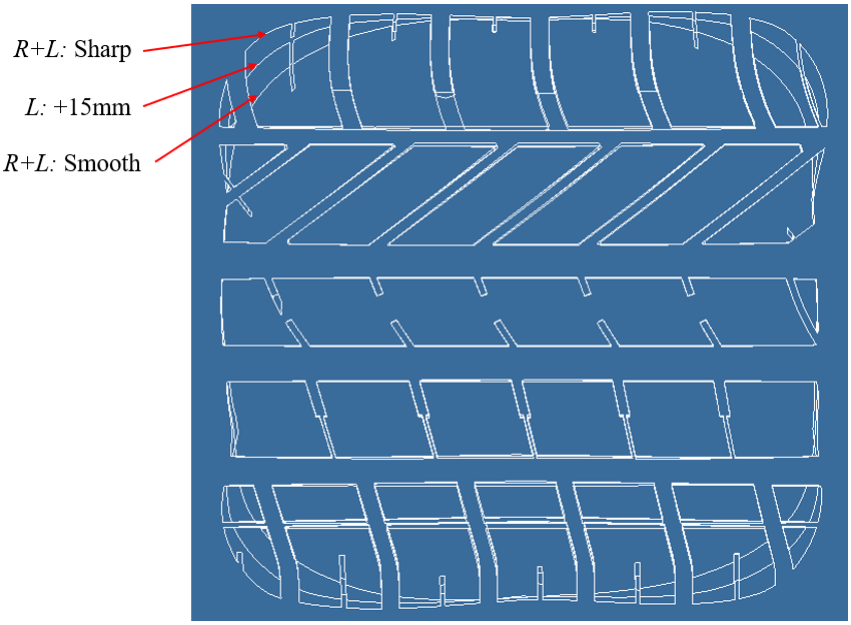


**Figure B.6:** Contact Patch Curvature over Length *R+L* deformations.

### B.2.4. Contact Patch Curvature over Width R+W

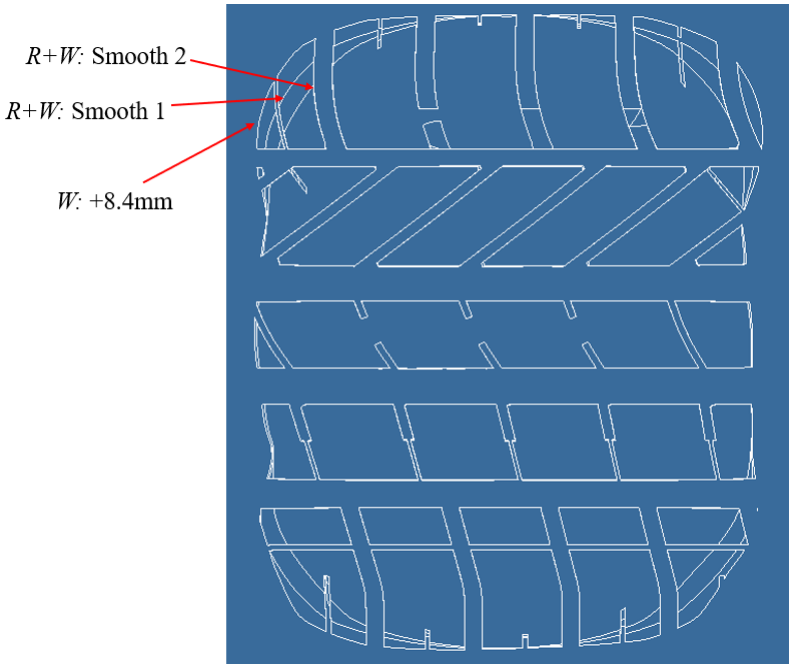


**Figure B.7:** Contact Patch Curvature over Length *R+W* deformations.

### B.2.5. Contact Patch Cambered Shape

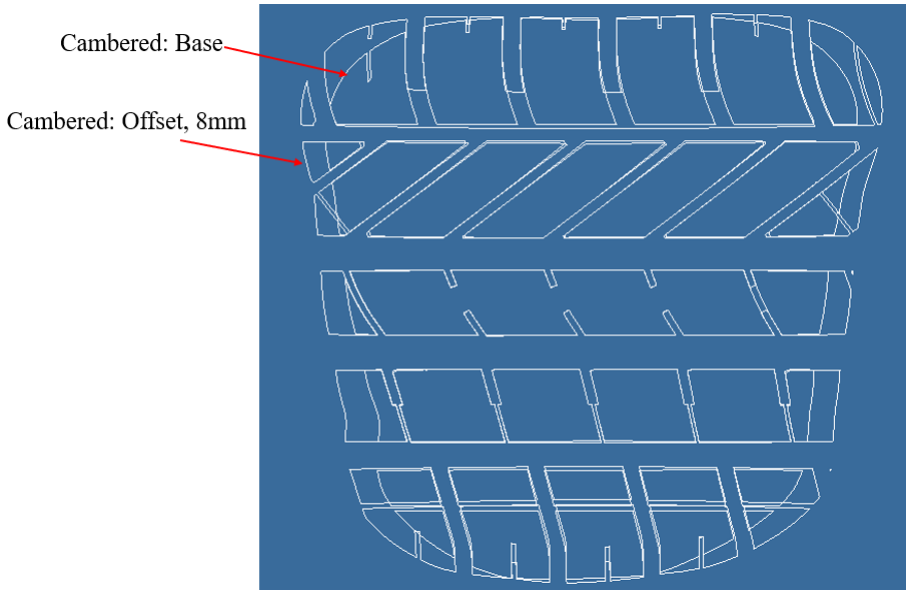


**Figure B.8:** Contact Patch Cambered Shape deformations.

### B.2.6. Contact Patch H-Shape

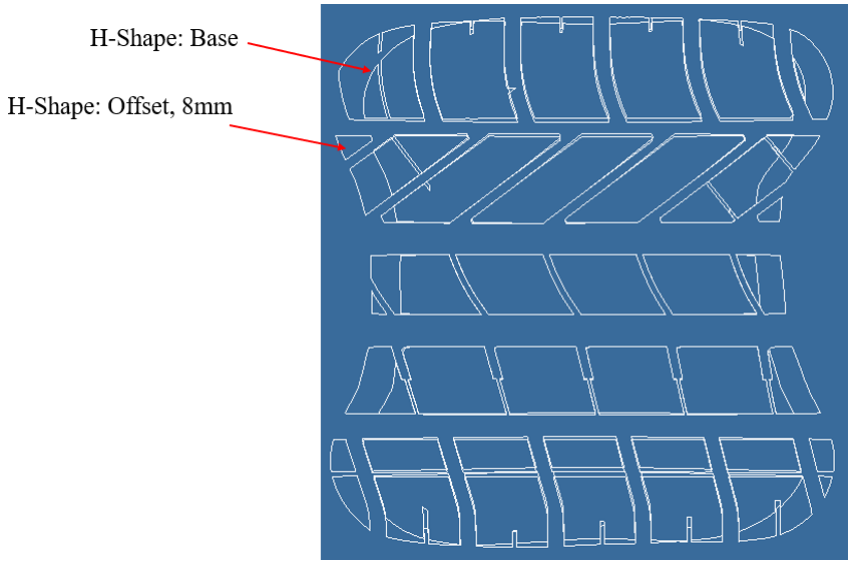


**Figure B.9:** Contact Patch H-Shape deformations.

# C

# Appendix C - VR Regions

This Appendix provides a depiction of the Variable Resolution (VR) regions 6, 7, 8 and 9 for the full vehicle setup described in Section 10.2.

## C.1. Full Vehicle: DrivAer

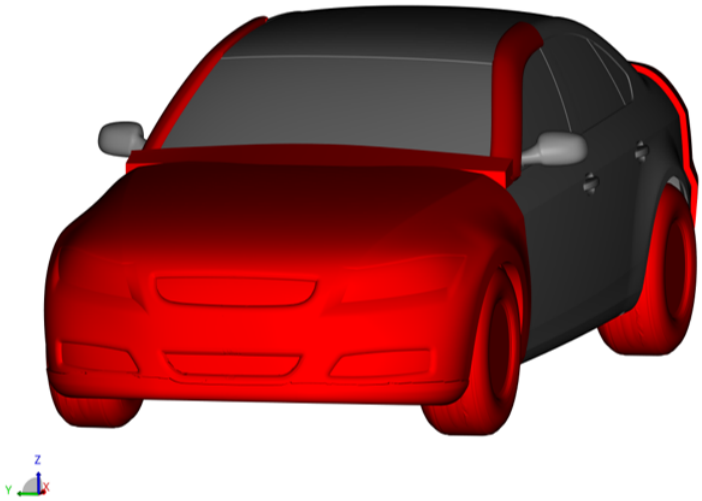

**Figure C.1:** VR 9 Region for full vehicle setup, ISO-view front.

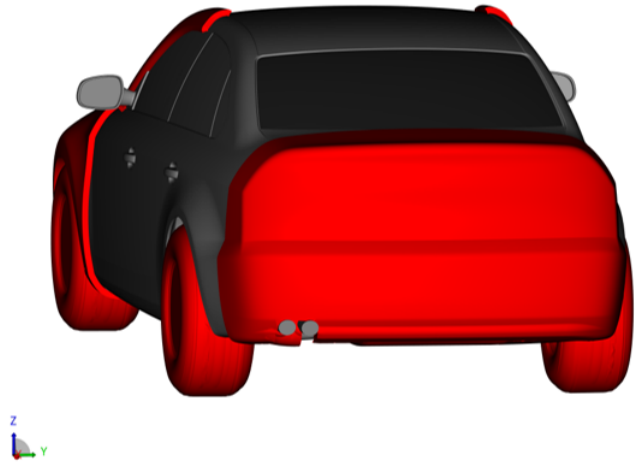

**Figure C.2:** VR 9 Region for full vehicle setup, ISO-view rear.

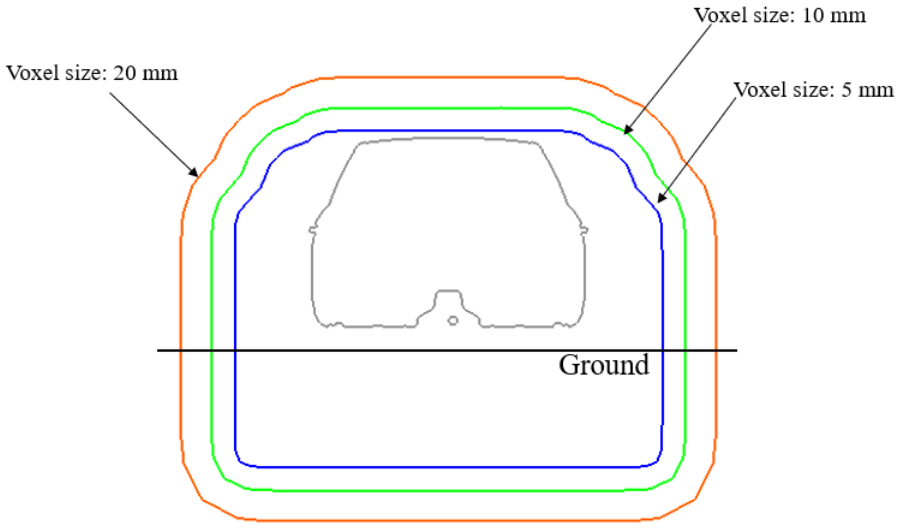


**Figure C.3:** VR Regions 8, 7 and 6 for full vehicle setup, front view.

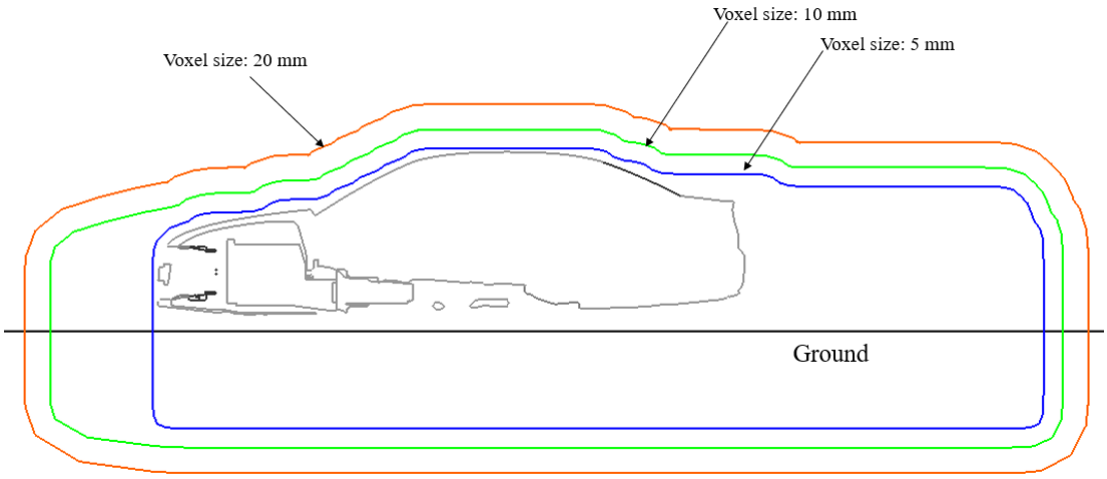


**Figure C.4:** VR Regions 8, 7 and 6 for full vehicle setup, side view.

# D

# Appendix D - Vortex Identification Methods

This Appendix provides the description of the vortex identification methods discussed in Section 4.2.

## D.1. $X$-Vorticity

The expression of vorticity magnitude: $\omega = \nabla \times \mathbf{u}$, is non-dimensionalized as $\frac{\nabla \times \mathbf{u}}{u_c/L_c}$ as shown in PowerFLOW's User's Guide [51], where $u_c$ is the characteristic velocity, and $L_c$ is the characteristic length. Then, the $x$-component of the vorticity $\omega_x$ is given by:

$$\omega_x = \frac{\partial w}{\partial y} - \frac{\partial v}{\partial z} \tag{D.1}$$

## D.2. Swirl

From [51], the swirl is given by:

$$\frac{u}{|u|} \cdot \nabla \times \mathbf{u} \tag{D.2}$$

Non-dimensionalized:

$$\frac{\frac{u}{|u|} \cdot \nabla \times \mathbf{u}}{u_c/L_c} \tag{D.3}$$

## D.3. $Q$-Criterion

As defined by [29], the $Q$-Criterion is expressed as:

$$Q = -\frac{1}{2}\left(\frac{\partial u}{\partial x}^2 + \frac{\partial v}{\partial y}^2 + \frac{\partial w}{\partial z}^2 + 2\frac{\partial v}{\partial x}\frac{\partial u}{\partial y} + 2\frac{\partial w}{\partial x}\frac{\partial u}{\partial z} + 2\frac{\partial w}{\partial y}\frac{\partial v}{\partial z}\right) \tag{D.4}$$

This expression is non-dimnesionalised in PowerFLOW by scaling with $u_c^2/L_c^2$.

## D.4. $\lambda_2$

$\lambda_2$ is the second eigenvalue of $S^2 + \Omega^2$, where $S$ is the symmetric deformation tensor [51]:

$$S_{ij} - \frac{1}{2}\left(\frac{\partial v_i}{\partial x_j} + \frac{\partial v_j}{\partial x_i}\right) \tag{D.5}$$

and $\Omega$ is the anti-symmetric spin tensor [51]:

$$\Omega_{ij} - \frac{1}{2}\left(\frac{\partial v_i}{\partial x_j} - \frac{\partial v_j}{\partial x_i}\right) \tag{D.6}$$